Mechanism of Inverse Bainitic Transformation in High Carbon Steels

by

Rangasayee Kannan

A thesis submitted in partial fulfillment of the
requirements for the degree of

Doctor of Philosophy

in
Materials Engineering
Department of Chemical and Materials Engineering
University of Alberta

ABSTRACT

The formation of bainite is the most studied and the most debated phase transformation in steels, with research spanning almost a century. With two theories of transformation, the transformation mechanism of bainite is still a disputed subject among physical metallurgists. Upper bainite and lower bainite are the two common bainite morphologies in engineering steels, but the microstructure of bainite is complex with several other possible morphologies of bainite. Though the transformation of other forms of bainitic microstructure can be explained in terms of either of the theories of bainite transformation, the transformation of inverse bainite which is reported in eutectoid and hypereutectoid steels is still unclear. Fundamental understanding of bainitic microstructure is a key element in the understanding of the bainitic transformation from austenite. Little work has been made over the years to verify the existence of inverse bainite although its existence is of great importance for understanding of the eutectoid decomposition of austenite. Majority of the information presented in the literature was focused on presenting two dimensional micrographs to prove the existence of inverse bainite. However, the mechanism of the transformation and the microstructure evolution during the decomposition of austenite to inverse bainite still remain unknown. This thesis, describes the fundamental understanding of the inverse bainite transformation using both advanced characterization techniques and theoretical approaches to reveal its true nature.

It was found that inverse bainite transformation proceeds by formation of cementite midrib from parent austenite through Negligible Partitioning Local Equilibrium (NPLE) kinetics as the first stage of transformation. During the second stage, inverse bainitic ferrite nucleation occurs in a Para-Equilibrium (PE) mode, and when the transformation time is increased, there is a transition in kinetics from PE to NPLE.

Two different orientations of secondary carbides were observed to nucleate through PE kinetics within inverse bainitic ferrite during the third stage of the transformation. Firstly the carbides near the cementite midrib/ferrite interface (V1 type) and the second type of carbides at the ferrite/martensite(prior austenite) interface oriented parallel to the growth direction of ferrite (V2 type). Through carbon concentration measurements within inverse bainitic ferrite, it was found that the inverse bainitic ferrite at the θ_m/α interface is supersaturated with carbon content much higher than the para-equilibrium carbon content. Carbon segregated θ_m/α interface acts as nucleation sites for the V1 type secondary carbides. The nucleation of secondary carbides in inverse bainite at the $\alpha/\alpha'(\gamma)$ interface is a consequence of the relative competition between the incomplete transformation phenomenon of ferrite and the resumption of ferrite transformation by the precipitation of carbides at the $\alpha/\alpha'(\gamma)$ interface.

When the transformation time is sufficiently long, inverse bainite microstructure becomes degenerated to be conventional upper bainite, which is the fourth stage of the transformation. It was found that the cementite midrib dissolution starts because of the C diffusion flux between the cementite midrib and secondary cementite. The carbon diffusion flux is caused by the NPLE growth kinetics of cementite midrib, whereas secondary cementite growth in ferrite follows a PE kinetics. By the time the C diffusion flux is nullified, the secondary carbides are coarser than the cementite midrib, and by Gibb's Thomson effect secondary carbides grow at the expense of cementite midrib. This results in transport of solutes from the cementite midrib to the secondary cementite. This process continues until the carbon concentration at the cementite midrib/ferrite interface reaches the matrix ferrite carbon concentration, and the location of the cementite midrib in the degenerated microstructure can be identified as a solute enriched region in ferrite.

The experimentally observed transformation and microstructure evolution is further supported using suitable theoretical calculations. CALPHAD based thermodynamic driving force nucleation model and mathematical thermo-kinetic model using the principles of PE diffusion and Johnson-Mehl-Avrami-Kolmogorov (JMAK) kinetics has been shown to provide fair predictions regarding the nucleation conditions and the growth kinetics of the transformation.

PREFACE

The materials presented in the current thesis are derived research project under supervision of Dr. Leijun Li, which has been funded by Natural Sciences and Engineering Research Council (NSERC) of Canada. Parts of the work has been published in peer-review journals.

Chapter 3 of this work has been submitted as Kannan, R., Wang, Y., and Li, L., “Banded Microstructure in a Low-Alloyed Eutectoid Steel”, to the journal *Materials Science & Technology*.

Chapter 4 of this work has been published in part in the following papers

Kannan, R., Wang, Y., and Li, L., “Identification of Inverse Bainite in Fe-0.84C-1Cr-1Mn Steel”, *Metallurgical & Materials Transactions A*, 2017, 48(3), 948-952.

Kannan, R., Wang, Y., and Li, L., “Microstructural Evolution of Inverse Bainite in a Hypereutectoid Low Alloy Steel”, *Metallurgical & Materials Transactions A*, 2017, 48(12), 6038-3054.

Kannan, R., Wang, Y., Nouri, M., Li, D.Y., and Li, L., “Instrumented Indentation Study of Bainite/Martensite Duplex Microstructure”, *Materials Science & Engineering A*, 2018, 713, 1-6.

Chapter 5 of this work has been published as Kannan, R., Wang, Y., and Li, L., “A thermodynamic study of inverse bainitic transformation”, *Journal of Materials Science*, 2018, 53(17), 12583–12603.

Chapter 6 of this work has been submitted as Kannan, R., Wang, Y., Poplawsky, J., Babu, S.,S., and Li, L., 2018 “Cascading phase transformations in high carbon steel resulting in the formation of inverse bainite : An atomic-scale investigation”, to the journal *Nature Scientific Reports*.

Chapter 7 of this work is to be submitted as Kannan, R., Wang, Y., Poplawsky, J., More, K., Babu, S.S., and Li, L., “Nucleation of secondary cementite during inverse bainitic transformation”, to the journal *Acta Materialia*.

Chapter 8 of this work is to be submitted as Kannan, R., Wang, Y., Poplawsky, J., Babu, S.,S., and Li, L., 2018 “Dissolution of Cementite Midrib During Inverse Bainitic Transformation”, to the journal *Scripta Materialia*.

Part of Appendix 1 of this work has been published as Kannan, R., Wang, Y., and Li, L., “A Dilatometric Investigation of Inverse Bainite Transformation”, *Journal of Materials Science*, 2018, 53(5), 3692-3708.

In these published and submitted papers, Rangasayee Kannan was responsible for conducting experiments, data analysis, and paper writing. Dr. Jonathan Poplawsky conducted the APT experiments and helped with the reconstruction of the APT data. Dr. Karen More helped with the TEM measurements. Dr. Meisam Nouri helped with the instrumented indentation tests under the supervision of Dr. D.Y. Li. Dr. Yiyu Wang’s role was to review papers and help with revisions. Dr. S.S. Babu helped with the APT data interpretation. Dr. Leijun Li was the supervisory author, provided advice for experiments and data interpretation, and helped with paper writing and revisions.

To my late grandparents, Ammama, Appa, Amma, and Akkum (Veeraraghavan Kannan) for your love, encouragement, and continued support without which I would have never made it to this stage.

ACKNOWLEDGMENTS

Words can not describe my gratitude towards my supervisor, Professor Leijun Li, for his appreciable inspiration, support and patience throughout my PhD studies. His love and enthusiasm for metallurgy, and his drive to think “one step deeper” has been truly inspiring throughout my degree and has significantly influenced on how I address scientific problems. It was a great pleasure to have the opportunity to work under his supervision. As the next stage of my career is ahead, I hope to keep in touch and maintain a friendship with Dr. Li in the years to come.

I deeply appreciate the great help from the several professors, especially Dr. Patricio Mendez for not only introducing myself and forwarding my e-mail to Dr. Li when I was seeking a potential supervisor, but also for letting me use the dilatometer and the metallographic sample preparation facilities at the Canadian Center for Welding and Joining (CCWJ), Dr. Hani Henien at the Advanced Materials and Processing Laboratory (AMPL), University of Alberta for letting me use the metallographic sample preparation facilities, Dr. Douglas Ivey for helping me with the TEM analysis, Dr. Dongyang Li providing access to the nanoindentation equipment, reviewing my manuscript, and providing helpful suggestions, Dr. Sudarsanam Suresh Babu at the University of Tennessee, Knoxville for the thoughtful discussions on the Atom Probe results and reviewing my manuscripts and providing helpful suggestions.

I also acknowledge the technical support from the nanoFAB staffs at the University of Alberta, especially Mr. Peng Li, Dr. Anqiang, Dr. Shihong Xu, Dr. Nancy Zhang, and Miss Shiau-Yin Wu for their help with training me in the characterization tools required for this study. Mr. Paul Mason and Dr. Weiwei Zhang from ThermoCalc Software Inc. are acknowledged for clarifying the technical issues I had with using the ThermoCalc software. I would like to acknowledge the researchers at Center for Nanophase Materials Sciences (CNMS) at the Oak Ridge National Laboratory, which is a U.S. DOE Office of Science User Facility for providing access to the Atom Probe, Focused Ion Beam, and Transmission Electron Microscopy facility. Special thanks to Dr. Jonathan Poplawsky from Oak Ridge National Laboratory for the Atom Probe Tomography experiments and discussion. Dr. Karren Leslie More and Ms. Dorothy W. Coffey from Oak Ridge National Laboratory are thanked for their help with the TEM sample preparation using Focussed Ion Beam and TEM microscopy. Dr. Muhammad Rashid of EVRAZ NA, Regina is acknowledged for letting me use the dilatomer at the EVRAZ R&D Center.

I would like to thank my colleagues Dr. Ata Kamyabi Gol for training me on the dilatometer and ThermoCalc, Dr. Meisam Nouri for the help with the nanoindentation experiments, Dr. Aziz Bogno for the help with DICTRA calculations. All members in the Leijun Li Research group are thanked for the stimulating discussion and help on experiments. Special thanks to Jason (Dr. Wang) for your help right from the start of my PhD studies. Thank you for training me on all the characterization tools, sharing your knowledge, reviewing my manuscripts, and critiquing my hypotheses. I certainly enjoyed all the stimulating research discussions we had. I believe we grew as friends apart from work too and hope to keep in touch in the years to come. Thanks to Neil Anderson, for reviewing my manuscripts in short notice, and for making our lab a safer and an organized place to work. Thanks to Rebekah for your help with the project during your undergrad and with the dilatometry experiments. Thanks to Daniel Yang for reviewing my manuscript and for the company. Thanks to Lucas for the funny conversation we had, swimming sessions we went.

I would like to gratefully acknowledge the Natural Sciences and Engineering Research Council (NSERC) of Canada, for the financial support. Special thanks to the ASM Edmonton chapter, Faculty of Graduate Studies and Research (FGSR), Graduate Students Association (GSA) for providing me with scholarships which helped me travel to conferences and present my research.

I would like to thank my friends Vivek Sengupta for the company and the travel we did together, Vignesh Nallasivam for letting me stay at your place during my short visit to Oak Ridge. Special thanks to my childhood friend, schoolmate, collegemate, and my roommate in Edmonton Uppiliappan Rengerajan for your help with settling down, all the travel we did, clearing my COMSOL doubts etc.. Our friendship (14 years and growing) just gets stronger with time!

I would like to thank Akkum (Veeraraghavan Kannan), Appa, Amma for their continued, unconditional, and endless support and patience throughout my life. They have always supported my choices, dreams, and take pride in smallest of my achievements. I would have not been in this stage if not for them.

Finally, I would like to thank god for all the things that have happened in my life so far.

Contents

List of Tables

List of Figures

Chapter 1

Introduction

1.1 Literature review

Iron shows several allotropic structures, namely δ, γ, and α with the temperature and alloying additions governing the stability of different allotropic forms. The addition of carbon as an alloying element to iron, gives steel. Though in general steel is defined as an alloy of iron and carbon, with several other alloying additions possible the complexity of the iron/carbon system increases. With several invariant points present in the iron/carbon system, the eutectoid point which involves the evolution of "high temperature" austenite to room temperature ferrite/cementite continues to be the most studied phase transformation in steels. Depending on the alloy content and the cooling rate, "high temperature" austenite can transform into different forms of room temperature microstructure, to name a few, pearlite, allotriomorphic ferrite, Widmanstätten ferrite, acicular ferrite, bainite, martensite. The eutectoid transformation of austenite to such different forms of room temperature microstructure has a significant impact on the properties/performance of the steel. Thus, a fundamental understanding of eutectoid transformations is necessary to tailor the room temperature microstructure suitable for the intended performance of the steel.

Amongst the above mentioned eutectoid transformation products, the transformation of bainite has gathered the most interest amongst physical metallurgists due to its high strength (similar to martensite) and relatively better ductility (similar to pearlite). Apart from its superior mechanical properties, owing to its formation at a temperature range between the reconstructive pearlite and displacive martensite, understanding the fundamental mechanism of its transformation has been challenging for the physical metallurgists with bainite showing evidence for both the reconstructive as well as the displacive transformation behavior, and therefore, bainitic transformation continues to be the most studied eutectoid phase transformation in steels.

1.1.1 Definition of the term Bainite

Aaronson [1] reviewed the available definitions [2–6] of the term “bainite”, and classified that bainite can be defined using three definitions, with each of them being incompatible to the other two. The three definitions of the term bainite were:

1. **Microstructural definition**, which states that bainite, unlike pearlite, is an eutectoid decomposition product of austenite with a non-lamellar dispersion of carbides and ferrite.

2. **Kinetic definition**, which states that bainite is a transformation product of austenite formed between pearlite and martensite transformation temperatures, characterized by its own C-curve in the TTT diagram. Also, as per the kinetic definition, bainite exhibits the incomplete reaction phenomenon, the tendency of which increases with the increase in transformation temperature.

3. **Surface-relief definition** which states bainite to be any precipitate plate which has a composition different from austenite, and exhibits surface relief, which is characteristic of martensitic type transformation.

Though there is adequate evidence of each of these definitions, the various definitions are inconsistent with each other, so a microstructure which can be classified as bainite according to one definition might not be classified as bainite as per the other definition. This indicates the complexity of the bainitic transformation, and gives rise to several possible eutectoid decomposition microstructure which can be classified as ”bainite”, these include, upper bainite, lower bainite, granular bainite, columnar bainite, and inverse bainite.

1.1.2 Mechanism of transformation of bainite - The two theories of transformation

Bainite was discovered as a dark etched acicular microstructure formed in a temperature range between pearlite and martensite. Since its discovery in 1926, the microstructure of bainite is a subject of controversy among physical metallurgists. With two schools of thoughts, one being bainite forms by a displacive-diffusionless mechanism of transformation, the other being bainite forms by a reconstructive-diffusional mechanism of transformation, research on bainite spans to a period of almost a century. Though today it is widely accepted amongst physical metallurgists that the bainite grows via a displacive mechanism i.e. as plate-shaped (or lath-shaped) transformation product exhibiting an invariant plane strain surface relief effect. But discussion still continues as to whether the transformation is diffusional or diffusionless in nature. This section aims to summarize the critical findings of both the theories of bainite since its inception. Detailed discussion can be found in the review article by Fielding [7].

Diffusionless theory

Though the term 'bainite' was used after the discovery by Davenport and Bain in 1930 [2], the microstructure of bainite was identified by Hultgren in 1926 [8], where he called 'bainite' as troosite (fine mixtures of ferrite and cementite). Hultgren referred to such microstructure a 'martensite-troosite' owing to the morphological similarity to martensite, which originally hypothesized the diffusionless theory for bainite transformation. Later Vilella in 1936 [9], proposed a mechanism for bainite similar to martensite, where the bainitic ferrite was supersaturated with carbon during the nucleation, and eventually reject the excess carbon to surrounding austenite. Vilella also mentioned that the growth of bainite was rapid similar to martensite and even called bainite as 'quasi-martensite'. Later in 1939, Mehl [10] proposed that lower bainite forms by a diffusionless mechanism similar to martensite which involves lattice shearing. Further evidence for the diffusionless ideology for bainite transformation was provided by Zener [11], where he found out that alloying elements which retarded the martensitic transformation and not the pearlitic transformation also retarded the bainitic transformation. This made him draw the conclusion that bainitic transformation was similar to the martensitic transformation and not pearlitic type transformation which involves diffusion. Zener also used thermodynamics to explain the growth of bainite, by what is called the $T_\circ$ temperature, or the temperature at which austenite and ferrite of the same composition have the same free energy. The illustration of the $T_\circ$ concept is shown in Figure 1.1 (from [12]). Later in 1965-1967 Shackleton and Kelly characterized the surface relief due to bainitic transformation and found that the surface relief to follow an invariant plane type surface relief, which is characteristic of martensitic transformation. Though Zener did not include the effect of shear due to the bainitic transformation the $T_\circ$ provided an important break through for the diffusionless ideology for bainitic transformation as both the incomplete nature of the bainitic transformation and the existence of B_s temperature in the TTT

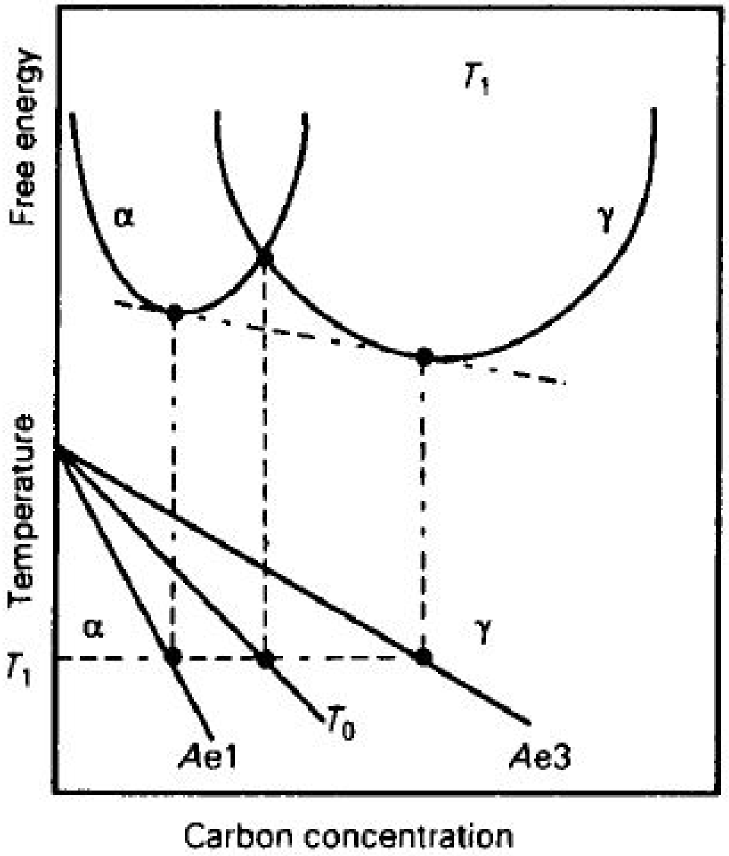

Figure 1.1: Illustration of the $T_\circ$ concept.

diagram could be explained. Following Zener's proposal, the hot stage microscopy experiments by Ko and Cottrell [6] imaged the surface relief due to the bainitic transformation, which was used as the evidence for bainitic transformation being similar to martensitic transformation which also involves the generation of surface relief.

The identification of ϵ carbides precipitation in lower bainite in 1961 [13], and the use of dilatometry to estimate the amount of ϵ carbide in lower bainite and comparing it to the total carbon content of the steel in 1965 [14] confirmed the fact that bainitic ferrite forms in a supersaturated state, thereby further providing evidence to a displacive type of transformation. Though the study was conducted on lower bainite, it was not conclusive as to whether upper bainitic ferrite was supersaturated as well. Christian in 1962 [15] proposed that lower banitic ferrite was supersaturated with carbon and upper bainitic ferrite was not supersaturated. Christian suggested that the crystallography of upper bainite was similar to low carbon martensite whereas the crystallography of lower bainite should match the martensite of the same alloy. Later in 1965-1967 Shackleton [16, 17] characterized the surface relief due to bainitic transformation and found that the surface relief due to bainitic transformation showed an invariant plane strain type of relief similar to martensitic transformation. Also, austenite and ferrite shared the KS orientation relationship similar to martensite, thus providing a crystallographic evidence for the diffusionless nature of bainitic transformation alone. In 1974, Nemoto [18] characterized the presence of dislocations in bainitic ferrite using thermionic emission microscopy. The existence of dislocations in bainitic ferrite can only be explained by the displacive nature of the transformation, which involves plastic relaxation accompanying the shape change.

Later in the 1980's, Bhadeshia [19] interpreted the crystallography of Widmanst*ä*ten ferrite and bainite and concluded that Widmanst*ä*ten ferrite is a result of back to back displacive growth of mutually accommodation ferrite plates and proposed that both Widmanst*ä*ten ferrite and bainite reactions involve carbon partitioning during the nucleation stage. During the growth, Widmanst*ä*ten ferrite involves carbon diffusion, whereas there is no carbon diffusion during the growth of bainite and bainite rejects the excess carbon into austenite only after the transformation is complete. Bhadeshia and Edmonds [20, 21] also refuted the ledgewise growth theory of bainite by conducting transmission electron microscopic investigation on high silicon steels. The addition of Si enabled the suppression of carbides in bainite. It was found that the sub-units of bainite grow even in the absence of carbide precipitation and therefore the sub-units cannot be compared to sympathetically nucleated ledges. The validity of local equilibrium model proposed by the ideologists of diffusion was also negated by the atom probe works conducted by Bhadeshia and Waugh [22], where no segregation of concentration spike of substitutional solutes was observed at the transformation interface. The atom probe work on bainite also showed that the carbon concentration within inverse bainitic ferrite was much higher than allowable carbon concentration in ferrite using the para-equilibrium approach. Bhadeshia also measured the growth rate of sub-units [23], and found that the rate of growth of sub-units of bainitic ferrite were three time the value predicted using the diffusional theory for bainite growth, further strengthening the argument that bainite transformation in diffusionless.

The quest to understand the true nature of bainitic transformation still continues with recent research in support of a diffusionless type of transformation, especially the one by Caballero *et al.* [24–27], where advanced characterization using atom probe has provided convincing evidence for the fact that bainitic ferrite is super-saturated, and the dislocation within bainitic ferrite act as nucleation sites for carbide precipitation within ferrite (Figure 1.2,from Ref. [25]), and no partitioning of substitutional solutes or ‘concentration spike’ is observed at the transformation interface (Figure 1.3, from Ref. [25])

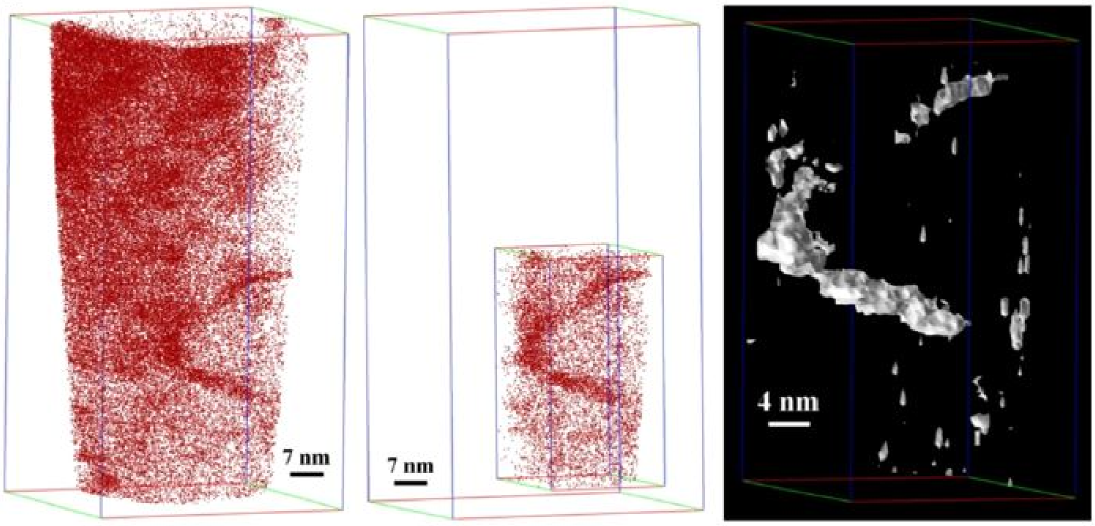

Figure 1.2: Carbon atom maps showing the presence of carbon clusters within bainitic ferrite. The high carbon region corresponds to austenite and the low carbon region corresponds to bainitic ferrite.

Diffusional theory

The idea of the diffusional theory for transformation of bainite stems from Robertson [3] in 1929. Robertson made the direct observation of the acicular bainite microstructure prior to the inception of the microstructure ‘bainite’. Robertson compared bainite to pearlite and suggested that the change in crystallography between pearlite and bainite was due to the change in nucleation sequence between pearlite (nucleated by carbide) and bainite (nucleated by ferrite). He believed that the growth of acicular Widmanst*ä*tten nature of the microstructure was accompanied by carbon diffusion. This was agreed by observations from Hultgren [28], Hillert [29], Davenport [30], and partially by Mehl [10] who suggested that upper bainite forms by a diffusion controlled process, whereas lower bainite forms via lattice shearing.

Amongst these researchers, Hultgren introduced the idea of paraequilibrium, wherein the bainitic ferrite/para-ferrite in alloy steels forms by the diffusion of C alone, and there is no diffusion of substitutional solutes across the transformation interface during the progress of the transformation. Hultgren also mentioned that in case of plain

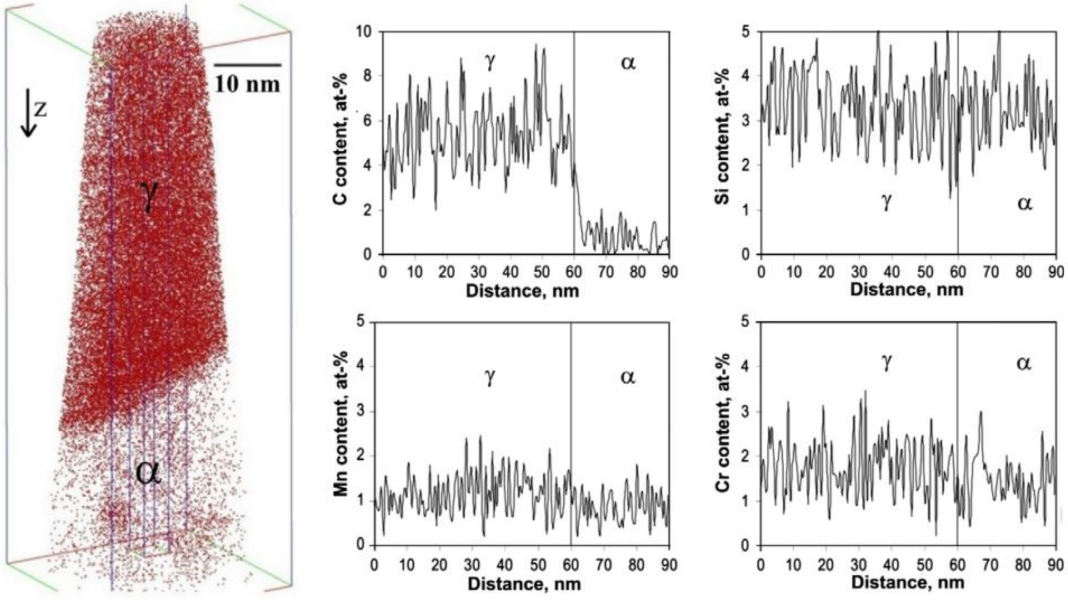

Figure 1.3: Carbon atom maps showing the presence of carbon clusters within bainitic ferrite. The high carbon region corresponds to austenite and the low carbon region corresponds to bainitic ferrite. Proximity histograms of the transformation interface show the absence of any substitutional solute 'concentration spike'.

carbon steels, bainitic ferrite/para-ferrite and martensite would be the same thing. The idea of the diffusional theory for bainite transformation was later supported by the hot-stage microscopy experiments of Ko and Cottrell [6] in 1952, where they measured the growth rate of bainitic ferrite, and found that the growth rate was slow enough to make a comparison to martensitic nature of the transformation, and a diffusional theory can explain the observed slower growth rates of bainite. However, the study by Ko and Cottrell also recorded surface reliefs, which are characteristic of martensitic type transformations. In order to overcome these contradictory observation, Ko and Cottrell went on to develop a new type of transformation called the 'Coherent Transformation' which allowed for transformation shear subject to the kinetic limitation of carbon diffusion into austenite. Though the growth rate measurements provided an inclination for bainitic transformation being diffusion controlled, the observed surface relief could not be explained by entirely a diffusional theory of transformation and the controversy surrounding the transformation continued. Although researchers claimed that upper bainite formed by diffusional process and lower bainite formed via. shearing of the lattice, Aaronson in 1962 [31] proposed a growth mechanism stating that both upper bainite and lower bainite formed by the same mechanism involving propagation of series of ledges controlled by a diffusive process. The ledgewise diffusion controlled growth model was validated by thermionic emission microscopy [18] to show that bainite growth occurred by continuous growth of ledges. A schematic of ledge-wise growth model for upper and lower bainte are shown in Figure 1.4

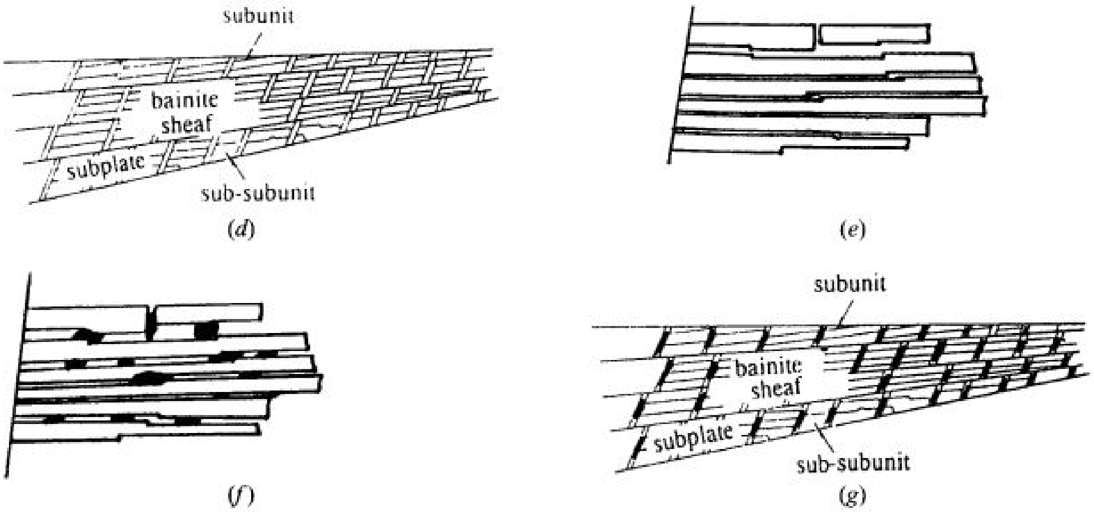

Figure 1.4: (a) Validation of Hillert's diffusionless model by comparing with experimental M_s temperature. (b) Comparison of diffusionless model to experimental B_s showing that there is no implication between the diffusionless $T_\circ$ and the B_s temperature.

Later in 1973 [32], the solute drag model and local equilibrium models, which were diffusion controlled were utilized to explain the nature of bainitic transformation. According to the local equilibrium (LE) model, a constant partial molar free energy among substitutional solutes is maintained across the transformation interface, meaning both carbon and substitutional solutes must diffuse across the transformation interface. In case of highly supersaturated phases (bainite), the LE model demands a narrow concentration spike (Negligible Partitioning Local Equilibrium (NPLE)) across the transformation interface. The NPLE type of transformation was used to explain the formation of upper bainite, whereas the PE concept was utilized to explain the low temperature microstructure of lower bainite. Hillert undertook thermodynamic analysis of the diffusionless transformation and the $T_\circ$ concept (including the strain energy term associated with bainite transformation) and showed that the B_s had no relation with the $T_\circ$ (Figure 1.5 from Ref. [33]) which corresponds to the diffusionless theory for bainite transformation. In 1990 [34], the Solute Like Drag Effect (SLDE) was used to explain the incomplete transformation phenomenon during

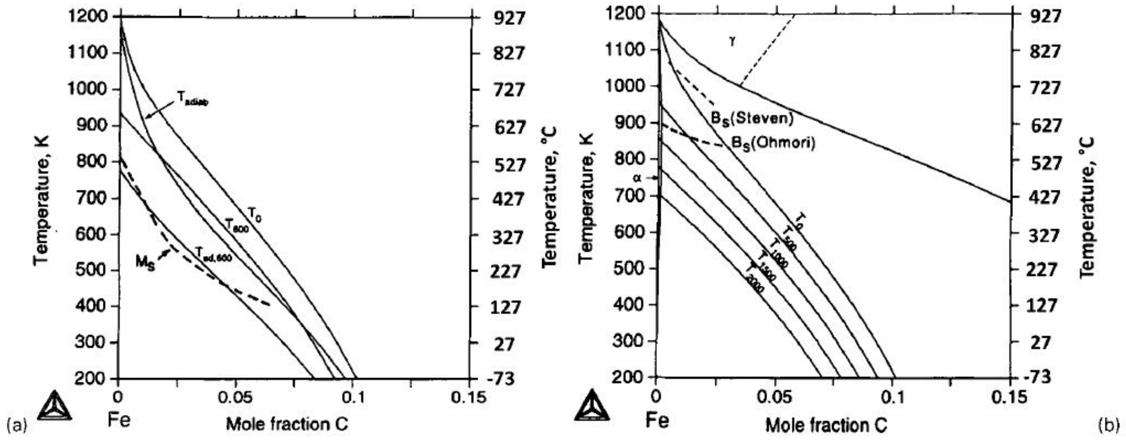

Figure 1.5: (a) Validation of Hillert's diffusionless model by comparing with experimental M_s temperature. (b) Comparison of diffusionless model to experimental B_s showing that there is no implication between the diffusionless $T_\circ$ and the B_s temperature.

bainite transformation. According to the SLDE, certain elements segregate at the austenite/ferrite transformation interface, thereby altering the carbon concentration gradient in austenite and retarding the growth of bainitic ferrite. Further in 1994, the TEM examination of carbides in lower bainite by Spanos [35] concluded the existence of three-phase crystallographic correspondence between ferrite, carbide, and austenite which was indicative that the carbides in lower bainite might have precipitated from austenite, which goes along with the diffusive theory of bainite transformation, but does not conclusively negate the fact that a displacive mechanism might be operating.

The quest to understand the true nature of bainitic transformation still continues with recent research in support of a diffusional type of transformation [36–41], with the most recent one being the work by Kolmskog and Borgenstam [38–41], where they used the existence of inverse bainite as a metallographic evidence for bainite transformation being diffusion controlled. The existence of inverse bainite provides direct evidence for the fact that there exists a symmetry among the eutectoid transformation products of austenite. The existence of inverse bainite and the metallographic evidence for the symmetry in the Fe-C system cannot be explained by the diffusionless nature of bainite transformation alone.

1.1.3 Summary of key transformation characteristics of eutectoid decomposition of austenite

Though the on-going controversy regarding bainitic transformation being diffusional or diffusionless, through extensive research spanning over the period of decades and studying different transformation characteristics, a systematic set of transformation characteristics exhibited by upper bainite, lower bainite, and Widmanst*ä*tten ferrite are presented in Table 1.1

Table 1.1: Key transformation characteristics in steels. ✓ represents consistency of the comment, × represents inconsistency, and • represents the case where the comment is sometimes consistent.

Characteristics	Upper bainite	Lower bainite	W_s ferrite
Nucleation and growth reaction	✓	✓	✓
Plate shape	✓	✓	✓
IPS Shape change with large shear	✓	✓	✓
Lattice correspondence during growth	✓	✓	✓
Co-operative growth of ferrite and cementite	×	×	×
High dislocation density	✓	✓	•
Has a glissile interface	✓	✓	✓
Always has an orientation within bain region	✓	✓	✓
Grows across austenite grain boundaries	×	×	×
High Interface mobility at low temperatures	✓	✓	✓
Reconstructive diffusion during growth	×	×	×
Bulk redistribution of X atoms during growth	×	×	×
Displacive transformation mechanism	✓	✓	✓
Reconstructive transformation mechanism	×	×	×
Diffusionless nucleation	×	×	×
Carbon diffusion during nucleation	✓	✓	✓
Reconstructive diffusion during nucelation	×	×	×
Often nucleates intragranularly on defects	×	×	×
Diffusionless growth	✓	✓	×
Local equilibrium at interface during growth	×	×	×
Para-equilibrium at interface during growth (NPLE)	×	×	✓
Diffusion of carbon during transformation	×	×	✓
Carbon diffusion controlled growth	×	×	✓
Incomplete reaction phenomenon	✓	✓	×

1.1.4 Microstructure of bainite

Several morphologies of eutectoid decomposition product of austenite have been called 'bainite' in the literature. Though upper bainite and lower bainite are widely studied, the morphology and microstructure of bainite is complicated with several other possible bainitic microstructures. Bhadeshia in Ref. [12] has reviewed the different morphologies of bainite, and analyzed if the morphology can be called as 'bainite' in the first place. The different morphologies of bainite quoted in the literature include:

Upper and Lower Bainite

Upper bainite and lower bainite are the two commonly quoted and widely researched microstructure of bainite. Upper bainite exhibits a characteristic lath shape of crystallographically matching ferrite sub-units, which are separated by carbide precipitates. Lower bainite is similar to upper bainite, except that in lower bainite the ferrite sub-units also contain fine distribution of carbide particles oriented at an angle of 55deg to the growth direction of ferrite sub-units. The typical micrograph of upper bainite and lower bainite [42] are shown in Figure 1.6.

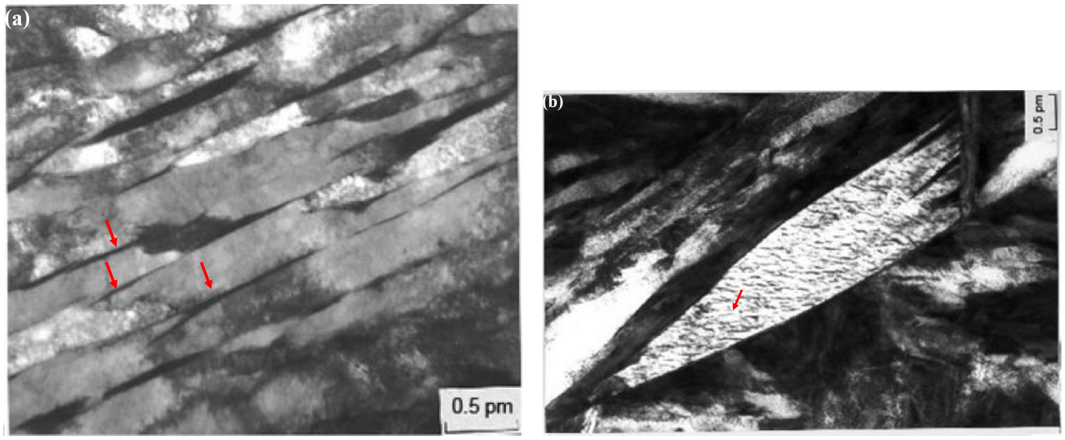

Figure 1.6: Transmission electron micrographs of upper bainite (a) and lower bainite (b). The inter-lath carbides of upper bainite and intra-lath carbide of lower bainite are indicted by red arrow.

Granular Bainite

Granular bainite is commonly found in continuously cooled low carbon steels which optically appears as coarse plates of ferrite (which provide the granular appearance) along with islands of martensite/retained austenite. Through TEM investigation it was found that the coarse plates of ferrite were individual sheaves of bainitic ferrite with very thin regions of austenite between the ferritic sub-units. The typical micrograph of granular bainite [43](adapted from [12]) is shown in Figure 1.7. Because of the low carbon concentration of the steels involved, no carbide precipitation is observed in bainite, which is one of the identifying factors for concluding the microstructure to be granular bainite. The carbon that is partitioned from the bainitic ferrite stabilizes the austenite, which is the reason for the presence of retained austenite in the final microstructure of granular bainite. It was found that granular bainite much similar to upper bainite and lower bainite shows no redistribution of substitutional solutes, and exhibits incomplete transformation phenomenon, which indicates that the transformation of granular bainite can be explained using conventional bainite transformation mechanism. From Bhadeshia [12], the peculiar morphology of granular bainite was a consequence of two factors, namely, the continuous cooling which permits extensive transformation of bainite during continuous cooling, and its existence in low-carbon steels which makes the identification of any sub-units difficult using optical microscopy.

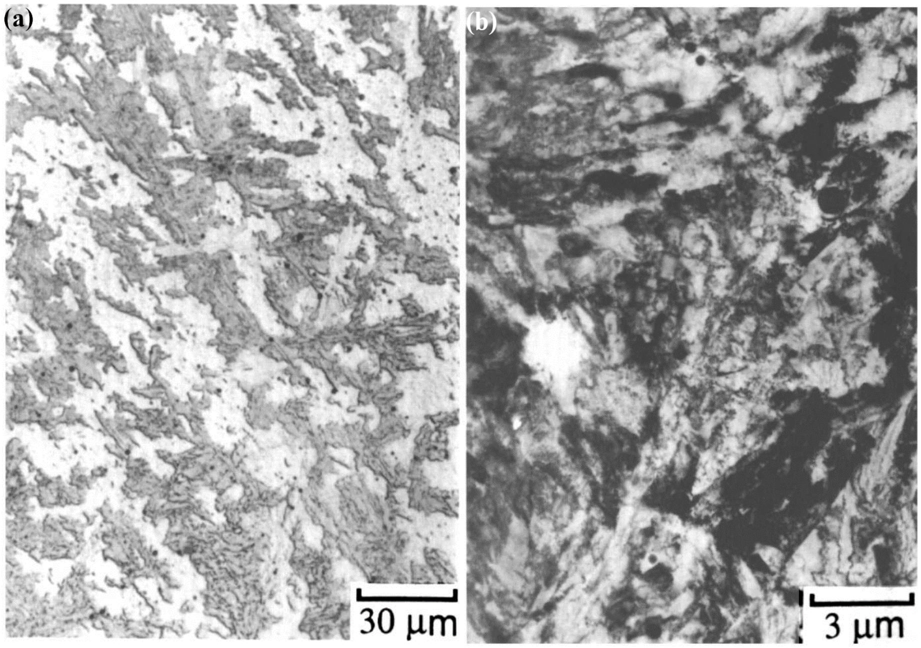

Figure 1.7: Optical micrograph (a) and TEM micrograph of granular bainite in Fe-0.15C-2.25Cr-0.5Mo wt% steel.

Columnar Bainite

The term columnar bainite stems from the microstructural definition of the term “bainite”, which is a non-lamellar aggregate of ferrite/carbides. Figure 1.8 [44](adapted from [12]) represents the typical micrograph of columnar bainite. In columnar bainite, two different orientations of carbides are observed, with the majority of carbides being aligned to the longer dimension of the colony, which is surrounded by a layer of coarse carbides at the austenite/ferrite interface. Bhadeshia [12] proposed that ”*It is probable that columnar bainite is more akin to pearlite than bainite, but further investigations are needed to make any sensible decisions about the mechanism of growth.*”

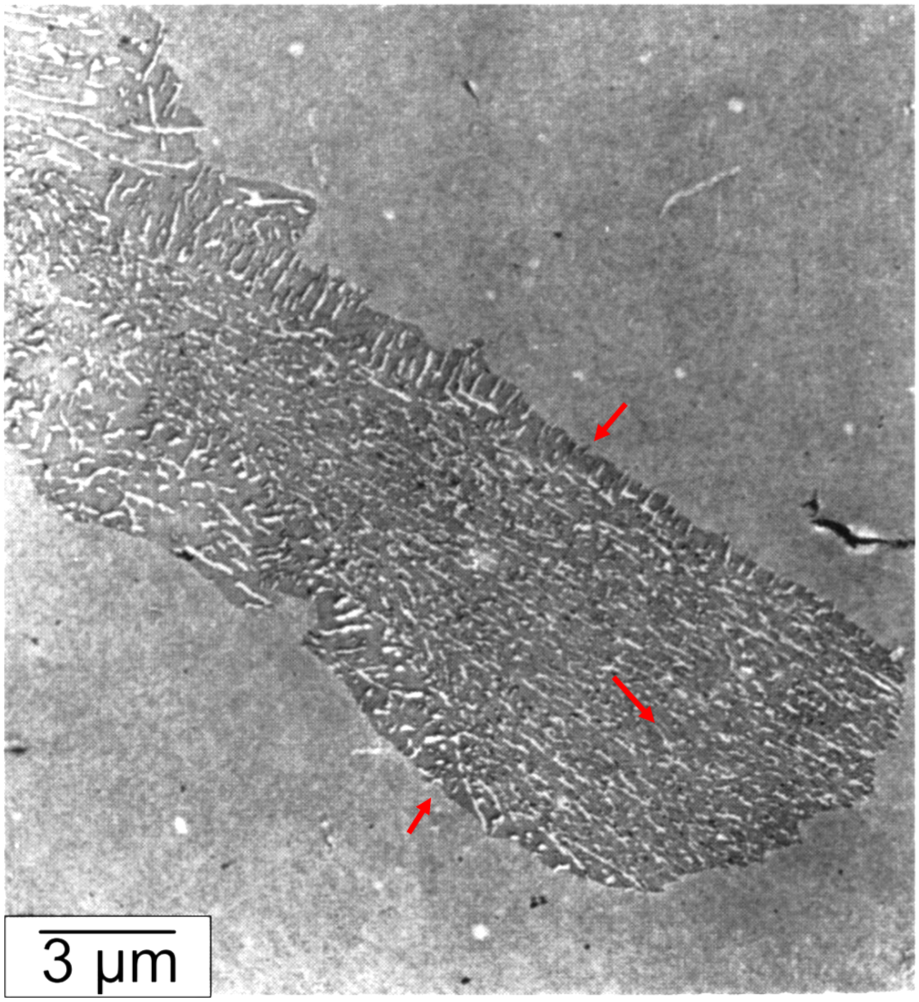

Figure 1.8: Scanning electron micrograph of columnar bainite in Fe-0.82C wt% steel following isothermal transformation at 288 ° Cand at a pressure of 30 kbar. Two different carbide orientations are observed and marked using red arrows.

Pearlitic bainite

In steels containing strong carbide forming elements, it is possible to obtain pearlite in which the carbide phase is an alloy carbide instead of cementite. The orientation dependence of interfacial energy of the alloy carbides results in the formation of crystallographic facets rather than rounded colonies of conventional pearlite. Because of such a faceting, TEM micrographs can be misleading with the presence of parallel ferrite plates with carbides, a microstructure on that scale similar to upper bainite. Typical appearance of pearlitic bainite is shown in Figure 1.9 (from Ref. [12]). Bhadeshia [12] concluded that the terminology "pearlitic bainite" is really just a pearlite with alloy carbide instead of cementite and the microstructure cannot be classified as bainite.

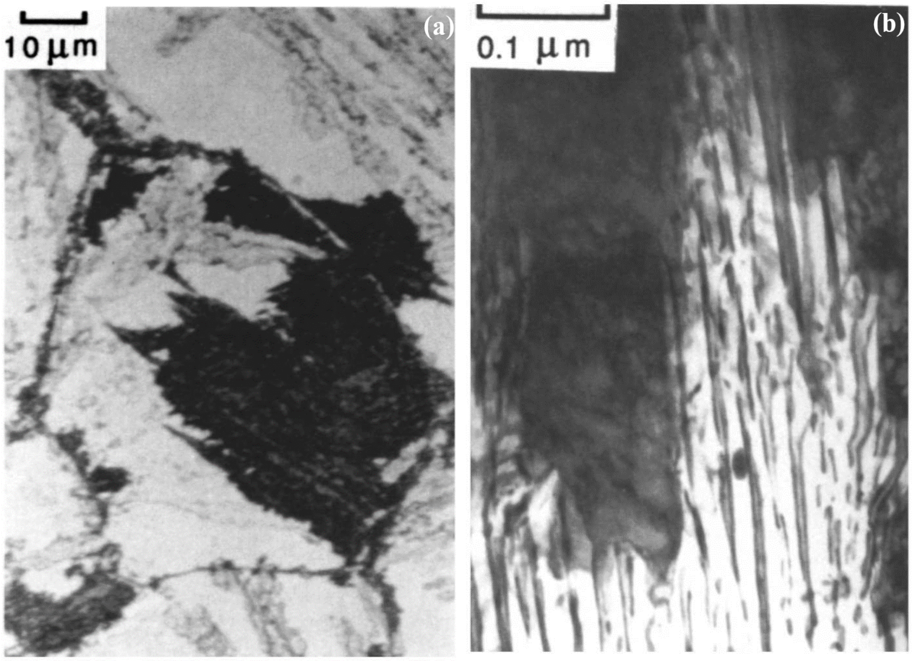

Figure 1.9: Optical micrograph (a) and TEM micrograph of pearlitic bainite.

Coalesced Bainite

At larger driving force and low temperatures, there is a tendency to form unusually coarse plates of bainite. The separately nucleated bainitic ferrite platelets which are of the same crystallographic orientation coalesce during prolonged growth. This results in bimodal distribution of bainitic ferrite plate thickness, with thickness ranging from 0.2 μm to several micron thick. Such thick bainitic ferrite plates have been referred to as coalesced bainite. The typical appearance of coalesced bainite is shown in Figure 1.10. Bhadeshia [12] has reviewed the detailed mechanism of formation of coalesced bainite, and concluded that the coalescence process requires a certain growth to establish itself. This is because the adjacent platelets are at first separately nucleated at the austenite grain boundaries. The nucleation process is not coordinated between the different platelets so there is an opportunity to reject excess carbon to form the intervening films of austenite. However, the platelets then can grow at a faster rate and advance into fresh austenite, leading to coalescence before the carbon has an opportunity to partition. A requirement for coalescence is therefore that the lengthening of sub-units must be allowed to proceed without hindrance. This implies that coalescence is only possible at the early stages in the decomposition of austenite, when growth cannot be hindered by impingement with other regions of bainite.

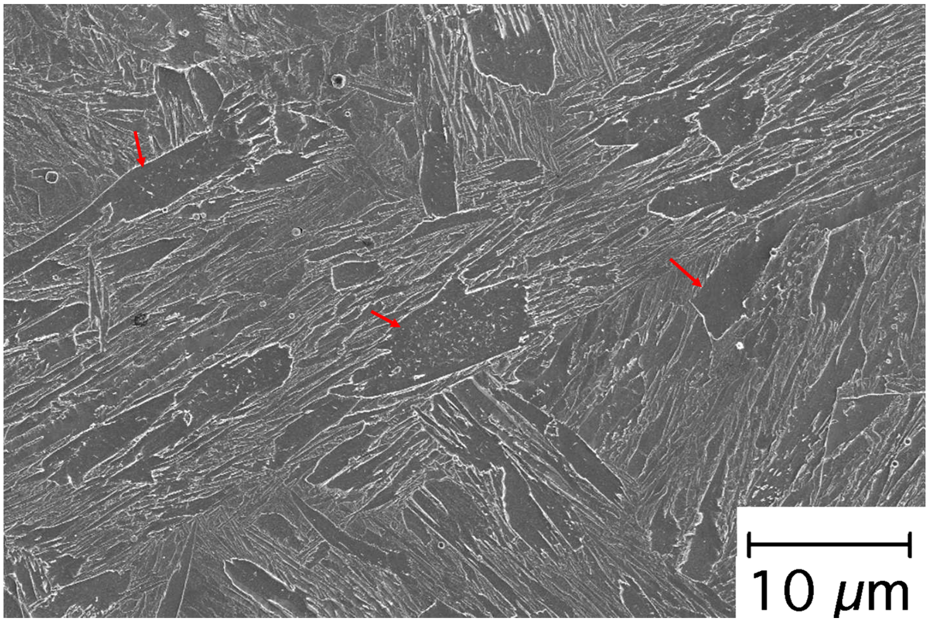

Figure 1.10: FESEM micrograph of coalesced bainite alongside conventional lower bainite. The coalesced bainite units are marked using red arrow.

1.1.5 Inverse Bainite

Inverse bainite was first suggested by Hillert [45] in 1957 when he proposed that there was a symmetry among the eutectoid transformation products in the iron-carbon system; pearlite forming as a result of cooperative growth of ferrite and cementite, and bainite forming as a consequence of ferrite being the leading nucleating phase along the growth direction of Widmanstatten ferrite at lower carbon contents. Hillert proposed that there must be a third eutectoid transformation product with cementite as the first phase to form along the growth direction of Widmanstatten cementite at higher carbon contents. In "conventional" bainite in hypoeutectoid steels, ferrite nucleation is the first event and carbide nucleation being the second event of the transformation. From Hillert's proposal, bainite formation in hypereutectoid steels proceeds by nucleation of carbide as the first event followed by the nucleation of ferrite as the second event. The bainite formed with carbide as the leading nucleating phase was called "inverse bainite".

Inverse bainite has been discussed only a few times since Hillert's proposal. Kinsman and Aaronson [46] have provided TEM micrographs indicating the characteristics of inverse bainite and proposed models for the development of inverse bainite microstructure. Lee et al. [47] in their work included inverse bainite in their morphology map, and Goldstein et al. [48, 49] presented a formation mechanism for the arborescent morphology of bainite which was similar to the inverse bainite microstructure proposed by Hillert. In 2011, Kolmskog and Borgenstam [39–41] studied the eutectoid transformations in a hypereutectoid steel alloy and used inverse bainite as evidence for the bainitic transformation being a diffusional-displacive controlled transformation. Goulas et al. in 2016 [50] studied the bainite formation in a medium carbon low silicon steel using dilatometry technique, and reported the formation of bainite and inverse bainite in a martensitic matrix in Cr segregated regions where the local composition of the alloy is hypereutectoid, resulting in the nucleation of cementite as the first phase from austenite during continuous cooling.

Though the inverse bainite microstructure is discussed in the literature, due to its existence in less common hypereutectoid engineering steels inverse bainite microstructure is not characterized or explained in detail in comparison to the upper bainitic and the lower bainitic microstructures, and as stated by Bhadeshia [12] "*The mechanism of the transformation is virtually unknown; there is no evidence that the growth of the ferrite occurs by a coordinated movement of atoms, and no crystallographic or chemical composition data. Judging from the shape alone, the ferrite probably forms by a reconstructive transformation mechanism. It is premature to classify the transformation as bainite.*"

1.2 Objectives of the thesis

The motivation behind this thesis is to provide a fundamental understanding of the physical foundation of the inverse bainite transformation. Owing to the very limited fundamental studies on inverse bainite, and the existing doubt in the physical metallurgy community as to whether to classify inverse bainite microstructure as 'bainite', this thesis aims to address the following objectives:

1. Characterize the microstructural evolution during the eutectoid decomposition of austenite to inverse bainite.

2. Apply thermodynamic principles to understand the nucleation sequence during inverse bainitic transformation and to predict the border line in the Fe-C phase diagram between inverse bainite and conventional bainite.

3. Characterize the elemental partitioning at the transformation interface, to understand the mechanism and growth kinetics of the transformation.

1.3 Outline of the thesis

This thesis consists of 8 chapters. Chapters 1 and 2 include brief literature review on the topic and discusses the materials and methodology used to address the objectives. A brief outline of each chapter is included below.

1. Chapter 3 focuses on positively identifying inverse bainite using isothermal dilatometry, and utilize interrupted isothermal hold and quench experiments to study the microstructural evolution during inverse bainitic transformation. Multi-scale characterization using FESEM/EBSD/FETEM are utilized to identify inverse bainite, understand the microstructural evolution during transformation, and to identify the crystallographic orientation relationships during the transformation.

2. Chapter 4 focuses on developing a generic thermodynamic model using the principles of driving force the onset of nucleation of cementite and ferrite from parent austenite, Hultgren extrapolation of A_{e3} and A_{cm} phase boundaries, and the molar Gibbs energy change for austenite to ferrite transformation. Using the developed model inverse bainite start (T_{SIB}) and inverse bainite finish (T_{FIB}) temperatures can be predicted for any steel. The thermodynamic predictions

were verified using experimental micrographs both on the steels used in this study as well as from the literature.

3. Chapter 5 focuses on characterizing the composition of the different transformation interfaces during inverse bainite transformation. Atomic scale characterization was carried out using atom probe to reveal the redistribution behavior of substitutional solute during inverse bainitic transformation.

4. Chapter 6 focuses on understanding the mechanism behind the nucleation of secondary carbides within inverse bainite. Carbon concentration measurements using Auger electron spectroscopy and atom probe were carried to identify the mechanism behind the nucleation of secondary carbides within inverse bainitic ferrite.

5. Chapter 7 utilized atom probe to provide three dimensional microscopic evidence for the cementite midrib dissolution during inverse bainitic transformation. The possible reasons for the dissolution of inverse bainitic cementite midrib, and the conversion of inverse bainite to upper bainite at prolonged transformation times are discussed.

Chapter 2

Materials and Methodology

2.1 Materials

The materials considered in this study are tabulated in Table 2.1. All the characterization work presented in this study were conducted on alloys A5 and E1.

2.2 Dilatometry

A completely pearlitic starting microstructure was used in all the heat treatments performed by annealing the samples to a peak temperature of 1050 °C. After annealing, cylindrical samples for dilatometry with a length of 10±0.1 mm and diameter 4±0.1 mm were machined. A RITA L78 high speed quench dilatometer was used to carry out the isothermal bainite transformation. The temperature was controlled and measured by using K type thermocouple spot welded on to the dilatometry samples, and He gas was used for controlling the cooling rate of the samples. The length change associated with phase transformations was measured using the LVDT attached to the push-rod dilatometry setup. The schematic of the dilatometry setup is shown in Figure 2.1. Samples were taken to an austenitization temperature of 1323 K[1] (1050 ° C) (at the rate of 10 K/s) and held there for 5 minutes, followed by cooling the samples (at a cooling rate of 5 K/s which is faster than the critical cooling rate required to form bainite upon continuous cooling) to isothermal holding temperatures ranging from 700 ° C- 400 ° C(with a 50 ° C interval), and 300 ° C and held for 10 minutes at the isothermal holding temperature before cooling down to room temperature at the rate of 5 K/s to form martensite. Martensitic transformation is promoted in the

---

[1] Reason for choosing the austenitization temperature as 1323 K can be found in Ref. [51]

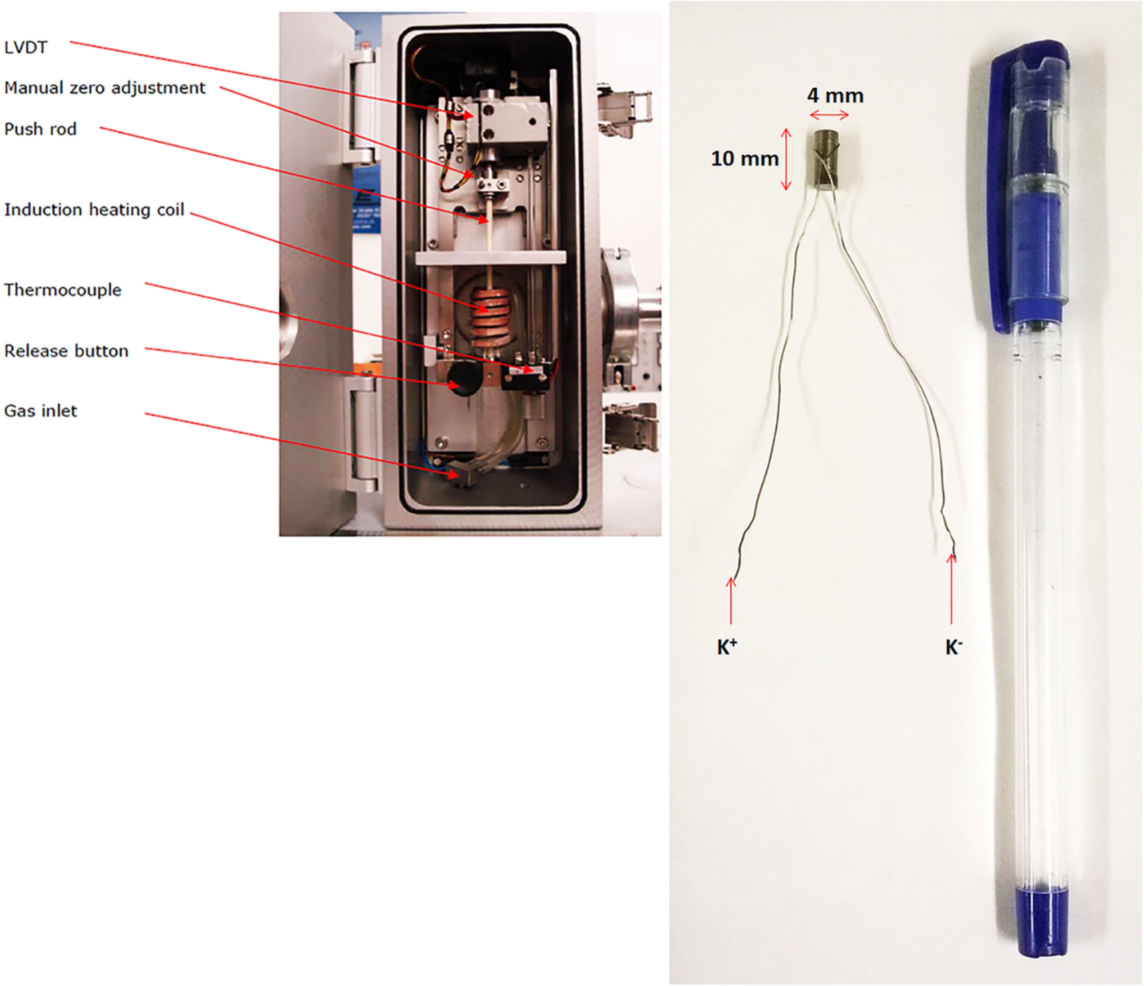

Figure 2.1: Experimental setup of the quench dilatometer sample chamber

Table 2.1: Chemical composition of steels used in the current study. Compositions are in Wt. %

Alloy	**C**	**Cr**	**Mn**	**Si**	**Ni**	**Cu**	**V**	**Fe**
A0[⋆]	0.84							Bal.
A1[⋆]	0.84		1.00					Bal.
A2[⋆]	0.84	0.25	1.00					Bal.
A3[⋆]	0.84	0.50	1.00					Bal.
A4[⋆]	0.84	0.75	1.00					Bal.
A5[†]	0.84	1.00	1.00					Bal.
A6[⋆]	0.84	1.10	1.00					Bal.
A7[⋆]	0.84	1.25	1.00					Bal.
A8[⋆]	0.84	2.25	1.00					Bal.
A9[⋆]	0.84	1.00						Bal.
A10[⋆]	0.84	1.00	0.25					Bal.
A11[⋆]	0.84	1.00	0.50					Bal.
A12[⋆]	0.84	1.00	0.75					Bal.
A13[⋆]	0.84	1.00	0.95					Bal.
A14[⋆]	0.84	1.00	1.25					Bal.
A15[⋆]	0.84	1.00	2.25					Bal.
E1[†]	0.92	0.60	0.90					Bal.
L1[‡]	1.65	0.48	0.24	0.26	0.01		0.01	Bal.
L2[‡]	1.18	0.055	0.33	0.14	0.019	0.004		Bal.
L3[‡]	0.86	0.03	0.19	0.23	0.01	0.03		Bal.
L4[‡]	0.88	4.12	0.08	0.03				Bal.

[⋆] Used for thermodynamic calculations.

[†] Used for thermodynamic calculations and experimental verification.

[‡] Used for thermodynamic calculations and verification of the thermodynamic model with experimental data from literature.

samples so that the high temperature austenite transforms in a displacive manner. This helps in studying the composition gradients in the high temperature austenite using the room temperature martensitic microstructure.

2.2.1 Instrumental drift associated with dilatometry setup

Since the heat treating cycle used here has sudden change in mode of operation of the dilatometer from quenching to isothermal holding, artificial length changes might be introduced in the dilation readings. In order to remove the inherent instrumental drift associated with the dilatometry setup, a sample that does not have any phase transformation during the isothermal temperature selected in this study was used to remove the inherent instrumental drift. Also, at the start of isothermal hold the entire microstructure in the steel considered is composed of austenite from which transformation products form. So, an austenitic stainless steel was used for comparison and calibration of the isothermal dilatation data. The same heat treatment profile was applied to a austenitic stainless steel (AISI 303) [52, 53] sample for isothermal hold at 773.15 K (500 ° C). The recorded dilatation of AISI 303 sample is shown in Figure 2.2. Since AISI 303 does not undergo any phase transformation during isothermal holding at 773.15 K (500 ° C), a constant dilatation is expected during isothermal hold. From Figure 2.2a, during the initial stage of isothermal hold, a small contraction (of 0.08 % strain) in the sample is observed (marked by red box), which is the instrumental drift due to sudden change in mode of operation of the dilatometer setup. The drift was observed to last for 30 seconds during the isothermal hold. After around 30 seconds during the isothermal hold, the volume of the sample was measured to be a constant. Thus, specimen contraction during the initial 30 seconds of isothermal hold is considered as instrumental drift. The dilatation readings of all the test samples are subtracted during the first 30 seconds of the instrumental drift. Test dilatation results thus treated are shown in Figure 2.2b. Dilation reading presented in this study were treated using this method for any further analysis.

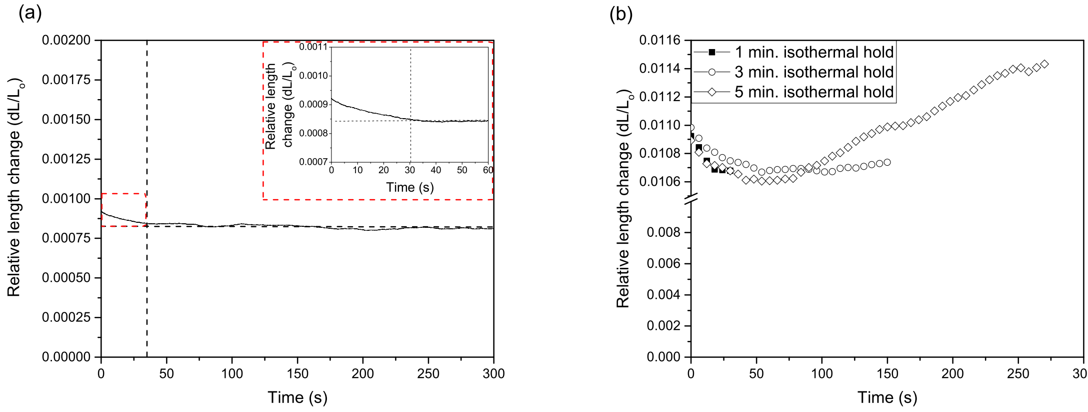

Figure 2.2: (a) Relative length change during isothermal hold of AISI 303 sample. The red box shows the region of instrumental drift and the inset is the zoomed portion of the red box. (b) Relative length change in the heat treated samples after removal of instrumental drift.

2.3 Microstructure characterization

Multi-scale characterization tools were used in the current study to understand the microstructure evolution during inverse bainitic transformation and propose a mechanism for the transformation.

2.3.1 Optical Microscopy

For microstructure characterization the heat treated samples were mounted, ground and polished by using an automatic polisher. Grit 180, 320, 600, and 1200 SiC sand papers were used for the grinding, and 3 μm and 1 μm diamond suspension, 0.5 μm and 0.05 μm alumina suspension and 0.02 μm colloidal silica were used for polishing. The polished surface was etched using 4% Picral with 1 mL HCl to reveal the microstructure. Two optical microscopes, Nikon Eclipse MA200 Inverted Microscope and Olympus BX53 Upright Metallurgical Microscope, were used for optical examinations for magnifications up to 1000X.

2.3.2 Hardness measurements

Vickers hardness measurements were carried out on the bainitic regions using a Tukon 2500 Vickers hardness tester to understand the effect of microstructure evolution on the hardness. A load of 0.05Kg[2] was used for a duration of 10 s to measure the hardness values.

Indentation tests were carried out using a Fischerscope H100C with a standard diamond pyramid Vicker's indenter. The load resolution and distance resolution of the instrument was < 0.04 mN and < 0.1 nm, respectively. The experiments were carried out in the load controlled mode with a peak load of 50 mN applied over a period of 20 seconds. Several indentations were carried out in the bainitic regions and the martensitic matrix of all the samples and the presented load-depth curves are representative. The load-depth curves were analyzed using the Oliver and Pharr analysis [54] for the indentations made and the reported values of elastic modulus and hardness are the average values.

---

[2] Lower load was used to characterize the hardness bainitic regions, whose fraction were low especially at lower isothermal holding time. The hardness measurements are validated using an instrumented indentation technique.

2.3.3 Field Emission Scanning Electron Microscopy (FESEM)-Energy Dispersive X-Ray Spectroscopy (EDX) - Electron Backscatter Diffraction (EBSD) - Transmission SEM (TSEM)

A Zeiss Sigma FESEM equipped with X-Max 150 EDX system with an accelerating voltage of 20 kV and 60 μm objective aperture was used to carry out microstructure observations at finer scales on the etched surface. EDX data were visualized as line concentration profiles or as elemental mapping. For crystallographic orientation analysis in the FESEM, an Oxford AZtec EBSD system was used. Step sizes of 20-80 nm were used for EBSD mapping. For indexing the Kikuchi bands, HKL and ICSD (Inorganic Crystal Structure Database) databases were used. EBSD data processing (reconstructed maps) was carried out using Channel 5 data processing software.The existence of orientation relationship (OR) between phases and the angular deviations from the ideal orientation relationships were identified using the OR boundaries component of Channel 5 data processing software and by matching the orientation data of individual phases [55]. A lattice parameter of a = 0.47042 nm, b = 0.43185 nm, and c = 0.28306 nm was used for indexing Fe_2C, and a = 1.1563 nm, b = 0.45730 nm, and c= 0.5058 nm was used for indexing Fe_5C_2. Mean deviation from the ideal OR was determined by calculating the average misorientation of the boundaries matching a particular OR. To visualize the dislocation structure and the microstructure in transmission mode in the FESEM, a Transmission SEM detector was used.

2.3.4 X-Ray diffraction (XRD)

X-Ray Diffraction (XRD) for quantitative phase identification and lattice parameter measurements was conducted on a Rigaku Ultima^{TM}IV X-Ray diffractometer with Cu K_α source. The scanning mode used was continuous scanning with a scan rate of 0.03 deg./sec. and sampling width of 0.05 degree. The scan range for the 2θ angle was 35° to 135°. X-Ray diffraction experiments were performed on the same polished surface which was used for EBSD data acquisition. Rietveld refinement of the XRD data to determine phase fraction was performed using open source software Profex with BGMN [56].

2.3.5 Auger Electron Spectroscopy (AES)

Since EDX is not reliable for light elements especially carbon, Auger Electron Spectroscopy was conducted to visualize the partitioning behavior of carbon. AES was conducted on the polished surfaces of the samples on a JEOL-9500F AES with argon ion sputtering and secondary electron imaging capabilities. The operating conditions of the AES system were 15 kV accelerating voltage, 30° specimen tilt. Ar sputtering for a duration of 60 s was carried out after secondary electron imaging and before the AES measurements were made to ensure the surface is free from any carbon contamination. Ar ion sputtering was carried out at 2 kV with a sputtering depth of 10 nm/min. AES results were processed by calculating the intensity of each pixel using (P-B)/B, where P and B are the peak and background intensity, respectively to minimize the topographically induced artifacts. Auger results were visualized as line scans and as elemental maps.

2.3.6 Field Emission Transmission Electron Microscopy

Site-specific TEM samples were prepared by FIB lift-out method using HITACHI NB5500 dual beam FIB/SEM. 40 kV accelerating voltage was used for Ga ion beam imaging and during the initial lift out, after which the samples were mounted on to standard 3 mm Cu grid. An accelerating voltage of 5 kV was used for ion beam thinning to prepare electron transparent samples suitable for TEM examination. A Fischione Model 1040 nano milling equipment was used right before the TEM examination to remove any oxide surface in the TEM sample. A HITACHI HF3300 Field Emission TEM (FETEM) with STEM at an accelerating voltage of 300 kV was used for TEM examination and diffraction analysis.

2.3.7 Atom Probe Tomography (APT)

Site-specific needles for APT analysis were extracted from the heat treated samples using FEI Nova 200 dual beam FIB/SEM technique [57]. Regions of interest were annularly milled and cleaned at low voltage (2 kV) with Ga ion beam to make the needle shaped specimens suitable for field evaporation. Atom Probe analyses were performed using a CAMECA Instruments LEAP 4000x HR local electrode atom probe. The atom probe needles were field evaporated in laser mode with a 200 kHz pulse repetition rate, 35 K specimen temperature, 50-70 pJ laser power, and a detection rate of 0.5%. The resulting data were reconstructed and analyzed using the

IVAS reconstruction software. It should be mentioned that the temperature, pulse frequency, pulse fraction of the APT needles were maintained a constant for all the experimental runs, and the laser power used is in the range where one can expect the carbon concentration in cementite to be 25 at. %, therefore, any variation in carbon concentration in cementite presented in this article is not due to the experimental condition used during the APT experiments [58, 59].

2.4 Thermodynamic and Kinetic simulations

All the thermodynamic calculations presented in this study, namely, equilibrium phase fractions, equilibrium phase composition, pseudo-binary phase diagrams along with metastable phase boundaries, driving forces for the onset of nucleation of ferrite and cementite from austenite, the molar Gibbs free energy for austenite to ferrite transformation, critical nucleus size, $T_\circ$ curve, and the interfacial energy between precipitate and matrix were calculated using the TCFE6/TCFE8 database of ThermoCalc [60]. It should be noted that ThermoCalc expresses the driving force per mole of the product phase as the decrease in Gibb's free energy for the formation of the product phase from the supersaturated parent phase (-ΔG_m) . Thus, a negative driving force predicted by ThermoCalc implies that the reaction raises the Gibb's free energy of the system and the reaction will not take place. Precipitation calculations, and the Time-Temperature-Precipitation (TTP) simulations were performed using MCFE thermodynamic and diffusion database of MatCalc software [61].

Chapter 3

Industrial significance of inverse bainite - A case study

3.1 Introduction

The relatively lower cost and the higher strength of the high carbon steels makes it a suitable candidate for industries involving high abrasion environments. The higher abrasion resistance to the steel is imparted by the martensitic transformation during the final stages of the processing. Since the increase in the carbon concentration in the steel also increases the stability of retained austenite, the martensitic transformation in such steel is not complete at room temperature. Thus, a dual phase martensite/retained austenite microstructure is generally observed at room temperature. On tempering the quenched-martensite, the dual phase microstructure of austenite/tempered martensite is a widely favored microstructure in industries using high carbon steel for abrasion and impact toughness applications. Despite the brittle nature of the martensitic microstructure, the existence of adequate amount of retained austenite can prevent the premature failure of such hypereutectoid steels [62].

Metallurgical processing and the process parameters at each stage of manufacturing play an important role in determining the final microstructure of such hypereutectoid steels [63–66]. Considering the spectrum of microstructures achievable in such high carbon steels, a fully tempered martensitic with adequate amounts of retained austenite in steel imparts a both superior wear resistance and impact toughness as compared to steel containing a fully pearlitic structure. Though a martensite/retained austenite dual phase microstructure is desired during the final quenching operation of high carbon steels, the required cooling rate might not be sufficient enough to render a completely martensite/retained austenite dual phase microstructure, especially when the cross-sectional thickness of the steel is increased. In such cases, the transformation of austenite into intermediate transformation product, bainite, is inevitable in such heavy section high carbon steels. Apart from the cooling rate, the extent of elemental segregation increases with increasing the cross-sectional thickness of high carbon steels. Segregation of solute elements in the interdendritic regions increases the hardenability in the interdendritc regions, and reduces the hardenability in the dendritic core regions where the solute concentration is relatively lower, which can in-turn promote transformation of bainite. Therefore, elemental segregation in heavy section high carbon steels becomes a crucial factor in determining the final microstructure of heavy section high carbon steels.

Extensive studies have been conducted on low and medium carbon hypoeutectoid steels on the effect of dual microstructure of bainite and martensite on the mechanical properties. The dual microstructure of bainite and martensite improves the impact property and the strength of the depending on the morphology of bainite. Abbaszadeh et al. [67] concluded that the dual microstructure of upper bainite and martensite significantly reduced that fracture toughness of the steel due the presence of coarser carbides in the upper bainite microstructure. Tomita [68] concluded that the presence of lower bainite in a martensitic matrix significantly improved the fracture toughness. This is related to the morphology of lower bainite, which is acicular and partitions prior austenite grains of the parent martensite thereby refining the martensitic packet size. Young and Bhadeshia [69] provided a quantitative explanation for the observed increase in strength of mixed bainite and martensite microstructure based on the carbon enrichment of austenite during the bainitic transformation, and the plastic constraint by the martensitic matrix.

The main objective of this study is to investigate the possible influences of the banded microstructure on the performance of a eutectoid steel. The analysis mainly focuses on the effects of metallurgical factors, including segregation, grain boundaries, non-equilibrium phase transformations, and cooling rates, which can promote the banded structure and study the influence of the banded structure on the performance of the eutectoid steel.

3.2 Results

3.2.1 Microstructure Characterization

Optical micrographs of the heavy sections are shown in Figure Figure 3.1. The low magnification optical micrographs show the presence of microstructural banding in Figure 3.1a, Figure 3.1c, Figure 3.1e. The extent of microstructural banding increases towards the core of the heavy section. The optical micrographs in Figure Figure 3.1b, Figure 3.1d, Figure 3.1f show the presence of a dark etching phase in a martensitic/retained austenite matrix (brown color). The fraction of the dark etched phase increases towards the core of the heavy section. High magnification optical micrography of the dark etched microstructure in Figure 3.2 shows that the dark etched microstructure tends to form surrounding a white etched phase (which appears to be a carbide).

Electron microscopic characterization reveals the structure of the dark etched microconstituent at finer scales. Secondary electron SEM image of the dark etched microstructure in the fractured heavy section is shown in Figure 3.3. It is seen in Figure 3.3a that the dark etched microstructure forms along the prior austenite grain boundaries in a tempered martensitic matrix. Figure 3.3b shows the higher magnification of the dark etched microconstituent. EDX line scan across the dark etched microconstituent in Figure 3.3b confirms that the dark etched microconstituent is an aggregate of ferrite and iron carbides (alternating carbon and iron peaks) and the white etched phase in Figure 3.2 is a carbide. Since the ferrite and iron carbide aggregates are non-lamellar, the dark etched microconstituent can be called bainite [12] and the dark etched microconstituent forms surrounding a carbide unit and therefore, the dark etched microconstituent in the fractured heavy section is upper bainite with coarser carbides in a tempered martensitic matrix. Confirmation of ferrite/carbide aggregate of bainite in the martensitic matrix will be provided in the following sections. Typical XRD patterns from the surface, 1/4 thickness and the center of the heavy section are shown in Figure 3.4. The XRD patterns show the presence of two dominant phases, ferrite and austenite, respectively supporting the identification of the microstructure in the heavy section. The ferrite peak is a convoluted peak of martensite/bainitic ferrite. Thus, from the XRD data, it can be concluded that the matrix microstructure is martensite/retained austenite and the dark etching microstructure is an aggregate of ferrite and cementite of the bainitic unit. Quantitative Rietveld analysis of the XRD data will be discussed next.

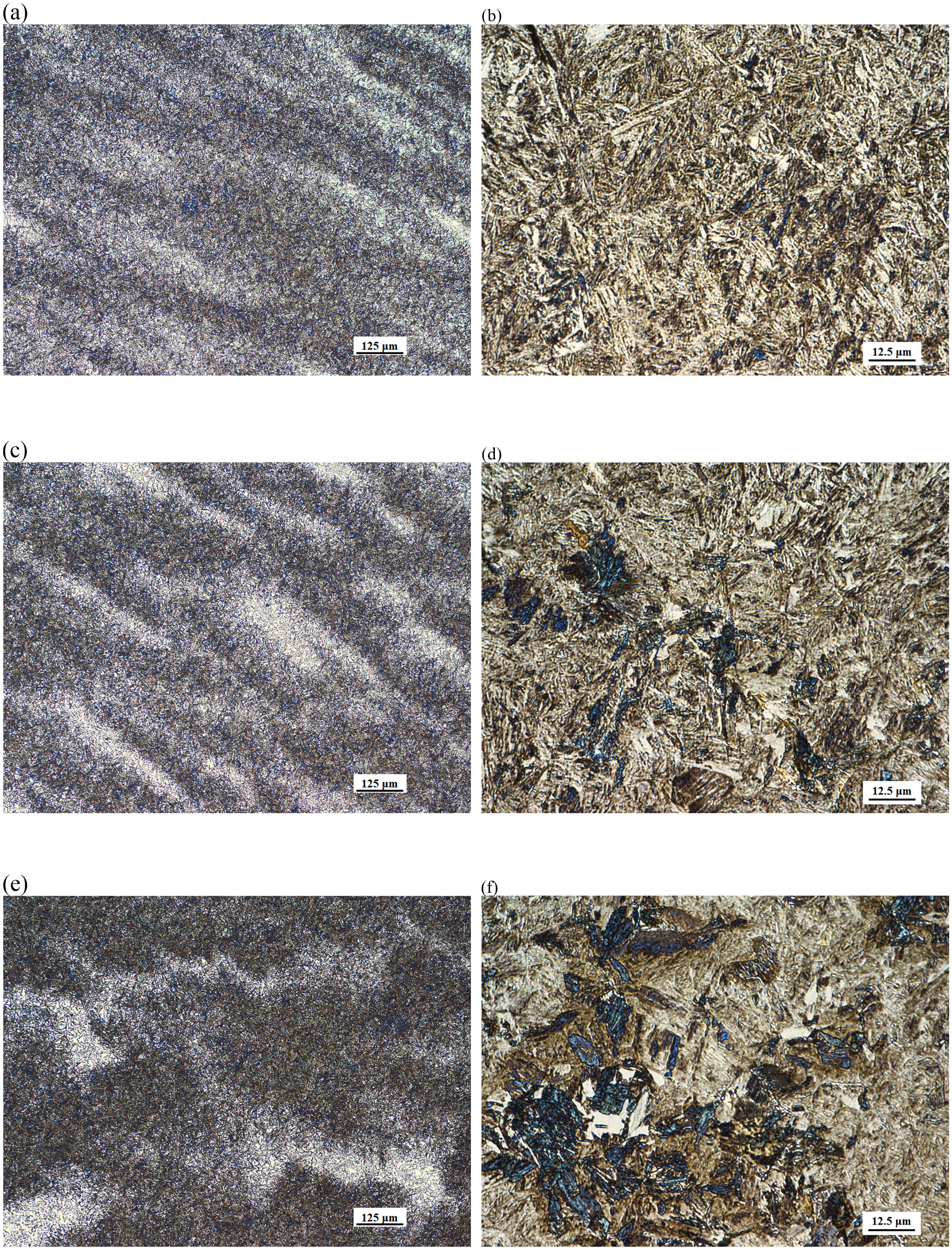

Figure 3.1: The microstructure of the heavy section at the surface (a,b), mid-Radius (c,d), and center (e,f). Low magnification images in (a), (c), and (e) were etched with 2% nital, the high magnification images in (b), (d), and (f) were etched with 4% picral.

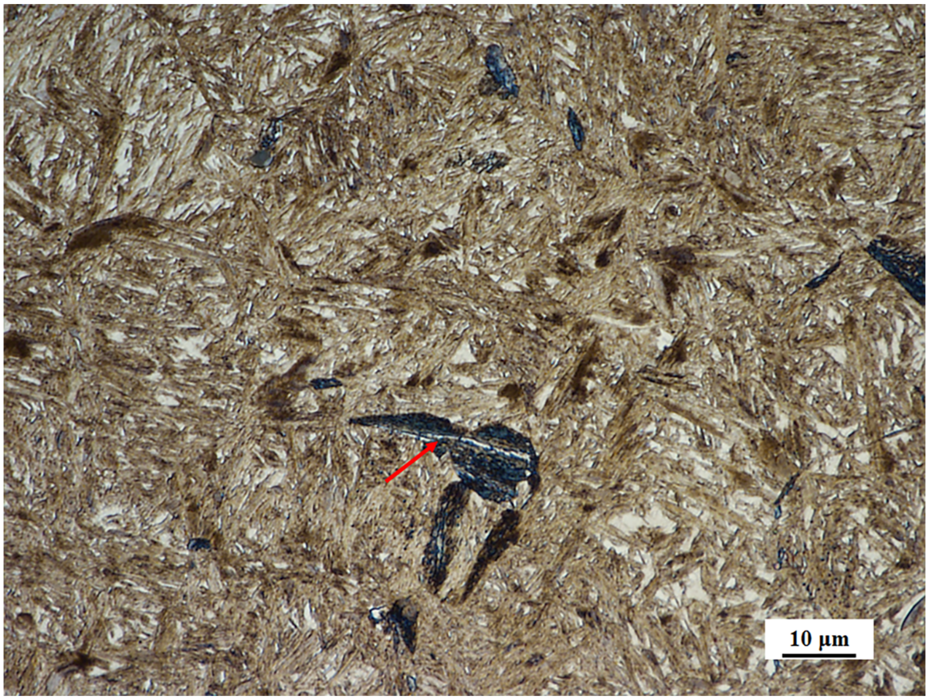

Figure 3.2: The growth of the dark etched micro-constituent surrounding white etched phase in the center of the heavy section.

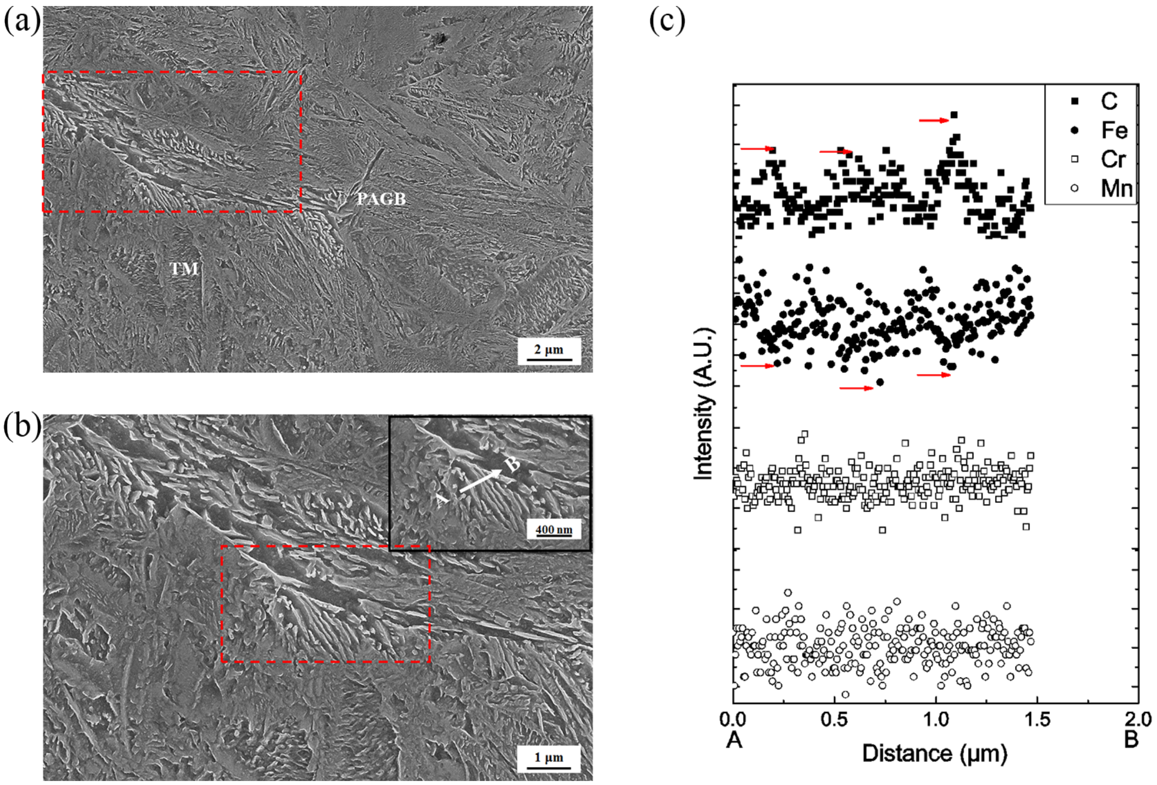

Figure 3.3: Secondary electron image and EDX analysis on the dark etched microconstituent. (a) Formation of the dark etched microconstituent along the PAGB (dotted lines). The tempered martensitic matrix is labeled TM. (b) Higher magnification of the dark etched microconstituent. The line AB represents the region where EDX line scan was performed. (c) EDX line scan profiles corresponding to line AB in (b)

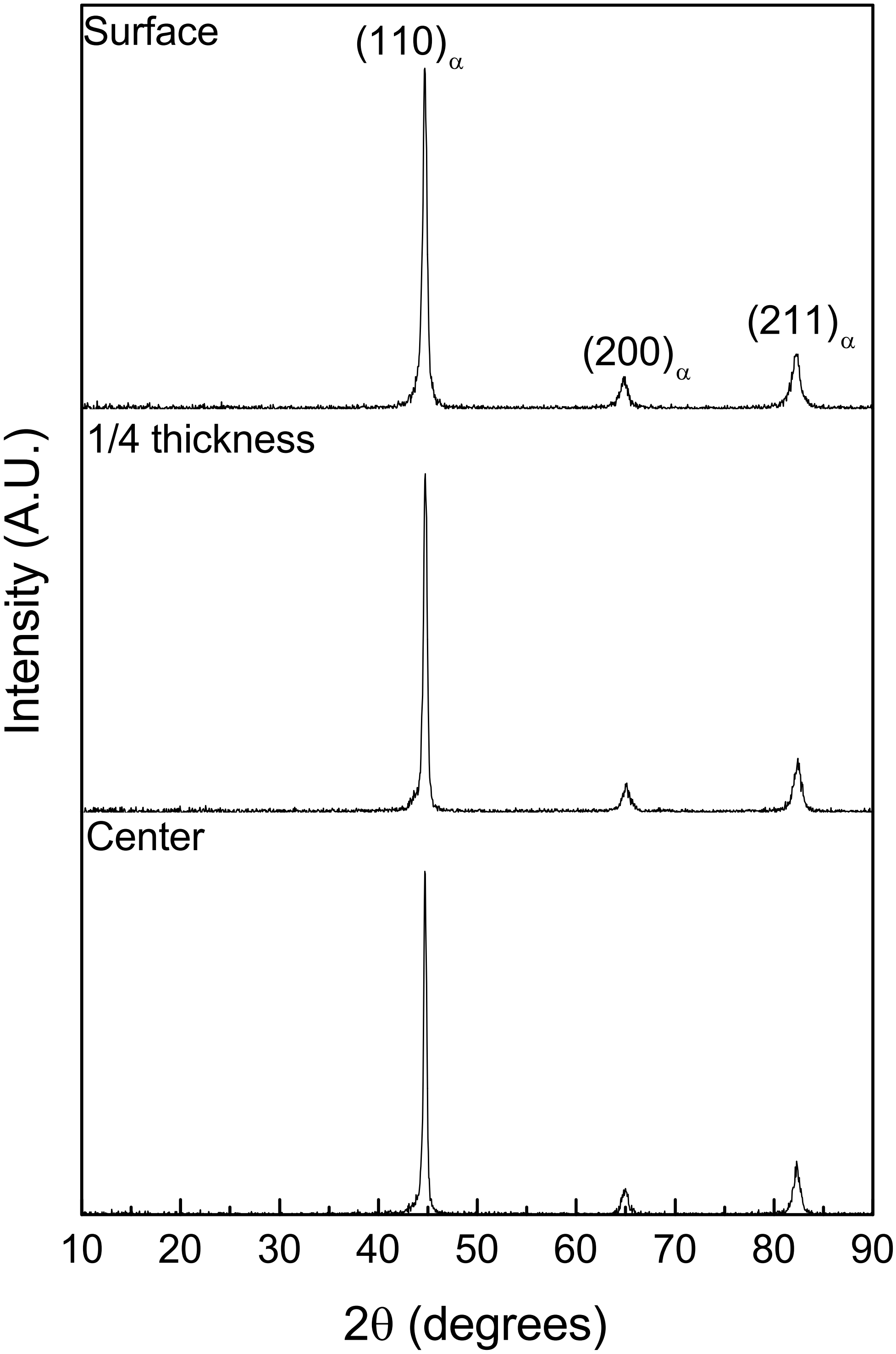

Figure 3.4: X-Ray diffraction patterns from the surface, 1/4 thickness, and center of the heavy section.

3.2.2 Quantitative phase evolution using XRD

Rietveld analysis of the XRD data was carried out to determine the phase composition, lattice parameters of martensite, and deconvolution of the ferrite peaks. Representative Rietveld refined XRD patterns at the surface, 1/4 thickness, and center of the heavy section are shown in Figure 3.5. Figure 3.5a shows the XRD patterns observed in the entire spectrum of the measurement subject to Rietveld refinement. The goodness of fit (χ^2) [70] of the Rietveld refinement was 1.24 respectively. The XRD pattern in Figure 3.5a show predominantly BCC diffraction peaks. Figure 3.5b shows the deconvoluted $(111)_\gamma/(110)_{bcc}$ peak in the heavy section. Bragg's diffraction peaks from (101) and (110) planes of martensite were distinguishable which enabled the measurement of lattice parameters (a and c) of martensite. The 2θ separation between the (101) and (110) martensite peaks was close to 0.4° as reported by other researchers [71]. The ferrite (110) peak is shifted to a lower 2θ value in comparison with the (101) and (110) peaks of martensite. Smaller peaks corresponding to the (211) and (102) diffraction of cementite is observed. Figure 3.5c shows the deconvoluted $(200)_{bcc}$ peak. The deconvolution of (200), (002) martensite and (200) bainitic ferrite was possible. Figure 3.5d shows the deconvoluted $(211)_{bcc}$ peak. The deconvolution of (211), (112) martensite and (211) bainitic ferrite was possible.
The lattice parameter of tempered martensite (c/a), volume fraction of bainitic ferrite (f_α), austenite (f_γ), and tempered martensite ($f_{\alpha'}$) in the heavy section measured using Rietveld refinement are tabulated in Table 3.1. As seen in Table 3.1, the martensite is well tempered, because the c/a ratio is approaching 1.0. It should be noted that the heavy section has a significantly higher fraction of bainitic ferrite. This observation agrees with the bainite fraction observed in the optical micrographs presented in Figure 3.1.

Table 3.1: Result of Rietveld refinement of X-ray diffraction pattern refinement and volume fraction of phases in fractured heavy section

Location	f_γ	$f_{\alpha'}$	f_α	f_θ	c/a
Surface	0.64	86.90	10.30	2.16	0.99803
Mid-Radius	0.37	18.50	71.20	10	1.007
Center	1.39	34.20	60.20	4.20	1.008

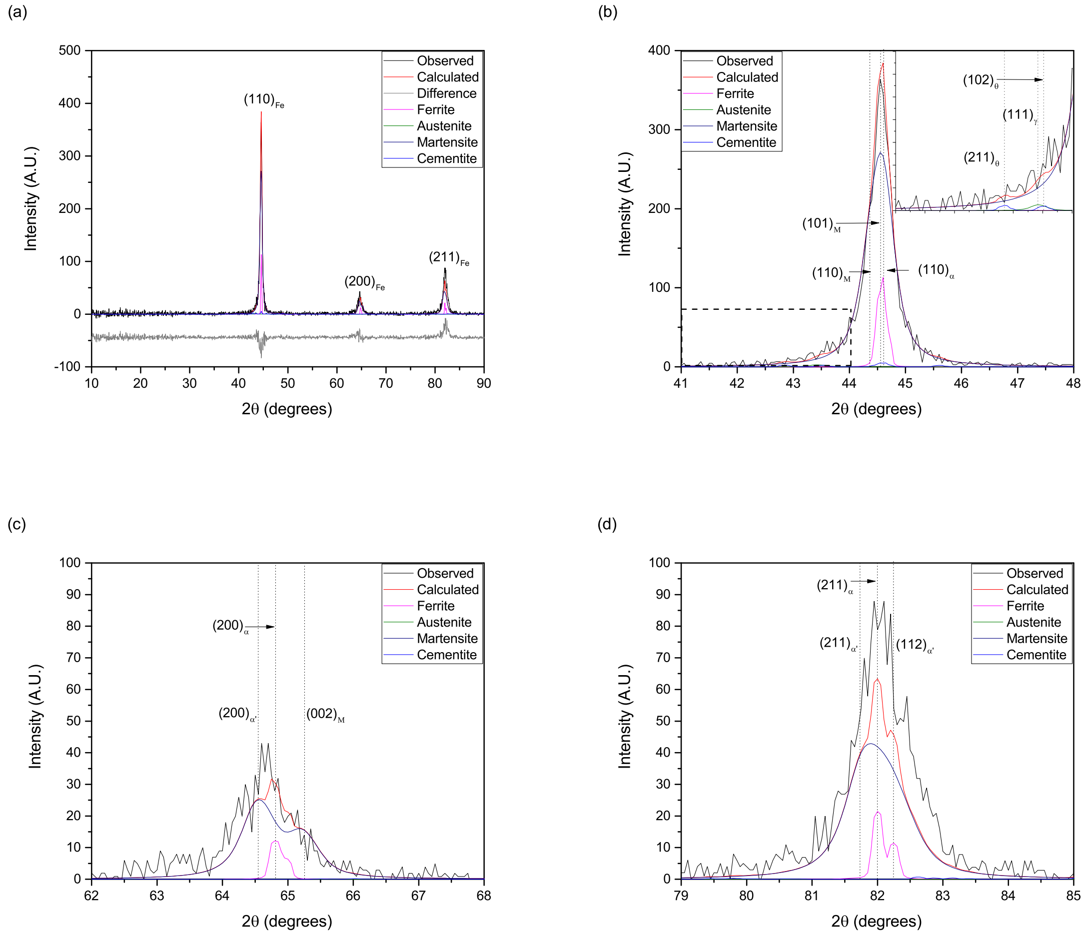

Figure 3.5: XRD patterns from the heavy section. (a) Entire profile subjected to Rietveld refinement. The difference between the observed and Rietveld refined peaks is represented by gray line in the bottom. (b) Deconvolution of $(111)_{\gamma}/(110)_{bcc}$ peak. (c) Deconvolution of $(200)_{bcc}$ peak. (d) Deconvolution of $(211)_{bcc}$ peak.

The position of the bainitic ferrite peaks extracted from the Rietveld refined XRD patterns are presented in Figure 3.6. It can be seen that the relative positions of the (110) ferrite peak in the heavy section shifts from a lower 2θ value to a higher 2θ from the surface to the core. The relative shift in the ferrite peaks as we move from the surface to the center likely suggests a non-uniform strain distribution in the heavy section [72].

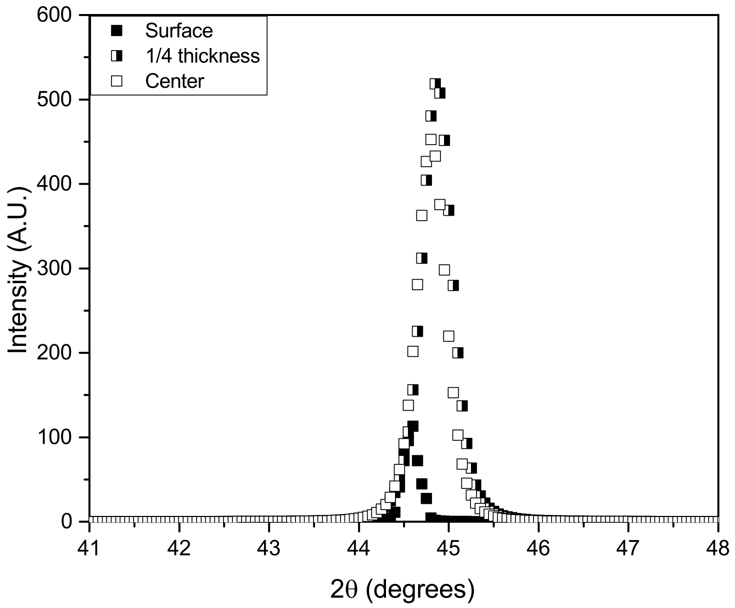

Figure 3.6: Relative 2θ positions of the bainitic ferrite peaks extracted from Rietveld refinement.

3.2.3 Influence of banded microstructure on the mechanical performance

In order to understand the influence of the banded microstructure on the performance of the high carbon steel, an in-house impact toughness testing was performed in the heavy section. The characteristic fractography of the heavy section at the surface, 1/4 thickness, and at the center of the heavy section are shown in Figure 3.7a-c The fracture surface of the heavy section exhibits a brittle intergranular fracture morphology. The presence of ductile fracture features become much prominent towards the surface of the heavy section (Figure 3.7a and Figure 3.7b) where a mixed mode

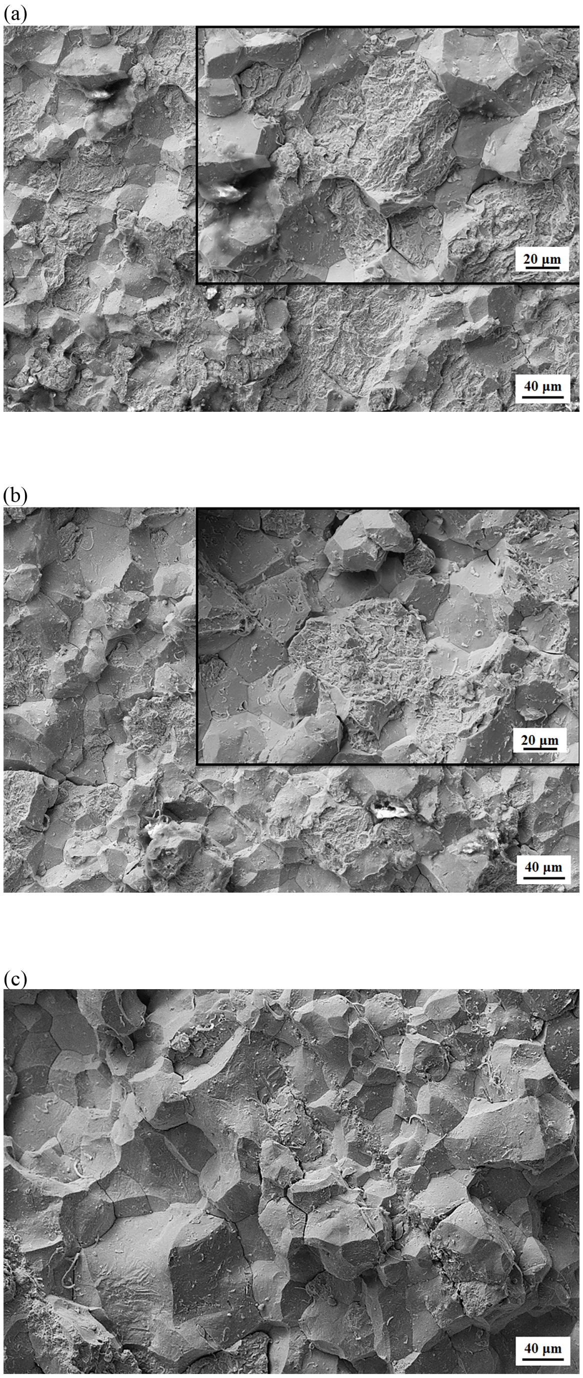

Figure 3.7: The fracture surface of the fractured heavy section at (a) Surface, (b) Mid-Radius, and (c) Center. The insets in (a) and (b) are higher magnification images showing ductile fracture features.

(brittle intergranular + transgranular) fracture features are seen.

3.3 Discussion

Transformation of bainite in the heavy section

Segregation of alloying elements which promotes the banded microstructure of bainite and martensite (Figure 3.1) seems to be an important factor for the transformation of bainite. Segregation of elements in the interdendritic regions increases the hardenability in the interdendritic regions and reduces the hardenability in the dendritic core regions where the solute concentration is relatively lower [73]. Apart from influencing the on-cooling phase transformations, segregation also affects the critical phase transformation temperatures during heating (A_{c1}, A_{c3}, and A_{cm}). The segregation of various heavy elements measured using EDX and their effect on the critical transformation temperatures during heating are shown in Figure 3.8a and Figure 3.8b. It can be seen that in the light etched bands, which comprise of martensite, the composition is higher than the nominal composition of the steel, whereas, in the dark-etched bands, which comprise of bainite, the composition is lower than the nominal composition of the steel. This affects the on-heating transformation temperatures as shown in Figure 3.8b, especially the A_{cm} temperature. Thus, the final austenitization temperature is another important factor for the transformation of bainite. A lower austenitization temperature and a shorter hold time at austenitization temperature will result in an austenite/cementite two phase microstructure especially in the interdenderitic regions, during the austenitization. Subsequent continuous cooling of the

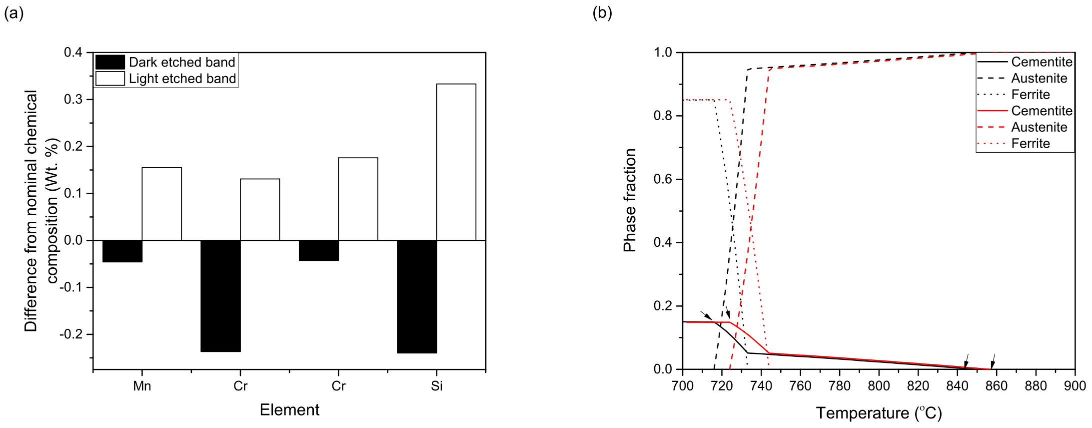

Figure 3.8: (a) Variation in chemical composition due to segregation within the light-etched and dark etched band, and (b) The effect of segregation on the critical phase transformation temperatures during heating.

heavy section will result in the retention of the proeutectoid cementite films along the prior austenite grain boundaries. One such instance of the presence of proeutectoid cementite along the grain boundaries is shown in Figure 3.9. Song *et al.* [74] have shown that the retained carbides after austenitization may act as nucleation sites for the low-temperature cementite in bainite. Thus, the retained proeutectoid cementite films along the grain boundaries act as the nucleation sites for bainite as seen in Figure 3.2 and Figure 3.3. Segregation in combination with the non-uniform thermal distribution in the heavy section affects the on-cooling phase transformations in the inter-dendritic and dendritic core regions. In the continuous cooling transformation (CCT) diagram, the bainitic 'C' curve is shifted towards longer time (slower cooling) in the interdendritic regions in comparison with the dendritic core regions. Thus, the heavy section is locally divided into regions of varying hardenability, and with a slow enough cooling rate, the bainitic transformation can be promoted in the dendritic core regions. The simulated continuous cooling transformation diagram using dilatometry for the surface and the core of the heavy section during final cooling stage is shown in Figure 3.10. It can be seen that the center of the heavy section which has a slower cooling rate, a higher fraction of dark-etched constituent, and hence a lower chemical composition than the nominal composition has a tendency to form bainite during continuous cooling.

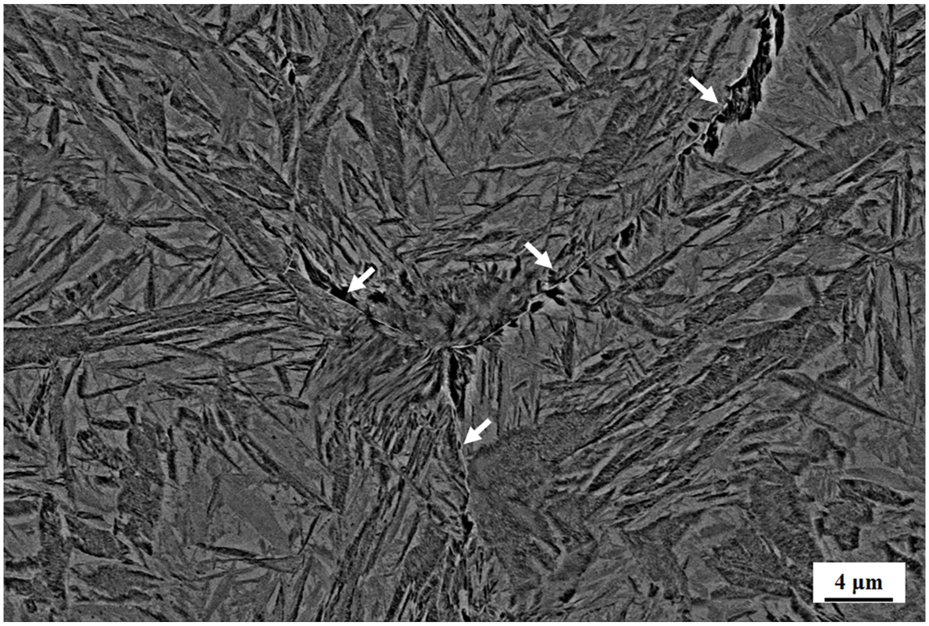

Figure 3.9: The Presence of the retained proeutectoid cementite films along the grain boundaries on a martensitic microstructure in the fractured heavy section.

Thus, bainitic transformation along the prior austenite grain boundaries can be pro-

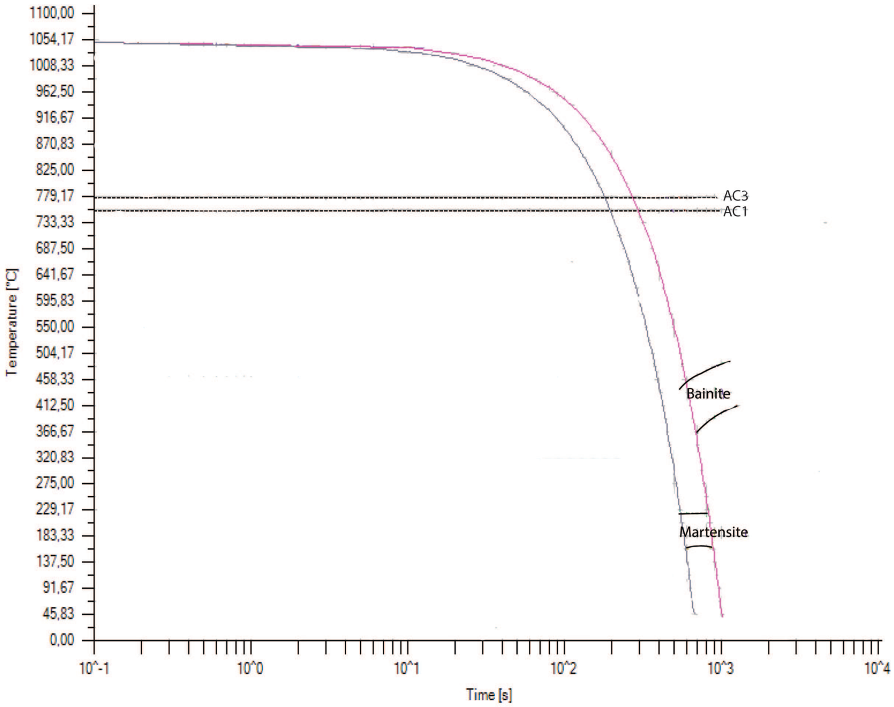

Figure 3.10: Continuous cooling curves along the surface and core of the heavy section during cooling to form martensite. The pink line and blue line represents the simulated cooling curve for the center and surface of the heavy section respectively.

moted by a combination of segregation of alloying elements which has occurred during the initial casting stage of the manufacturing, the non-uniform thermal gradient across the heavy section, and the choice of the austenitization temperature prior to final quenching/tempering cycle.

Effect of bainite/martensite microstructure on the mechanical performance of the steel

From Figure 3.6, it is seen that the (110) ferrite peaks are shifted towards higher 2θ angles towards the center of the heavy section. The lattice parameter at the surface is higher in comparison with the core of the heavy section. The lattice expansion of bainitic ferrite at the surface creates a compressive stress field in the surrounding martensite in comparison with the center of the heavy section [75, 76]. Considering the impact of the heavy section to be a Hertzian contact [77], the stress components near the surface of the heavy section are compressive in relation to the core of the heavy section. EBSD local misorientation maps at the surface (tempered martensitic microstructure) and center (tempered martensitic and bainitic microstructure) are shown in Figure 3.11 and further confirm the non-uniform strain distribution along the surface and the center of the heavy section. The KAM maps in Figure 3.11a and Figure 3.11c represent the local strain distribution. It is seen that the KAM is relatively lower in the tempered martensitic region (Figure 3.11a) in comparison with the bainitic + tempered martensitic region (Figure 3.11c). In Figure 3.11c, the local strain is higher at the interface between bainite and tempered martensite. Figure 3.11b and Figure 3.11d classifies the grain as deformed, recrystallized, and sub-structured. It is seen that the fraction of deformed grains in the tempered martensitic region (Figure 3.11b) is much lower (15%) in comparison with the bainitic + tempered martensitic region (26%) (Figure 3.11d). In both Figure 3.11c and Figure 3.11d, the strain is concentrated at the bainite/tempered martensite interface. Thus, from the misorientation maps, it can be suggested that the local strain concentration in the bainitic+tempered martensitic region is much higher in comparison with the tempered martensitic region and a microstructure of tempered martensite must aid

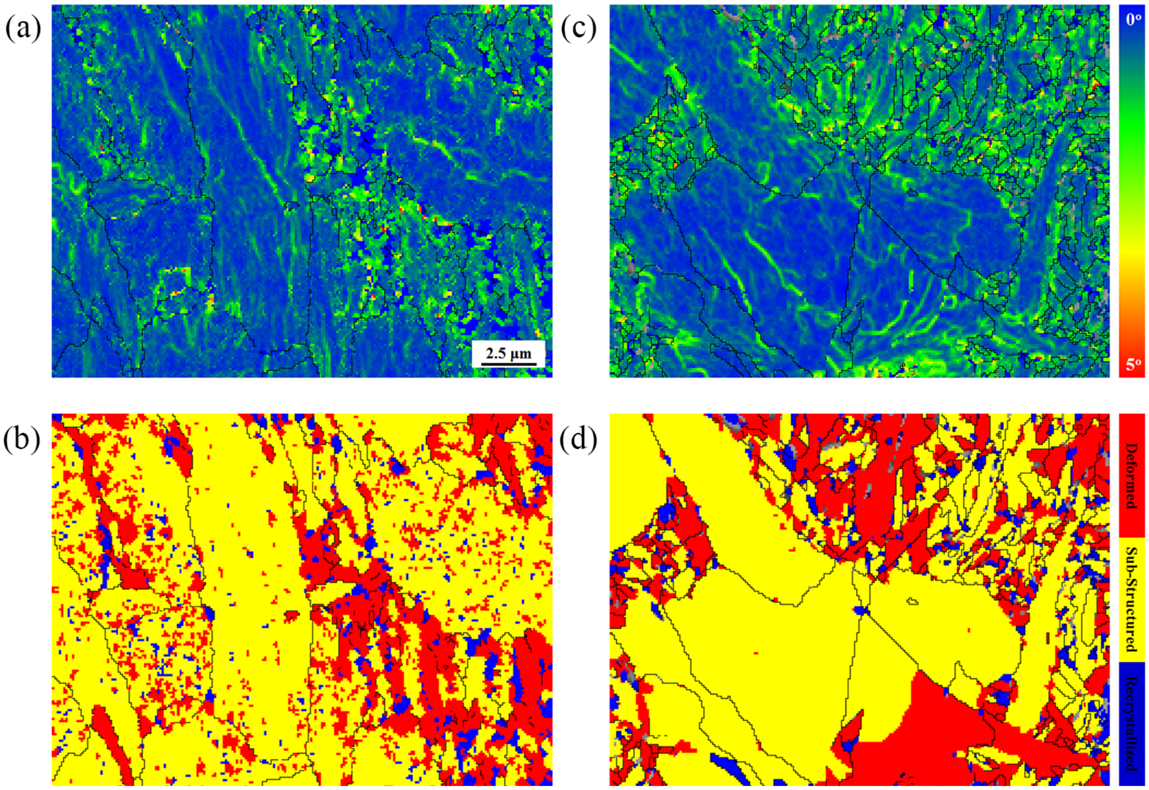

Figure 3.11: EBSD misorientation maps. The black line represents high angle grain boundaries (HAGBs) with misorientation greater than 10°. (a) Kernel Average Misorientation (KAM) map, (b) Grain Average Misorientation (GAM) map of the same view field as (a). (c) Kernel Average Misorientation (KAM) map, (d) Grain Average Misorientation (GAM) map of the same view-field as (c). (a),(b) are maps acquired from the tempered martensitic region (c),(d) are maps acquired from bainite + tempered martensite region.

in arresting the propagation of a crack. This hypothesis is further supported by the secondary electron images of a crack propagating in bainite/tempered martensite region as shown in Figure 3.12 and the presence of dark etched bainitic microstructure along the cross-section of the fracture surface in Figure 3.13. Thus, it is likely

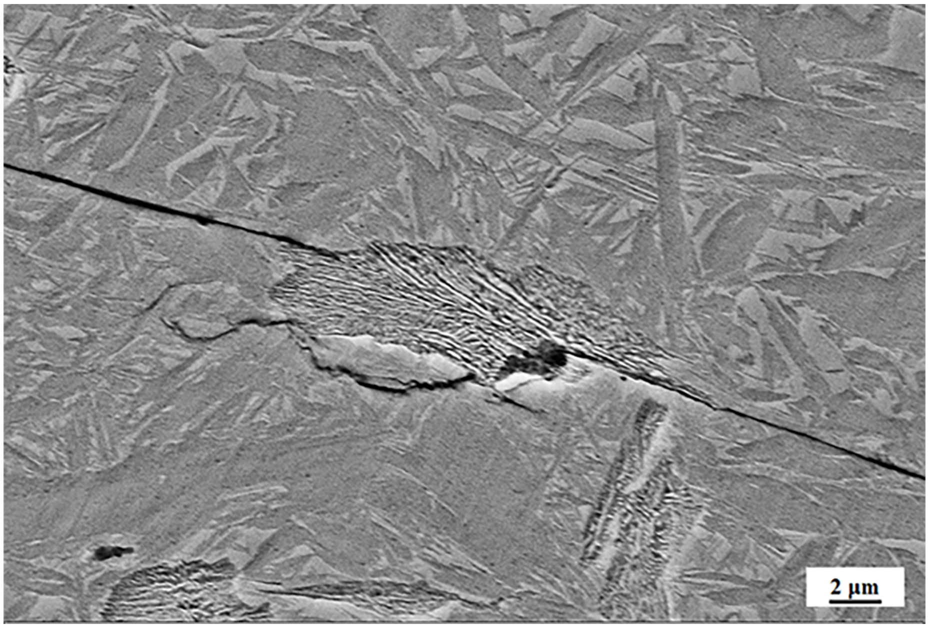

Figure 3.12: Propagation of crack across the bainite/tempered martensite region.

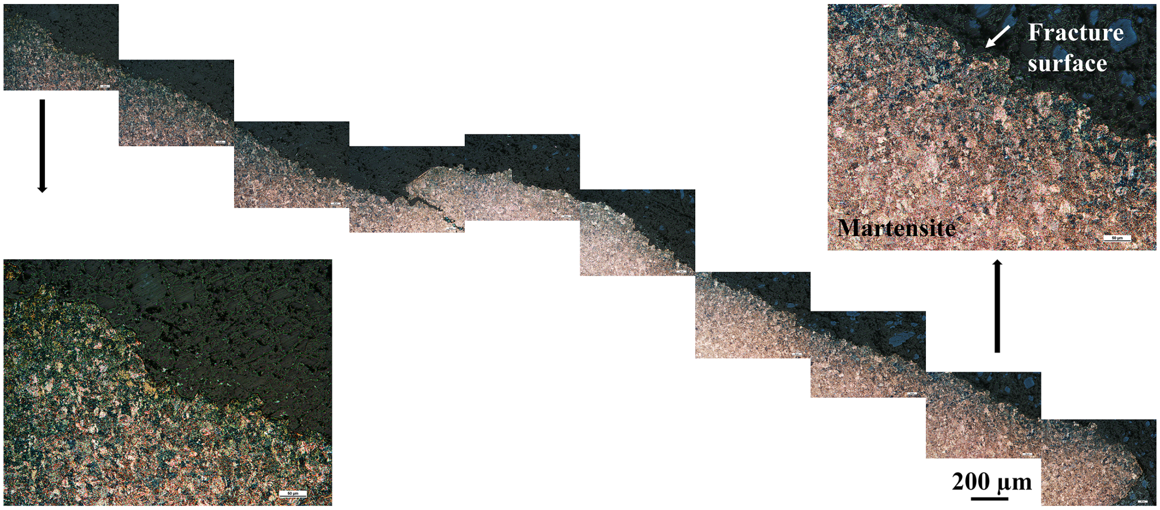

Figure 3.13: Montage of microstructure at the cross section of the fracture surface.

that the core of the heavy section, which is in a state of tensile stress, is where the crack initiation occurs. The surface, which is in a state of compression, resists the propagation of the crack, which results in a considerable plastic deformation before the failure. The presence of bainite in a tempered martensitic matrix creates a non-uniform strain distribution at the bainite/martensite interface thereby creating a higher stress concentration at the bainite/martensite interface (Figure 3.11c). The higher stress concentration initiated at the bainite/martensite interface leads to failure in a brittle manner as reported by Tomita [68]. Therefore, a complete intergranular fracture surface is observed near the center of the heavy section and a mixed mode of fracture is observed near the surface of the heavy section (Figure 3.7).

The morphology of bainite present in bainite/martensite mixed microstructure also affects the impact property significantly. This is mainly attributed to the size of carbides present in bainite and the extent of refinement of martensitic packets due to the transformation of bainite. When bainite transformed in upper bainite, it fills the prior austenite grain boundary in comparison to lower bainite which forms dividing the prior austenite grains. The formation of lower bainite refines the packet size on which the transformation occurs, in turn, refining the lath size of martensite. On the other hand, the formation of upper bainite reduces the packet area to form martensite. A finer lath size of martensite has superior impact property. From Bhadeshia [12], the fracture toughness is inversely related to the carbide thickness in bainite as

$$\sigma_F = \sqrt{\frac{4E\sigma_P}{\pi(1-\gamma^2)c}} \tag{3.1}$$

where E is Young's Modulus of bainitic ferrite, γ is Poisson's ratio, σ_P is the plastic work of fracture per unit area of crack surface, and c is the carbide thickness. Thus, upper bainite with coarser carbides (Figure 3.2) near the center of the heavy section, reduces the fracture toughness of the heavy section.

3.4 Summary and Motivation on Inverse Bainite

In this study, an experimental analysis was performed to investigate the possible influence of banded microstructure on the performance of high carbon steel heavy section. The banded microstructure was found to be alternating layers of bainite/martensite. It is likely that the nucleation of bainite proceeded by the formation of cementite along the prior austenite grain boundaries first, followed conventional upper bainite type transformation. The transformation of bainite was promoted by a combination of segregation of alloying elements which occurred during the initial casting stage of the manufacturing, the non-uniform thermal gradient across the heavy section, and the insufficient austenitization prior to the final heat treating cycle. The transformation of upper bainite along the PAGBs introduced a non-uniform strain distribution at the bainite/martensite interface and a higher stress concentration. This may eventually lead to the failure of the heavy section in a brittle manner.

Possible solutions to avoid premature failures include use of higher austenitization temperature, minimizing segregation, and design new alloys which can hinder the formation of bainite. Since segregation cannot be avoided completely, and increasing the austenitization temperature is not an economically viable option, a fundamental understanding of bainitic transformation in such high carbon steel systems including the effect of alloying elements on the kinetics of the transformation will prove beneficial in designing new-generation high carbon steel with suitable microstructure for service conditions.

Chapter 4

Identification and microstructural evolution during inverse bainitic transformation

4.1 Introduction

This chapter focuses on the microstructural evolution of inverse bainite during isothermal bainite transformation through a series of interrupted isothermal experiments using a quench dilatometer. Inverse bainite transformation proceeds by formation of cementite midrib as the first stage of transformation, followed by the transformation of ferrite from carbon-depleted austenite in the second stage. Crystallographic analysis under EBSD revealed that the nucleation of secondary carbides (Fe_3C, Fe_2C, and Fe_5C_2) happens from inverse bainitic ferrite, which is the third stage of transformation. When the transformation time is sufficiently long, inverse bainite microstructure becomes degenerated to be conventional upper bainite, which is the fourth stage of the transformation. Possible mechanisms behind the observed microstructure evolution are discussed through suitable thermodynamic calculations

4.2 Results

4.2.1 Dilatometry

A representative complete dilatation profile for the 1 minute isothermal hold sample is shown in Figure 4.1a. It shows the absence of any phase transformation upon cooling from 1323 K (1050 ° C) to the 773 K (500 ° C) isothermal hold. On cooling from the 773 K (500 ° C) isothermal hold to room temperature (at a cooling rate of 5K/s), martensitic transformation is recorded at around 443 K (170 ° C). Thus, all untransformed austenite at the end of the isothermal hold will be fully transformed into martensite/retained austenite constituents, thus enabling a measurement of phases that have transformed during the isothermal hold. On cooling and 773 K (500 ° C) isothermal holding dilatation profiles for all the heat-treated samples is shown in Figure 4.1b. It can be seen that the relative length change at isothermal hold decreases initially, following which, there is an increase in relative length change. The dilatation data expressed as relative length change with transformation time is shown in Figure 4.1c. The dilatation is found to occur in two stages, with a transition in kinetics from volumetric contraction to volumetric expansion approximately after 75 seconds in all the samples as shown in the inset in Figure 4.1c.

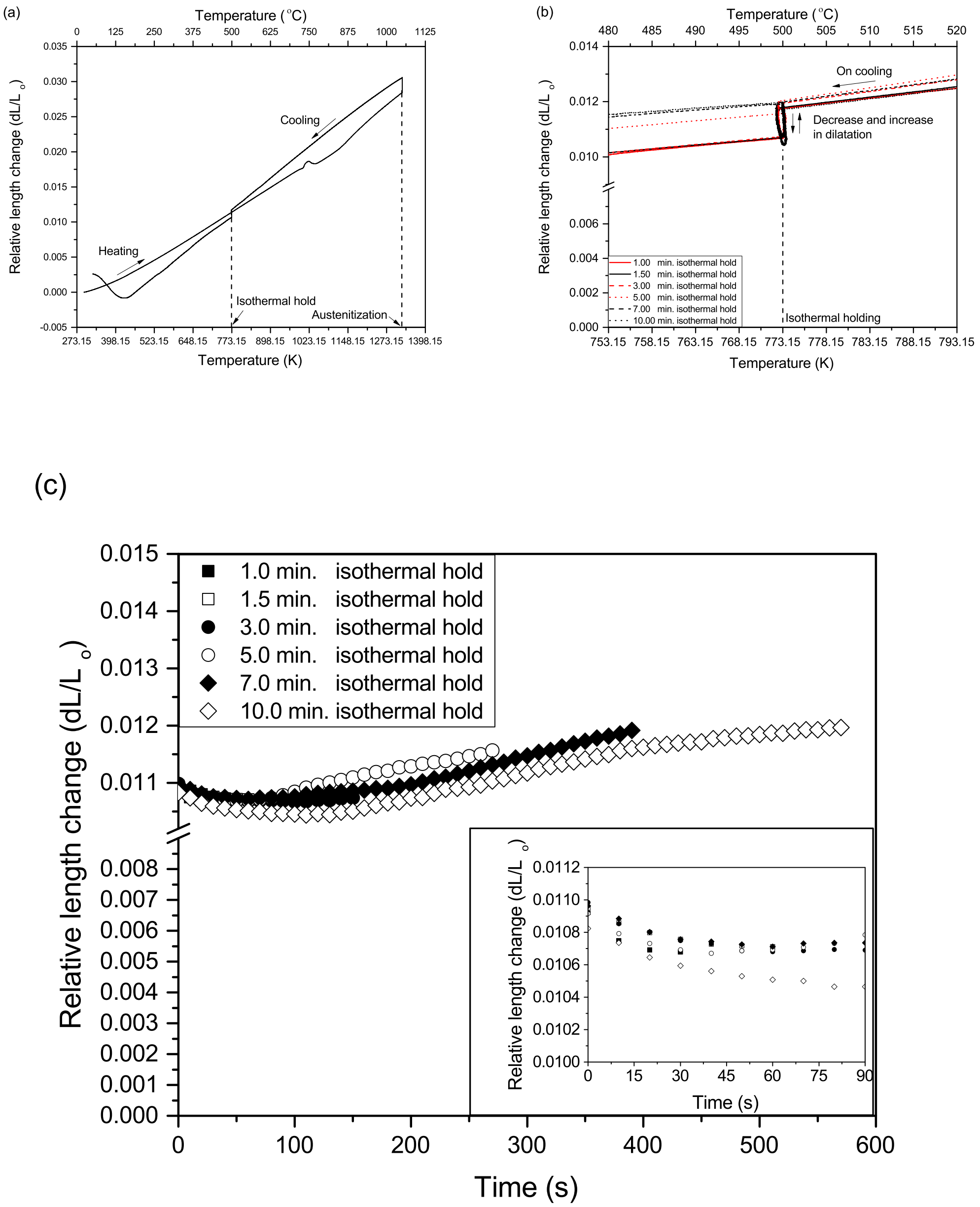

Figure 4.1: (a) Representative complete dilatation profiles for the heat treatment schedule. (b) Dilatation recording on cooling and isothermal holding in all the heat treated samples. (c) Dilatation recording after the removal of instrumental drift represented as relative length change with isothermal holding time. The inset in (c) shows the zoomed in portion of the dilatation during the 1 minute and 1.5 minute isothermal hold.

4.2.2 Microstructure Evolution

Identification of Inverse Bainite

Representative optical micrographs of the 3 minutes and 7 minutes heat treated samples in Figure 4.2 show the formation of a dark etching microstructure in a brown etched matrix. When the isothermal holding time is 3 minutes, the dark etched microstructure appears more needle like (Figure 4.2a). When the transformation time is increased to 7 minutes, the morphology of the dark etched microstructure changes from needle-like to nodular (Figure 4.2c). The higher magnification images in Figure 2b and Figure 2d represents the martensitic plates formed during the continuous cooling after the isothermal hold at 773 K (500 ° C). In the 3 minutes heat treated sample, a midrib white etching phase can be seen as indicated by the arrow in Figure 4.2b. Secondary electron SEM images of all the heat treated samples representing the evolution of the dark etched microstructure at finer scales are shown in Figure 4.3. It appears that the dark etched microstructure comprises of ferrite/carbide aggregates in a martensitic matrix (confirmation for ferrite/carbide aggregates in martensitic matrix will be provided in the following sections). In the case of shorter holding times of 1 minute and 1.5 minutes, the microstructure comprises of carbide platelets in the martensitic matrix. Figure 4.3c of the 3 minutes isothermal hold sample represents the formation of ferrite surrounding a carbide platelet. The transformation of austenite to ferrite is not complete in the case of 3 minutes isothermally heat treated sample. The untransformed regions between the carbide/austenite interface during the isothermal hold transformed to martensite/retained austenite during subsequent quenching as seen in Figure 4.3c. When the transformation time is increased to 5 minutes, secondary carbide units and ferrite are observed to form surrounding the midrib carbide. The presence of the carbide midrib is still evident in Figure 4.3d.

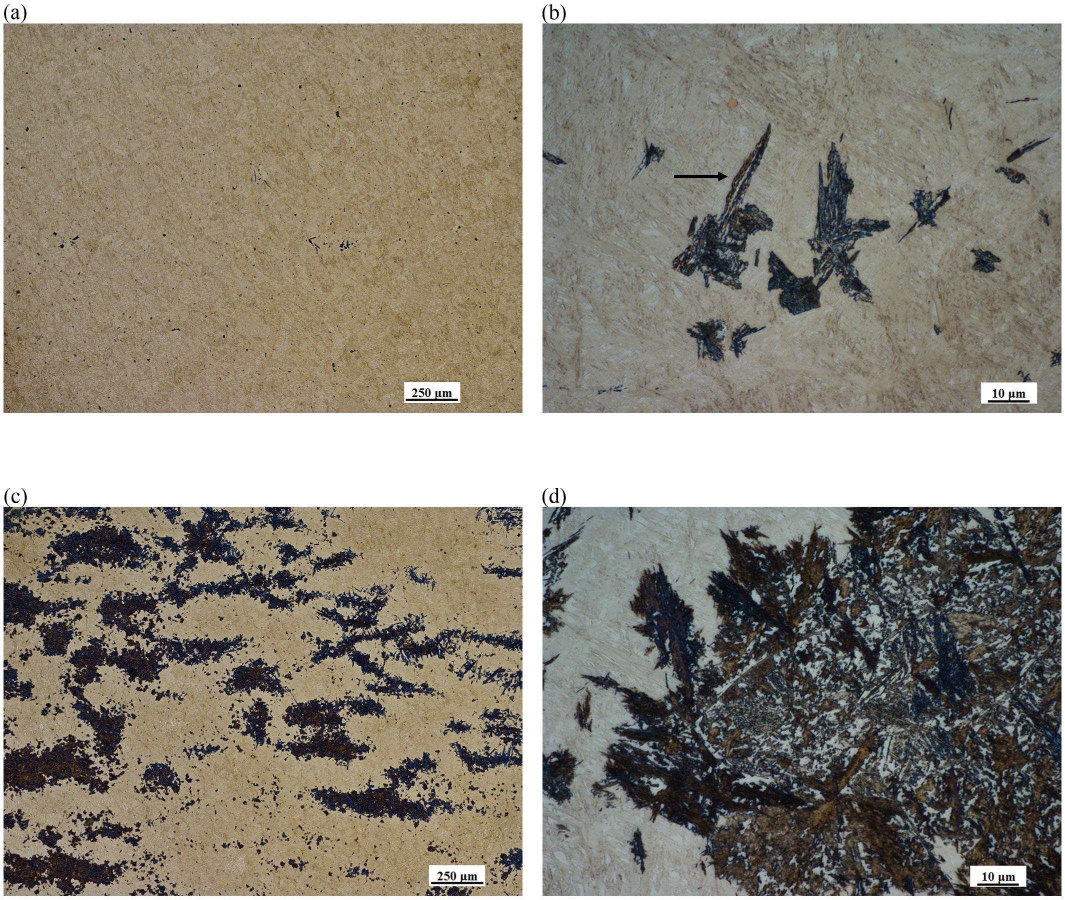

Figure 4.2: Optical micrographs of the 3 minutes (a), (b) and 7 minutes (c), (d) isothermal hold samples. (b) and (d) are the higher magnification images of (a) and (c) respectively. The arrow mark in (b) represents the midrib white etching phase.

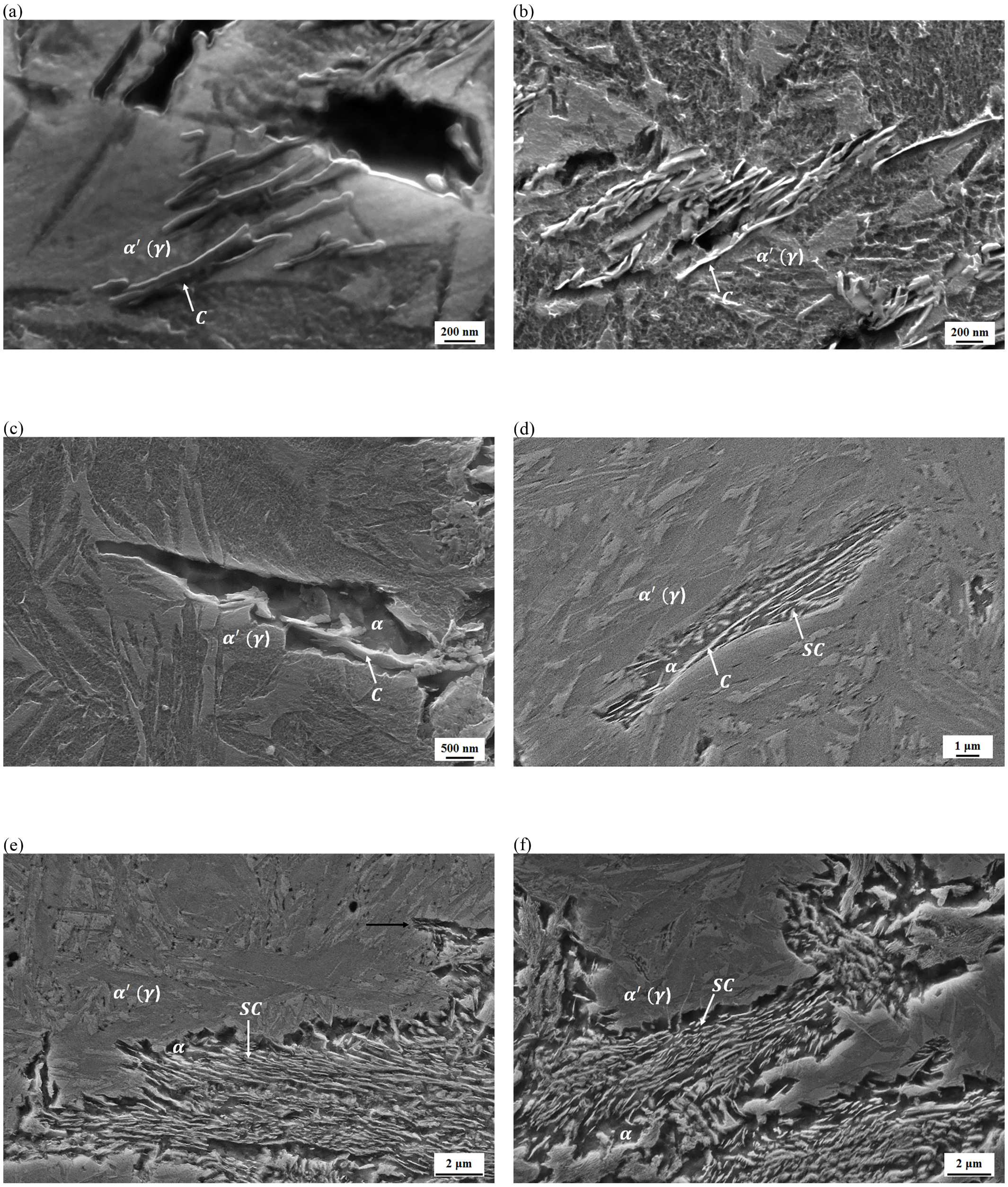

Figure 4.3: Secondary electron images of (a) 1 minute isothermal hold sample, (b) 1.5 minutes isothermal hold sample, (c) 3 minutes isothermal hold sample, (d) 5 minutes isothermal hold sample, (e) 7 minutes isothermal hold sample, and, (f) 10 minutes isothermal hold sample. The carbide unit is marked with white arrow mark in (a) and (b). The carbide unit nucleating first from austenite is marked as C. The martensite/retained austenite formed during continuous cooling after the isothermal hold is marked as $\alpha'(\gamma)$. The secondary carbide units are marked as SC. The black arrow mark in (e) shows the initial unit of inverse bainite alongside the degenerated microstructure.

Secondary electron images and EDX line scan analysis for identification of the phases for different heat treated samples are shown in Figure 4.4.

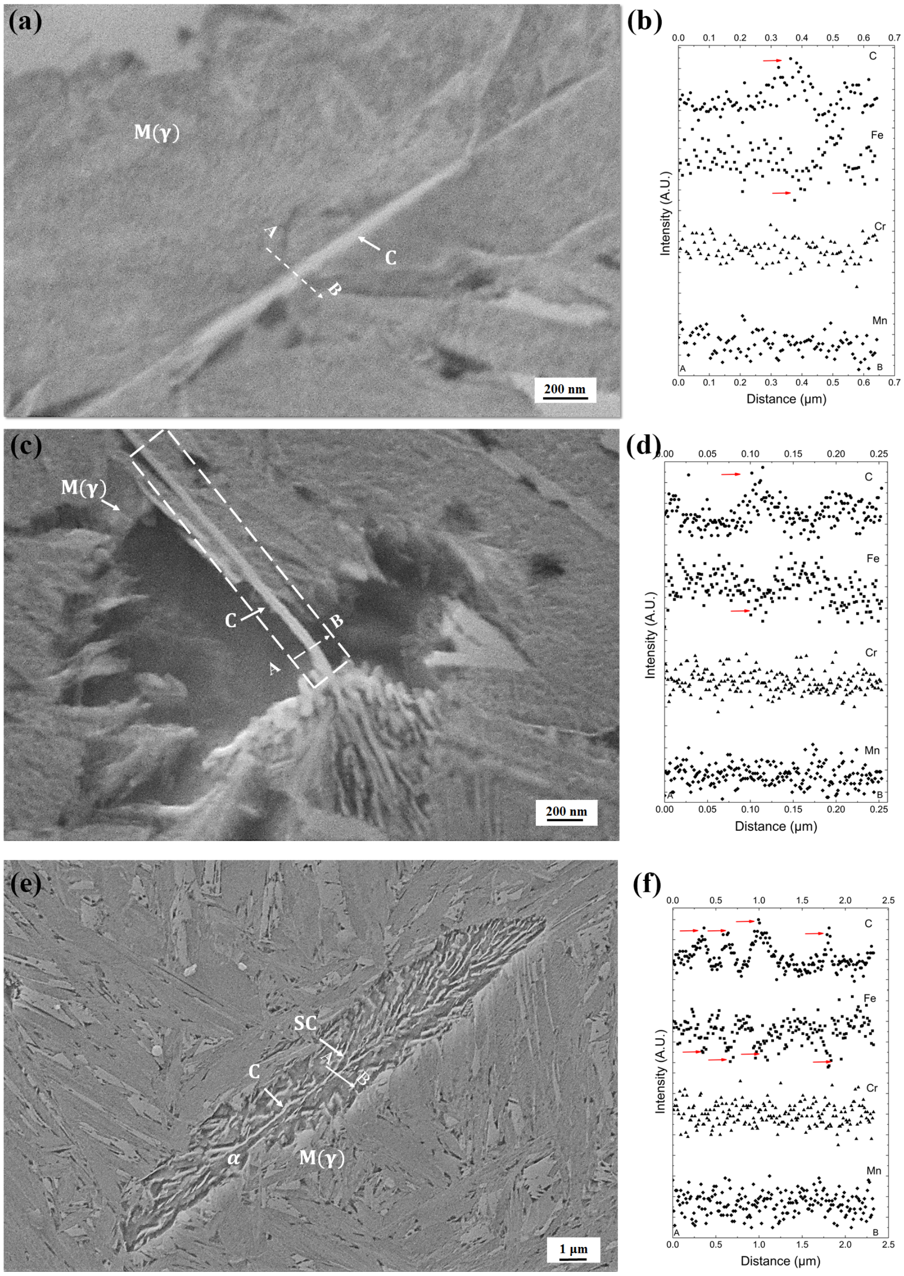

Figure 4.4: (a)Secondary electron SEM image of 1 minute isothermal hold sample. (b) EDX line scan profile corresponding the the direction AB shown in (a). (c) Secondary electron SEM image of 3 minute isothermal hold sample. (d) EDX line scan profile corresponding the the direction AB shown in (c). (e) Secondary electron SEM image of 5 minute isothermal hold sample. (f) EDX line scan profile corresponding the the direction AB shown in (ef). In (a), (b) the dark etched microstructure is marked by black arrow. In (a), (c), (e) the carbide midrib is marked with C, secondary carbides are marked with SC, martensite/retained austenite matrix is marked with M(γ).

It can be seen that in the 1 minute isothermally transformed sample, a needle shaped phase has formed in the dark etching micro constituent (Figure 4.4a). EDX line scan analysis across one phase confirms that it has a high carbon concentration (Figure 4.4b) and the phase is likely cementite or transition carbides of iron. Thus it can be suggested that 1 minute isothermal hold involves formation of carbide unit. In the 3 minutes isothermally transformed sample, formation of a new phase surrounding the midrib carbide unit is observed (Figure 4.4c). EDX line scan across the carbide unit suggests that the carbide is either cementite or transition carbides of iron and the newly formed phase surrounding the carbide unit is ferrite (iron peak away from the carbide unit (Figure 4.4d). It is of particular interest to mention that the transformation of ferrite has not completed during the 3 minutes isothermal hold, this is clear from the SEM image in Figure 4.4e where the untransformed region between ferrite/austenite interface during isothermal hold later transformed to martensite (indicated by arrow). When the transformation time is increased to 5 minutes, ferrite transformation has completed and carbides surrounding the midrib carbide (secondary carbides) start to form within the bainitic unit (Figure 4.4e). EDX line scan across the carbide units seems to suggest that the carbides are cementite or transition carbides of iron in a ferrite matrix. The relative intensity of carbon in the secondary carbides is lower than that of the carbide midrib (Figure 4.4f). No partitioning of Cr or Mn is observed in any of the samples, indicating that the carbides are some crystallographic forms of Fe carbide.

The EDX line scan analysis confirms that the initial nucleating phase is carbide (Figure 4.3a,b) and not ferrite, therefore, the morphology alone strongly suggests the bainitic unit to be inverse bainite. When the transformation time is further increased to 7 minutes and beyond, the characteristic carbide midrib of the inverse bainite microstructure disappears. The carbide midrib can no longer be distinguished from the secondary carbides in the case of 7 minutes and 10 minutes isothermal holds, and all the carbides have the morphology of the secondary carbides in Figure 4.3e and f. The microstructure has degenerated to upper bainite. Though the formation of upper bainite on either side of the inverse bainitic cementite midrib was reported in the model proposed by Kinsman [46], to the author's knowledge, the conversion of an entire unit of inverse bainite into upper bainite was not reported. Further details regarding the conversion of inverse bainite into upper bainite will be discussed in the subsequent sections. It is of particular interest to mention that in the 7 minutes and 10 minutes heat treated samples, the initial microstructure of the inverse bainite (indicated by the black arrow in Figure 4.3e) is observed alongside the degenerated microstructure.

Phase distribution in inverse bainite microstructure.

XRD profiles and hardness measurements for the different transformation times are shown in Figure 4.5 and Figure 4.6 respectively. XRD profiles in Figure 4.5 show the formation of two main phases, namely BCC and FCC. Detailed indexing of the diffraction data using Rietveld refinement procedure shows the presence of cementite (θ), ferrite (α), austenite (γ), and martensite (α') diffractions. It is notable that in the 1 minute and 1.5 minutes heat treated samples, introduction of ferrite along with the martensitic matrix resulted in a poorer Rietveld fitting ($\chi^2 = 1.45$) in comparison to the refinement with martensitic matrix only and without any ferrite (goodness of fit [70] $\chi^2 = 1.0194$). The lattice parameters of martensite and the fraction of phases after Rietveld refinement are tabulated in Table 1. Cementite (θ) is clearly detected by XRD in the 1 minute and 1.5 minutes heat treated samples, but not ferrite. From the 3 minutes isothermally transformed sample and beyond, ferrite peaks are identified. The intensity of the ferrite peaks increases gradually with the increase in transformation time, which indicates an increase in the fraction of the ferritic unit of inverse bainite. Typical load progression curves during the instrumented indentation experiments are shown in Figure 4.6a.

Table 4.1: Lattice Parameters and Fraction of Phases after Rietveld Refinement of the Raw XRD Data

Transformation time	$c_{\alpha'}$ ($\dot{A}$)	$a_{\alpha'}$ ($\dot{A}$)	$c_{\alpha'}/a_{\alpha'}$	$f_{\alpha'}$ (%)	f_{γ} (%)	f_{α} (%)	f_{θ} (%)
1 minute	2.88820	2.8510	1.01304	81.29	12.90	-	5.15
1.5 minutes	2.89526	2.85529	1.01400	72.05	15.70	-	-
3 minutes	2.88810	2.85105	1.01302	76.57	16.40	5	2.03
5 minutes	2.91382	2.86802	1.01596	78.41	6.73	7	7.86
7 minutes	2.89070	2.87651	1.00493	40.44	20.40	36.70	3.46
10 minutes	2.86805	2.8553	1.0044	35.45	6.40	42.10	16.05

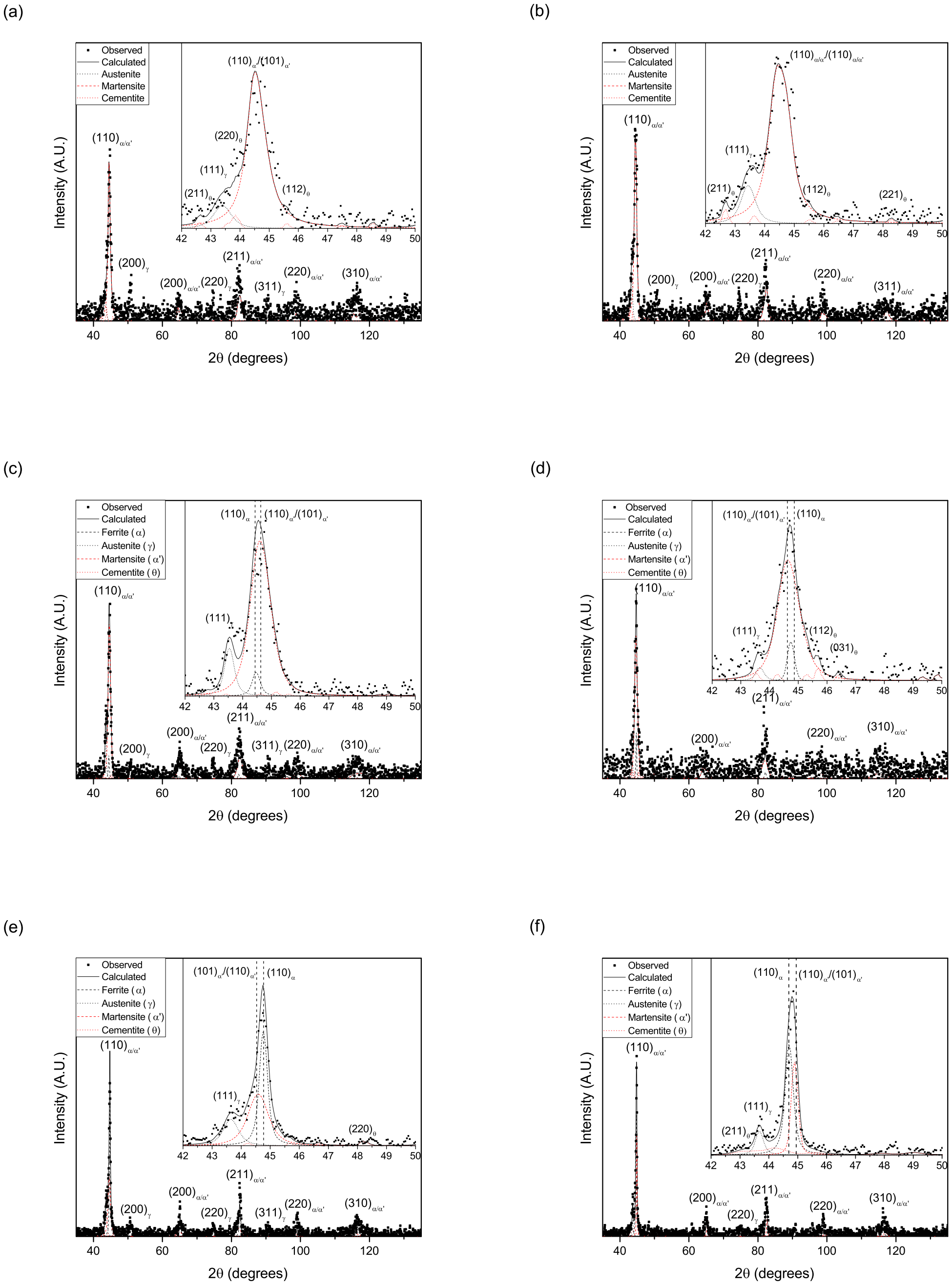

Figure 4.5: XRD patterns from (a) 1 minute, (b) 1.5 minutes, (c) 3 minutes, (d) 5 minutes, (e) 7 minutes, and (f) 10 minutes heat treated samples. The inset shows zoomed in portion of the $(110)_{BCC}/(111)_{FCC}$ diffraction patterns obtained after Rietveld refinement of the raw XRD data.

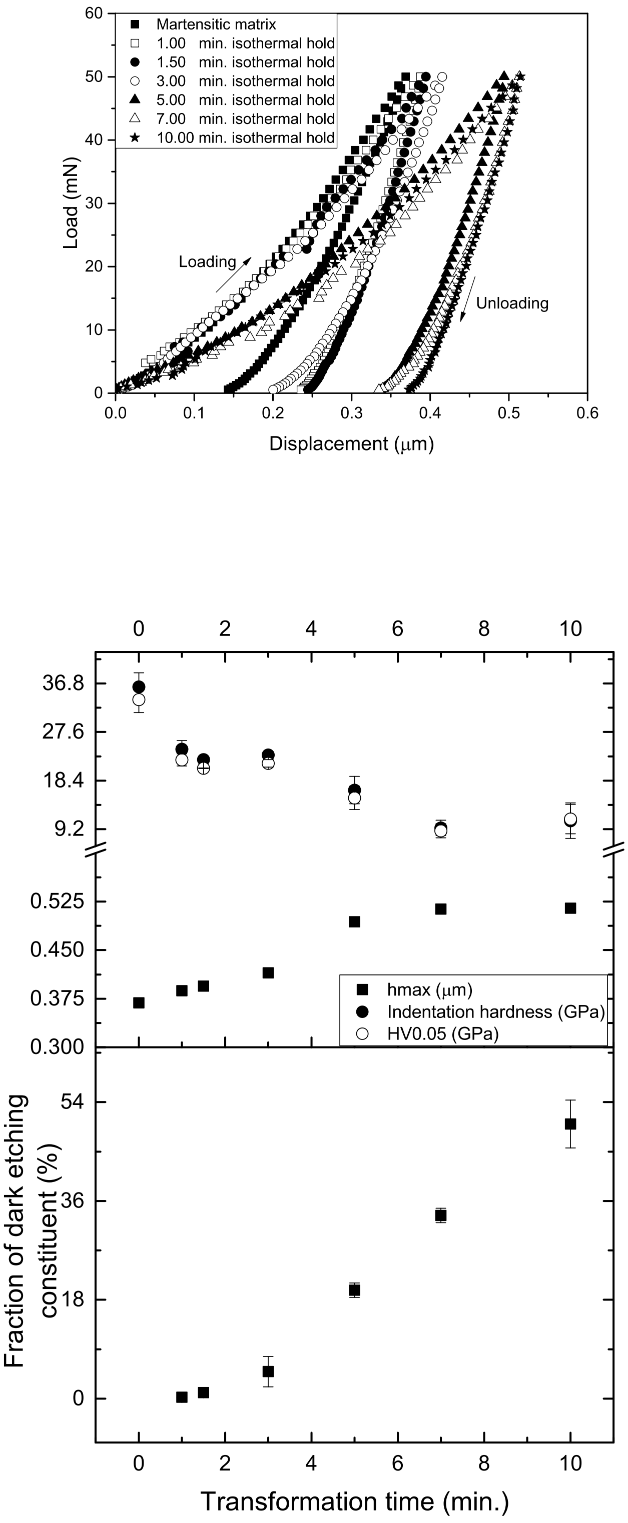

Figure 4.6: Variation in the load-depth response, indentation hardness, HV0.05, maximum depth of penetration, and the fraction of inverse bainite with the increase in transformation time. Time 0 in the graph represents the as-quenched martensitic matrix.

It can be seen that the martensitic matrix has the least slope of the load-displacement curve. For the bainitic regions, the slope initially increases and appears to be a constant with an increase in the transformation time. The increase in slope and the maximum penetration depth indicates that the hardness of the inverse bainitic microstructure progressively decreases with an increase in transformation time. The maximum depth of penetration for the as-quenched martensitic matrix, 1 minute isothermal hold, 1.5 minutes isothermal hold, and the 3 minutes isothermal hold samples are similar. When the isothermal transformation time is increased to 5 minutes and longer, there is a sudden increase in the maximum depth of penetration. The indentation hardness and elastic modulus obtained by using the Oliver-Pharr analysis [54] for the load-displacement curves are shown in Figure 4.6b and Table 4.2. The average indentation hardness is the highest for the as-quenched martensitic matrix. Though such a higher hardness is not commonly reported in the literature for as-quenched martensite, the results are close to the ones reported by Furnemont *et al.* [78] and Li *et al.* [79]. The higher indentation hardness obtained in our current experiments can be likely due to the higher carbon content of our steel; also the measurements by Li *et al.* [79] were on tempered martensitic structure in comparison to the as-quenched martensitic structure in our experiments. For the inverse bainite, it can be seen that the indentation hardness decreases with an increase in transformation time and the fraction of inverse bainite. The maximum penetration depth of inverse bainite, which is representative of the ductility of the microstructure, is initially close to the as-quenched martensitic matrix. When the degenerated microstructure of upper bainite begins to form from inverse bainite (5 minutes and longer), there is a sudden jump in the maximum penetration depth due an increase of ferrite content in

Table 4.2: Indentation hardness and Young's modulus obtained from the Oliver-Pharr analysis.The micro Vicker's hardness is also included for comparison. Time 0 represents the data for the as-quenched martensitic matrix

Time (min.)	Indentation hardness (GPa)	Vicker's hardness (GPa)
0	36.15±2.68	33.74±2.47
1	24.34±1.67	22.34±1.14
1.5	22.37±0.08	20.75±0.06
3	23.27±0.63	21.67±0.70
5	16.62±2.58	15.14±2.23
7	9.50±1.44	8.92±1.34
10	10.84±3.36	11.14±2.78

the microstructure. The decrease in hardness values further provides evidence to the conclusion from the optical metallographs that the fraction of martensite decreases and the fraction of ferrite increases with the increase in transformation time. Thus the XRD data and hardness measurements further provide evidence for the matrix being martensite and retained austenite, and it can thus be concluded that the matrix microstructure is martensite/retained austenite and the dark etching microstructure is an aggregate of ferrite and cementite of the inverse bainitic unit.

To verify the phase identification from metallography, and XRD, the 1 minute, 3 minutes, 5 minutes, and 10 minutes heat treated samples were characterized using HRTEM/EBSD. HRTEM images along with corresponding FFT, and the reconstructed EBSD phase maps are shown in Figure 4.7, Figure 4.8, Figure 4.9 ([80]), and Figure 4.10 respectively.

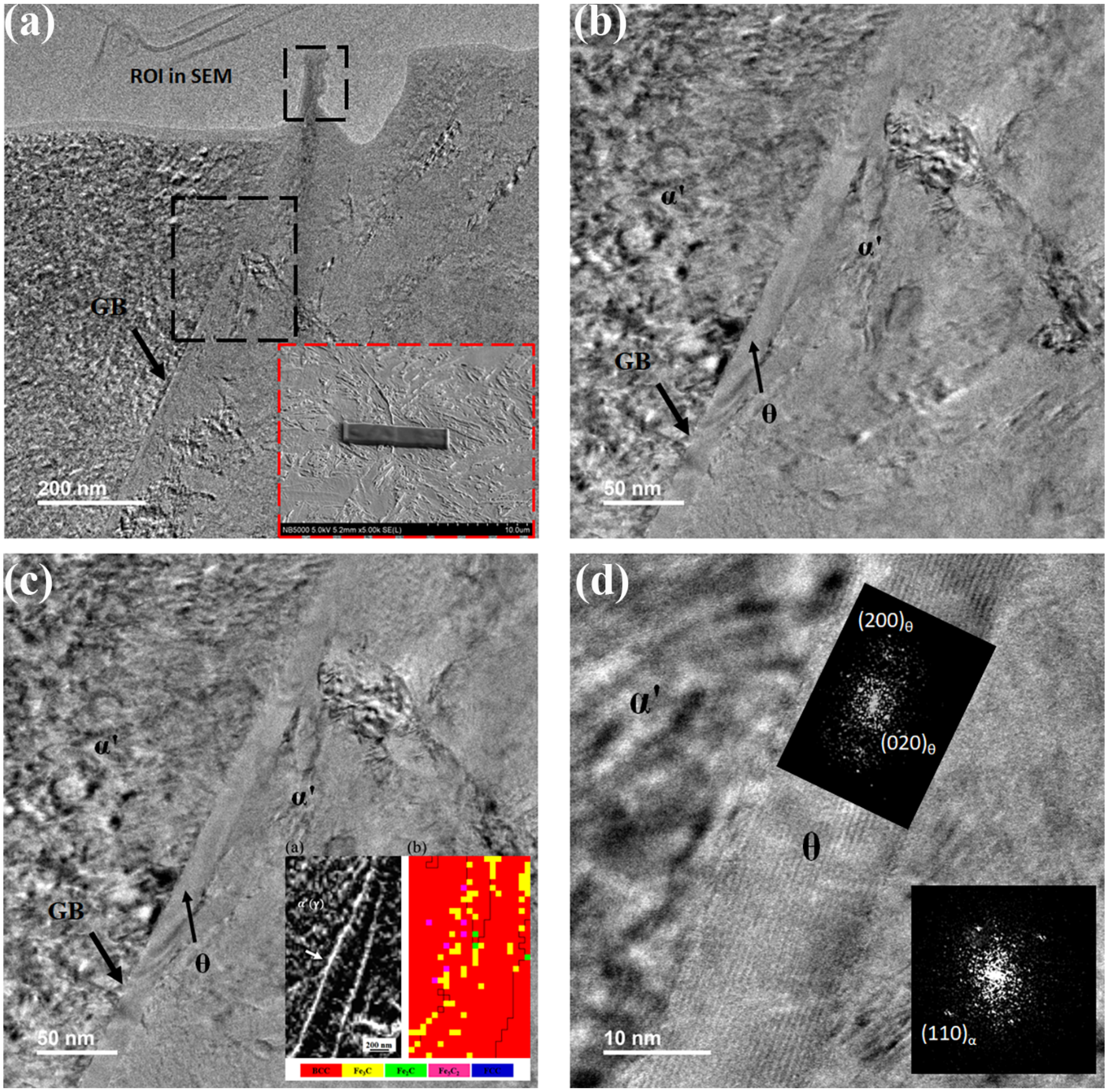

Figure 4.7: STEM/HRTEM analysis on the 1 minute isothermal hold sample. (a) FIB liftout region, (b) STEM image showing carbide along the grain boundary in martensitic matrix, (c) STEM image showing carbide along the grain boundary in martensitic matrix along with EBSD phase analysis. The yellow phase is cementite and red phase is BCC (martensite), (d) HRTEM image and corresponding FFT indicating that the carbide is cementite and the matrix is martensite.

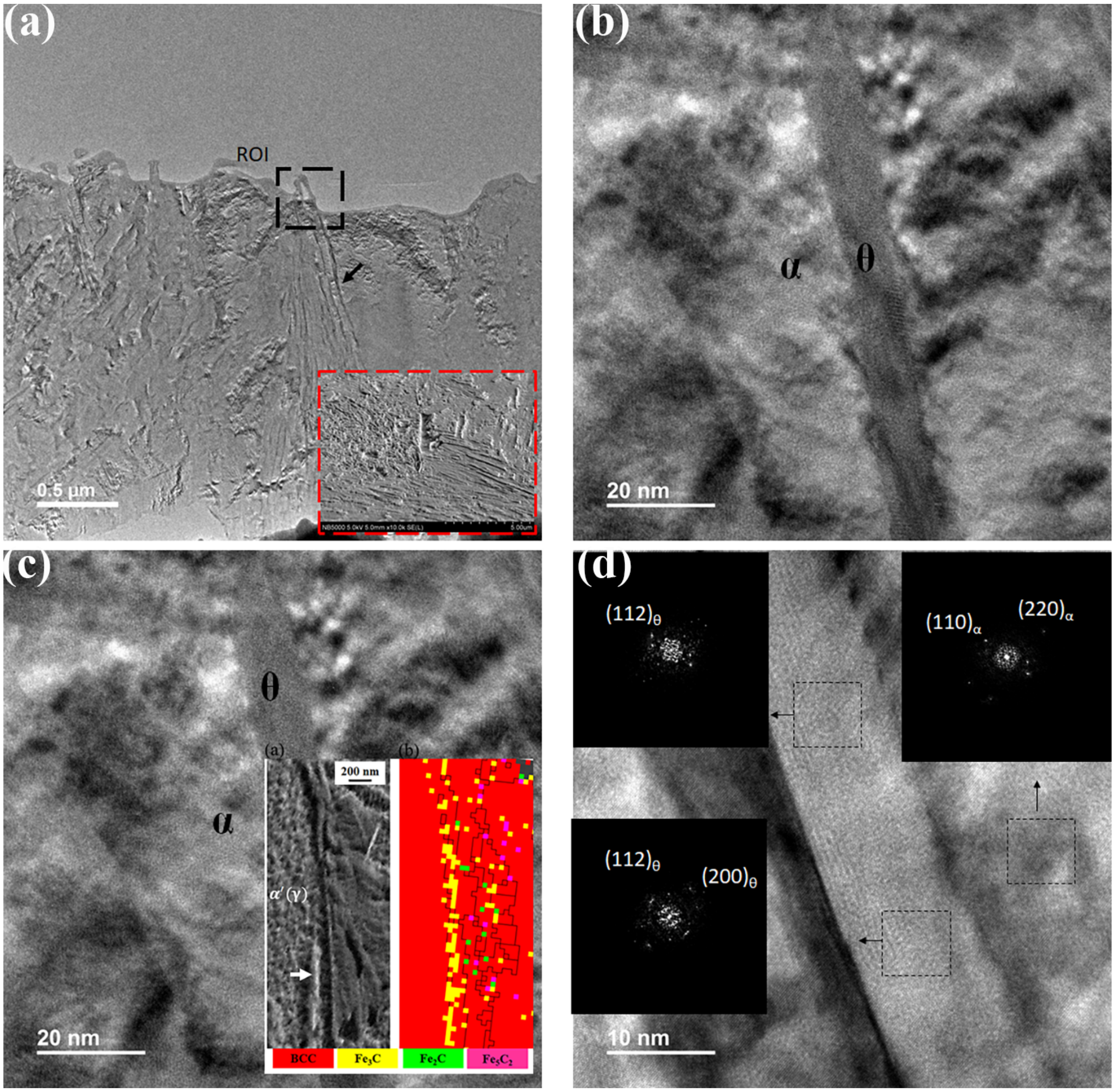

Figure 4.8: STEM/HRTEM analysis on the 3 minute isothermal hold sample. (a) FIB liftout region, (b) STEM image showing carbide along the grain boundary and ferrite surrounding the carbide in martensitic matrix, (c) STEM image showing carbide along the grain boundary and ferrite surrounding the carbide in martensitic matrix along with EBSD phase analysis. The yellow phase is cementite and red phase is BCC (martensite), (d) HRTEM image and corresponding FFT indicating that the carbide is cementite and the matrix is martensite.

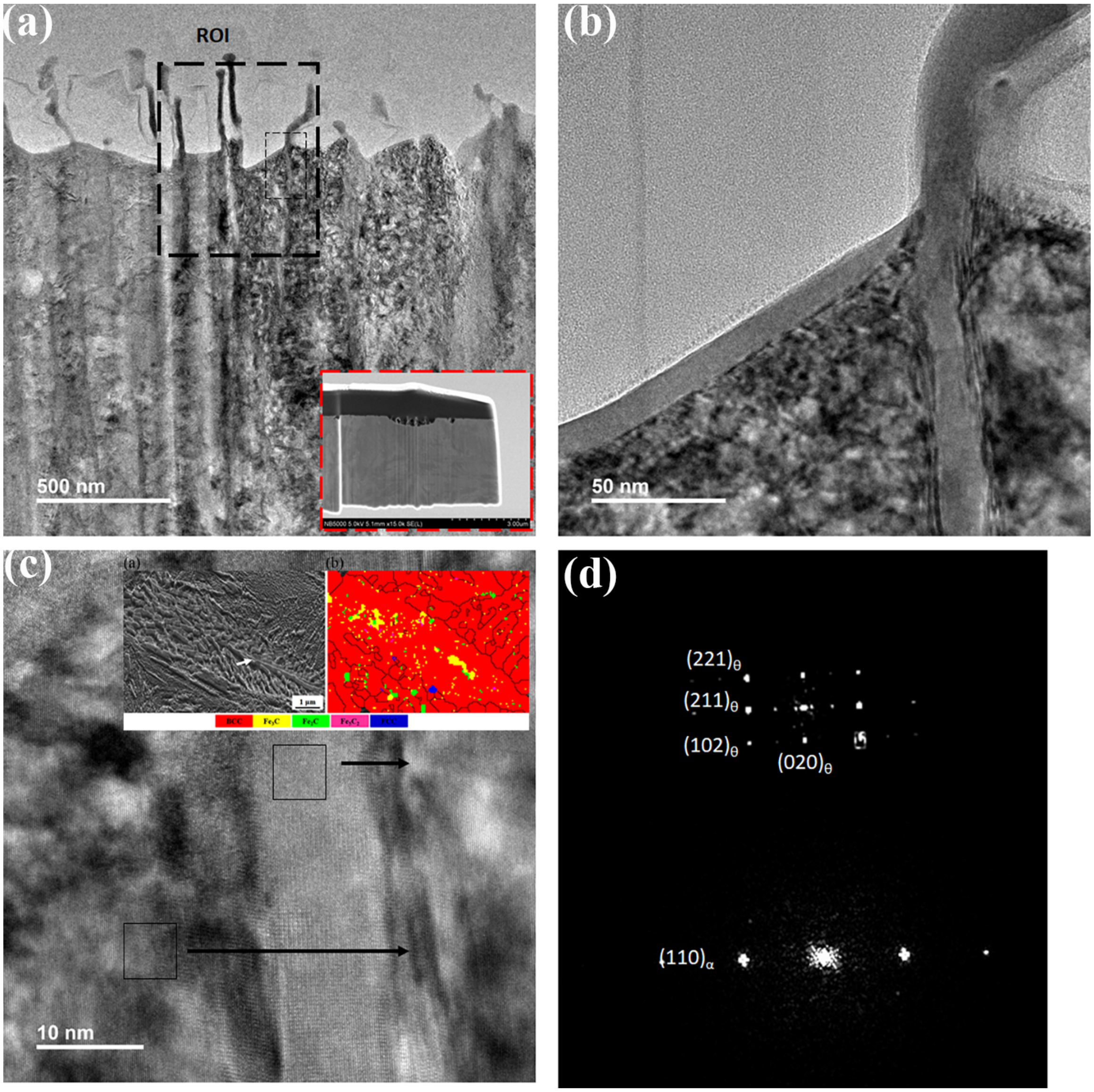

Figure 4.9: STEM/HRTEM analysis on the 5 minute isothermal hold sample. (a) FIB liftout region, showing secondary carbides in ferrite (b) STEM image showing carbide along the grain boundary and ferrite surrounding the carbide in martensitic matrix, (c) STEM image showing carbide along the grain boundary and ferrite surrounding the carbide in martensitic matrix along with EBSD phase analysis. The yellow phase is cementite and red phase is BCC (martensite), (d) HRTEM image and corresponding FFT indicating that the carbide is cementite and the matrix is martensite.

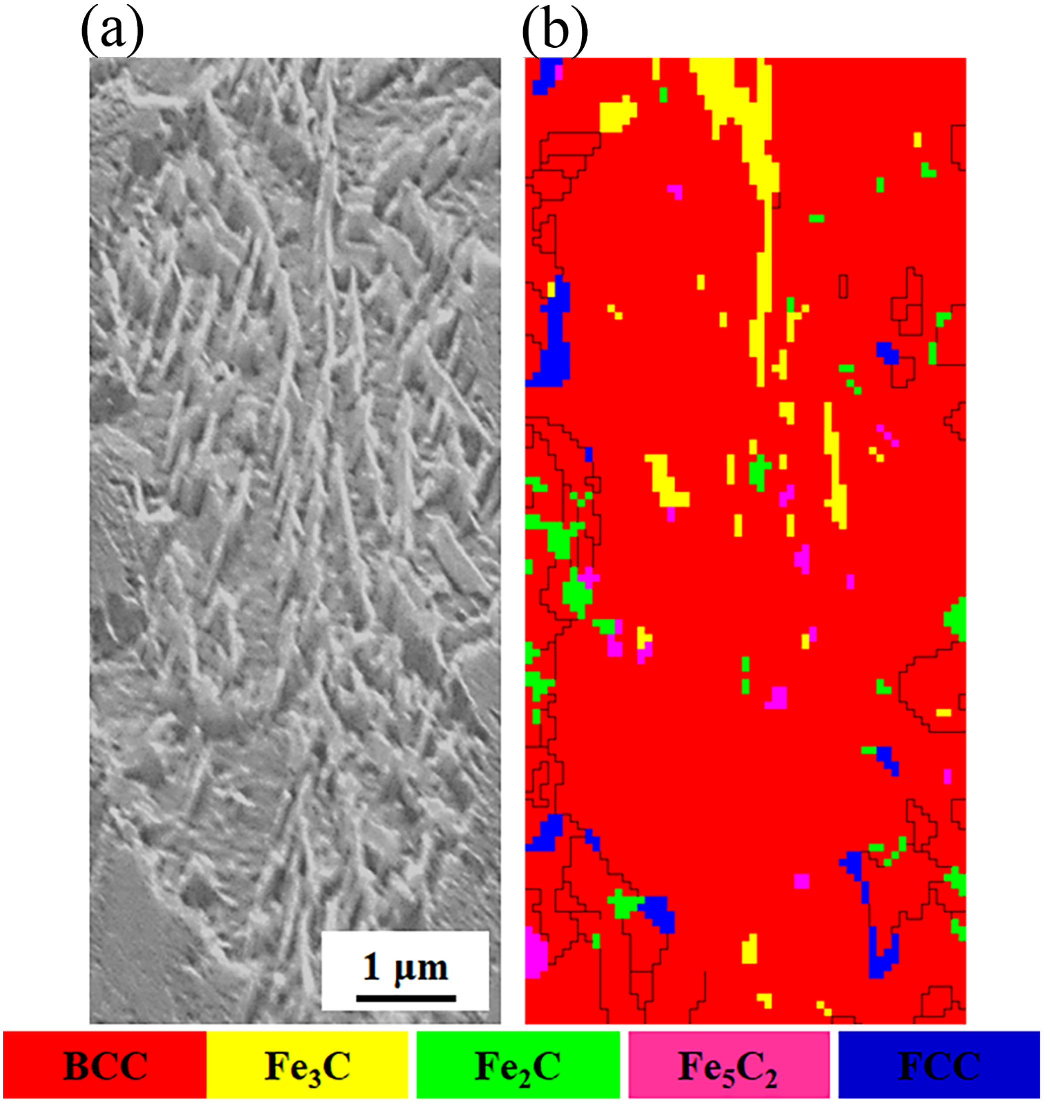

Figure 4.10: EBSD analyses on 10 minutes heat treated sample. (a) Secondary electron image of the region from where EBSD map was obtained, (b) Reconstructed EBSD Phase map with HAGB's (misorientation greater than 10°).

The phase maps of 1 minute and 3 minutes (Figure 4.7b, Figure 4.8b) heat treated samples show that carbide midrib which forms from parent austenite during the isothermal hold is cementite. Other types of carbides (Fe_5C_2, and Fe_2C) are present in the martensitic matrix formed following the isothermal transformation. In the case of 5 minutes and 10 minutes heat treated samples, the phase maps (Figure 4.9b [80], Figure 4.10b) confirm that the carbide midrib is cementite and the secondary carbides shown in Figure 4.3d are mainly Fe_3C, Fe_2C, and Fe_5C_2. EBSD detects the presence of Fe_2C and Fe_5C_2 type carbides but the XRD results (Figure 4.5) could not pick up the Fe_2C and Fe_5C_2 carbides probably because of the small dilatometry samples used for the XRD data acquisition and the lower fraction of Fe_2C and Fe_5C_2 carbides. It should be brought to the readers attention that although the steel contains Cr, Cr mainly affects the finish temperature of inverse bainite and does not partition during the transformation as presented in our previous article (Ref. Figure 4 in [80]). Also, precipitation simulation using MatCalc calculations indicate that Cr_7C_3 and $Cr_{23}C_6$ form at prolonged transformation times (greater than 10,000 sec) and not during the initial stage of the transformation, in which case cementite is the favored transformation product. In some cases retained austenite is observed closer to the bainitic unit, which enabled the measurement of the three phase OR discussed in the next section. It can be seen that in Figure 4.9 [80], the cementite midrib is starting to disappear, marking the onset of the degenerate microstructure formation. In Figure 4.10, the cementite midrib has completely degenerated to a typical upper bainite microstructure.

4.2.3 Orientation Relationship of the Transformation

The OR between individual phases of inverse bainite was obtained directly by matching the α/γ, $\alpha/\theta_{secondary}$, and α/θ_{midrib} relationships from the orientation data acquired using EBSD. Crystallographic orientations in the inverse bainitic unit are represented as reconstructed inverse pole figure maps. Figure 4.11 represents the crystallographic orientation in the 3 minute heat treated sample (Figure 4.11 a and b). Pole figures in column c (Figure 4.11c1-Figure 4.11c4) represent the pole figures of the planes in cementite ($\{\bar{2}21\}, \{211\}$) and ferrite ($\{110\}$). Pole figures in column d (Figure 4.11d1-Figure 4.11d3) represent the pole figures of the directions in cementite ($< 1\bar{1}0 >$) and ferrite ($< 111 >$). Parallel planes and directions where crystallographic orientation matching occurs is marked by arrow marks in the combined pole figure of ferrite (black empty circles) and cementite (green dots) in Figure 4.11c4 and

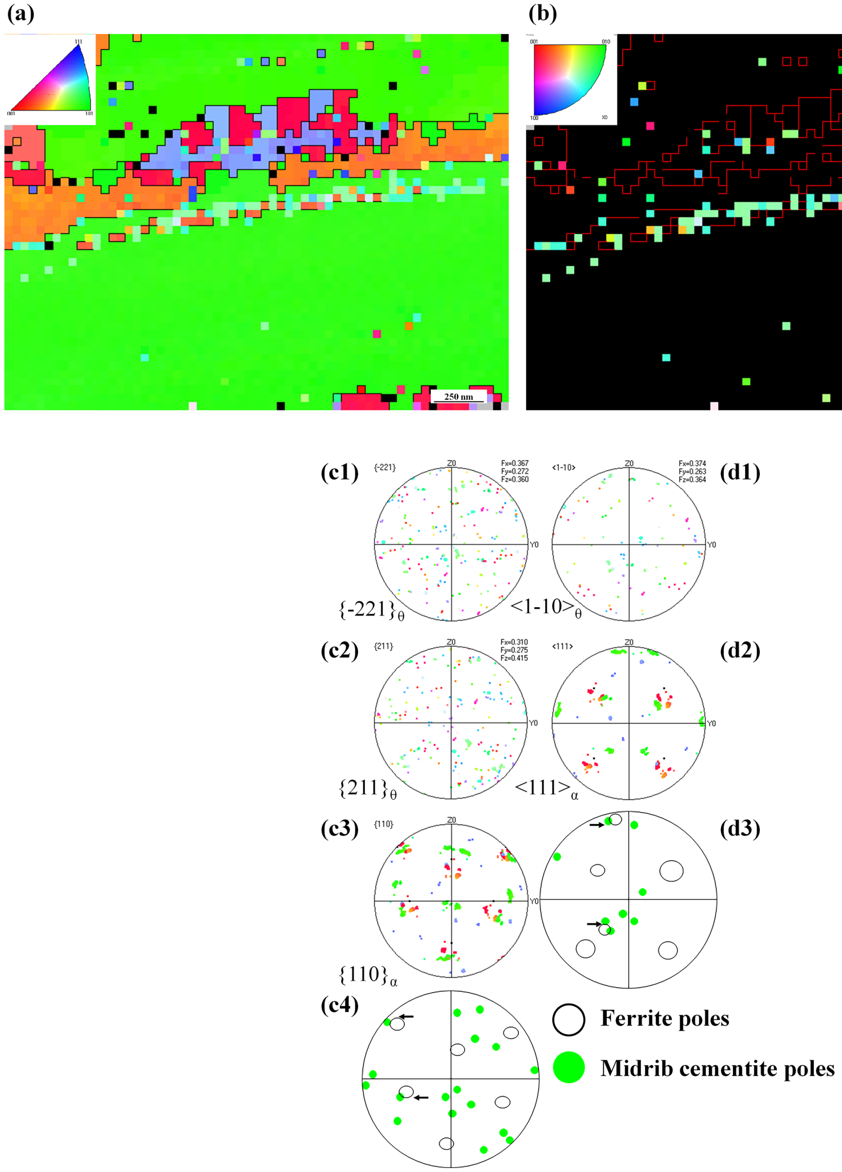

Figure 4.11: Pole figure analysis in the 3 minute heat treated sample. (a) Reconstructed inverse pole figure (IPF) map with high angle grain boundaries ($\theta > 10°$). (b) Reconstructed inverse pole figure (IPF) map of Fe_3C phase with high angle grain boundaries ($\theta > 10°$). (c1) $\{\bar{2}21\}$ pole figure of cementite, (c2) $\{211\}$ pole figure of cementite, (c3) $\{110\}$ pole figure of ferrite, (c4) Combined pole figure of $\{\bar{2}21\}_\theta$, $\{211\}_\theta$ (green dots), and $\{110\}_\alpha$ (empty black circles) crystallographic orientation matching is represented by arrow. (d1) $< 1\bar{1}0 >$ pole figure of cementite, (d2) $\{111\}$ pole figure of ferrite, (d3) Combined pole figure of $< 1\bar{1}0 >_\theta$ (green dots), and $< 111 >_\alpha$ (empty black circles). Crystallographic orientation matching is represented by arrow.

Figure 4.11d3. Since the $\{\bar{2}21\}, \{211\}$ planes of cementite are parallel to the ferrite $\{110\}$ planes separated by a minimum angular deviation, and the $< 1\bar{1}0 >$ direction in cementite is parallel to the $< 111 >$ direction in ferrite separated by minimum angular deviation, the OR between cementite midrib and ferrite likely obeys:

$$< 111 >_\alpha \;||\; < 1\bar{1}0 >_\theta$$

$$\{110\}_\alpha \;||\; \{\bar{2}21\}_\theta$$

$$\{110\}_\alpha \;||\; \{211\}_\theta$$

The cementite midrib ferrite orientation relationship calculated by EBSD is further confirmed by the electron diffraction patterns from HR-TEM in Figure 4.12. Figure 4.13 represents the crystallographic orientation in the 10 minute heat treated sample (Figure 4.13 a and b). Pole figures in column c (Figure 4.13c1- Figure 4.13c5) represent the pole figures of planes in cementite ($\{\bar{2}21\}, \{211\}$), ferrite ($\{110\}$) and austenite ($\{111\}$). Pole figures in column d (Figure 4.13d1- Figure 4.13d4) represent the pole figures of the directions in cementite ($< 1\bar{1}0 >$), ferrite ($< 111 >$) and austenite ($< 110 >$). Parallel planes and directions where crystallographic orientation matching occurs are marked by arrow marks in the combined pole figures of ferrite (empty black circles), cementite (green dots represents the central carbide variant, red dots indicate the secondary carbide variants of cementite) and austenite (blue dots) in Figure 4.13c5 and Figure 4.13d4. In the pole figure analysis of the 10 minutes isothermally treated sample, retained austenite was observed closer to the inverse bainitic unit which enabled the measurement of the three phase (θ, γ, and α) crystallographic orientation matching. The three phase crystallographic orientation matching is represented by the blue arrow in the combined pole figures (Figure 4.13c5 and Figure 4.13d4). The pole figure analysis in Figure 4.13c5 shows that the $\{\bar{2}21\}, \{211\}$ planes of cementite are parallel to the ferrite $\{110\}$ planes, which are in turn parallel to the $\{111\}$ planes of austenite. In Figure 4.13d4, the $< 1\bar{1}0 >$ directions in cementite is parallel to the $< 111 >$ directions in ferrite, which are in turn parallel to the $< 110 >$ directions in austenite. Thus, a three phase crystallographic orientation matching between parent austenite, cementite midrib and inverse bainitic ferrite is observed in the 10 minutes heat treated sample, and the OR likely

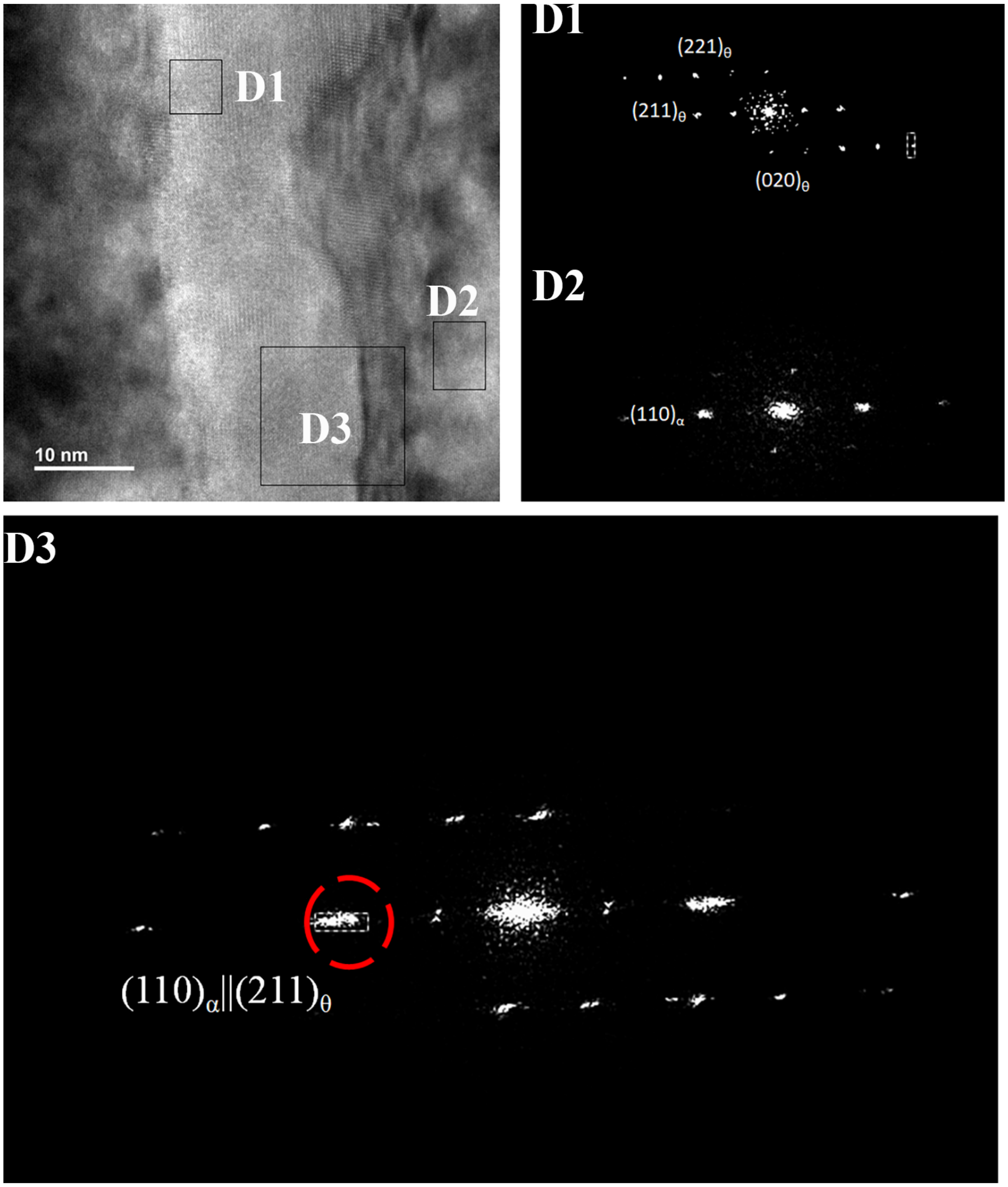

Figure 4.12: HR TEM image and corresponding diffraction patterns of cementite midrib and ferrite in the 5 minute heat treated sample. The orientation matching between the cementite midrib and ferrite is represented by a dotted circle in the diffraction pattern D3.

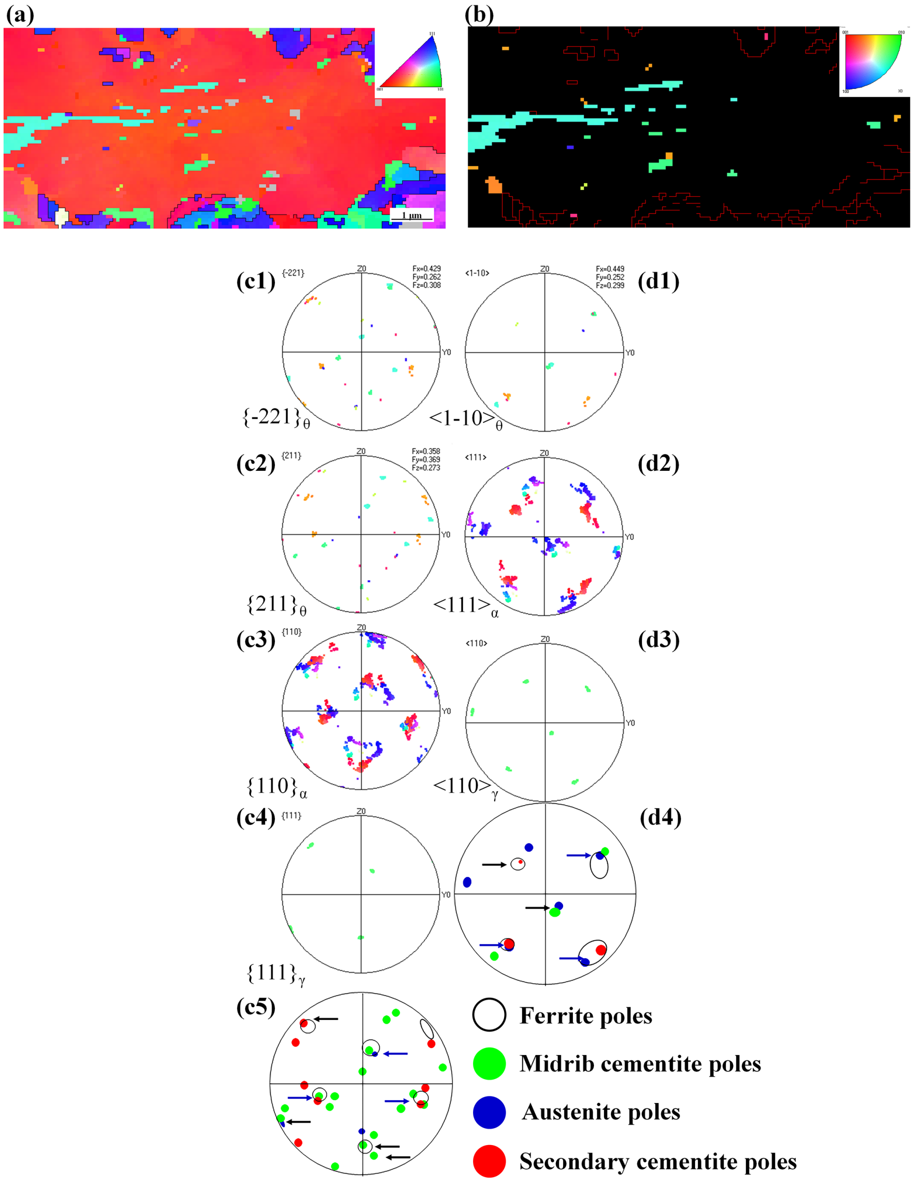

Figure 4.13: Pole figure analysis in the 10 minute heat treated sample. (a) Reconstructed inverse pole figure (IPF) map with high angle grain boundaries ($\theta > 10°$). (b) Reconstructed inverse pole figure (IPF) map of Fe_3C phase with high angle grain boundaries ($\theta > 10°$). (c1) $\{\bar{2}21\}$ pole figure of cementite, (c2) $\{211\}$ pole figure of cementite, (c3) $\{110\}$ pole figure of ferrite, (c4) $\{111\}$ pole figure of austenite, (c5) Combined pole figure of $\{\bar{2}21\}_\theta$, $\{211\}_\theta$ (green dots represents the central carbide variant, red dots indicate the secondary carbide variants of cementite), $\{110\}_\alpha$ (empty black circles) and $\{111\}_\gamma$ (blue dots). Crystallographic orientation matching is represented by arrow, three phase crystallographic orientation matching is represented by blue arrow. (d1) $< 1\bar{1}0 >$ pole figure of cementite, (d2) $< 111 >$ pole figure of ferrite, (d3) $< 110 >$ pole figure of austenite, (d4) Combined pole figure of $< 1\bar{1}0 >_\theta$ (green dots represents the central carbide variant, red dots indicate the secondary carbide variants of cementite), $< 111 >_\alpha$ (empty black circles) and $< 110 >_\gamma$ (blue dots). Crystallographic orientation matching are represented by arrow, three phase crystallographic orientation matching is represented by blue arrow.

obeys

$$\begin{array}{ccc} <110>_{\gamma} \;||\; <1\bar{1}0>_{\theta} & <111>_{\alpha} \;||\; <1\bar{1}0>_{\theta} & <110>_{\gamma} \;||\; <111>_{\alpha} \\ \{111\}_{\gamma} \;||\; \{\bar{2}21\}_{\theta} & \{110\}_{\alpha} \;||\; \{\bar{2}21\}_{\theta} & \{111\}_{\gamma} \;||\; \{110\}_{\alpha} \\ \{111\}_{\gamma} \;||\; \{211\}_{\theta} & \{110\}_{\alpha} \;||\; \{211\}_{\theta} & \end{array}$$

The secondary cementite/ferrite orientation relationship calculated by EBSD is further confirmed by the electron diffraction patterns from HR-TEM in Figure 4.14. The OR between ferrite and cementite observed in the 10 minutes heat treated sample is similar to the OR between ferrite and cementite observed in the 3 minutes heat treated sample; this provides consistency in the measured OR between ferrite and cementite.

The results of pole figure analyses are presented statistically as the reconstructed OR maps in Figure 4.15. From the orientation relationship maps it can be seen that the inverse bainitic ferrite and parent austenite follow the KS OR with a deviation of <10°, and Fe_3C and ferrite follow the $[01\bar{1}]_{\theta}||[111]_{\alpha}, (2\bar{2}1)_{\theta}||(1\bar{1}0)_{\alpha}$ OR. Figure 4.15d represents the angular deviations of OR boundaries presented in Figure 4.15a-c from the ideal OR. It is seen that the inverse bainitic ferrite follows the KS OR with a mean angular deviation of 3.5^{o} and the mean angular deviation between Fe_3C and inverse bainitic ferrite is 13^{o}. The angular deviation between Fe_3C and α decreases with the progress of the transformation. Thus, from the experimental pole figures analysis of the orientation correspondence of γ, α, and θ (Figure 4.11, Figure 4.13) and from the analysis of the angular deviations from the ideal OR in Figure 4.15, it can be concluded that the OR in inverse bainite transformed isothermally at 773 K (500 ° C) in the steel under study is:

$$\begin{array}{ccc} <110>_{\gamma} \;||\; <1\bar{1}0>_{\theta} & <111>_{\alpha} \;||\; <1\bar{1}0>_{\theta} & <110>_{\gamma} \;||\; <111>_{\alpha} \\ \{111\}_{\gamma} \;||\; \{\bar{2}21\}_{\theta} & \{110\}_{\alpha} \;||\; \{\bar{2}21\}_{\theta} & \{111\}_{\gamma} \;||\; \{110\}_{\alpha} \\ \{111\}_{\gamma} \;||\; \{211\}_{\theta} & \{110\}_{\alpha} \;||\; \{211\}_{\theta} & \end{array}$$

The observed carbide-ferrite orientation relationship is closer to the OR proposed by Zhong *et al.* [81] in eutectoid low alloy steels. The proposed ORs are further supported by the characteristic intensities of the XRD peaks in Figure 4.5. The maximum intensities for ferrite, austenite, and cementite, which correlate to the preferred orientation of the individual phases, are from the $\{110\}_{\alpha}$, $\{111\}_{\gamma}$, and the $\{211\}_{\theta}/\{220\}_{\theta}$

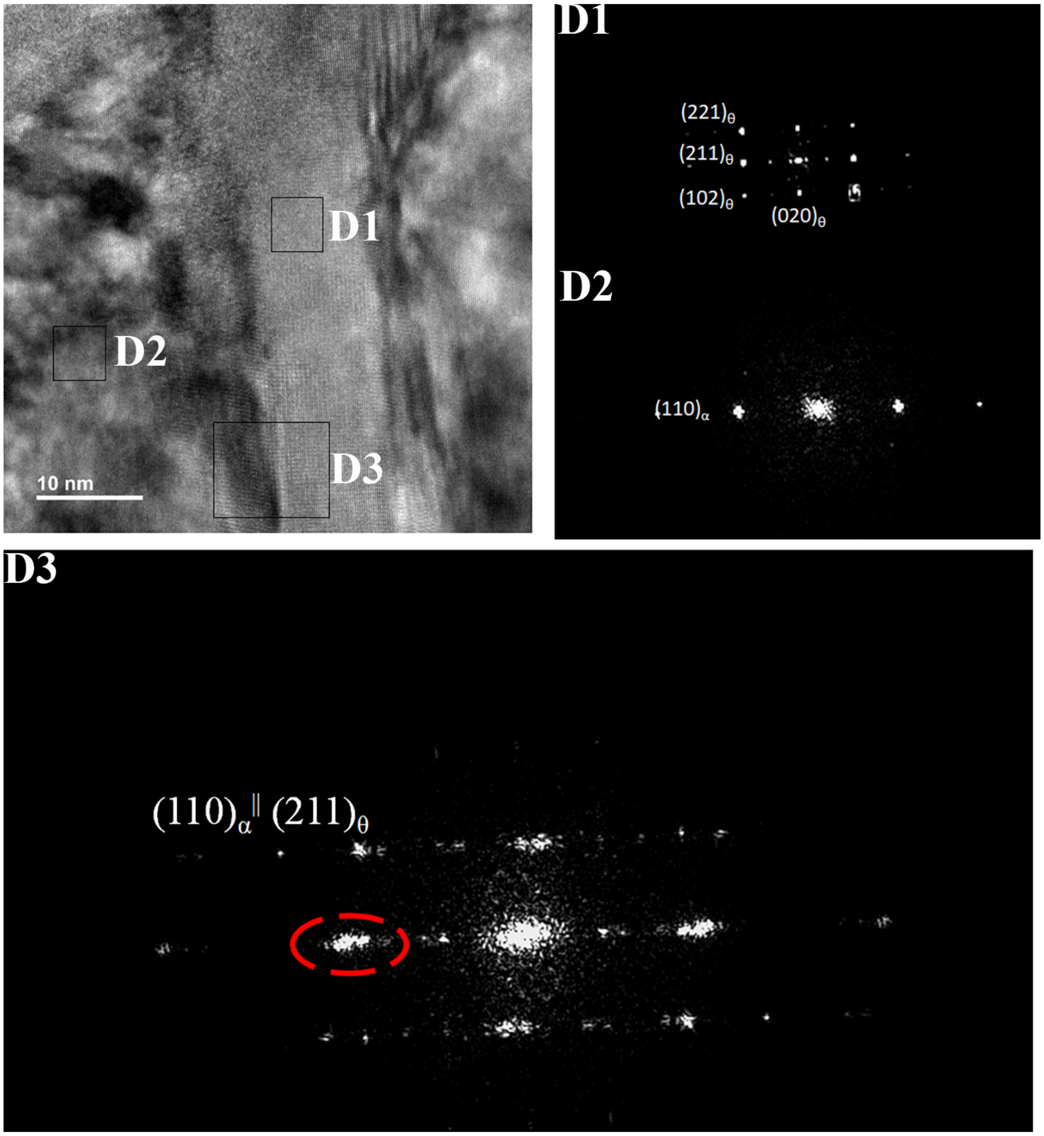

Figure 4.14: HR TEM image and corresponding diffraction patterns of secondary cementite and ferrite in the 5 minute heat treated sample. The orientation matching between the secondary cementite and ferrite is represented by a dotted circle in the diffraction pattern D3.

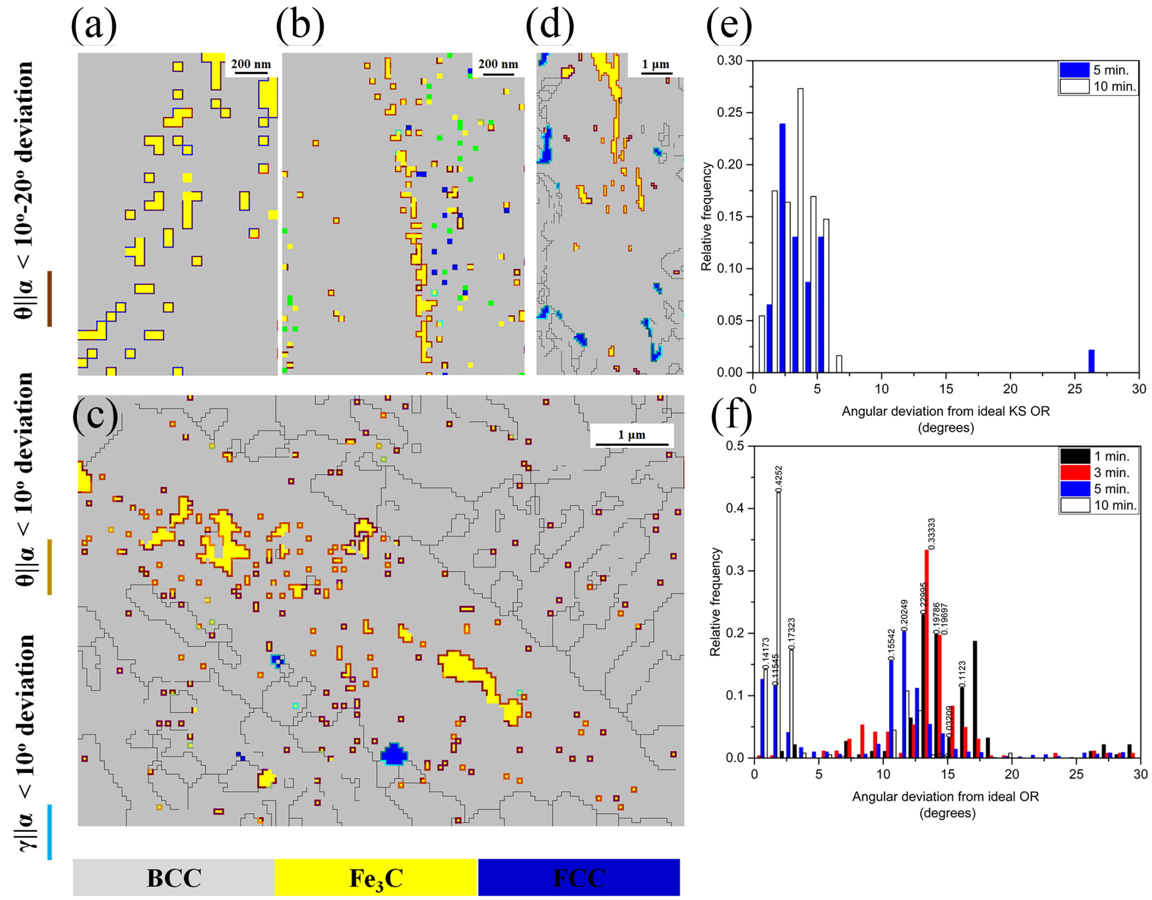

Figure 4.15: OR boundary map indicating the OR between secondary carbides and inverse bainitic ferrite ($[01\bar{1}]_\theta||[111]_\alpha, (2\bar{2}1)_\theta||(1\bar{1}0)_\alpha$) and inverse bainitic ferrite and austenite (KS OR). The ferrite matrix is colored grey and cementite is colored yellow. The orange and maroon boundaries indicate deviation less than 10 ^{o} and between 10^o - 20^o from the ideal OR $[01\bar{1}]_\theta||[111]_\alpha, (2\bar{2}1)_\theta||(1\bar{1}0)_\alpha$. The blue boundaries indicate deviation less than 10 ^{o} from the ideal KS OR. (a) 1 minute isothermal hold, (b) 3 minutes isothermal hold, (c) 5 minutes isothermal hold, and (d) 10 minutes isothermal hold. (e),(f) Statistical analyses representing the deviation from the ideal γ/α (KS) and θ/α ORs respectively. The numbers on (f) represent the fraction of boundaries corresponding to the angular deviation from the OR for each heat treatment condition.

planes, respectively. This shows that majority of the ferrite, austenite, and cementite are oriented along $\{110\}_{\alpha}$, $\{111\}_{\gamma}$, and the $\{211\}_{\theta}/\{220\}_{\theta}$ planes respectively which provides confidence in the OR measured using EBSD.

Comparison of the pole figures of the 3 minutes and the 10 minutes isothermally treated samples reveal the orientation changes occurring during the degeneration of the inverse bainitic microstructure. Pole figure analysis in Figure 4.11 and Figure 4.13 shows that the cementite midrib in the 3 minutes transformed sample and the remnant of the central cementite midrib in the 10 minutes transformed sample is of a specific variant (bluish green color). In the 10 minutes heat treated sample which has the degenerated structure of inverse bainite, apart from the cementite midrib, the secondary carbides are composed of two different variants. The first variant, with a similar orientation to that of the cementite midrib, dominates near the cementite midrib and inverse bainitic ferrite interface. A second variant with a different orientation (yellow orientation in the inverse pole figure) is observed closer to the inverse bainitic ferrite/martensite interface (Figure 4.13b). Though the orientation of the secondary carbides are different within the inverse bainitic unit, three phase crystallographic matching is still observed. Figure 4.15f shows that the angular deviations between the planes and directions of the proposed orientation relationships between ferrite and cementite are minimum in the 10 minutes heat treated sample in comparison with the angular deviations observed in the 3 minutes isothermally treated sample. This shows that with the evolution of the inverse bainitic microstructure into upper bainite, a better crystallographic match is observed between the parent γ, θ, and the inverse bainitic ferrite.

4.3 Conclusions

In this work, a series of interrupted isothermal heating and quenching experiments were conducted to study the evolution of inverse bainite microstructure in Fe-0.84%C-1%Mn-1%Cr low alloy steel. Microstructure characterization and thermodynamic calculations were performed using FESEM, EBSD, XRD, and ThermoCalc. The following conclusions were made:

1. Inverse bainite transformation proceeds by formation of cementite midrib as the first stage of transformation, followed by the transformation of ferrite from carbon depleted austenite in the second stage.

2. Crystallographic analysis revealed that the nucleation of secondary carbides

(Fe_3C, Fe_2C, and Fe_5C_2) happens from inverse bainitic ferrite. This is the third stage of transformation.

3. The OR between different phases of inverse bainite microstructure was found to be

$$\begin{array}{ccc}
<110>_{\gamma} \; || \; <1\bar{1}0>_{\theta} & <111>_{\alpha} \; || \; <1\bar{1}0>_{\theta} & <110>_{\gamma} \; || \; <111>_{\alpha} \\
\{111\}_{\gamma} \; || \; \{\bar{2}21\}_{\theta} & \{110\}_{\alpha} \; || \; \{\bar{2}21\}_{\theta} & \{111\}_{\gamma} \; || \; \{110\}_{\alpha} \\
\{111\}_{\gamma} \; || \; \{211\}_{\theta} & \{110\}_{\alpha} \; || \; \{211\}_{\theta} &
\end{array}$$

4. When the transformation time is sufficiently long, inverse bainite microstructure becomes degenerated to be "conventional" upper bainite. This is the fourth stage of the transformation

Chapter 5

Thermodynamics of nucleation of inverse bainite

5.1 Introduction

This chapter focuses on developing a thermodynamic model using the principles of driving force that is calculated for the onset of nucleation of cementite and ferrite from parent austenite, Hultgren extrapolation of A_{e3} and A_{cm} phase boundaries, and the molar Gibbs energy change for austenite to ferrite transformation. Through the proposed approach, the effect of Cr, Mn, and the isothermal holding temperature on inverse bainitic transformation in hypereutectoid steels can be predicted. Through experimental validation of the proposed thermodynamic model, it was found that for a given carbon concentration above the eutectoid carbon concentration, inverse bainite is favored at a lower Cr and higher Mn concentrations in the steel. With an increase in Cr concentration, the inverse bainitic start temperature has been found to increase. Cr partitioning from parent austenite to form Cr_7C_3 or $Cr_{23}C_6$ occurs only at prolonged transformation time (10000 s and above), when the inverse bainitic transformation is complete. Cementite is the favored carbide nucleating from parent austenite during the inverse bainitic transformation. With an increase in Mn concentration, both the inverse bainitic start and finish temperatures have been found to decrease. For a given chemical composition, inverse bainite is generally favored below the pearlitic transformation temperature. Inverse bainitic transformation gets suppressed when the isothermal transformation temperature is lowered to a certain extent, in which case conventional upper/lower bainite is the favored transformation product.

5.2 Thermodynamic Methodology and Experimental Procedures

5.2.1 Thermodynamic calculations

In order to understand the effect of Cr and Mn on the transformation of inverse bainite, thermodynamic calculations were performed on several alloys with varying Cr and Mn concentrations. Pseudo-binary phase diagrams along with $\gamma/\gamma+\alpha$ and $\gamma/\gamma+\theta$ metastable phase boundaries, driving forces for the onset of nucleation of ferrite and cementite from austenite by making ferrite and cementite as dormant phases (thereby supersaturating the austenite) [82], and the molar Gibbs free energy for austenite to ferrite transformation were calculated using the TCFE6 database of ThermoCalc [60]. Precipitation calculations were performed using the MCFE thermodynamics and diffusion database of MatCalc software [61].

5.2.2 Application of the concept of driving force for the onset of nucleation to inverse bainitic transformation

The formation of cementite as the lead nucleating phase can be explained on the basis of the driving force for the onset of nucleation proposed by Miroshnichenko [83, 84] in 1966, which was further elaborated by Hillert [82] and Purdy [85]. We have used this concept to explain the nucleation of cementite as the lead nucleating phase from parent austenite [86]. This driving force for nucleation be mathematically represented as:

$$DRF_{\theta} = -\Delta G_m^{\theta} = \Delta x_C^{\gamma} \frac{d^2 G_m^{\gamma}}{dx_C^2} (x_C^{\theta} - x_C^{\gamma}) \tag{5.1}$$

for the formation of cementite (θ) from austenite (γ), and

$$DRF_{\alpha} = -\Delta G_m^{\alpha} = \Delta x_C^{\gamma} \frac{d^2 G_m^{\gamma}}{dx_C^2} (x_C^{\alpha} - x_C^{\gamma}) \tag{5.2}$$

for the formation of ferrite (α) at the cementite carbon depleted austenite (γ) interface. In the above equations D_{α} and D_{θ} are the decrease of the driving force per mole for the formation of ferrite and cementite, Δx_C^{γ} is the extent of supersaturation of carbon in austenite, x_C^{γ}, x_C^{θ}, x_C^{α} are the carbon concentration of austenite in equilibrium with cementite and ferrite, the carbon concentration of cementite in equilibrium with austenite, and the carbon concentration of ferrite in equilibrium with austenite. From the above equations, the driving force for the formation of bainitic ferrite from austenite is low because its composition is closer to the parent phase; therefore, its nucleation is difficult. Hillert suggested that the nucleation of a metastable phase with a very different composition (in this case, cementite), and hence a higher driving force for nucleation (refer to Equation (5.2)), will assist in the nucleation of the stable phase (in this case, bainitic ferrite).

5.2.3 Theoretical highest temperature (T_{SIB}) below which inverse bainite transformation is possible

Theoretically, the highest temperature for inverse bainite transformation can be regarded as the lowest temperature for pearlite transformation. Thus, predicting the pearlite finish temperature will indicate the start temperature or the upper bound of inverse bainite. The pearlite finish temperature can be obtained from the pseudo-binary phase diagrams, and the metastable extrapolation of A_{cm} and A_{e3} phase boundaries (or the Hultgren extrapolation). In the current methodology, the following approximations were made to obtain a theoretical lower limit for pearlite transformation (or theoretically the highest temperature at which inverse bainite can start to form):

1. In the TTT diagram calculated by Hultgren [28], a deviation from linearity occurs in the extrapolated A_{cm} phase boundary. Below the deviation, a delay in pearlite transformation is observed and cementite nucleation is recorded. A delay in pearlite transformation below the linear deviation from the extrapolated A_{cm} phase boundary eventually leading to bainitic transformation is also observed in the Fe-0.8C-0.77Mn steel reported by Kennon and Kaye [87,88] (represented with the thermodynamic phase boundary extrapolation in Figure 5.1). Thus, the deviation in the linearity of the the extrapolated A_{cm} phase boundary is taken as the lower limit for pearlite transformation (T_h).

2. Though at extremely large grain size (diameter larger than 120 μm) pearlite transformation can happen outside of the Hultgren extrapolation [89], the grain size effect is ignored.

3. The point of deviation in the linearity of the the extrapolated A_{cm} phase boundary is taken as the lower limit for pearlite transformation (T_h) or theoretically the highest temperature below which inverse bainite transformation is possible.

4. ThermoCalc calculations of the interfacial energy of alloy A5 show a similar values of interfacial energies for γ/α (0.04 Jm^{-2}) and γ/θ (0.07 Jm^{-2}) interfaces

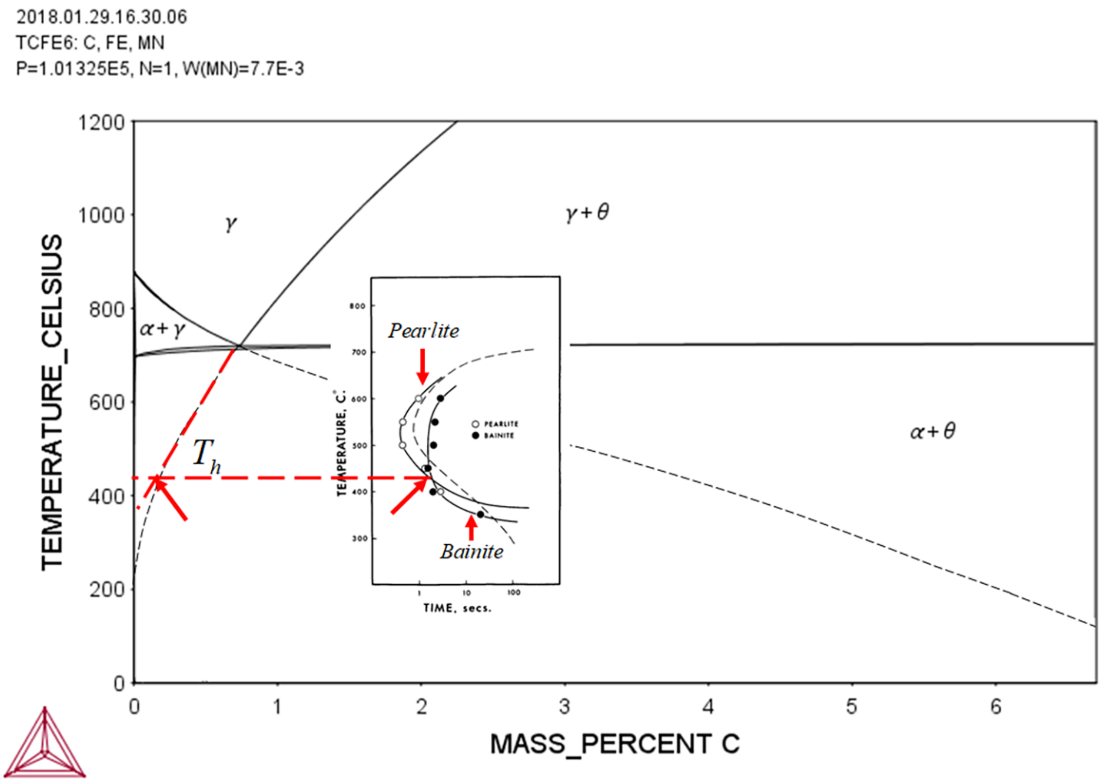

Figure 5.1: Extrapolated A_{cm} and A_{e3} phase boundaries in Fe-0.80C-0.77Mn steel. The deviation from linearity marks the onset of bainitic transformation as represented in the inset TTT diagram. The TTT diagram is adapted from.

in the inverse bainite formation temperature range (480 ° C– 600 ° C). Thus, any influence of interface energy on the nucleation event is ignored and the nucleation event in the present study is considered solely on the basis of the driving force for the onset of nucleation

The thermodynamic calculation procedure is depicted as a flowchart in Figure 5.2.

5.2.4 Inverse bainite finish temperature T_{FIB}

Based on our earlier results [80, 86], inverse bainitic transformation proceeds by a two-stage transformation mechanism involving the nucleation of cementite as the first event, followed by the nucleation and growth of inverse bainitic ferrite. The deciding factor in the formation of either inverse bainite or conventional bainite is the initial nucleating phase from parent austenite. The formation of ferrite or cementite as the initial nucleating phase is governed by the thermodynamic driving force for the onset of nucleation of the product phases (ferrite or cementite). Thus, the initial step in predicting the inverse bainite finish temperature is to determine the driving force

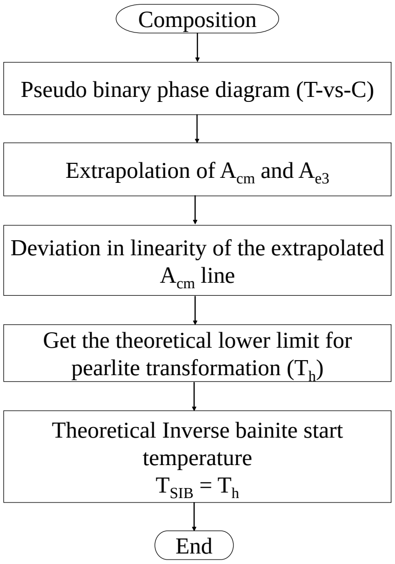

Figure 5.2: Schematic flowchart indicating the thermodynamic calculation procedure for predicting the inverse bainite start temperature.

for the onset of nucleation of ferrite and cementite as a function of transformation temperature. Once the driving force for the onset of nucleation of ferrite and cementite have been calculated, two possibilities exist. The first being, the driving force for the onset of nucleation of cementite alone is positive in a particular temperature range, in which case isolation of inverse bainite from conventional bainite is possible. The second being, the driving force for the onset of nucleation of both ferrite and cementite is positive in the temperature range, in which case inverse bainite and conventional bainite co-exist. These two cases are analyzed next.

Detection and isolation of inverse bainite from “conventional” bainite

In order to accurately determine the transformation temperature, the molar Gibbs free energy change of austenite to ferrite transformation was computed as a function of carbon concentration of parent austenite. This was in turn iterated with respect to temperature in order to have the molar Gibbs free energy for austenite to ferrite transformation as a function of carbon concentration of austenite, in turn, as a function of transformation temperature. Thus, one can determine the carbon concentration of austenite and the temperature below which the austenite to ferrite transformation is thermodynamically feasible. If the carbon concentration below which austenite to ferrite transformation is thermodynamically feasible is less than the original carbon concentration of austenite, and the critical temperature below which the austenite to ferrite transformation is thermodynamically feasible at the bulk carbon concentration of austenite is less than the Hultgren extrapolated temperature, the critical temperature is taken as the inverse bainite finish temperature. This is schematically depicted as a flow chart in Figure 5.3. Since the driving force for the onset of nucleation of ferrite is negative at any given temperature, inverse bainitic ferrite does not form until the local carbon concentration of austenite drops below the thermodynamic level required for the transformation of austenite to ferrite. The time required (kinetic delay) for the parent austenite to become carbon depleted to form inverse bainitic ferrite can be measured as the volumetric contraction in dilatometry, which is mathematically given by the Equation (5.3) [90]:

$$\left(\frac{\delta L}{L_o}\right)_{total} = \frac{1}{3}\frac{\left[V_\gamma a_\gamma^3 + \frac{V_\theta}{3} a_\theta b_\theta c_\theta - V_\gamma^o (a_\gamma^o)^3\right]}{V_\gamma^o (a_\gamma^o)^3} + \left(\frac{\delta L}{L_o}\right)_{thermal} \tag{5.3}$$

It can be seen that the relative length change during the transformation is related to the lattice parameter of austenite. The lattice parameter of austenite is, in turn related to its local carbon concentration as per Equation (5.4) [91]:

$$a_{o\gamma} = 0.3573 + 0.33 w_c^\gamma + 0.0095 w_M n^\gamma + 0.006 w_C r^\gamma \tag{5.4}$$

Thus, any reduction in the local carbon concentration in austenite lowers its lattice parameter, thereby causing a volumetric contraction in the sample. Once the local carbon concentration of austenite is below the thermodynamic level required for ferrite transformation, the relative length change is given by Equation (5.5) [90]:

$$\left(\frac{\delta L}{L_o}\right)_{total} = \frac{1}{3}\frac{\left[2a_\alpha^3 V_\alpha + V_\gamma a_\gamma^3 - V_\gamma^o (a_\gamma^o)^3 - \frac{V_\theta^o}{3} a_\theta^o b_\theta^o c_\theta^o\right]}{V_\gamma^o (a_\gamma^o)^3 + \frac{V_\theta^o}{3} a_\theta^o b_\theta^o c_\theta^o} + \left(\frac{\delta L}{L_o}\right)_{thermal} \tag{5.5}$$

Once the inverse bainitic ferrite transformation starts, there will be a local increase in carbon concentration of austenite, which in-turn increases its lattice parameter (Ref. Equation (5.4)), thereby causing a net volumetric expansion in the sample. Thus, the detection and isolation of inverse bainitic transformation from "conventional" bainite is possible through experimental techniques such as dilatometry.

The above mentioned methodology is schematically illustrated in Figure 5.4. Figure 5.4a represents the driving force for the onset of nucleation of ferrite and cementite from austenite. It can be seen that at the bulk carbon concentration of austenite the driving force for ferrite is negative. Figure 5.4b represents the molar Gibbs free energy for austenite and ferrite. The transformation of austenite and ferrite is not thermodynamically feasible at the bulk carbon concentration (Figure 5.4b). The transformation of cementite from parent austenite will proceed until the local carbon concentration of austenite reduces to the level indicated in Figure 5.4b. The transformation of cementite locally reduces the carbon concentration of austenite (Figure 5.4c), thereby facilitating the transformation of inverse bainitic ferrite. Once inverse bainitic ferrite transformation starts, the local carbon concentration of austenite increases (Figure 5.4c). This change in the local carbon concentration will be reflected as the variation in dilatation data (using Equation (5.3) and Equation (5.5)) as illustrated in Figure 5.4d.

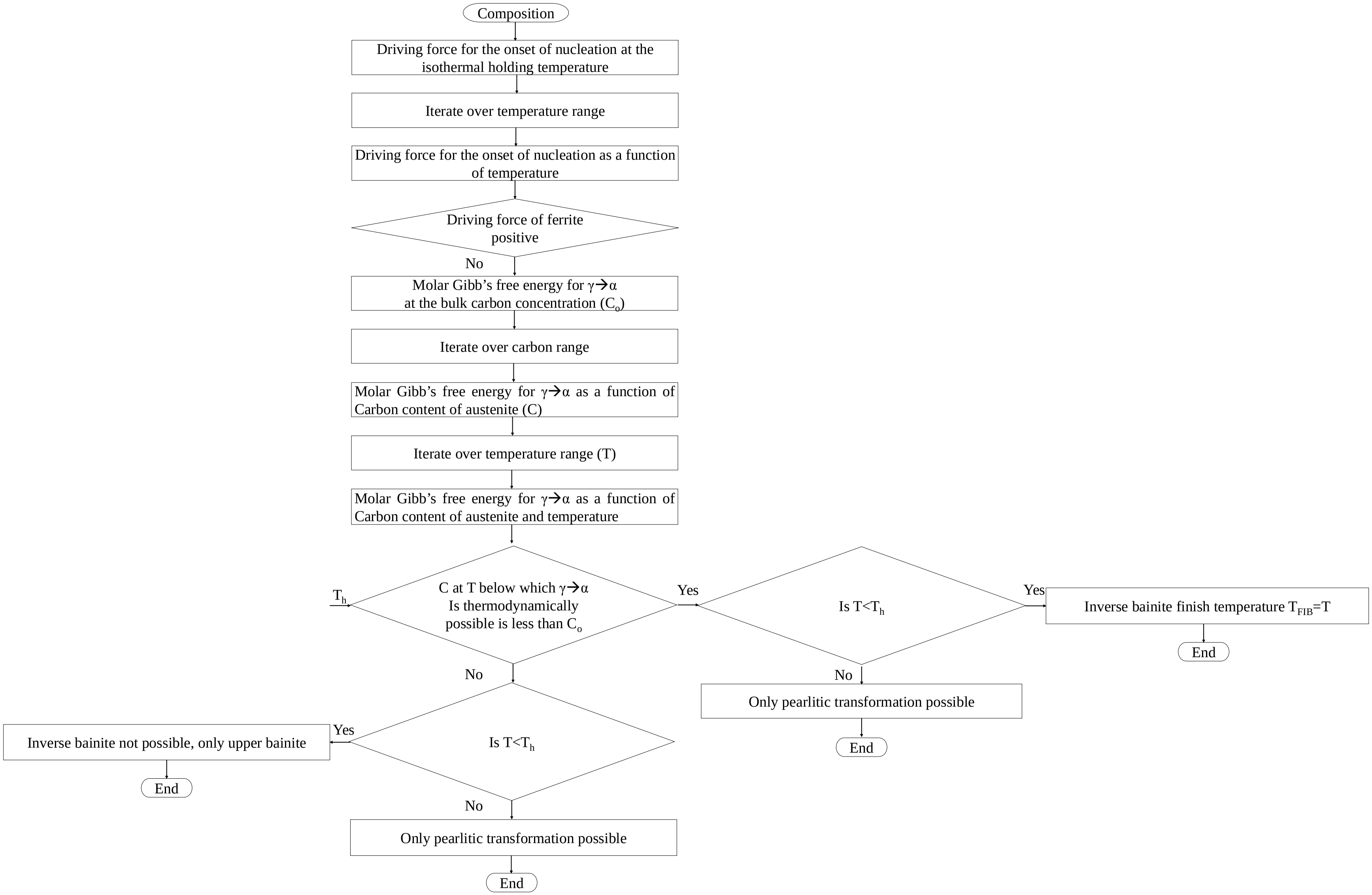

Figure 5.3: Schematic flowchart indicating the thermodynamic calculation for predicting the transformation temperature range of inverse bainite.

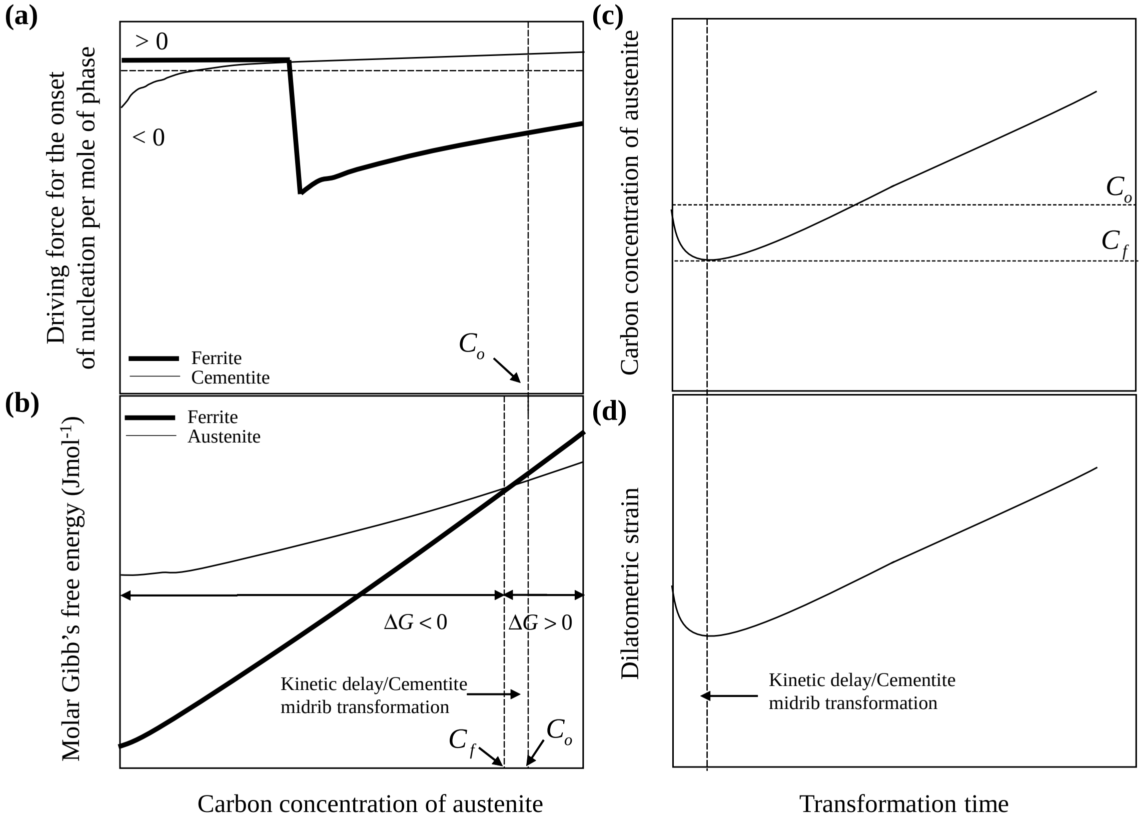

Figure 5.4: Illustration of the thermodynamics behind the isolation of inverse bainite from "conventional" bainite. (a) Variation in the driving force for the onset of nucleation of ferrite and cementite from supersaturated parent austenite with carbon concentration. (b) Variation in the molar Gibbs free energy change for austenite and ferrite with carbon concentration. (c) Variation in the local carbon concentration of austenite with transformation time. (d) Variation in the dilatometry strain with transformation time.

Coexistence of inverse and conventional bainite

In this case, to determine the inverse bainitic finish temperature, a similar method proposed in Section 5.2.4 is used. In the current situation, the driving force for nucleation of ferrite from austenite is positive. Thus, ferrite nucleation is thermodynamically possible during the inverse bainitic cementite nucleation. Also, the molar Gibbs free energy for austenite to ferrite transformation is negative at the bulk carbon concentration of austenite; therefore no kinetic delay is required for parent austenite to become carbon depleted to form inverse bainitic ferrite. Even though the transformation of the "bainitic" unit may initiate by the nucleation of cementite, once cementite starts nucleating, the surrounding carbon depleted austenite may transform into inverse bainitic ferrite. Once the cementite midrib nucleation starts, the inverse bainitic ferrite transformation starts simultaneously. Thus, the final transformation microstructure will consist of degenerated inverse bainite (upper bainite) [86] alongside initial units of inverse bainite (but nucleated near the end of the isothermal hold). According to the lever rule, the fraction of ferrite is much higher than that of the cementite; therefore, the net volume change due to the transformation will be a volumetric increase. Therefore, a conventional bainitic transformation will be detected through experimental techniques like dilatometry (illustrated in Figure 5.5). Figure 5.5a represents the driving force for the onset of nucleation of ferrite and cementite from austenite. It can be seen that at the bulk carbon concentration of austenite the driving force for both ferrite and cementite are positive. Figure 5.5b represents the molar Gibbs free energy for austenite and ferrite. The transformation of austenite and ferrite is thermodynamically feasible at the bulk carbon concentration (Figure 5.5b). Thus, even though the bainitic transformation may be initiated by formation of cementite from parent austenite, the transformation of bainitic ferrite starts simultaneously. Thus, there will be a local carbon enrichment of austenite (Figure 5.5c). This change in the local carbon concentration will be reflected as the variation in dilatation data (using Equation (5.3) and Equation (5.5)) as illustrated in Figure 5.5d.

5.3 Results

5.3.1 Effect of Cr and Mn on inverse bainitic transformation at 773.15 K

Figure 5.6 shows the representative thermodynamic calculations for alloys A0, A3, and A8 (effect of Cr). Figure 5.6a, Figure 5.6c, and Figure 5.6e represents the driving force for the onset of nucleation of ferrite and cementite from parent austenite. The calculations were performed by setting the status of ferrite and cementite as dormant phase, thereby supersaturating parent austenite. It is to be noted that ThermoCalc predicts the decrease in Gibbs free energy per mole for the formation of ferrite/cementite from austenite, i.e. -($\Delta G_m^{\alpha/\theta}$). Therefore, a positive driving force indicates that the transformation product will form and a negative driving force indicates that the transformation product will not form. From Figure 5.6a, Figure 5.6c, and Figure 5.6e it can be seen that the driving force for the onset of nucleation of cementite at 773.15 K (500 °C) is positive for all the alloys. The driving force for the onset of nucleation of ferrite is positive above a chromium concentration of 1.1

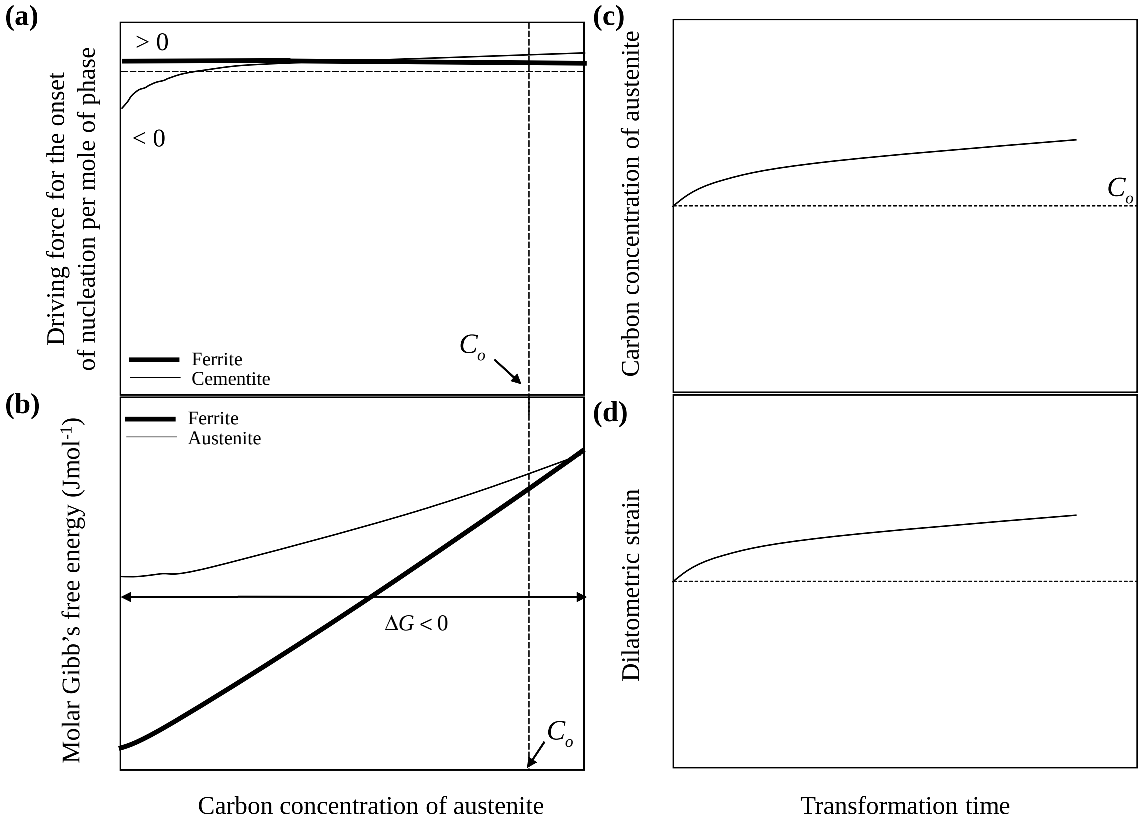

Figure 5.5: Illustration of the thermodynamics behind the coexistence of inverse bainite and "conventional" bainite. (a) Variation in the driving force for the onset of nucleation of ferrite and cementite from supersaturated parent austenite with carbon concentration. (b) Variation in the molar Gibbs free energy change for austenite and ferrite with carbon concentration. (c) Variation in the local carbon concentration of austenite with transformation time. (d) Variation in the dilatometry strain with transformation time.

wt. % (alloy A8 in Figure 5.6c). To further understand the transformations happening at 773.15 K (500 °C), pseudo-binary phase diagrams were calculated for the alloys. Figure 5.6b, Figure 5.6d, and Figure 5.6f represents the calculated pseudo-binary phase diagrams. Metastable phase boundaries (extrapolated A_{cm} and A_{e3}) are also appended in the pseudo-binary phase diagram. It can be seen that alloy A0 falls within the Hultgren extrapolation region. When the chromium content in the alloy is increased, the slope of the A_{cm} phase boundary changes. The change in slope of the A_{cm} phase boundary increases the Hultgren extrapolation region to a higher temperature. Therefore, alloy A3 and beyond are cooled below the lower limit of the Hultgren extrapolated region (T_h) at 773.15 K (500 °C). This is represented using ΔT_s in Figure 5.6d, and Figure 5.6f. With an increase in chromium content, the extent of cooling below the lower limit of the Hultgren extrapolated zone increases.

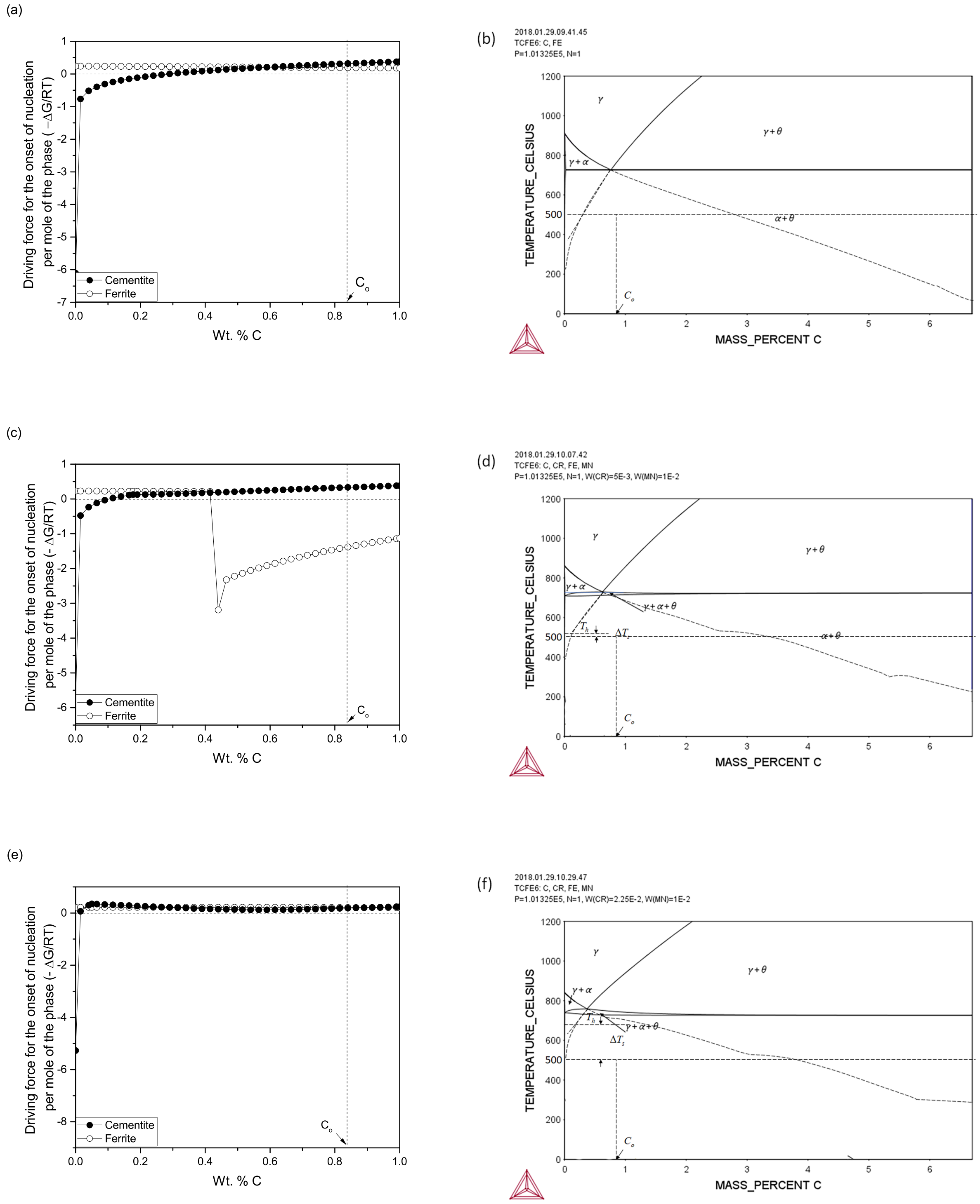

Figure 5.6: Driving force for the onset of nucleation for ferrite and cementite from austenite (a, c, and e), and pseudo-binary phase diagrams with metastable phase boundaries (b, d, and f) for alloys A0, A3, and A8 respectively. The driving force calculations were performed at the isothermal holding temperature of 773.15 K (500 °C).

Similarly, using the above approach for the effect of Cr, the effect of Mn can be understood. Table 5.1 summarizes the magnitude of the cooling below the Hultgren extrapolated zone for all the alloys and the transformation product predicted calculated using ThermoCalc. From the above-presented results, it can be seen that alloys A0, A1, and A2 are located within the Hultgren extrapolated zone at 773 K (500 °C); therefore, pearlite will form. Alloys A3, A4, A5, A13, A14, and A15 have a positive driving force for the nucleation of cementite and a negative driving force for the formation of ferrite from parent austenite and are located outside the Hultgren extrapolated zone at 773 K (500 °C), therefore forming inverse bainite. Alloys A6, A7, A8, A9, A10, A11, and A12 have a positive driving force for the nucleation of ferrite and cementite from austenite at 773 K (500 °C) forming conventional bainite. It should be noted that the driving force for the onset of nucleation of ferrite from supersaturated parent austenite is negative when the extent of supercooling (ΔT_s) is smaller than 80 ° C (Ref. Table Table 5.1). Thus it can be concluded that at 773

Table 5.1: Magnitude of cooling below the Hultgren extrapolated zone and the predicted transformation product for isothermal holding at 773 K (500 °C) for the alloys.

Alloy	**C**	**Cr**	**Mn**	**Si**	**Ni**	**Cu**	**V**	**Fe**	ΔT_s	Transformation product
A0	0.84		0					Bal.	⋆	P
A1	0.84		1.00					Bal.	⋆	P
A2	0.84	0.25	1.00					Bal.	⋆	P
A3	0.84	0.50	1.00					Bal.	18.00	P
A4	0.84	0.75	1.00					Bal.	38.26	IB
A5	0.84	1.00	1.00					Bal.	70.43	IB
A6	0.84	1.10	1.00					Bal.	78.63	IB/B
A7	0.84	1.25	1.00					Bal.	123.07	IB/B
A8	0.84	2.25	1.00					Bal.	169.20	IB/B
A9	0.84	1.00						Bal.	120.5	IB/B
A10	0.84	1.00	0.25					Bal.	93.91	IB/B
A11	0.84	1.00	0.50					Bal.	87.71	IB/B
A12	0.84	1.00	0.75					Bal.	79.73	IB/B
A13	0.84	1.00	0.95					Bal.	66.66	IB
A14	0.84	1.00	1.25					Bal.	46.49	IB
A15	0.84	1.00	2.25					Bal.	48.18	IB

⋆ At 773.15 K (500 °C), the alloy lies within the Hultgren extrapolated zone therefore, pearlite transformation occurs. P denotes pearlite, IB denotes inverse bainite, and B denoted conventional bainite.

K (500 °C) inverse bainite with cementite nucleating first from parent austenite is possible at higher manganese contents and lower chromium contents. At extremely lower chromium contents in the alloy, pearlite is the favored transformation product at 773.15 K (500 °C). Neither inverse bainite nor conventional bainite transformation is possible at very low chromium contents in the alloy.

5.3.2 Transformation temperature range of inverse bainite

Applying the proposed approach in Section 5.2.4 and Section 5.2.3, the change in driving force for the onset of nucleation with temperature and the molar Gibbs free energy change for austenite to ferrite transformation for alloys A0, A6, and A13 are presented in Figure 5.7. Figure 5.7a, Figure 5.7c, and Figure 5.7e represent the change in driving force for the onset of nucleation for alloy A0, A6, and A13 respectively. It can be seen that for alloy A13, the driving force for the onset of nucleation of ferrite is negative above a temperature of 573 K (300 °C). Thus, it is likely that for alloy A13, the inverse bainitic start temperature is above 573 K (300 °C). To accurately measure the start temperature of inverse bainite, the molar Gibbs free energy for austenite to ferrite transformation was calculated and iterated over temperature and the critical temperature above which the transformation of austenite to ferrite is not thermodynamically feasible at the bulk carbon concentration of the alloy was taken as the inverse bainite finish temperature. The molar Gibbs free energy curves for alloys A0 (Figure 5.7b), A6 (Figure 5.7d) and A13 (Figure 5.7f) at the critical temperatures of 673 K (400 °C), 745 K (472 °C), and 747 K (474 °C) respectively are shown in Figure 5.7. The molar Gibbs free energy curves intersect at the bulk carbon concentration of the alloys at the specified temperature. For alloy A0, even below the lower limit of Hultgren extrapolated temperature, equilibrium transformation of austenite to ferrite is possible. It is to be mentioned that for temperatures below the specified temperatures, the curves intersect at a higher carbon concentration than the bulk carbon concentration of the alloy and for temperatures greater than the specified temperatures, the curves intersect at a lower carbon concentration. This indicates that for any transformation temperature below the specified temperature, equilibrium transformation of parent austenite to inverse bainitic ferrite is thermodynamically feasible, and once the cementite midrib nucleation starts, the inverse bainitic ferrite transformation starts simultaneously. Thus, the degenerated microstructure of inverse bainite i.e, upper bainite will be the final transformation product for temperatures below the specified critical temperature (or the inverse bainite finish temperature).

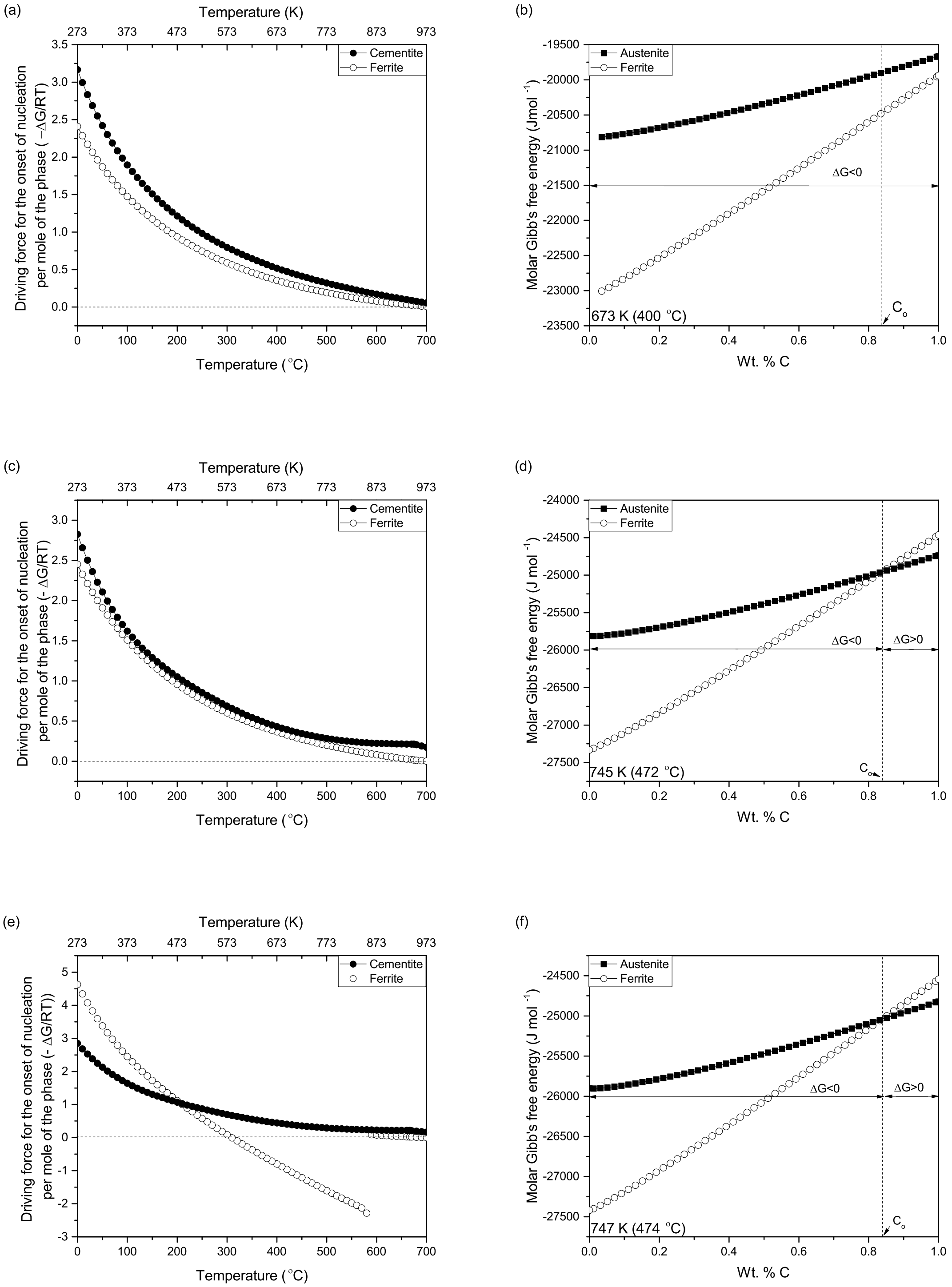

Figure 5.7: Variation in the driving force for the onset of nucleation for ferrite and cementite from austenite with temperature for alloys A0 (a), A6 (c), A13 (e). Molar Gibbs free energy change for austenite to ferrite transformation for alloys A0 (b) at 673 K (400 ^{o}C), A6 (d) at 745 K (472 ^{o}C), A13 (f) at 747 K (474 ^{o}C).

Calculated inverse bainite start and finish temperatures based on the proposed approach for all the alloy systems studied are tabulated in Table 5.2. It can be seen that for alloys with a constant manganese content and a varying chromium content (A1-A8), the inverse bainitic finish temperature remains the same at 745 K (472 °C), while with an increase in chromium content of the alloy, the inverse bainitic start temperature is increased. For alloys with a constant chromium content and a varying manganese content (A9-A15), the inverse bainitic start temperature remains the same at 773 K (500 °C), while with an increase in manganese content of the alloy, the inverse bainitic finish temperature is decreased. For alloys A0, A1, and A2 the inverse bainitic transformation is not possible. This is because even at the lower limit of the Hultgren extrapolated zone, the equilibrium austenite to ferrite transformation is thermodynamically feasible. Any increase in the isothermal holding temperature above the lower limit of the Hultgren extrapolated zone for A0, A1, and A2 will result in pearlitic transformation, and the reduction in isothermal holding temperature below the Hultgren extrapolated zone will result in conventional bainitic transformation/martensitic transformation.

Table 5.2: Inverse bainite start and finish temperature for the alloys.

Alloy	**C**	**Cr**	**Mn**	**Si**	**Ni**	**Cu**	**V**	**Fe**	T_{FIB}	T_{SIB}
A0	0.84							Bal.	$\star$	$\star$
A1	0.84		1.00					Bal.	$\star$	$\star$
A2	0.84	0.25	1.00					Bal.	$\star$	$\star$
A3	0.84	0.50	1.00					Bal.	472	516.36
A4	0.84	0.75	1.00					Bal.	472	542.72
A5	0.84	1.00	1.00					Bal.	472	573.63
A6	0.84	1.10	1.00					Bal.	$472^{\dagger}$	580.00
A7	0.84	1.25	1.00					Bal.	$472^{\dagger}$	627.24
A8	0.84	2.25	1.00					Bal.	$472^{\dagger}$	683.63
A9	0.84	1.00						Bal.	$497^{\dagger}$	636.36
A10	0.84	1.00	0.25					Bal.	$492^{\dagger}$	600.00
A11	0.84	1.00	0.50					Bal.	$485^{\dagger}$	586.36
A12	0.84	1.00	0.75					Bal.	$479^{\dagger}$	579.09
A13	0.84	1.00	0.95					Bal.	474	570.00
A14	0.84	1.00	1.25					Bal.	466	565.45
A15	0.84	1.00	2.25					Bal.	438	548.18

$\star$ Inverse bainitic transformation not possible.

† Inverse bainite and "conventional" bainite co-exist in the final microstructure.

5.3.3 Experimental results supporting the thermodynamic predictions

In order to verify the proposed thermodynamic approach on understanding the effect of Cr, Mn, and isothermal holding temperature on inverse bainitic transformation, similar thermodynamic calculations were performed for alloy E1 and the existence of inverse bainite is verified experimentally. Figure 5.8 shows the thermodynamic calculations and the microstructural evidence for the existence of inverse bainite in alloy E1.

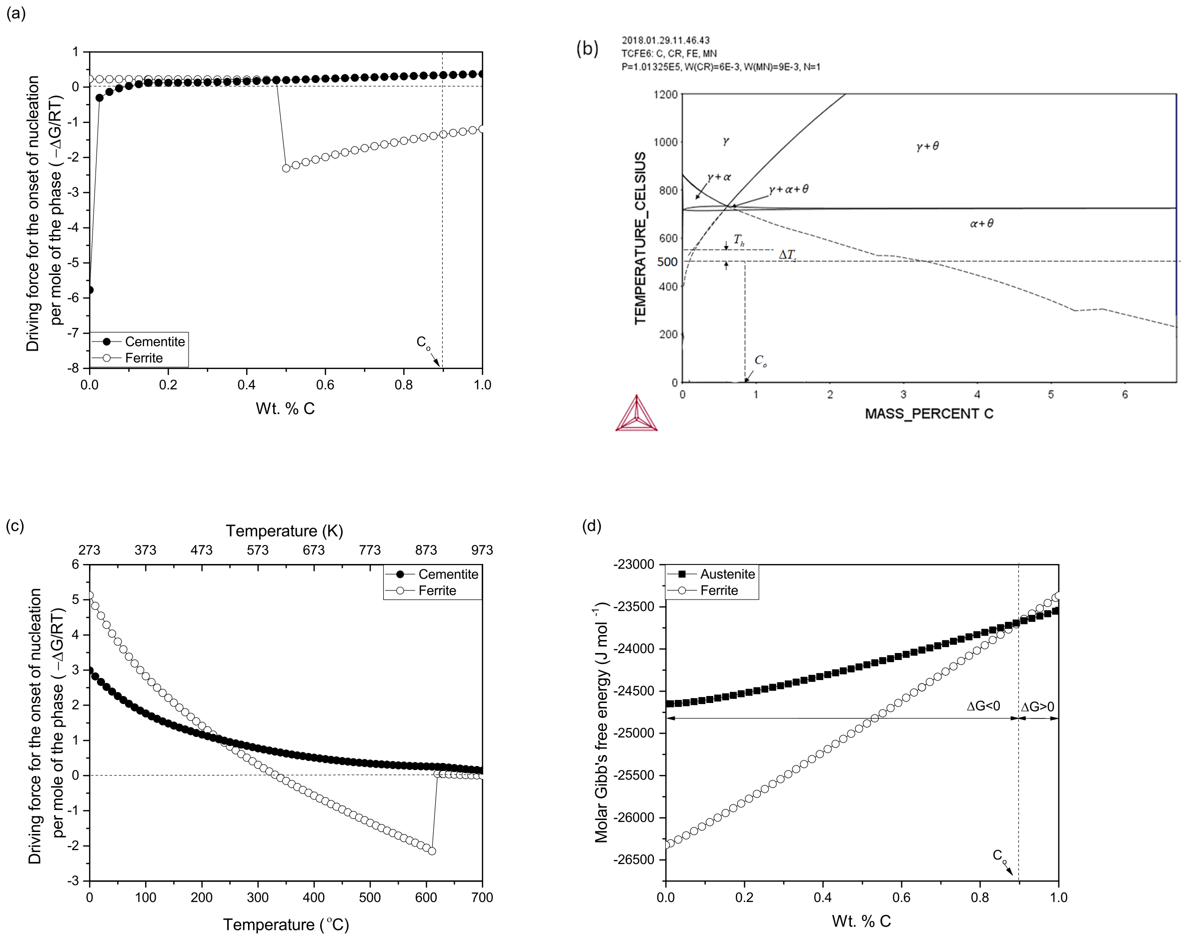

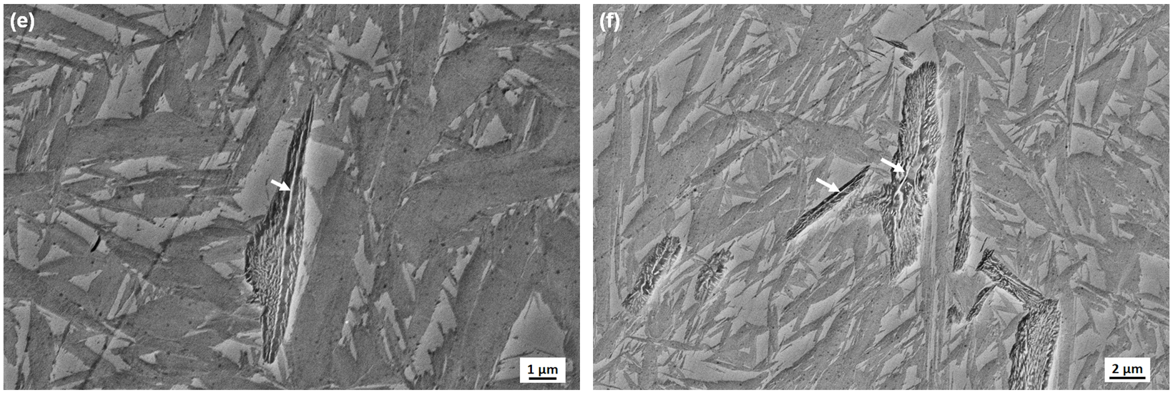

Figure 5.8: Experimental results to support the thermodynamic methodology on understanding the effect of Cr and Mn on inverse bainitic transformation in alloy E1 (Fe-0.9C-0.6Cr-0.92 Mn steel). (a) Driving force for the onset of nucleation of ferrite and cementite at 773.15 K (500 ^{o}C), (b) Pseudo-binary phase diagram with metastable phase boundaries, (c) Variation in the driving force for the onset of nucleation of ferrite and cementite with temperature, (d) Molar Gibb's free energy curve for ferrite to austenite transformation at 728 K (455 ^{o}C), (e) and (f) Microstructure evidence for the existence of inverse bainite in the steel. White arrows indicate the cementite midrib of inverse bainite.

From Figure 5.8a it can be seen that the driving force for the onset of nucleation of cementite at 773.15 K (500 °C) is positive, while the driving force for the onset of nucleation of ferrite is negative for the carbon content of alloy E1. Figure 5.8b represents the pseudo-binary phase diagram for alloy E1, and it can be seen that at 773.15 K (500 °C), the alloy is well below the Hultgren extrapolated zone. The degree of cooling below the Hultgren extrapolated zone (T_h), as measured by using ThermoCalc was found to be 289.29 K (16.29 °C). The results presented in Figure 5.8a-c confirm the existence of inverse bainite in alloy E1.

To identify the inverse bainitic transformation start and finish temperatures, the methodology proposed was applied to alloy E1. Figure 5.8c and Figure 5.8d represent the results from the proposed thermodynamic approach. From Figure 5.8c and Figure 5.8d, it can be concluded that for alloy E1, the inverse bainitic finish temperature is 728 K (455 °C) and the inverse bainitic start temperature is 789.29 K (516.29 °C). Based on the thermodynamic calculations on alloy E1 using the proposed approach, it can be confirmed that alloy E1 forms inverse bainitic microstructure between 728 K (455 °C) and 789.29 K (516.29 °C). Alloy E1 was austenitized and continuous cooled using water quenching, and Figure 5.8e and Figure 5.8f confirm the existence of inverse bainite in alloy E1.

In order to understand the effect of isothermal holding temperature on the phase transformation, alloy A5 was studied at different isothermal holding temperatures, namely 573 K (300 °C), 623 K (450 °C), 823 K (550 °C), and 873 K (600 °C). To understand the phase transformations undergoing at different isothermal holding temperatures, the pseudo-binary phase diagram of alloy A5 was calculated along with metastable phase boundaries in Figure 5.9. It can be seen that alloy A5 at 873 K (600 °C) falls within the Hultgren extrapolated zone and pearlitic transformation is expected. At 823 K (550 °C), the alloy is closer to the Hultgren extrapolated zone with a very small cooling of 273.35 K (0.25 °C) below the Hultgren extrapolated zone. Comparing with the transformation temperature predicted in Table 5.2, inverse bainitic transformation is expected. At 623 K (450 °C), the alloy is well below the Hultgren extrapolated zone with a cooling of 355 K (82 °C) below the Hultgren extrapolated zone. Comparing with the transformation temperature predicted in Table 5.2, "conventional" bainitic transformation is expected. At 573 K (300 °C), the alloy is well below the Hultgren extrapolated zone with a cooling of 507 K (234 °C). Comparing with the transformation temperature predicted in Table 5.2, "conventional" bainitic transformation is expected.

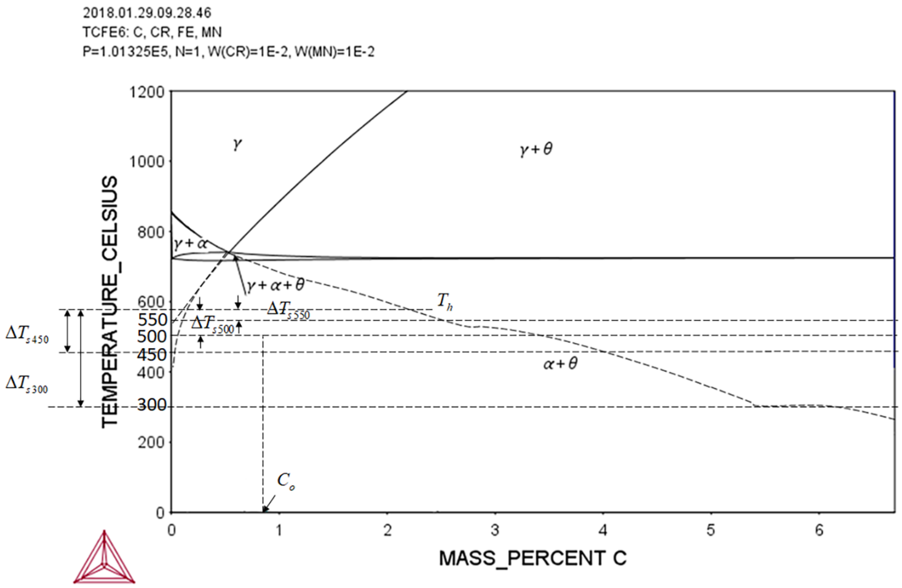

Figure 5.9: Pseudo-binary phase diagram of alloy A5 along with metastable phase boundaries.

Figure 5.10 represents the experimental dilatometry readings and the electron micrographs for all the heat treated samples.

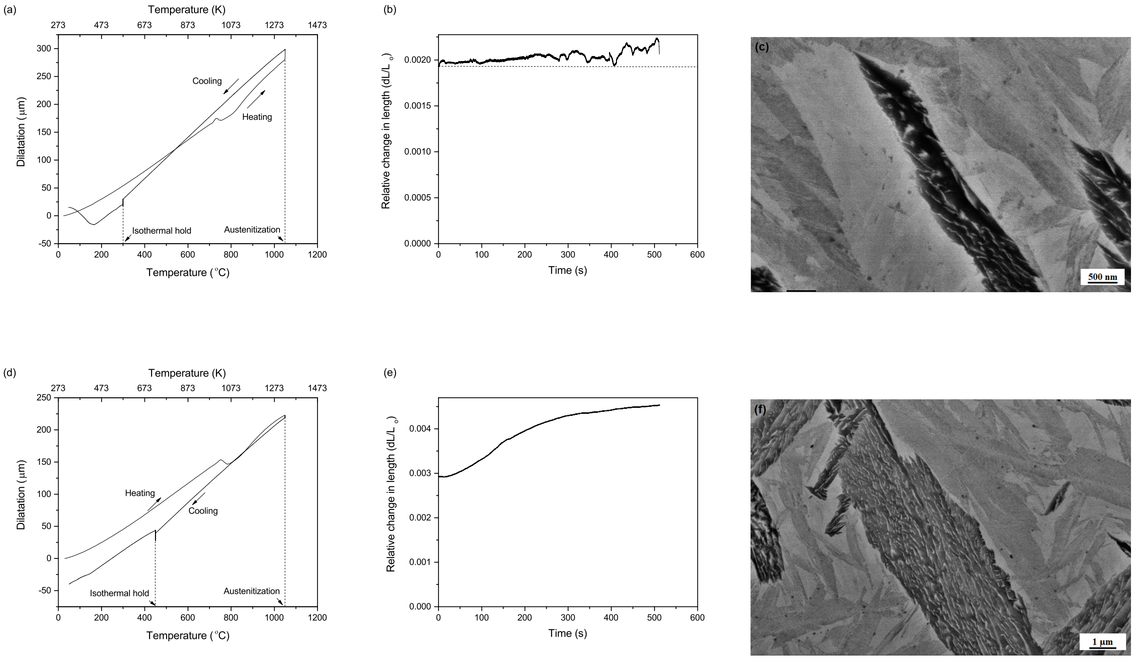

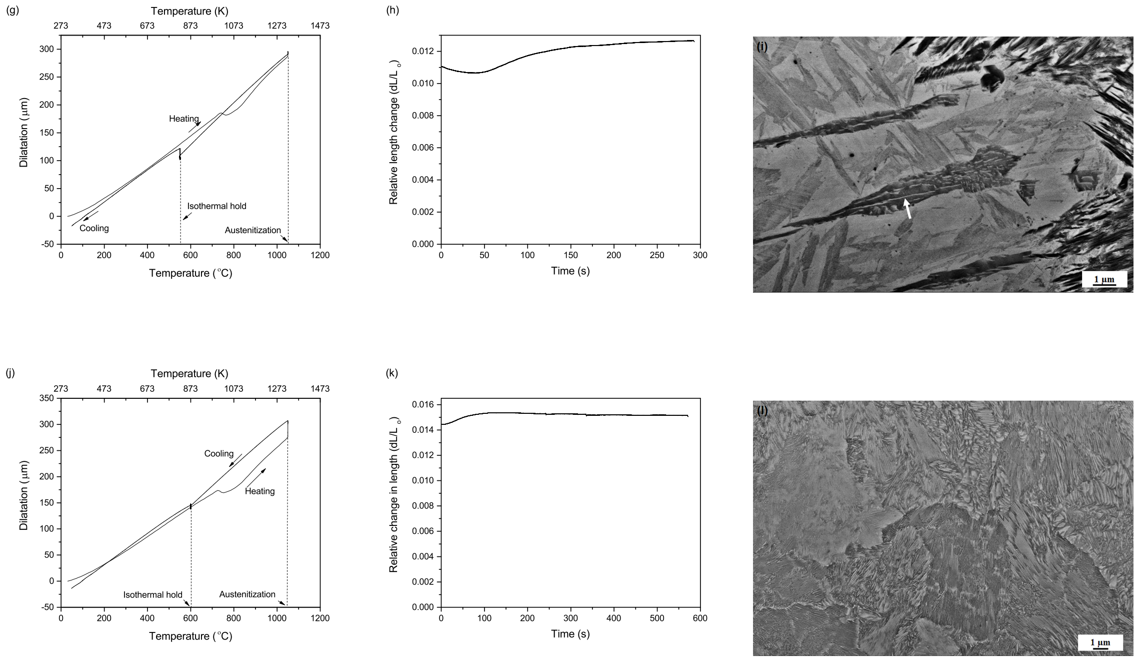

Figure 5.10: Experimental results to support the thermodynamic methodology on understanding the effect of isothermal holding temperature on inverse bainitic transformation in alloy A5. (a) Complete dilatometry recording for isothermal holding at 573 K (300 °C) , (b) Relative length change with isothermal holding time at 573 K (300 °C), (c) BSE-SEM image of the heat treated sample, (d) Complete dilatometry recording for isothermal holding at 723 K (450 °C) , (e) Relative length change with isothermal holding time at 723 K (450 °C), (f) BSE-SEM image of the heat treated sample, (g) Complete dilatometry recording for isothermal holding at 823 K (550 °C) , (h) Relative length change with isothermal holding time at 823 K (550 °C), (i) BSE-SEM image of the heat treated sample, (j) Complete dilatometry recording for isothermal holding at 873 K (600 °C) , (k) Relative length change with isothermal holding time at 873 K (600 °C), (l) BSE-SEM image of the heat treated sample showing pearlitic microstructure.

The complete dilatometry recordings for all the heat treated samples (Figure 5.10a, Figure 5.10d, Figure 5.10g, and Figure 5.10j) show the absence of any phase transformation during continuous cooling after austenitization and prior to the isothermal hold. After the isothermal hold, martensitic transformation is recorded in the 573 K (300 °C) sample. Martensitic transformation is not recorded on the other heat treated samples. The relative length change in the heat treated samples with isothermal holding time shows a net volumetric expansion in all the heat treated samples except the 823 K (550 °C) heat treated sample. The 823 K (550 °C) heat treated sample shows a two-stage dilatation profile with a transition in kinetics from volumetric contraction to volumetric expansion after 50 seconds into the transformation. It can be speculated from the dilatometry recordings that the transformation product at 823 K (550 °C) isothermal hold sample is inverse bainite, owing to its two-stage dilatation change [80, 86]. For the 573 K (300 °C) and the 723 K (450 °C) heat treated sample it can be speculated that the transformation product is "conventional" bainite, owing to a net volumetric expansion [92–94]. For the 873 K (600 °C) heat treated sample, since the isothermal holding temperature is higher, it can be speculated that the transformation product is pearlite, owing to net volumetric expansion at the higher isothermal holding temperature [95].

The SEM micrographs of the heat treated samples (Figure 5.10c, Figure 5.10f, Figure 5.10i, and Figure 5.10l) confirm the microstructures speculated from the relative length change in the heat treated samples. For isothermal holding at 573 K (300 °C), the electron micrographs show the presence of carbides (white particles) in ferrite (black) in a martensitic matrix (gray). The carbides are oriented at an angle (approximately 55°) to the primary growth direction of ferrite and the microstructure is similar to lower bainite reported by Borgenstam et al. [39]. For isothermal holding at 723 K (450 °C), the electron micrographs show the presence of carbides (white particles) in ferrite (black) in a martensitic matrix (gray). The carbides are oriented at parallel to the primary growth direction of ferrite and the microstructure is similar to upper bainite consisting of ferrite and inter-lath carbides [12]. For isothermal holding at 823 K (550 °C), bainitic microstructure with cementite midrib (white arrow in Figure 5.10i) is observed. The microstructure is similar to inverse bainite reported in our previous studies [80, 86]. A completely lamellar and pearlitic microstructure is observed for isothermal holding at 873 K (600 °C).

5.3.4 Comparison with other steels from literature - Alloys L1 - L4

It would be interesting to verify the proposed thermodynamic approach in predicting the inverse bainitic transformation to other hypereutectoid steels, especially the steels in the work by Borgenstam et al. [39], which includes the metallographic studies by Modin and Modin, and the work by Kolmskog and Borgenstam [40] where they studied the eutectoid transformation in a 4.12 wt.% Cr - 0.88 wt.%C steel. Performing similar calculations to alloys L1-L4, the gradual change in the eutectoid transformation products with the isothermal holding temperature can be derived for the alloys. The predicted microstructures for alloys L1-L4 are tabulated and compared with the ones reported by Kolmskog and Borgenstam [39, 40] in Table 5.3. It is to be mentioned that, for transformations occurring near the inverse bainitic finish temperature, "fan-like" eutectoid transformation product was assumed based on the experimental results presented (Discussion on this assumption is presented in Section 5.4). The predictions of the microstructure for alloys L1-L4 using the proposed approach at different isothermal holding temperature agrees with the experimental microstructure reported in Ref. [39, 40, 96]. Also, the thermodynamic predictions for the existence of inverse bainite in alloys E1 and A5 are in general agreement with the experimental measurements. This provides confidence that the developed approach is generic and

Table 5.3: Comparison between the predicted microstructures and the microstructures reported in literature at different isothermal holding temperatures

Temperature (°C)	**L1†**	**L1**	**L2†**	**L2**	**L3†**	**L3**	**L4†**	**L4**
650	P	⋆	P	⋆	P	P(I)	P	P
600	P	PW	P	P(I)	P	P(I)	I	A
550	P	PW	P	P(I)	P	PB	I	A
500	PI	IW	PI	P(I)	PI	B	I	AW
450	I	I(F)	I	I	FB	B	FB	AW
400	FI	F(I)	FI	IF	B	B	B	IF
375	FB	⋆	FB	⋆	B	⋆	B	F
350	B	F(I)	B	FB	B	B	B	F(B)
300	B	F(B)	B	B	B	B	B	B
250	B	⋆	B	B	B	B	B	B
200	B	B	B	B	B	⋆	B	B

† Predictions from the current work.
⋆ Microstructure not reported in literature
P - Pearlite, B - "Conventional" bainite, I - Inverse bainite, A - Acicular Pearlite, W - Widmanstatten plates, F - Fan-like Bainite.

can be applied to any hypereutectoid steel systems to understand the inverse bainitic transformation.

5.4 Discussion

5.4.1 Effect of Cr and Mn on inverse bainitic transformation

From the results presented in Section 5.3.1, it can be seen that cementite nucleation from parent austenite is favored at lower chromium contents and higher manganese contents in the steel. Ferrite nucleation being the primary transformation event from parent austenite at higher chromium content or lower manganese content, and cementite nucleation being the primary transformation event from parent austenite at lower chromium content or higher manganese content needs further discussion.

The formation of ferrite as the primary nucleation phase at higher chromium contents can be explained using Hultgren extrapolation and the degree of under-cooling below the Hultgren extrapolated zone. From Figure 5.6 and Table 5.1, it can be seen that with an increase in chromium concentration, the degree of under-cooling below the Hultgren extrapolated zone increases. Also, it can be seen that the driving force for the nucleation of ferrite from parent austenite becomes positive above a certain chromium concentration (in the current study, for chromium concentration above 1.1 wt.%). Figure 5.11 represents the schematic of Hultgren extrapolation and the corresponding TTT diagram adapted from Ref. [28]. As reported by Hultgren [28], between the A_{cm} and K, cementite transformation occurs from parent austenite. Between K and L or the Hultgren extrapolated zone in the phase diagram, austenite is supersaturated with respect to both ferrite and cementite resulting in cooperative growth to form pearlite. Below L (deviation from linearity in the metastable A_{cm} phase boundary), which is the lower limit of the Hultgren extrapolated zone in the phase diagram, there is a delay in pearlite transformation, but cementite can still nucleate from parent austenite until M. Below M, a certain degree of under-cooling below the Hultgren extrapolated zone ΔT_s, nucleation of ferrite leads the transformation resulting in “conventional” bainitic microstructure between M and N. Militzer et al. [97] quantified the degree of under-cooling required to form ferrite from parent austenite in Fe-C-Mn steels. According to Militzer et al. [97], a minimum under-cooling of 313 K (40 °C) is required for the nucleation of ferrite from parent austenite irrespective of the cooling rate and the grain size of parent austenite. It is likely that in the studied system (Fe-C-Cr-Mn), the minimum under-cooling required for ferrite

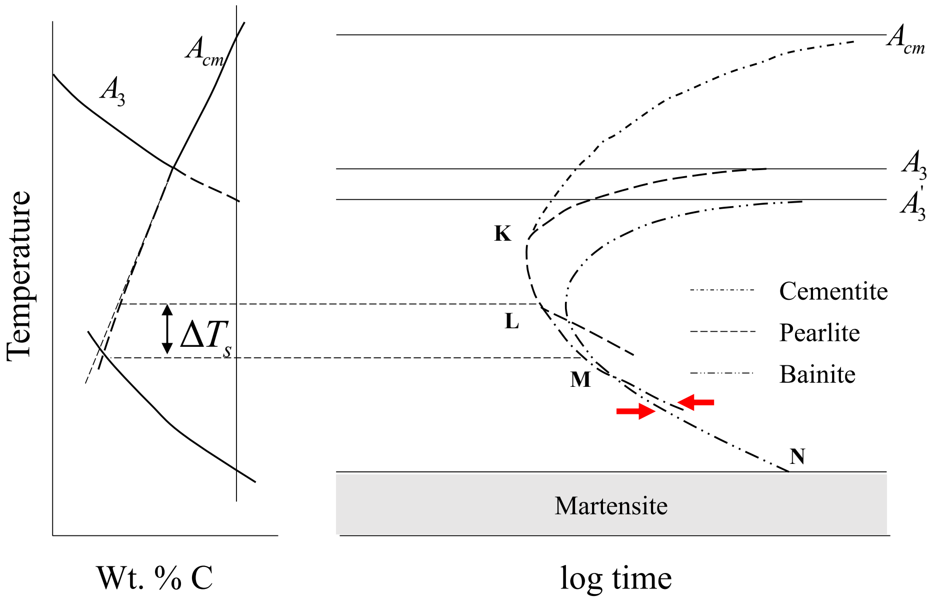

Figure 5.11: Schematic of Hultgren extrapolation and TTT diagram depicting the start curves for eutectoid transformation products for hypereutectoid steels.

nucleation is roughly 80 ° C (Ref. Table 5.1). Also, below M in Figure 5.11 conventional bainitic transformation happens from parent austenite, the parent austenite is still supersaturated with cementite, where the cementite 'C' curve extends to higher transformation time (marked by the red arrow in Figure 5.11). Thus, even below the required amount of under-cooling to form ferrite from parent austenite, cementite nucleation is still possible.

The increase in under-cooling below the Hultgren extrapolated zone with an increase in chromium content of the steel for a constant isothermal holding temperature can be explained by the ferrite stabilizing effect of Cr [98, 99]. With the increase in Cr content of the steel, the γ phase field contracts by the increase in slope of the A_{cm} phase boundary (Ref. Figure 5.6), thereby stabilizing ferrite. The increase in slope of the equilibrium A_{cm} phase boundary moves the metastable A_{cm} phase boundary to higher temperatures, thereby increasing the under-cooling below the Hultgren extrapolated zone. Comparing the evidences presented from Hultgren extrapolation (Figure 5.11), and the requirement of a minimum under-cooling required to form ferrite from austenite [97] to the results presented in Figure 5.6 and Table 5.1, one can explain the coexistence of conventional bainite and inverse bainite at high chromium contents and the presence of inverse bainite alone at lower chromium contents in the steel.

The other question which needs to be addressed is the effect of Cr on the formation of Cr-rich carbides as the initial nucleating phase from parent austenite. In order to study the effect of Cr on the formation of Cr-rich carbides, the alloy with the highest Cr content (alloy L4) was chosen. MatCalc was used to simulate the isothermal heat treatments and obtain the Temperature-Time-Precipitation (TTP) curves for the alloy. Figure 5.12 represents the precipitation kinetics for the alloy. Figure 5.12a represents the TTP curve for the formation of 0.05 vol. fraction of cementite and $Cr_{23}C6$. Isothermal precipitate fraction at 500 °C, 550 °C, and 600 °C in Figure 5.12b-d show that the cementite is the leading nucleating phase from parent austenite. $Cr_{23}C6$ and Cr_7C_3 do not form until 10,000 seconds into the transformation even for the higher Cr concentration studied. By the time the transformation time reached 10,000 seconds, the carbon depleted austenite at the austenite/cementite interface

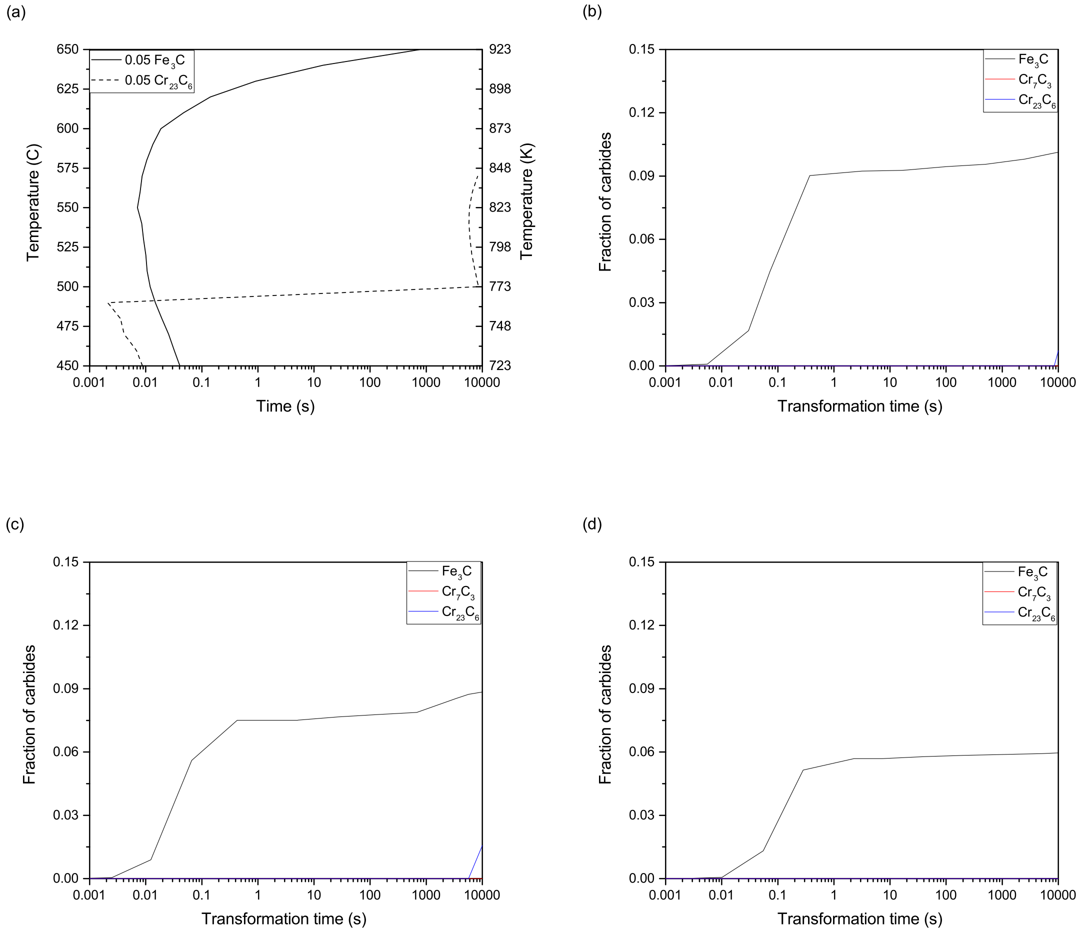

Figure 5.12: MatCalc precipitation simulation for alloy L4 with 4.12 wt. % Cr. (a) TTP curve for cementite and $Cr_{23}C_6$. (b) Precipitate fraction at 500 °C. (c) Precipitate fraction at 550 °C. (d) Precipitate fraction at 600 °C.

gets transformed into inverse bainitic ferrite and the inverse bainite gets degenerated to upper bainite [86] and the transformation of inverse bainite goes to completion. Thus, from Figure 5.12, it can be concluded that Cr does not have a significant influence on the mechanism of transformation of inverse bainite, rather Cr alters the transformation finish temperature owing to the change in slope of the metastable A_{cm} phase boundaries.

Arguing along the similar lines, we suggest the following explanation for the effect of Mn on the transformation of inverse bainite. Mn can delay the ferrite nucleation and lowers the diffusivity of carbon in ferrite, thereby impeding the growth of ferrite [100–102]. Furthermore, owing to the similar electronic structure and the atomic number of Mn and Fe, Mn substitutes for Fe in cementite, making cementite thermodynamically more stable [103,104]. This explains the stabilization of cementite at higher manganese contents and the formation of inverse bainite as the transformation product at higher manganese content in steel.

5.4.2 Effect of isothermal holding temperature on the transformation

With a decrease in the isothermal holding temperature, the eutectoid transformation products gradually shift from pearlite to inverse bainite, and finally to “conventional” bainite. Experimental evidence presented in Figure 5.10 shows that with the decrease in isothermal holding temperature, the microstructure changes from lamellar, to acicular, to nodular, and finally to acicular. Borgenstam and Kolmskog [39,40] observed a similar phenomenon and called this a symmetry in the eutectoid transformation products with respect to temperature. Such a symmetry in the eutectoid transformation products with temperature needs further discussion.

With an increase in temperature the free energy change for the transformation of austenite to inverse bainitic ferrite drops to a lower carbon content. This indicates that the parent austenite needs to be carbon depleted to a greater extent to form ferrite. This is possible by the nucleation of cementite from parent austenite since the driving force for the nucleation of cementite from austenite is positive. Borgenstam et al. [39] have reported that the cementite formed is Widmanstatten in nature, which explains the acicular nature of the transformation product at a higher temperature. At very low isothermal holding temperature, the driving force of nucleation for both ferrite and cementite is positive. Also, the integrated driving force for the transformation of austenite to ferrite is higher. Even though cementite has a positive driving force for nucleation, owing to the higher integrated driving force for austenite to ferrite transformation, ferrite transformation starts once the cementite nucleation starts, and a degenerated microstructure of inverse bainite [86] is expected. From the equilibrium phase diagram it is clear that the volume fraction of ferrite formed in the eutectoid mixture is much higher than cementite. Thus, any inverse bainite unit formed will be much lesser in fraction comparison to conventional bainite. Since the driving force for nucleation of ferrite from austenite is positive, and the volume fraction of ferrite is higher, acicular Widmanstatten ferrite like bainitic units are observed in the final microstructure. This explains the presence of acicular bainitic units at low isothermal holding temperature.

At intermediate isothermal holding temperatures, the bainitic unit becomes nodular as represented in Figure 5.10f. Borgenstam et al. [39] also observed such a phenomenon and called the nodular bainitic microstructure as "fan-like" bainite. Such a "fan-like" eutectoid is observed just below the lower limit of inverse bainite finish temperature both in our study and in the results reported by Borgenstam et al. Though one may expect "conventional" bainite as the transformation product, the temperature is closer to the inverse bainite finish temperature, and the integrated driving force for the formation of ferrite from parent austenite is less in comparison to the low-temperature isothermal hold. Though ferrite transformation is expected simultaneously at the start of the nucleation of inverse bainitic cementite, the formation of ferrite locally increases the carbon content of parent austenite at the austenite/ferrite interface reducing the integrated driving force for ferrite transformation at the austenite/ferrite interface and increasing the driving force for the cementite transformation from parent austenite. Thus, at intermediate transformation temperatures, one can expect a combination of upper bainite and degenerated inverse bainite (upper bainite) as the likely transformation products. Figure 5.13 confirms that the "fan-like" eutectoid formed by isothermal holding near the inverse bainite finish temperature range (in the current experiments 723 K (450 °C)) is indeed the degenerated microstructure of inverse bainite.

It can be seen that there are two variants of carbide within the bainitic unit. The first parallel to the growth direction of ferrite (formed by degeneration of inverse bainitic cementite midrib), the second parallel to the thickening direction of ferrite at the ferrite/martensite (parent austenite) interface. We have reported the presence of two variants of carbides within the inverse bainitic unit in Ref. [86]. The presence of two variants of carbides within the bainitic unit can also be observed in the fan-like eutectoid reported by Borgenstam et al. (Figure 5 in Ref. [39]). The degenerated mi-

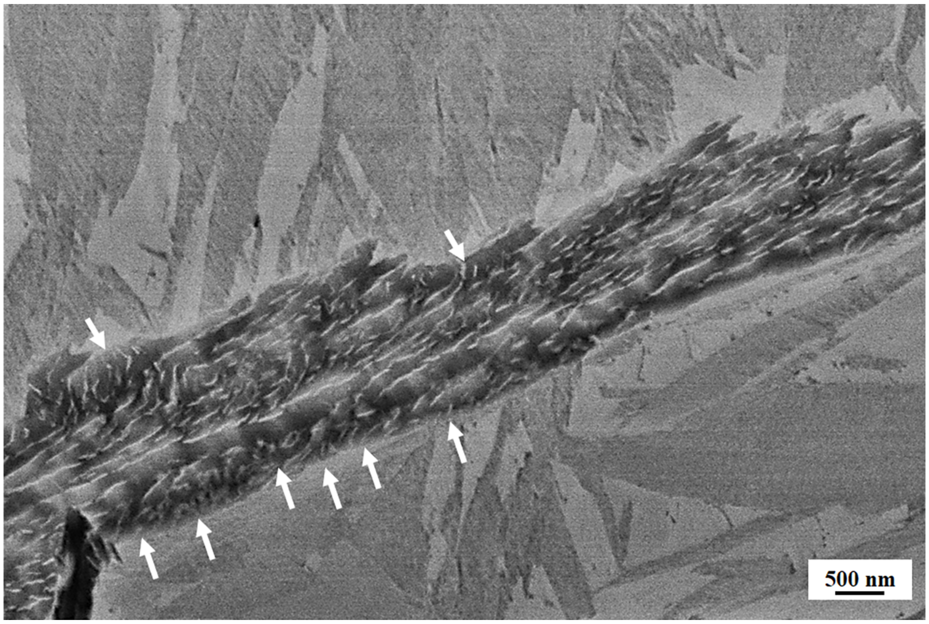

Figure 5.13: SEM micrograph showing the presence of two-variants of carbides in sample transformed close to the inverse bainite finish temperature (723 K) in alloy A5. Carbides parallel to the ferrite thickening direction are marked with white arrow.

crostructure of inverse bainite is nodular in comparison to the initial microstructure of inverse bainite with the Widmanstatten cementite midrib. This explains the nodular nature of the transformation product at an intermediate temperature. Thus, using the principles of integrated driving force for austenite to ferrite transformation, the driving force for the onset of nucleation of ferrite and cementite, an explanation for the change in eutectoid transformation product morphology from acicular to nodular to acicular can be provided. This also thermodynamically explains the observed symmetry by Borgenstam et al.

5.5 Conclusions

A generic thermodynamic approach is developed to understand the effect of Cr, Mn, and the isothermal holding temperature on the inverse bainitic transformation.The proposed approach involves the calculation of thermodynamic driving force for the onset of nucleation of cementite from austenite, Hultgren extrapolation of A_{e3} and A_{cm} phase boundaries, and the molar Gibbs free energy change for austenite to ferrite transformation. The following conclusions were made from the present study:

1. For a given carbon concentration slightly above the eutectoid carbon content,

inverse bainite is favored at a lower chromium and higher manganese concentration.

2. For a chemical composition that favors inverse bainitic transformation, inverse bainite is generally favored below the pearlitic transformation temperature. Inverse bainitic transformation gets suppressed when the isothermal transformation temperature is below the T_{FIB}, in which case conventional upper/lower bainite is the favored transformation product.

3. The transition in the morphology of eutectoid transformation products, and hence the symmetry with respect to the temperature in the Fe-C system can be explained by the variation in driving force for the onset of nucleation of ferrite and cementite with the transformation temperature.

Such a thermodynamic approach of inverse bainitic transformation helps in predicting the metastable phase boundaries in the Fe-C phase diagram between eutectoid transformation products.

Chapter 6

Partitioning of Substitutional Solutes During Inverse Bainitic Transformation

6.1 Introduction

This chapter focuses on the use of Atom Probe Tomography (APT) to characterize the redistribution of solutes during inverse bainitic transformation at atomic level resolution. Different stages of the transformation, namely the cementite midrib formation, inverse bainitic ferrite formation, secondary carbide formation, and the degenerated microstructure of inverse bainite have been characterized in detail. Solute profiles across the different interfaces indicate Negligible Partitioning Local Equilibrium (NPLE) type growth kinetics for inverse bainitic cementite midrib, whereas a transition in growth kinetics from Para Equilibrium (PE) to Negligible Partitioning Local Equilibrium (NPLE) is observed for secondary carbides and inverse bainitic ferrite. The results provide an indication that inverse bainitic transformation occurs in a similar manner to Widmanstätten ferrite/bainitic ferrite with carbon diffusion controlled growth, and without any reconstructive or long range diffusion of substitutional solutes.

6.2 Results

6.2.1 Microstructure of inverse bainite

Representative microstructural evolution during the isothermal bainitic transformation are shown in Figure 6.1. Figure 6.1a shows the microstructure of the 1 minute (cementite midrib formation) isothermal hold sample indicating the formation of carbide along prior austenite grain boundary. Figure 6.1b shows the microstructure of the 3 minutes isothermal hold sample representing the formation of ferrite surrounding the cementite. When the transformation time is increased to 5 minutes, carbides within ferrite nucleate as shown in Figure 6.1c. Figure 6.1c represents the inverse bainitic microstructure with carbide midrib (formed during 1 minute into the transformation), ferrite surrounding the carbide midrib (formed during 3 minutes into the transformation), and secondary carbides within ferrite surrounding the carbide midrib (formed during 5 minutes into the transformation). For the 10 minutes isothermal hold sample in Figure 6.1d, carbide midrib can no longer be identified and the microstructure represents an upper-bainitic type microstructure.

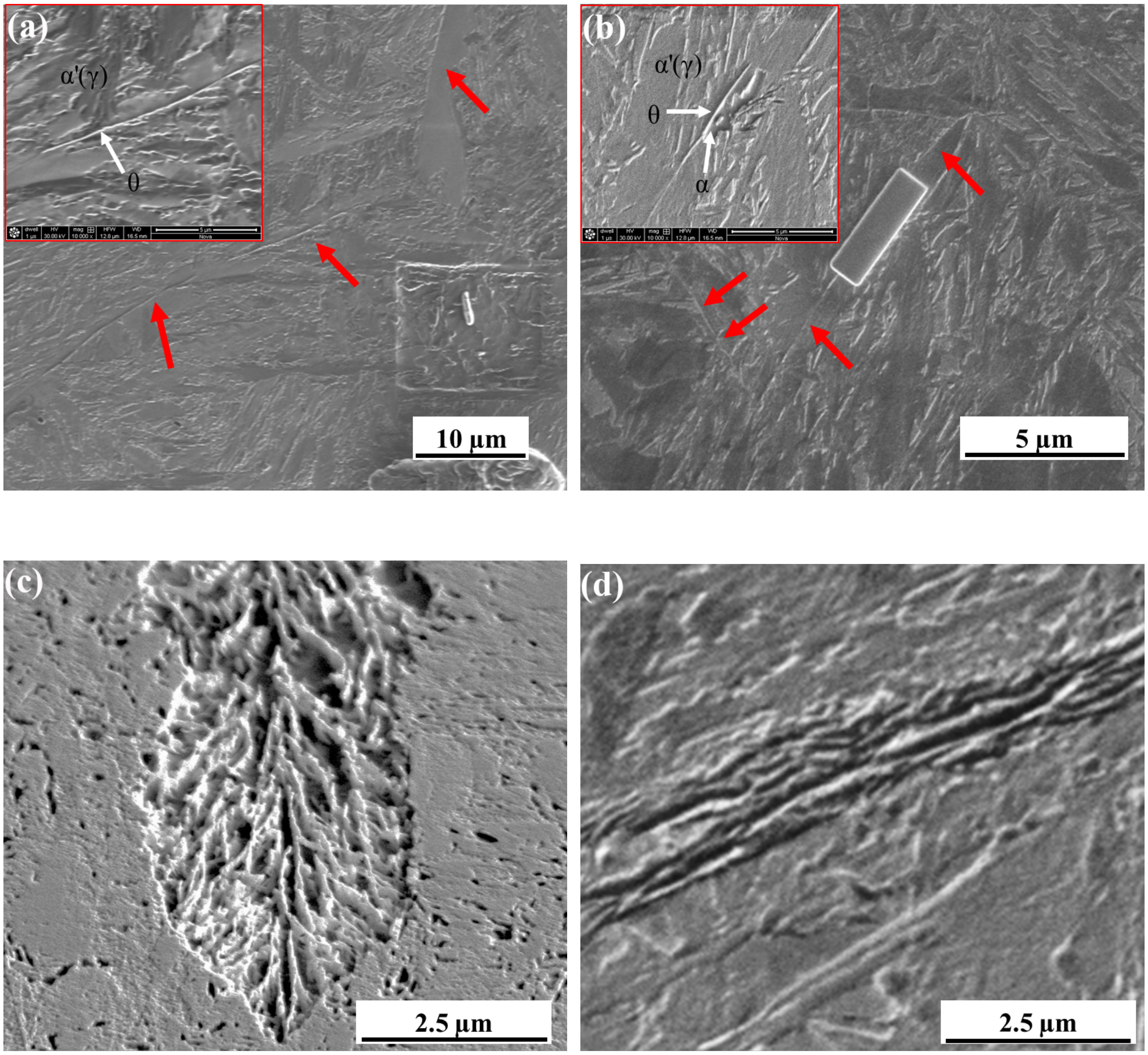

Figure 6.1: Microstructural evolution during isothermal bainite transformation. (a) Secondary electron micrograph of the 1 minute isothermal hold sample, (b) Secondary electron micrograph of the 3 minutes isothermal hold sample, (c) Secondary electron micrograph of the 5 minutes isothermal hold sample, and (d) Secondary electron micrograph of the 10 minutes isothermal hold sample. Prior austenite grain boundary are indicated by red arrows in (a) and (b).

Atom probe needles were site specifically lifted-out from these locations, and the atom probe reconstructions are discussed next.

6.2.2 Solute redistribution during inverse bainitic cementite midrib transformation

Figure 6.2 shows the APT results of the 1 minute isothermal hold sample, representing the formation of inverse bainitic cementite in a martensitic matrix. From the carbon atom map, a carbon enriched carbide region is observed with a carbon cluster filled martensitic matrix with approx 15 at.% C is observed next to the carbide region. The carbon concentration of clusters is similar to the ones reported by Peet *et al.* [105] and Caballero *et al.* [25,27]. The high sensitivity of the LEAP allows for identification and visualization of trace elements like B, Cu, and Si at the carbide/martensite interface . Proximity histograms across the carbide/martensite interface, and the ratio of substitutional solutes to iron across the interface are shown in Figure 6.2b and Figure 6.2c, respectively. It can be seen that the carbide has a carbon concentration of around 25 at. %, martensite has a carbon concentration of around 4 at. %, which is the nominal carbon concentration of the steel. The carbon concentration of the carbide suggests that the carbide is cementite, confirming our earlier EBSD analysis that the initial nucleating carbide is cementite. Si concentration in cementite is almost 0 at. %, whereas martensite has a nominal Si concentration of 0.4 at.%. A Si concentration spike is observed at the cementite/martensite interface. The concentration of Cr and Mn are 1 at. % in both martensite and cementite, and no partitioning of Cr/Mn is observed at the interface. It can also be seen that the ratio of Cr/Fe as well as Mn/Fe is maintained across the cementite/martensite interface, confirming that no long range diffusion of substitutional solutes takes place. To further understand the redistribution of substitutional solutes during cementite midrib formation, the cementite midrib/inverse bainitic ferrite was imaged in the atom probe using the 3 minute isothermal hold sample. The results of the cementite midrib/ferrite interface are shown in Figure 6.3

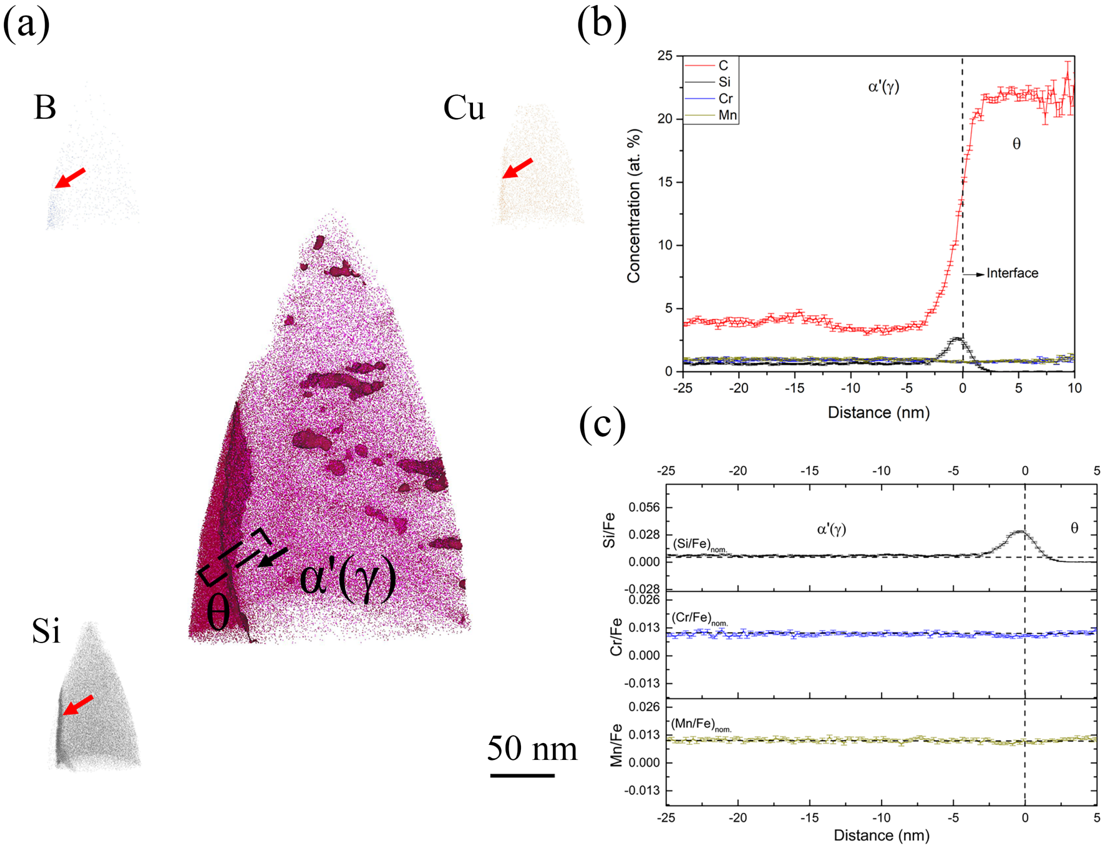

Figure 6.2: APT reconstructions across the cementite/martensite interface in the 1 minute isothermal hold sample. (a) Atom maps of C, B, Cu, and Si. (b) Proximity histogram across the cementite/martensite interface showing the solute redistribution, (c) Ratio of substitutional solute concentration to iron concentration (Cr/Fe and Mn/Fe) across the cementite/martensite interface.

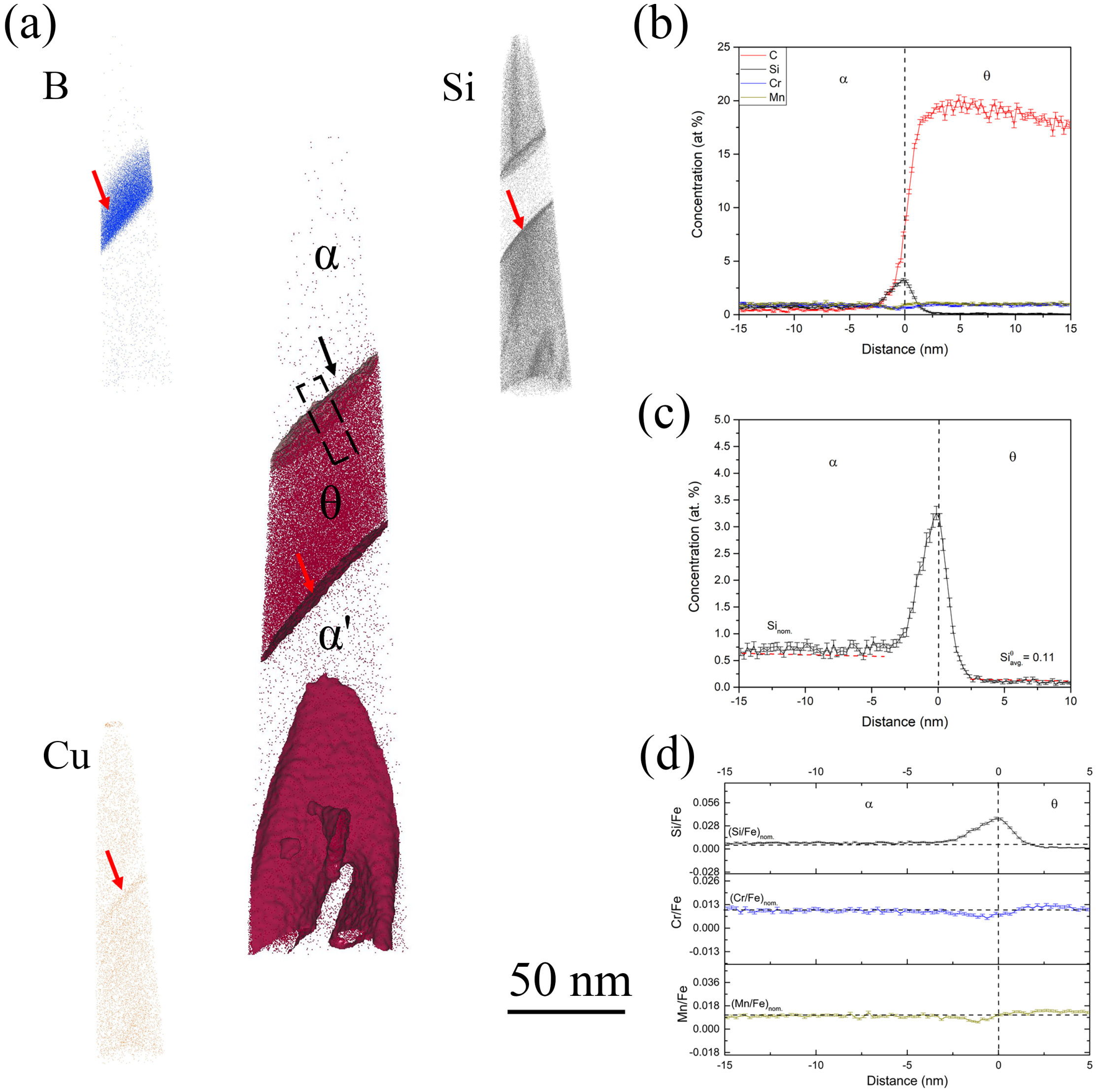

Figure 6.3: APT reconstructions across cementite/ferrite interface in the 3 minute isothermal hold sample. (a) Atom maps of C, B, Cu, and Si. (b) Proximity histogram across the cementite/ferrite interface showing the solute redistribution, (c) Proximity histogram across the cementite/ferrite interface showing the Si redistribution across the interface (d) Ratio of substitutional solute concentration to iron concentration (Cr/Fe and Mn/Fe) across the cementite/ferrite interface.

Figure 6.3a shows the C, B, Si, and Cu atom maps. From the carbon atom map, a carbon enriched carbide region is observed. Below the carbide, martensitic matrix with carbon clusters is observed, and above the carbide, inverse bainitic ferrite (low carbon region) is observed. At the cementite/martensite interface, segregation of Si, Cu, and B is observed. In order to characterize the cementite/ferrite interface, proximity histograms were reconstructed. Figure 6.3b shows the redistribution of solutes across the cementite midrib/inverse bainitic ferrite. It can be seen that the carbide has a carbon concentration of around 25 at. % indicating that the carbide is cementite, and ferrite has a much lower carbon concentration of 0.5 at. %. No change in the Cr/Mn concentration is observed across the cementite/ferrite interface, and both cementite and ferrite have nominal concentration of Cr and Mn (1 at.% each). Figure 6.3c displays the proximity histogram for Si across the cementite/ferrite interface. It can be seen that cementite has some Si retained in it (around 0.1 at.%, which is much greater than the equilibrium solubility of Si in cementite) whereas the concentration of Si in ferrite is the nominal Si content (around 0.5 at. %). The ratio of Cr/Mn to iron shown in Figure 6.3d confirms that no long range diffusion of Cr/Mn takes place across the transformation interface.

6.2.3 Solute redistribution during inverse bainitic ferrite transformation

The 5 minutes and 10 minutes isothermal hold samples were used for the analysis of growth kinetics of inverse bainitic ferrite. APT results across the ferrite/martensite interface of the 5 minutes and 10 minutes isothermal hold samples are shown in Figure 6.4 and Figure 6.5 respectively. Figure 6.4a displays the carbon atom map, Si atom map, and the 3 at.% iso-concentration surface showing all the interfaces for the 5 minutes isothermal hold sample. Figure 6.4b displays the proximity histogram showing the solute redistribution across the ferrite/martensite interface. C redistribution can be seen across the martensite/ferrite interface. As for as the substitutional solutes are concerned, no partitioning of Cr/Mn is observed. The Cr/Mn concentration is the nominal concentration (1 at.% each) in both ferrite and martensite. Si redistribution with concentration spike is observed at the interface. Figure 6.4c displays the ratio of substitutional solute to iron atoms across the ferrite martensite interface. The ratio of substitutional solute to iron is preserved, indicating that no long range diffusion of substitutional solutes takes place across the interface.

Figure 6.5a displays C atom map for the 10 minutes isothermal hold sample. Alternating layers of secondary carbides (carbon rich regions) distributed in inverse bainitic ferrite (carbon depleted regions) can be seen. Below the ferrite, high carbon martensite/retained austenite region is observed. A 8 at.% iso-concentration surface of the martensite/retained austenite region close to the inverse bainitic ferrite delineates austenite (free from carbon clusters) from martensite (with carbon clusters with carbon concentration of approx. 15 at.% similar to the ones reported by Peet *et al.* [105] and Caballero *et al.* [25, 27]). Figure 6.5b displays the proximity histogram across the ferrite/retained austenite interface. The carbon concentration in ferrite is low, whereas the carbon concentration in austenite close to the interface is around 6 at.%. Away from the ferrite/austenite interface, the carbon concentration in austenite reaches the nominal carbon concentration of 4 at.%. It can also be seen from Figure 6.5b that a Cr/Mn concentration spike with a width of around 4 nm is observed at the interface, with the concentration reaching the nominal

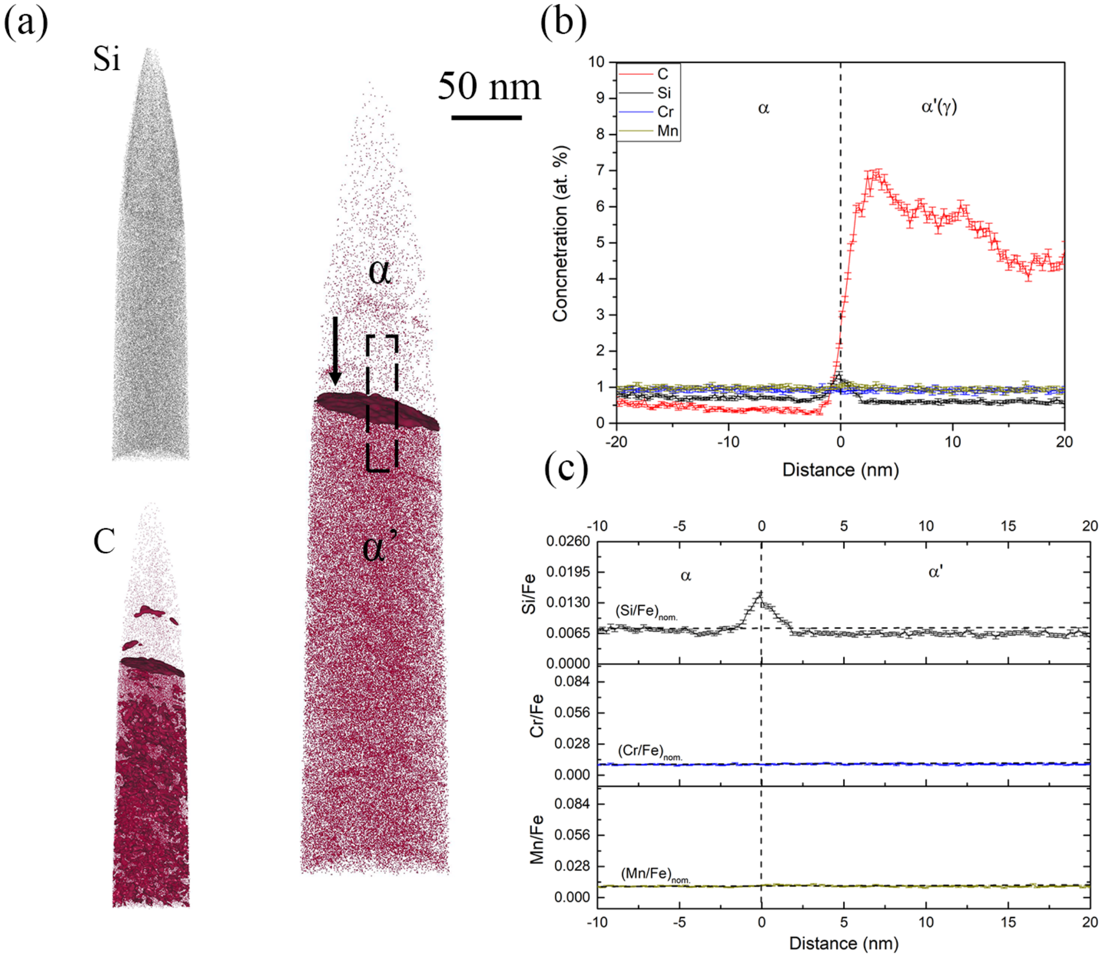

Figure 6.4: APT reconstructions across the ferrite/martensite interface in the 5 minute isothermal hold sample. (a) Atom maps of C, Si, 3 at.% iso-concentration surface showing the low/high carbon interfaces in the APT datasets. (b) Proximity histogram across the ferrite/martensite interface showing the solute redistribution, (c) Ratio of substitutional solute concentration to iron concentration across the ferrite/martensite interface.

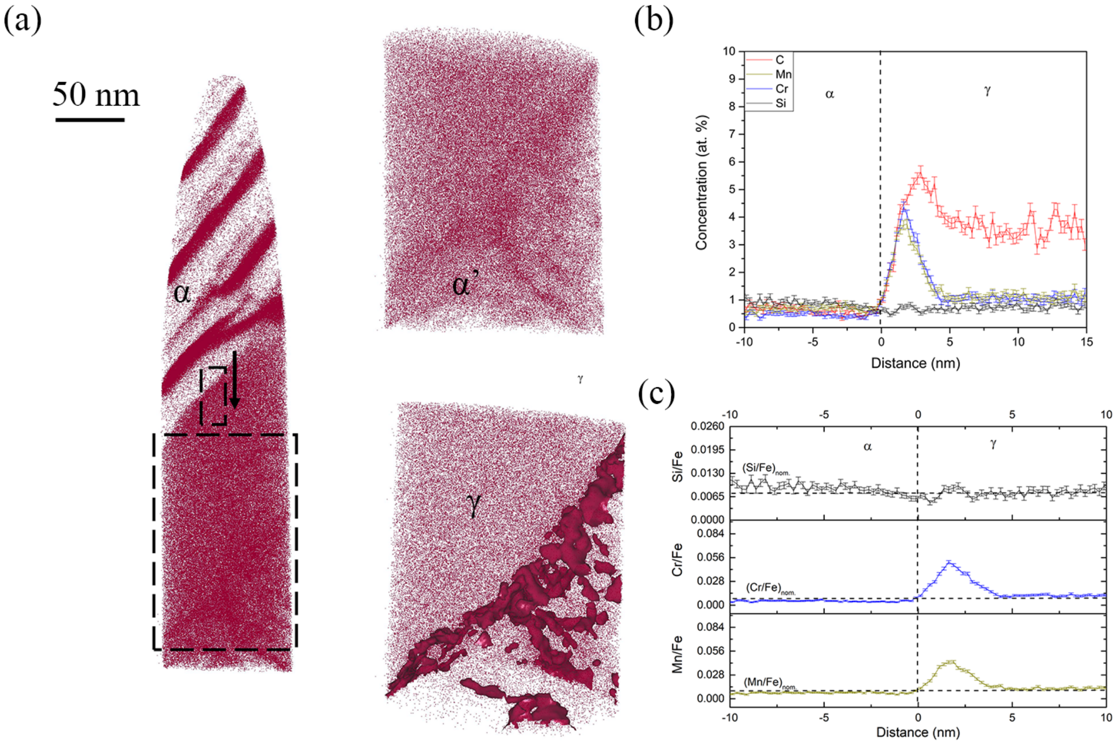

Figure 6.5: APT reconstructions across the ferrite/martensite(retained austenite) interface in the 10 minute isothermal hold sample. (a)Atom maps of C for the full data set and a clipped region containing the, austenite/ martensite, and an the austenite/martensite interface with an 8 at.% iso-concentration surface showing the austenite/martensite interface. (b) Proximity histogram across the ferrite/austenite interface showing the solute redistribution, (c) Ratio of substitutional solute concentration to iron concentration across the ferrite/austenite interface.

concentration of 1 at.% each away from the concentration spike. Unlike the 5 minute isothermal hold sample in Figure 6.4, Si does not partition across the interface. The ratio of substitutional solutes to iron shown in Figure 6.5c shows that the Si/Fe ratio is preserved across the interface, indicating no long range diffusion of Si. Cr, Mn concentration spike is evident, but the Cr/Fe and Mn/Fe ratio is preserved away from the interface, indicating no long range diffusion of Cr/Mn across the transformation interface.

6.2.4 Solute redistribution during the formation of secondary carbides in inverse bainite

To characterize the solute redistribution during the secondary carbide growth, the 5 minutes, and 10 minutes isothermal hold samples were characterized for carbides within inverse bainitic ferrite. Figure 6.6 and Figure 6.7 display the APT results for the 5 minutes and 10 minutes isothermal hold samples respectively. Figure 6.6a shows the carbon atom map and the 5 at.% iso-concentration surface showing the different secondary carbide/inverse bainitic ferrite interface. A representative proximity histogram across one of the secondary carbide/ferrite interface is shown in Figure 6.6b. It can be seen that carbon redistributes between the inverse bainitic ferrite and secondary carbide. The carbon concentration in the secondary carbide is around 20 at.%, indicating that the carbide is cementite. Carbon concentration is lower in inverse bainitic ferrite (approx. 0.227 at. %). No redistribution of Cr, Mn, or Si is observed. The ratio of substitutional solutes (Cr, Mn, and Si) to iron atoms is shown in Figure 6.6c. Figure 6.6c confirms that the concentration of substitutional solutes is preserved across the interface, and no long range diffusion of substitutional solutes takes place across the transformation interface.

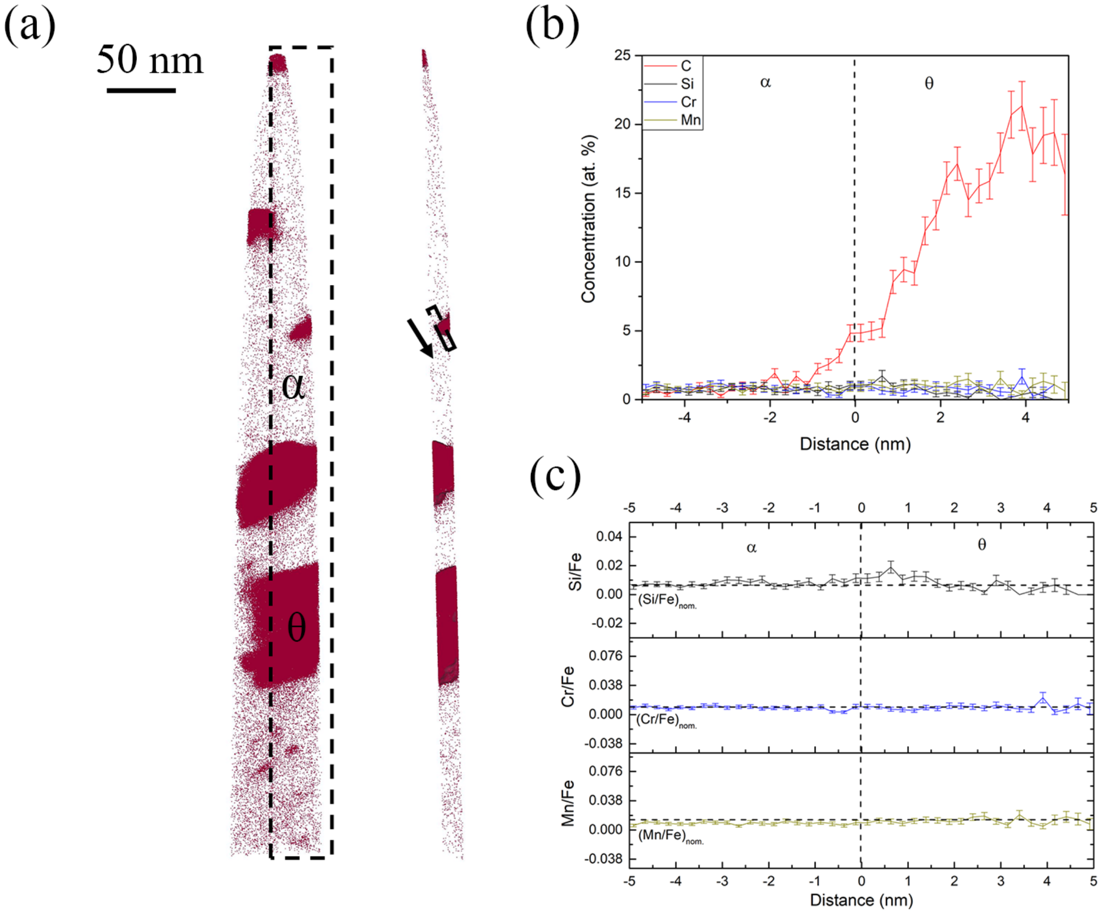

Figure 6.6: APT reconstructions across in the 5 minute isothermal hold sample showing secondary cementite. (a) Atom maps of C within the full needle and a 5 at. % iso-concentration surface from a slice showing the secondary cementite/ferrite interfaces. (b) Proximity histogram across the secondary cementite/ferrite interface showing the solute redistribution, (c) Ratio of substitutional solute concentration to iron concentration Cr/Fe and Mn/Fe across the secondary cementite/ferrite interface.

Figure 6.7a shows the carbon atom map and the 5 at.% iso-concnetration surface showing the secondary carbide/inverse bainitic ferrite interfaces when the isothermal holding time is increased to 10 minutes. Figure 6.7b shows the representative proximity histogram across one of the secondary carbide/inverse bainitic ferrite interface. From Figure 6.7b, it can be seen that carbon redistributes across the secondary carbide/inverse bainitic ferrite interface. The carbon concentration in the carbide is around 20 at.% indicating that the carbide is cementite. The carbon concentration in ferrite is low (0.12 at.%) and close to the para-equilibrium carbon concentration in ferrite. It can also be seen that there is Cr/Mn enrichment and Si depletion at both of the cementite/inverse bainitic ferrite interfaces. The concentration of Cr, Mn, and Si appears to have reached the nominal concentration away from the cementite/inverse bainitic ferrite interface. In order to verify that equilibrium is established with respect to the substitutional solutes away from the cementite/ferrite interfaces, the ratio of substitutional solutes to iron were calculated and plotted in Figure 6.7c. Figure 6.7c confirms that the concentration of substitutional solutes reaches the nominal value away from both the cementite/ferrite interfaces and no long range diffusion of substitutional solutes take place.

6.3 Discussion

6.3.1 Si concentration spike at the interface and growth kinetics during inverse bainitic transformation

It can be seen from Figure 6.2 and Figure 6.3 that Si concentration spike is observed at the cementite midrib/martensite interface and the cementite midrib/ferrite interface. The amount of Si in cementite in Figure 6.2 is almost 0 at.% but the amount of Si in cementite in Figure 6.3 is 0.11 at. %. Because the transformation time is increased for the sample shown in from Figure 6.2 compared to that shown in Figure 6.3, one would expect the Si concentration in cementite to be the sample value of 0 at. % as the cementite midrib grows. It can also be seen that in Figure 6.4, a Si concentration spike at the ferrite/martensite interface is observed, but no Si spike is observed at the ferrite/austenite interface in Figure 6.5. Because the transformation time is higher for the sample in Figure 6.5 compared to that in Figure 6.4, one would expect the concentration of Si at the interface to have increased with the growth of ferrite, but no Si partitioning is observed in Figure 6.5. This behavior of Si at the transformation interface needs further discussion.

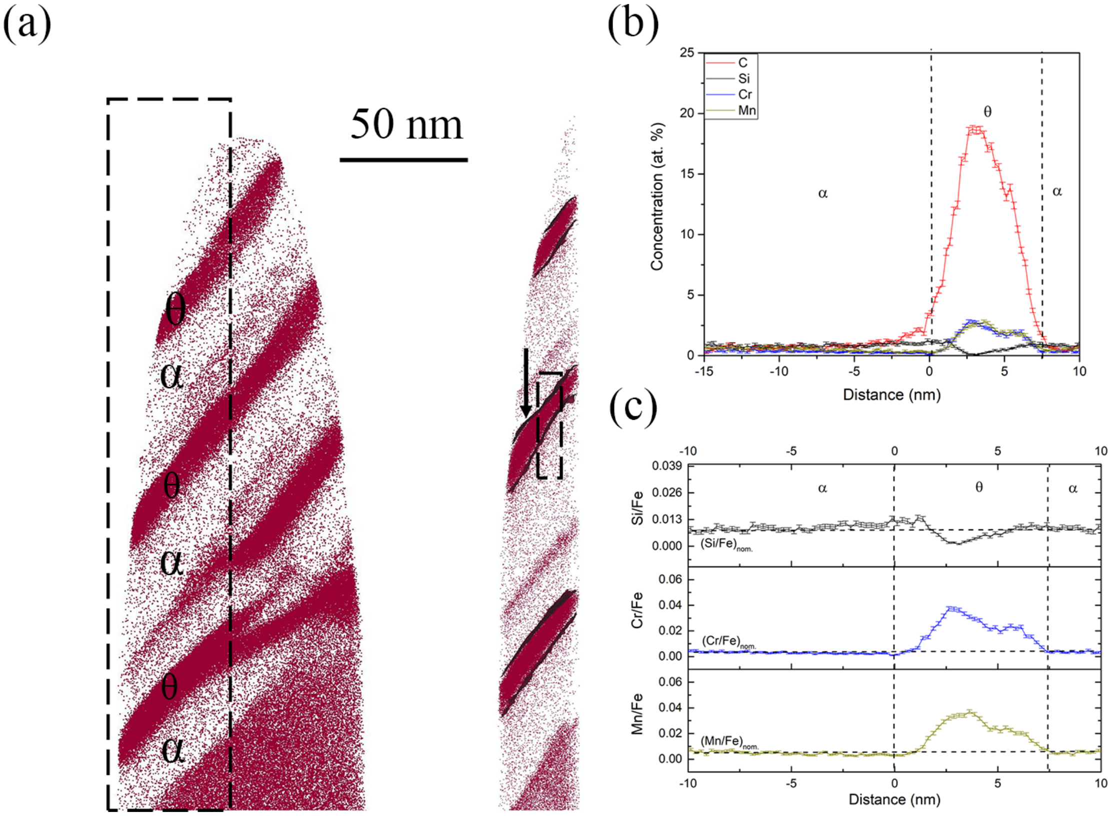

Figure 6.7: APT reconstructions across of the 10 minute isothermal hold sample showing secondary cementite in ferrite. (a) Atom maps of C and 5 at. % iso-concnetration surface showing the secondary cementite/ferrite interfaces. (b) Proximity histogram across the secondary cementite/ferrite interface showing the solute redistribution, (c) Ratio of substitutional solute concentration to iron concentration Cr/Fe and Mn/Fe across the secondary cementite/ferrite interface.

Cementite midrib growth kinetics

It can be seen from Figure 6.1a and Figure 6.1b, that the inverse bainitic cementite midrib nucleates along the prior austenite grain boundary, marked by the red arrow. Thus the analyzed interface in Figure 6.2 is a prior austenite grain boundary/cementite midrib interface, whereas in Figure 6.3 is the cementite/ferrite interface and cementite/prior austenite (martensite) interfaces are present. Considering the heat treatment used in the current study, additional point defects may be introduced at the prior austenite grain boundaries during the quenching following the austenitization [106]. These point defect can act as solute sinks, thereby forming solute-vacancy complexes. This phenomenon was reported as thermally induced non-equilibrium segregation. Si also has higher thermodynamic potential to segregate along the prior austenite grain boundaries at 500 ° C as shown in Ref. [106]. Thus, it can be hypothesized that Si concentration spike in Figure 6.2 is a consequence of the prior austenite grain boundary segregation rather than solute redistribution during the growth of cementite midrib. This hypothesis is further supported by the B and Cu atom maps in Figure 6.2 and Figure 6.3, where B and Cu segregation[1] is also observed at the prior austenite grain boundary (marked by red arrow in Figure 6.2). Faulkner [108] and Wu [109] have reported that when an elemental spike due to the thermally induced non-equilibrium segregation occurs, a solute depletion trough is observed ahead of the prior austenite grain boundary. Thus, the cementite midrib forms from austenite with a lower Si concentration ahead of the prior austenite grain boundary and not the equilibrium Si concentration of 0.5 at.%.

From the above mentioned segregation behavior of Si to the prior austenite grain boundaries, the "true" growth kinetics of cementite can only be characterized by analyzing the cementite midrib/ferrite interface in Figure 6.3. In Figure 6.3, no partitioning of Cr or Mn is observed across the cementite/ferrite interface. A Si concentration spike is observed at the cementite/ferrite interface, and the concentration of Si in cementite is much higher than the equilibrium solubility of Si in cementite. Since an elemental spike usually indicates that negligible partitioning local equilibrium is reached at the interface, and the concentration of Si in cementite being much higher than the partitioning local equilibrium (PLE) prediction (0 at. %) it can be suggested that the cementite midrib growth follows NPLE type of growth kinetics and during the nucleation stage, the cementite midrib might have formed in a true PE type nucleation.

---

[1] B, and Cu are reported as prior austenite grain boundary segregation elements during thermally induced non-equilibrium segregation [107].

Inverse bainitic ferrite growth kinetics

It can be seen that in Figure 6.4, the analyzed interface is ferrite/martensite interface, whereas in Figure 6.5, the analyzed interface is ferrite/prior austenite interface. It can be seen from the 5 at.% iso-concentration surface in Figure 6.4 that close to the ferrite/martensite interface, a carbide particle is observed. Thus, the analyzed proximity histogram has more than one interface. Miller [110] has reported that when the proximity histogram has more than one interface, an average concentration will be obtained. Thus, it can be hypothesized that the Si spike in Figure 6.4, and the high carbon concentration of martensite (7 at.%) closer to the interface is due to the cementite particle in martensite closer to the inverse bainitic ferrite/martensite interface. This hypothesis is further supported by the Si atom map in Figure 6.4, where no enrichment of Si at the inverse bainitic ferrite/martensite interface is observed. Thus, it can be suggested that the inverse bainitic ferrite follows a true PE type growth kinetics at the initial stage of the transformation. When the transformation time is increased, Cr/Mn concentration spike is observed (Ref. Figure 6.5). It should be noted that the concentration of Cr spike is approximately 4.5 at. % for both Cr/Mn which agrees with the concnetration described by NPLE thermodynamics (4.36 at. % for Cr and 5.11 at. % Mn), therefore we conclude that the kinetics of growth had changed from PE to NPLE.

Inverse baintic secondary cementite growth kinetics

Solute redistribution during the growth of secondary carbides is shown in Figure 6.6 and Figure 6.7. From Figure 6.6, it can be seen that no substitutional solute partitioning is observed across the secondary cementite/ ferrite interface, and the ratio of substitutional solutes is preserved across the interface. Carbon partitioning is observed across the cementite/ferrite interface. Since no substitutional solute partitioning is observed, and the ratio of substitutional solutes is preserved across the interface, it can be concluded that the growth of secondary cementite follows PE type kinetics when the transformation time is shorter. When the transformation time is increased, Cr, Mn, and Si concentration spike is observed at the cementite/ferrite interfaces in Figure 6.7. The concentration of the Cr/Mn spike is much lesser than the PLE concentration (6.5 at. % for Cr and 5.5 at. % for Mn). Also, the ratio of substitutional solutes is preserved across the cementite/ferrite interfaces. Therefore, it can be concluded that the secondary cementite growth kinetics transitions from PE to NPLE when the transformation time is increased because the concentration spike occurs at the cementite/ferrite interfaces, while the ratio of substitutional solutes to iron is preserved across the interface.

6.3.2 Transition in kinetics from PE to NPLE

In order to understand the reason for the change in growth kinetics from PE to NPLE, the ferrite/martensite (parent austenite) interface velocity was compared with the critical interface velocity required for the transition in growth kinetics from PE to NPLE. Since the inverse baintic ferrite growth occurs in a pure PE mode when the transformation time is shorter, and only carbon redistribution occurs across the transformation interface. The evolution in carbon concentration at the interface is shown schematically in Figure 6.8. From Figure 6.8a, it can be seen that the inverse bainitic ferrite nucleates from carbon depleted austenite ($C_{\gamma CD}$). The carbon depletion in austenite is caused by the nucleation of cementite, which depletes the carbon concentration of austenite in the vicinity of the cementite/austenite interface. Once the inverse bainitic ferrite nucleates and grows, carbon is rejected into the austenite at the austenite/inverse bainitic ferrite interface. The growth of ferrite increases the carbon concentration in austenite at the austenite/ferrite interface (Figure 6.8b), and eventually the carbon concentration of austenite at the austenite/ferrite interface reaches the nominal carbon concentration (Figure 6.8c).

Using the principles of diffusion and Zener's linear approximation of the interface composition profile [111], the velocity of the inverse bainitic ferrite/austenite interface (v_i) at time (t_i) can be estimated as

$$v_i = \frac{1}{2}\frac{(C_o - C_{\gamma CDi})}{(C_{\gamma CDi} - C_{\alpha\gamma}}\sqrt{\frac{D}{t_i}} \tag{6.1}$$

where $C_\circ$ is the bulk carbon concentration, $C_{\gamma CDi}$ is the carbon concentration of the carbon depleted austenite at the ferrite/austenite interface, and $C_{\alpha\gamma}$ is the carbon concentration of ferrite in equilibrium with austenite. The value of $C_{\gamma CD}$ at time t_i can be estimated using the isothermal dilation curves using the expression

$$C_{i+1} = \frac{\left[1 - \frac{1}{\left[\frac{(L_{i+1}-L_i)-B_i(f\gamma_{i+1}-f\gamma_i)}{A(f\gamma_i-f_i)} + \frac{1}{1-0.0146C_i}\right]}\right]}{0.0146} \tag{6.2}$$

Detailed derivation of Equation (6.2) is given in Appendix. Once the velocity of the inverse bainitic ferrite/austenite interface is calculated using Equation (6.1), the

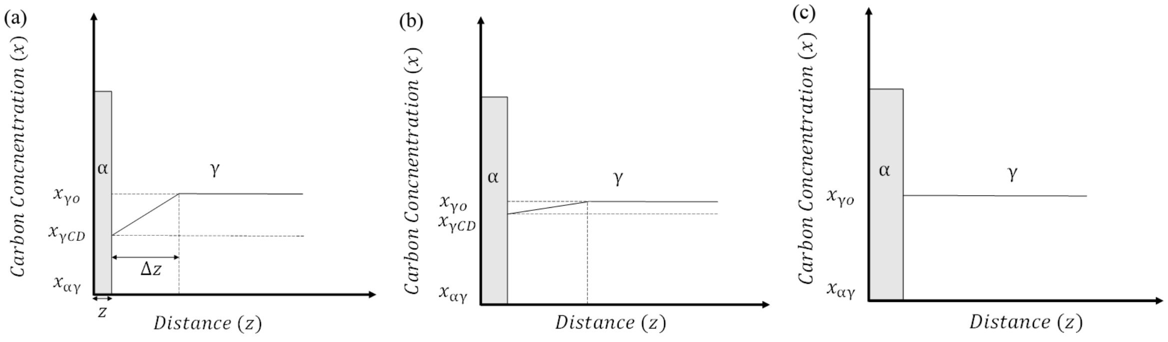

Figure 6.8: Schematic of the carbon concentration evolution at the ferrite/austenite interface during the growth of inverse bainitic ferrite. (a) Ferrite nucleation occurs from carbon depleted austenite, (b) As ferrite grows, carbon concentration of austenite increases at the interface, (c) Growth instant where the carbon concentration of austenite closer to the ferrite/austenite interface reaches the nominal carbon concentration/

velocity is compared with the critical velocity required for conversion to NPLE as reported by Inden in Ref. [112] as:

$$v_{crit} = \frac{\bar{x}}{t_{crit}} \tag{6.3}$$

where $\bar{x}$ is taken as inter-atomic spacing corresponding to four BCC unit cells [113], and t_{crit} can be calculated as the time for diffusion of Mn (substitutional solute with slowest diffusivity) over $\bar{x}$ as

$$t_{crit} = \frac{\bar{x}^2}{2D_{\alpha}^{Mn}} \tag{6.4}$$

The results of the experimental interface velocity calculated using Equation (6.1) and Equation (6.2), compared with the critical velocity for PE to NPLE transition is shown in Figure 6.9. It can be seen that the carbon concentration of the austenite at the ferrite/austenite interface increases from an initial carbon depletion ($x_{\gamma CD}$) of approx. 0.8 wt.% to around 0.9 wt.% towards the end of the transformation. The initial reduction in the carbon concentration at the ferrite/austenite interface is due to the inverse bainitic cementite midrib formation. It can also be seen that the velocity of the ferrite/austenite interface decreases with an increase in the transformation time. The reduction in the interface velocity is because of the time needed for the buildup of carbon at the ferrite/austenite transformation front. The experimental interface velocity calculated using Equation (6.1) drops below the theoretically calculated velocity required for Mn diffusion across the ferrite/austenite interface when the transformation time is greater than 310 s. Thus, when the transformation time is increased, the reduction in the interface velocity allows for redistribution of the substitutional solutes with local equilibrium being maintained at the ferrite/austenite interface through the development of a substitutional solute concentration spike at the interface. This explains why the 5 minutes isothermal hold sample shows a pure PE growth kinetics at the ferrite/martensite interface and the kinetics changes to NPLE when the transformation time is increased. Mesquita *et al.* [114] have studied cementite precipitation in low silicon steels and have found that if the early cementite precipitation is not inhibited by Si, the alloying elements do not have carbon to form alloy carbides, but the diffusion distance of alloying elements increases when the transformation time is increased. Therefore the alloying elements like Cr/Mn diffuse into cementite and stabilize it and retard its growth, rather than the dissolution of cementite to form alloy carbides. This reported behavior in low Si steels is consistent with our observations, where the early secondary cementite precipitation in ferrite is

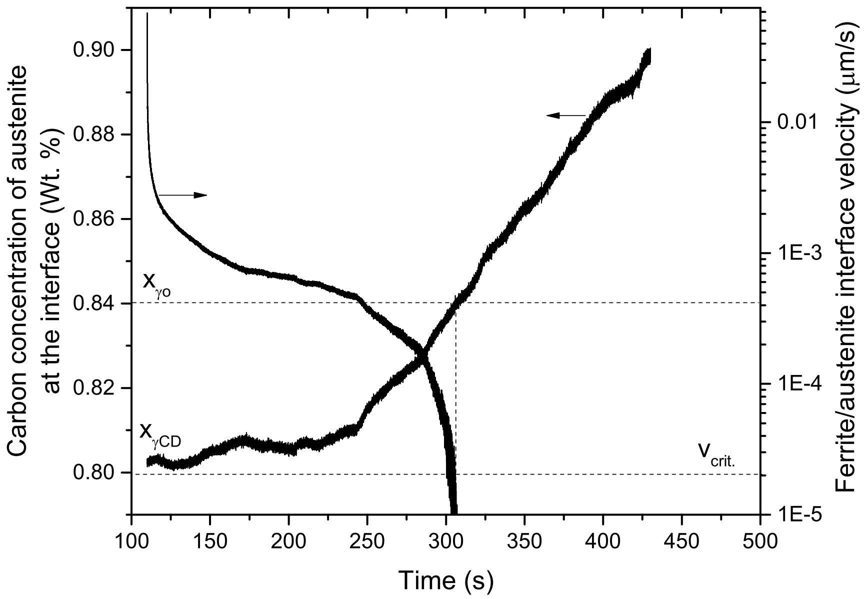

Figure 6.9: Change in carbon concentration and ferrite/austenite interface velocity with the transformation time. Carbon concentration was calculated from the dilatometry data using Equation (6.2), interface velocity was calculated using Equation (6.1), and the critical velocity for PE to NPLE transition was calculated using Equation (6.3).

not inhibited by Si (Figure 6.6) and Cr and Mn partitioning into cementite is observed at longer transformation times (Figure 6.7). Similar transition in kinetics of the cementite growth in ferrite was reported by Caballero *et al.* [25, 27] during tempering of nanocrytalline bainitic steel. Thus it can be concluded that the non-availability of carbon atoms to form alloy carbides and the increased diffusion of alloy carbides as the transformation time is increased explains why the secondary carbide growth kinetics change from pure PE to NPLE when the transformation time is increased.

The APT results presented in this study on the growth kinetics of inverse bainite provide a strong indication that the inverse bainitic transformation occurs as a consequence of individual cascading phase transformations starting from parent austenite. When parent austenite is quenched to the isothermal hold temperature, metastable cementite is nucleated as a consequence of higher thermodynamic driving force. This results in the redistribution of carbon across the parent austenite/cementite interface. When the transformation time is increased, Si redistributes across the parent austenite/cementite interface along with carbon resulting in a NPLE type of growth kinetics. The partitioning of carbon from parent austenite into cementite locally reduces the carbon concentration of austenite, thereby increasing the driving force for ferrite formation, resulting in the nucleation of ferrite at the cementite/carbon depleted austenite interface. During the ferrite nucleation and growth, there is redistribution of carbon without any redistribution of substitutional solutes at the ferrite/austenite interface. Apart from the above mentioned cascading reactions from parent austenite, secondary cementite particles nucleate within ferrite by redistribution of carbon at the ferrite/cementite interface. Thus, the combination of cascading phase transformations from parent austenite and the nucleation of carbides from ferrite results in the formation of inverse bainitic microstructure. When the transformation time is increased further, the para-equilibrium microstructure of inverse bainite transitions towards an negligible partitioning local equilibrium structure by partitioning of substitutional solutes at the interfaces, resulting in the formation of the degenerated microstructure of inverse bainite (upper bainite). It is likely that when the transformation time is increased beyond the formation of degenerated microstructure, auto-tempering of bainite will occur resulting in gradual transition of NPLE - PLE as reported by Caballero *et al.* [25]. The different cascading phase transformations and the corresponding elemental partitioning behavior are schematically shown in Figure 6.10. Results provide an indication that inverse bainitic transformation proceeds in a similar manner to Widmanstätten ferrite/bainitic ferrite with carbon

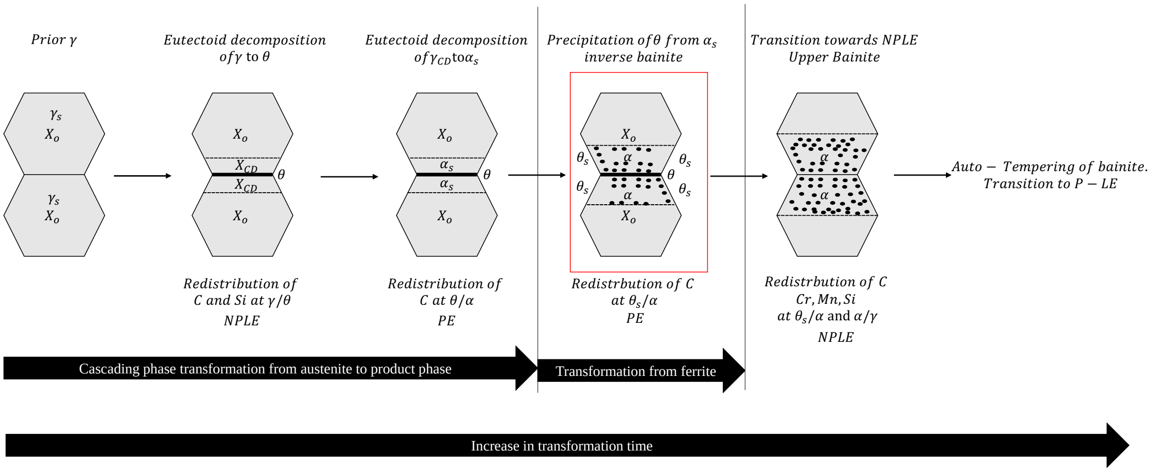

Figure 6.10: Summary of cascading reactions from supersaturated parent austenite leading to the formation of inverse bainite microstructure. The red box represents the microstructure of inverse bainite formed as a result of individual cascading reactions from parent austenite and supersaturated ferrite.

diffusion controlled growth, and without any reconstructive or long range diffusion of substitutional solutes.

6.4 Conclusion

Solute redistribution during isothermal transformation of austenite to inverse bainite have been characterized at atomic scale for the first time. The APT results presented in the present study on the growth kinetics of inverse bainite provide a strong indication that the inverse bainitic transformation occurs as a consequence of individual cascading phase transformations starting from parent austenite. Solute concentration profiles at different transformation interfaces indicated growth kinetics, and the following conclusions were made:

1. Cementite midrib of inverse bainite follows NPLE type growth kinetics. Though exact nucleation stage of the cementite midrib could not be characterized, it is likely that the cementite midrib nucleation occurs in a PE mode.
2. Inverse bainitic ferrite nucleation occurs in a PE mode, and when the transformation time is increased, there is a transition in kinetics from PE to NPLE. Interface velocity calculations showed that a deviation from PE occurs when the carbon concentration of the austenite at the interface reaches the bulk carbon concentration, by when the velocity of the interface drops below the critical velocity required for substitutional solute diffusion. The reduction in the interface velocity due to the carbon enrichment at the interface is the likely reason for the transition in kinetics from PE to NPLE.
3. Secondary cementite within inverse bainitic ferrite nucleates in a PE mode and when the transformation time is increased, there is a transition in kinetics from PE to NPLE.

The results provide an indication that inverse bainitic transformation occurs in a similar manner to Widmanstätten ferrite/bainitic ferrite with carbon diffusion controlled growth, and without any reconstructive diffusion.

Chapter 7

Nucleation of secondary cementite during inverse bainitic transformation

7.1 Introduction

Two different orientations of secondary carbides within the inverse bainitic ferrite (refer to Chapter 4), namely the carbides near the cementite midrib/ferrite interface oriented at 55° to the growth direction of ferrite (V1 type) and the second type of carbides at the ferrite/martensite(prior austenite) interface oriented parallel to the growth direction of ferrite (V2 type). Such two orientations of secondary carbides was also observed in the inverse bainite microstructure reported by Kolmskog *et al.* [39–41] suggesting that the observations in the current work are not alloy system dependent, but rather a physical phenomenon occurring during inverse bainitic transformation Ref. Figure 7.1. This chapter focuses on proposing a mechanism for the nucleation of two different orientations of secondary carbides within the inverse bainitic ferrite. Detailed characterization using Atom Probe Tomography (APT) in combination with dilatometry, and Auger electron spectroscopy (AES) reveals that the V1 type carbides nucleate in the carbon enriched regions of the cementite midrib/ferrite interface and the V2 type carbides nucleate as a consequence of the resumption of the Incomplete transformation (ICT) of inverse bainitic ferrite.

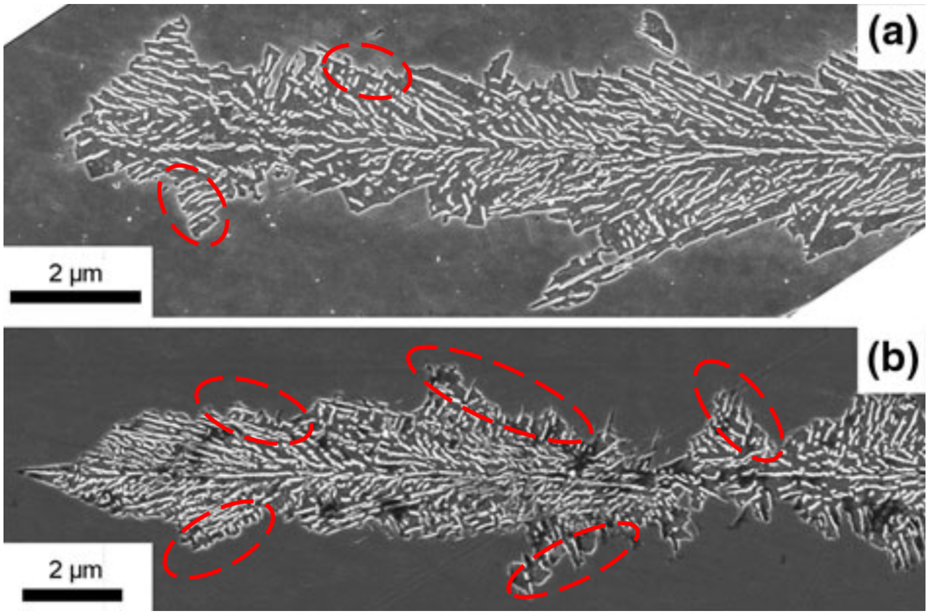

Figure 7.1: Existence of two orientations of secondary carbides within ferrite in inverse bainite. Microstructure taken from Kolmskog *et al.*

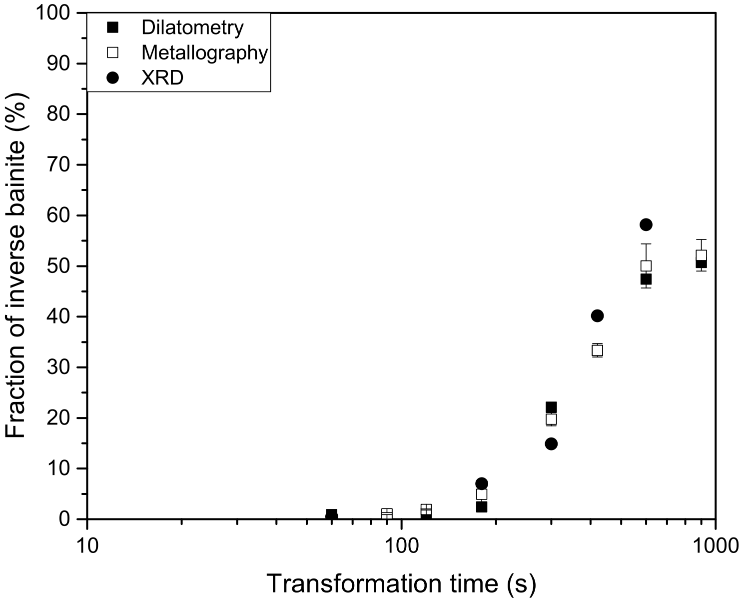

Figure 7.2: Phase fraction evolution of inverse bainite at 500 ° C with the transformation time.

7.2 Results

7.2.1 Microstructure and phase fraction evolution of inverse bainite

We found that for the steel considered in this study, inverse bainitic transformation happens in a narrow temperature range of 470 to 550 ° C. A temperature of 500 ° C was chosen to understand the transformation of inverse bainite. The phase fraction evolution is shown in Figure 7.2. It can be seen from Figure 7.2 that the transformation rate of inverse bainite is higher following the initial incubation stage of the transformation. Beyond 10 minutes (600 seconds) into the transformation, the phase fraction is almost a constant. No appreciable increase in the phase fraction is observed even when the isothermal holding time is increased by 5 minutes to a total transformation time of 15 minutes (900 seconds). For detailed microstructure characterization and microstructure evolution during the transformation, refer to [86].

The typical completely developed microstructure of inverse bainite (5 minutes isothermal hold sample) is shown in Figure 7.3. The characteristic cementite midrib (θ_m), the inverse bainitic ferrite (α) (darker etched phase in Figure 7.3), and sec-

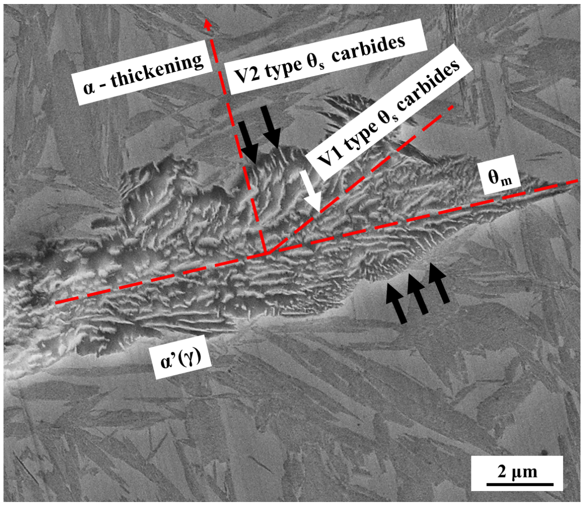

Figure 7.3: Completely developed microstructure of inverse bainite (5 minute isothermal hold) showing the cementite midrib (marked as C) and the black etched inverse bainitic ferrite in martensitic/retained austenite matrix (marked as $\alpha'(\gamma)$). Two orientations of secondary cementite are observed. Cementite oriented at an angle to the growth direction of ferrite is marked using white arrow, and cementite parallel to the ferrite growth direction are marked using black arrow.

ondary cementite (θ_s) (indicated by arrows in Figure 7.3) in a martensitic/retained austenite matrix $\alpha'(\gamma)$ is observed. It can be noticed that there are two orientations of θ_s. Cementite near the θ_m/α interface oriented at at an angle to the growth direction of ferrite (V1 type cementite marked using white arrow in Figure 7.3) and the second type of cementite at the $\alpha/\alpha'(\gamma)$ interface oriented parallel to the growth direction of ferrite (V2 type cementite marked using black arrows in Figure 7.3). Such an orientation of secondary cementite is also observed in the inverse bainite microstructure reported by Borgenstam *et al.*(Figure 5 in Ref. [39]) and Kolmskog *et al.*(Figure 16 in Ref. [40]). Based on our earlier proposal in Ref. [86], the inverse bainitic ferrite is likely supersaturated with carbon and the deviation from the ideal orientation at the interfaces (θ_m/α and $\alpha/\alpha'(\gamma)$) is the likely reason for the formation of the two orientations of θ_s. In order to verify the supersaturation of inverse bainitic ferrite ferrite, AES and APT were conducted and the extent of supersaturation is compared with the maximum carbon concentration in ferrite allowable under para-equilibrium conditions (0.09 at. %).

7.2.2 Carbon concentration measurements in inverse bainitic ferrite

In the alloy system under study, the inverse bainitic ferrite transformation at 500 ° C starts when the isothermal holding time is 3 minutes and longer. In order to verify the supersaturation on inverse bainitic ferrite, 3 minutes, 5 minutes, and 10 minutes isothermal hold samples have been analyzed.

Auger Electron Spectroscopy

Representative regions from where the Auger electron line scans were performed and the corresponding carbon profiles are shown in Figure 7.4. In the 3 minutes isothermal hold sample in Figure 7.4a the carbon concentration in ferrite is highest near the θ_m, and away from the θ_m/α phase boundary, the carbon concentration in ferrite drops to a minumum at the $\alpha/\alpha'(\gamma)$ phase boundary. In the case of the completely developed inverse bainite microstructure in Figure 7.4b, for the 5 minutes isothermal hold sample, the carbon concentration of ferrite is high near the θ_m/α phase boundary. Similar to the earlier stage of inverse bainitic ferrite formation in Figure 7.4a, the carbon concentration in ferrite decreases as the distance from the θ_m/α phase boundary increases and reaches a minimum at the $\alpha/\alpha'(\gamma)$ phase boundary. In the degenerated upper bainitic microstructure in Figure 7.4c for the 10 minutes isothermal hold sample, the carbon concentration in ferrite is the lowest in comparison to Figure 7.4a and Figure 7.4b. A gradient in carbon concentration is also not observed in the ferrite of the degenerated inverse bainite, i.e. no peak carbon concentration at the θ_s/α interface is detected. At all the stages of the evolution of inverse bainite microstructure, the carbon concentration at the $\alpha/\alpha'(\gamma)$ phase boundary is the lowest and the intensity of the C at the $\alpha/\alpha'(\gamma)$ phase boundary remains the same in all the stages of the microstructure evolution. Since the Auger Electron Spectroscopic measurements in Figure 7.4 provides the qualitative evidence for the likely supersaturation of inverse bainitic ferrite, quantitative carbon concentration in inverse bainitic ferrite at the θ_m/α phase boundary are measured by site-specific APT measurements in regions similar to ones shown in Figure 7.4a-c.

Atom Probe Tomography

Atom probe proximity histograms at the θ_m/α interface for the three thermal treatments are shown in Figure 7.5. It can be seen from Figure 7.5a that the carbon concentration is highest in the carbon enriched region (20 at. % - 23 at. %). This

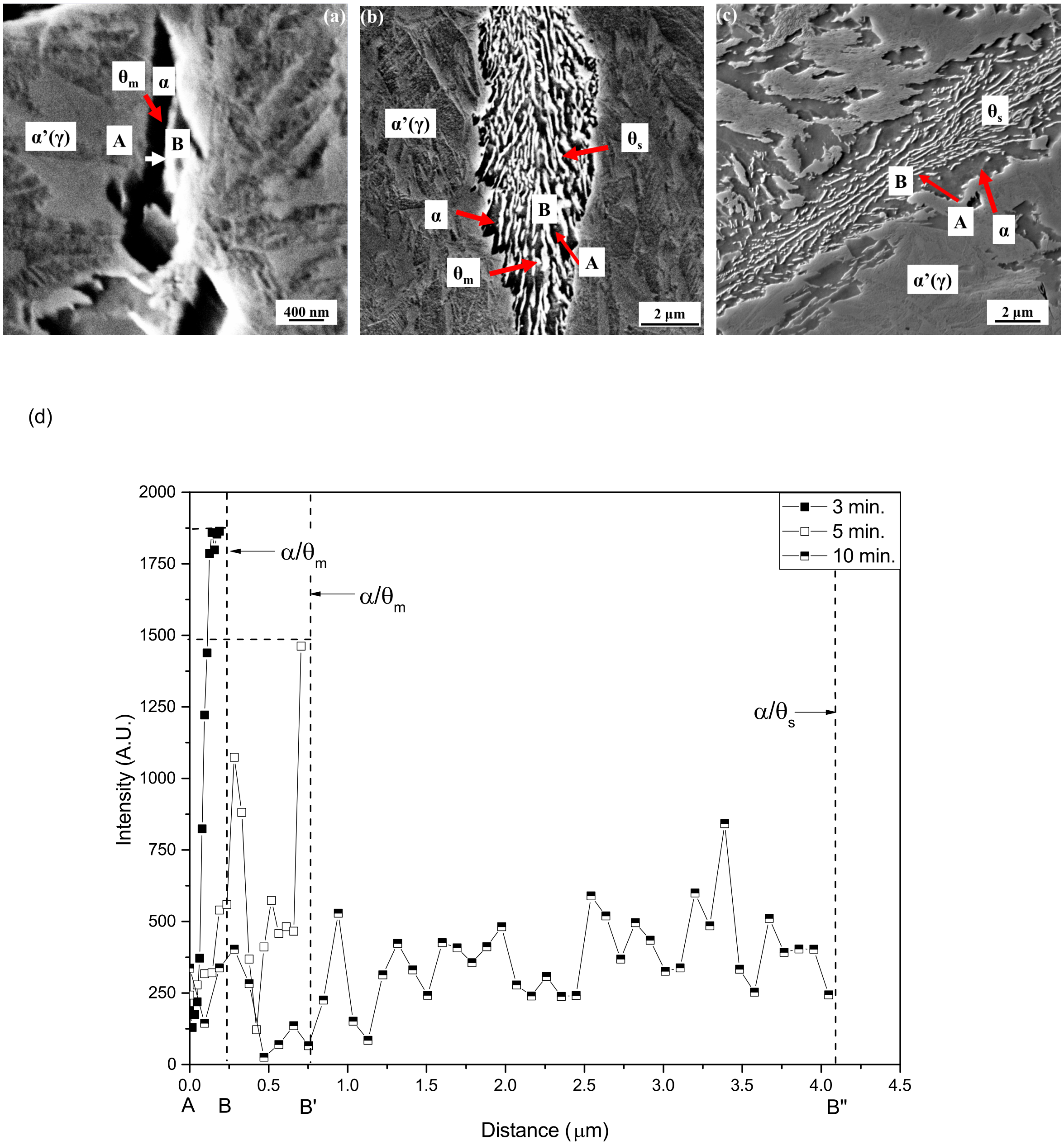

Figure 7.4: AES line scans for carbon concentration profiles within inverse bainitic ferrite. (a) 3 minutes isothermal hold sample, (b) 5 minutes isothermal hold samples, (c) 10 minutes isothermal hold sample. The scanning direction is marked by an arrow starting from point A to point B in (a), (b), and (c). In (d) the cementite/inverse bainitic ferrite phase boundary is marked using the dashed vertical lines.

carbon concentration indicates that the carbide can be identified as cementite [1], confirming our earlier observations using EBSD in Ref. [86]. Away from the θ_m/α interface, the carbon concentration drops drastically in the ferrite and reaches a constant value at 2 nm away from the interface. In order to visualize the carbon concentration variation within ferrite, magnified portions of the proximity histograms for the 3 minutes, 5 minutes, and 10 minutes isothermal hold samples are plotted in Figure 7.5b-d. Considering the carbon concentration away from growth front [115], the carbon concentration in ferrite in the 3 minutes and 5 minutes isothermal hold samples (Figure 7.5b and Figure 7.5c) is considerably higher than the para-equilibrium carbon concentration in ferrite (0.09 at. %). In the case of the 10 minutes isothermal hold sample, apart from few data points which show a relatively higher carbon concentration in inverse bainitic ferrite, the carbon concentration in ferrite is closer to the para-equilibrium carbon concentration. The average carbon concentration measured away from the growth front of ferrite is 0.519 at. % for the 3 minutes isothermal hold sample, 0.227 at. % for the 5 minutes isothermal hold sample, and 0.129 at. % for the 10 minutes isothermal hold sample. The carbon concentration measurements from APT thus provide a quantitative verification for the carbon supersaturation in inverse bainitic ferrite during the earlier stages of the inverse bainitic transformation as measured using the AES in Figure 7.4.

---

[1] Though the carbon concentration in cementite is 20 at. % which is lower than the ideal 25 at. % of carbon in cementite, similar carbon concentration anomaly in cementite is also observed by other researchers, as in Ref. [24].

(a)

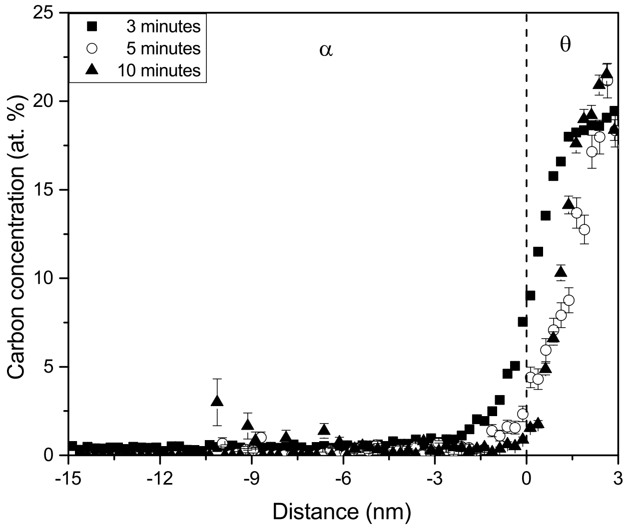
3 minutes
5 minutes
10 minutes
α
θ
Carbon concentration (at. %)
Distance (nm)
0
5
10
15
20
25
-15
-12
-9
-6
-3
0
3

(b)

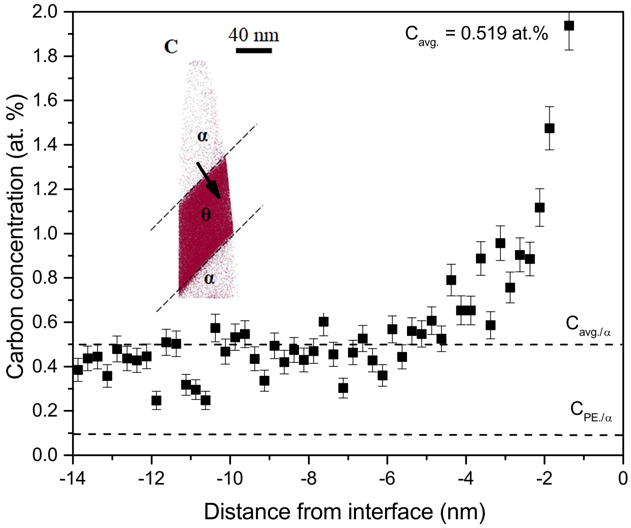
C
40 nm
α
θ
α
$C_{avg.}$ = 0.519 at.%
$C_{avg./α}$
$C_{PE./α}$
Carbon concentration (at. %)
Distance from interface (nm)
0.0
0.2
0.4
0.6
0.8
1.0
1.2
1.4
1.6
1.8
2.0
-14
-12
-10
-8
-6
-4
-2
0

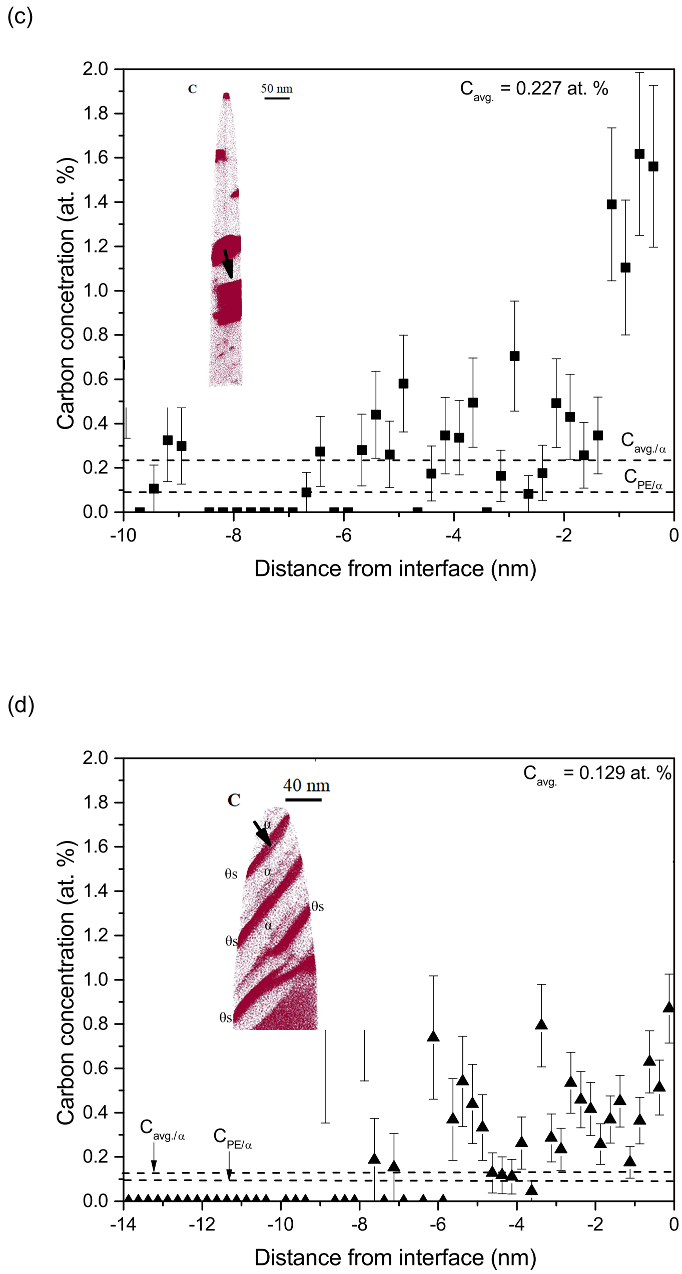

Figure 7.5: Proximity histograms at the θ_m/α for the three thermal treatments. (a) Complete proximity histogram for the samples, (b) Reduced proximity histogram showing the carbon concentration variation in ferrite away from the θ_m/α interface for the inverse bainitic ferrite formation stage, (c) Reduced proximity histogram showing the carbon concentration variation in ferrite away from the θ_m/α interface for the fully developed microstructure of inverse bainite, (d) Reduced proximity histogram showing the carbon concentration variation in ferrite away from the θ_m/α interface for the degenerate microstructure of inverse bainite. In (b), (c), and (d) the para-equilibrium carbon concentration in ferrite is indicated by a horizontal dashed line. C atom maps are attached in the inset for reference. In (b), (c), and (d) 0 represents the θ_m/α interface.

7.2.3 Crystallography of cementite/ferrite interface

The crystallography of the cementite/ferrite interface for the 1 minute isothermal hold sample (cementite midrib formation), 3 minute isothermal hold sample (inverse bainitic ferrite formation), 5 minute isothermal hold sample (secondary cementite formation), and the 10 minute isothermal hold sample (transition to upper bainite) were analyzed using HR-TEM and EBSD. The results are presented in Figure 7.6. For the 1 minute isothermal hold sample, it can be seen from Figure 7.6a that the cementite midrib is plate shaped. Electron diffraction patterns obtained by Fast Fourier Transform (FFT) of the HRTEM image in positions 1 and 2 confirm that the carbon enriched region in APT is cementite and the matrix is retained austenite. It can also be seen that Moire fringes are present at the interface between ferrite and cementite. The presence of Moire fringes suggest that the cementite/ferrite interface is not a flat plane, but rather a distorted one. Lattice images obtained by Inverse Fast Fourier Transform (IFFT) of the cementite/austenite interface (position 3) is shown in Figure 7.6a1 and Figure 7.6a2. It can be seen that atomic correspondence is lost at the cementite/austenite interface. The misfit of atoms at the cementite/austenite interface suggest that dislocations are generated at the interface. The absence of any extra-half planes, and the parallel nature of the Burgers vector to the dislocation line suggests that screw type dislocations are present along the interface. The dislocation line makes an angle of approximately 70° with respect to the austenite lattice.

For the 3 minute isothermal hold sample, it can be seen from Figure 7.6b that the cementite midrib is plate shaped. Electron diffraction patterns obtained by Fast Fourier Transform (FFT) of the HRTEM image in positions 1 and 2 confirm the formation of inverse bainitic ferrite surrounding the cementite midrib. It can also be seen that Moire fringes are present at the interface between ferrite and cementite. The presence of Moire fringes suggests that the cementite/ferrite interface is not a flat plane, but rather a distorted one. Lattice images obtained by Inverse Fast Fourier Transform (IFFT) of the cementite/ferrite interface (position 2) is shown in Figure 7.6b1 and Figure 7.6b2. It can be seen that atomic correspondence is lost at the cementite/ferrite interface, and atomic correspondence is maintained away from the interface. The misfit of atoms at the cementite/ferrite interface suggest that dislocations are generated at the interface. The absence of any extra-half planes, and the parallel nature of the Burgers vector to the dislocation line suggests that screw type dislocations are present along the interface. It should be noted that the angle which the dislocation line makes with respect to ferrite is reduced (50 °) in comparison to the 1 minute isothermal hold sample.

For the 5 minute isothermal hold sample, it can be seen from Figure 7.6c that the cementite midrib is plate shaped. Electron diffraction patterns obtained by Fast Fourier Transform (FFT) of the HRTEM image in positions 1 and 2 confirm the formation of inverse bainitic ferrite surrounding the cementite midrib. It can also be seen that Moire fringes are present at the interface between ferrite and cementite. The presence of moire fringes suggest that the cementite/ferrite interface is not a flat plane, but rather a distorted one. Lattice images obtained by Inverse Fast Fourier Transform (IFFT) of the cementite/ferrite interface (position 3) is shown in Figure 7.6c1 and Figure 7.6c2. It can be seen that atomic correspondence is lost at the cementite/ferrite interface, and atomic correspondence is maintained away from the interface. The misfit of atoms at the cementite/ferrite interface suggest that dislocations are generated at the interface. The absence of any extra-half planes, and the parallel nature of the Burgers vector to the dislocation line suggests that screw type dislocations are present along the interface. It should be noted that the angle which the dislocation line makes with respect to ferrite is reduced (14 °) in comparison to the 1 minute and 3 minute isothermal hold samples.

For the 10 minute isothermal hold sample, it can be seen from Figure 7.6d that the cementite midrib is plate shaped. Electron diffraction patterns obtained by Fast Fourier Transform (FFT) of the HRTEM image in positions 1 and 2 confirm the formation of inverse bainitic ferrite surrounding the cementite midrib. Unlike the 1 minute, 3 minutes, and the 5 minutes samples, no lattice distortion or Moire fringes are present at the interface. Lattice images obtained by Inverse Fast Fourier Transform (IFFT) of the cementite/ferrite interface is shown in Figure 7.6c1 and Figure 7.6c2. It can be seen that unlike the 1 minute, 3 minute and, 5 minute isothermal hold samples, in the 10 minute isothermal hold sample (i.e. when inverse bainite gets converted to upper bainite), atomic correspondence is maintained across the cementite/ferrite interface.

Based on the HRTEM analysis of the cementite/ferrite interface, it appears that the cementite/ferrite interface is distorted with the presence of dislocations when the transformation time is short, and when the transformation time is longer, crystallographic matching is achieved at the cementite/ferrite interface.

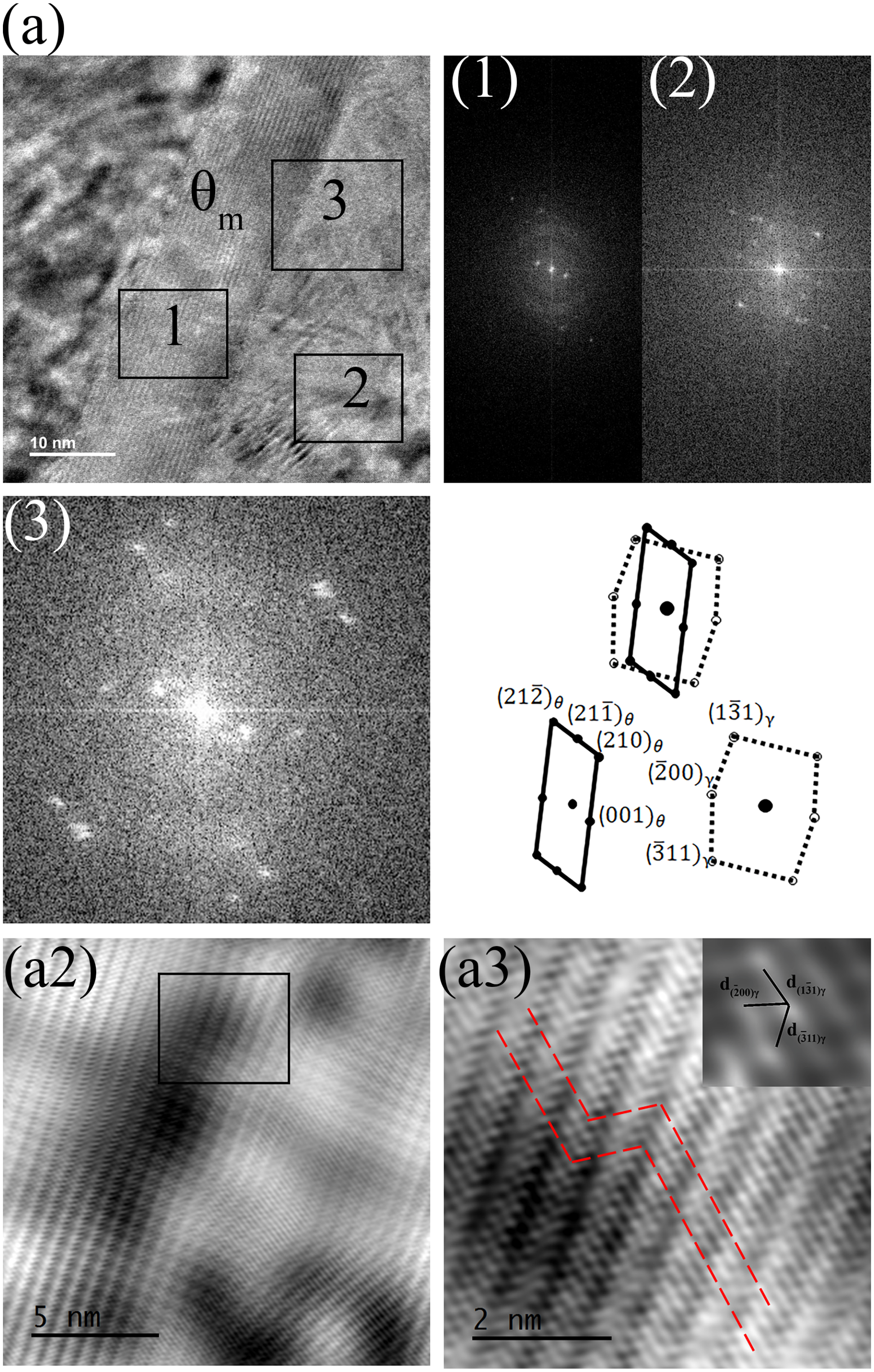
(a)
θm
3
1
2
10 nm
(1)
(2)
(3)
$(21\bar{2})_\theta$
$(21\bar{1})_\theta$
$(210)_\theta$
$(001)_\theta$
$(1\bar{3}1)_\gamma$
$(\bar{2}00)_\gamma$
$(\bar{3}11)_\gamma$
(a2)
5 nm
(a3)
$d_{(\bar{2}00)\gamma}$
$d_{(1\bar{3}1)\gamma}$
$d_{(\bar{3}11)\gamma}$
2 nm

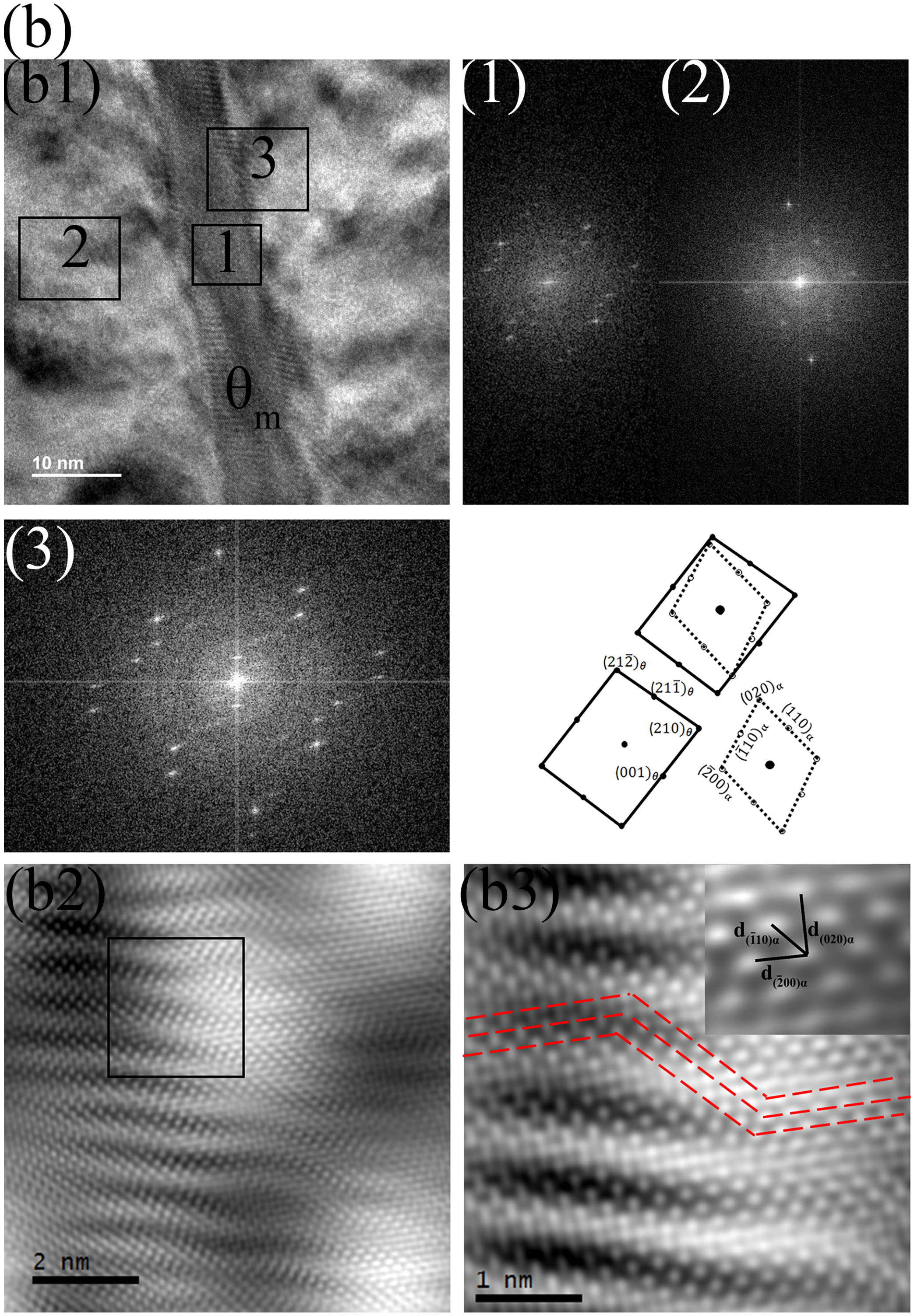
(b)
(b1)
3
2
1
θ_m
10 nm
(1)
(2)
(3)
$(21\bar{2})_\theta$
$(21\bar{1})_\theta$
$(210)_\theta$
$(001)_\theta$
$(020)_\alpha$
$(110)_\alpha$
$(\bar{1}10)_\alpha$
$(\bar{2}00)_\alpha$
(b2)
2 nm
(b3)
$d_{(\bar{1}10)\alpha}$
$d_{(020)\alpha}$
$d_{(\bar{2}00)\alpha}$
1 nm

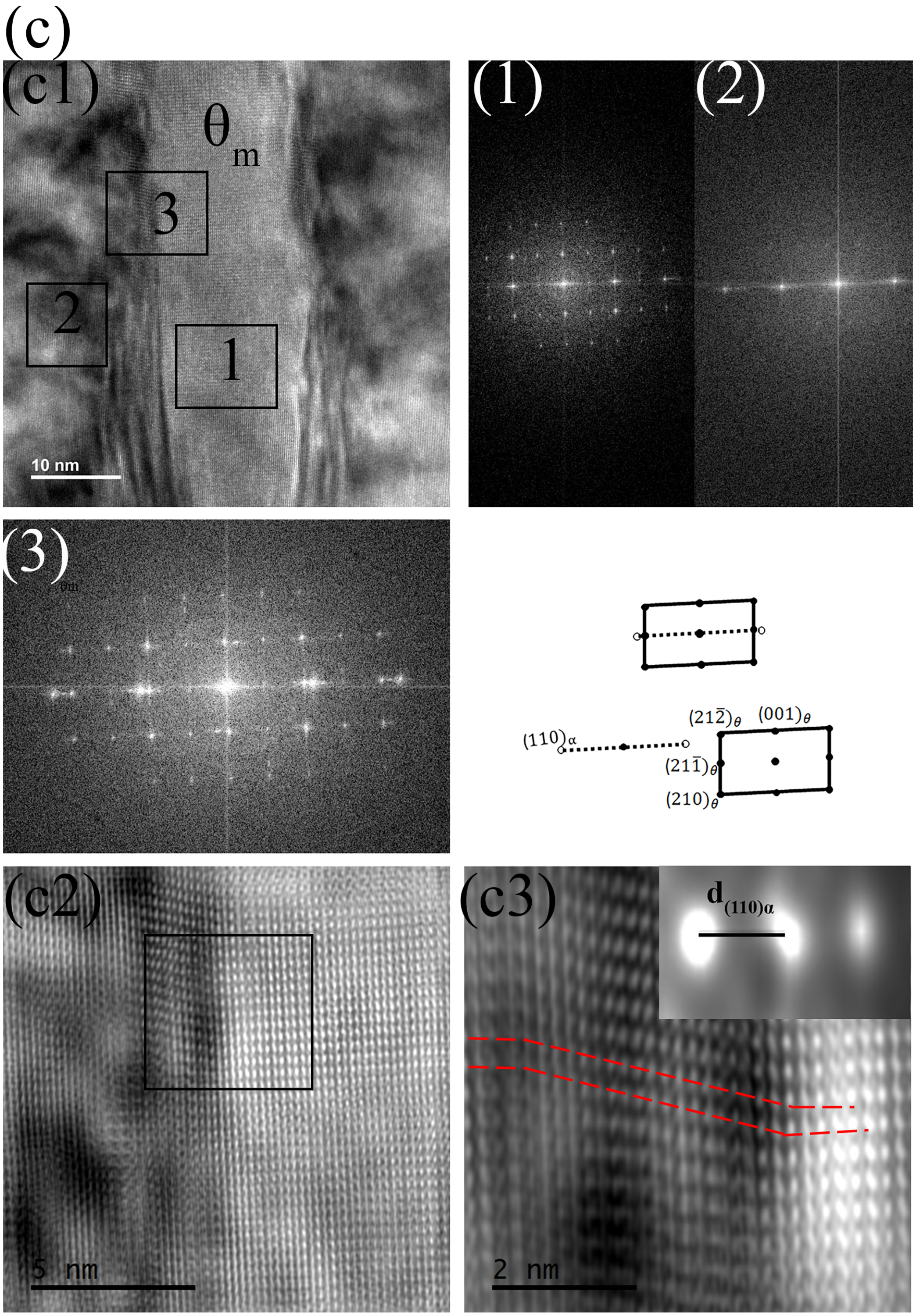
(c)
(c1)
θ_m
3
2
1
10 nm
(1)
(2)
(3)
$(110)_\alpha$
$(21\bar{2})_\theta$
$(001)_\theta$
$(21\bar{1})_\theta$
$(210)_\theta$
(c2)
5 nm
(c3)
$d_{(110)\alpha}$
2 nm

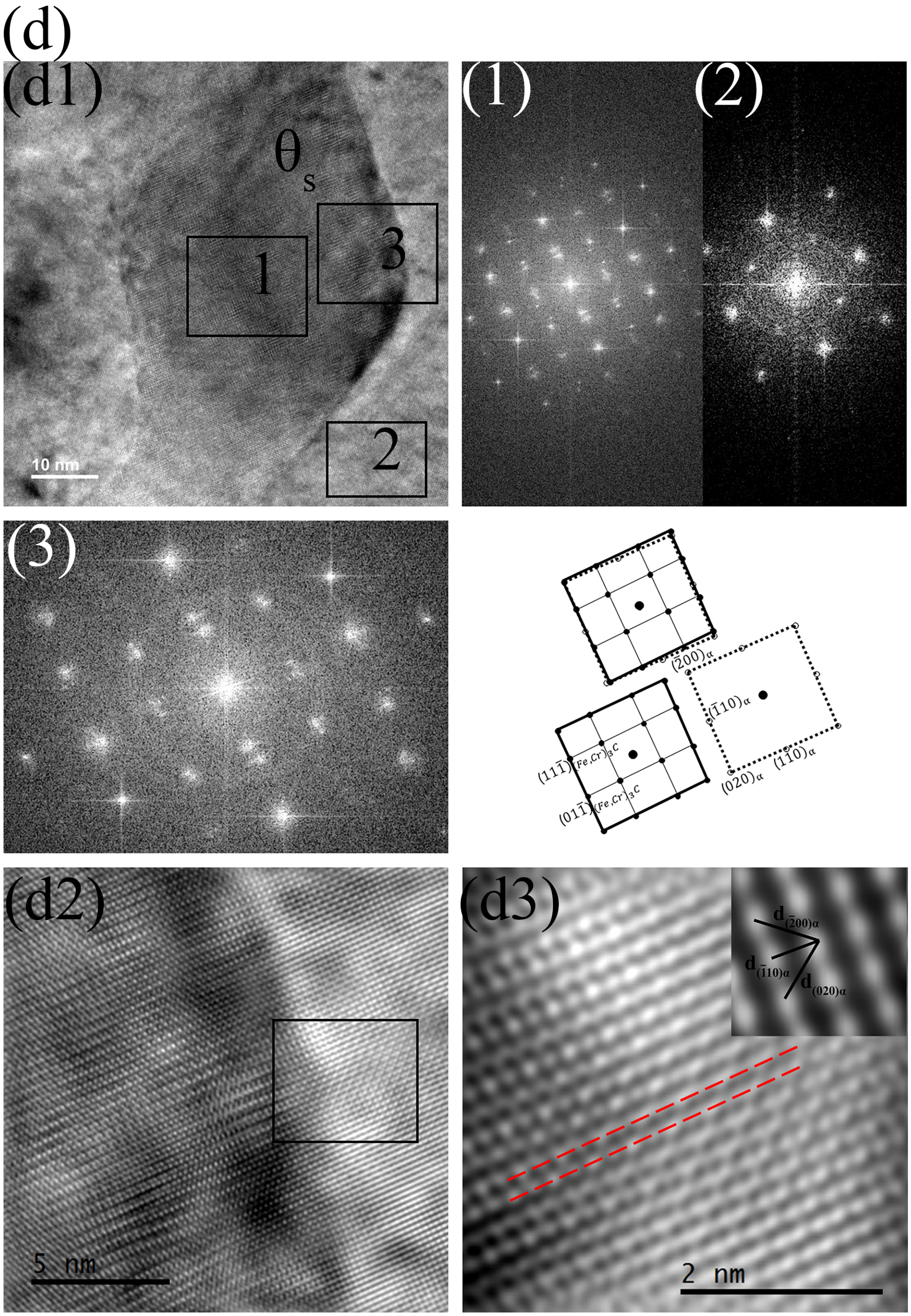

Figure 7.6: HRTEM FFT and IFFT analysis to image the lattice structure of the cementite/ferrite interface in (a) 1 minute isothermal hold sample, (b) 3 minute isothermal hold sample, (c) 5 minute isothermal hold sample, and (d) 10 minute isothermal hold sample.

It should also be noted that the $(21\bar{2})$ planes of cementite are crystallographically aligned with the (110) planes of inverse bainitic ferrite. To visualize the lattice incoherence at microscopic level, EBSD was carried out on the 1 minute, 3 minute, 5 minute, and the 10 minute isothermal hold samples. EBSD results are presented in Figure 7.7. Phase maps in Figure 7.7a - Figure 7.7d show the formation of cementite midrib (yellow colored phase) and inverse bainitic ferrite in martensitic matrix for various isothermal hold times. In Figure 7.7a - Figure 7.7d, the angular deviation between $(21\bar{2})$ cementite/ (110) ferrite phase boundaries are also plotted with varying levels of misorientation. The results of the angular deviation are statistically plotted in Figure 7.7e. It can be seen that the angular deviation of the phase boundary between the $(21\bar{2})$ cementite/ (110) ferrite is the highest in the case of the 1 minute heat treated sample, and the angular deviation gradually decreases to less than 5° in the 10 minute heat treated sample. The results from the EBSD further confirm the HRTEM lattice analysis and provide a statistical distribution of the angular deviation of the phase boundary between the $(21\bar{2})$ cementite/ (110) ferrite.

7.3 Discussion

7.3.1 Secondary cementite at θ_m/α interface - V1 type

It is clear from the AES and APT results in Figure 7.4 and Figure 7.5 that the inverse bainitic ferrite is supersaturated with carbon. The average carbon concentration measured using APT (0.519 at. %) is much higher than the para-equilibrium carbon content in ferrite (0.09 at. %). The reason for the carbon supersaturation of inverse bainitic ferrite, and the incubation period for the nucleation of V1 type secondary cementite within inverse bainitic ferrite need further discussion.

Comparing Figure 7.6 and Figure 7.7 it can be seen that the θ_m/α interface is semi-coherent with the presence of dislocations at the interface. From Figure 7.7, the angular deviation between the θ_m/α is the highest during the inverse bainitic ferrite formation (3 minutes isothermal hold) and the angular deviation gradually decreases once the secondary cementite nucleates. The presence of lattice misfit of the cementite/ferrite interface can be traced back to the nucleation of cementite from parent austenite. Zhang *et al.* [116] through *ab initio* simulation have found that when austenite transforms into cementite, a metastable intermediate structure (MIS) is formed at the interface, which serves as a link between austenite and cementite. The MIS which is few atomic layers wide and progresses with the growth of cemen-

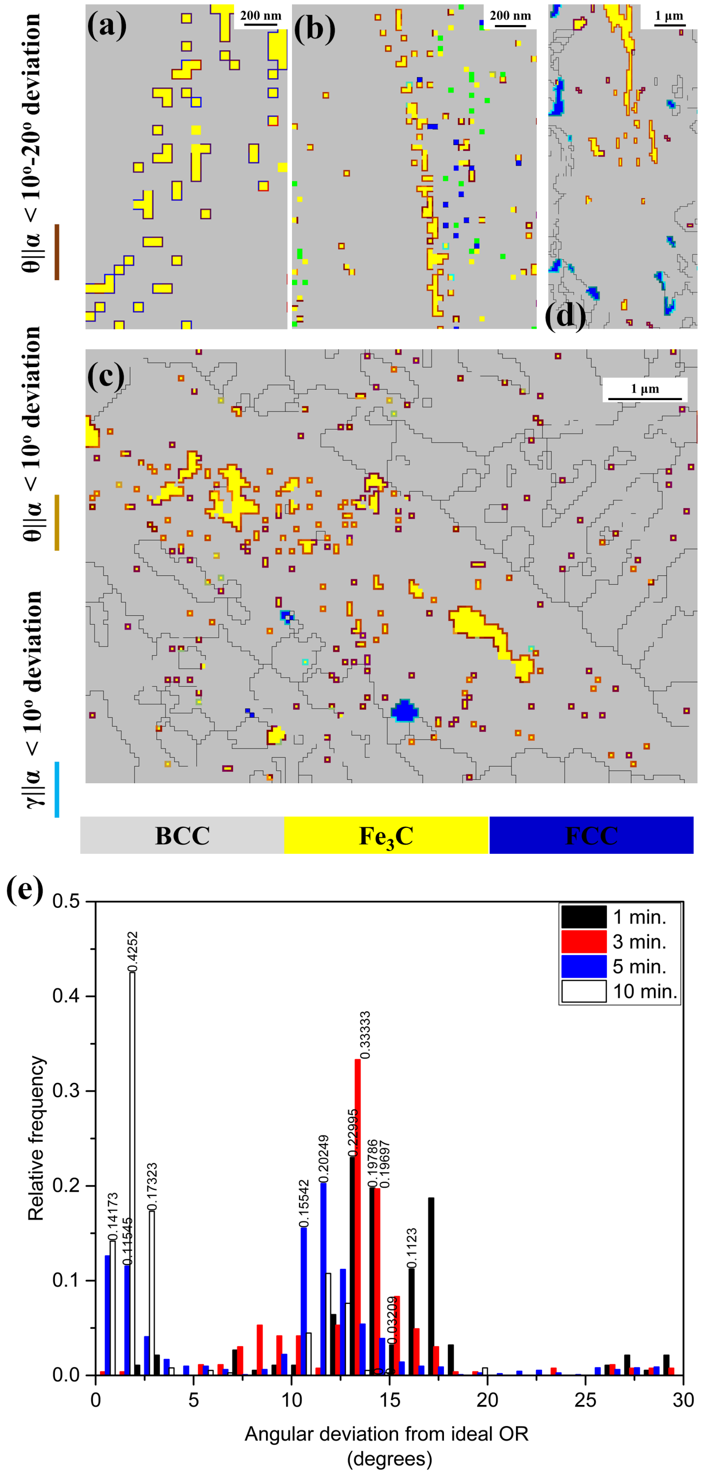

Figure 7.7: EBSD analysis of the change in angular deviation between the (21$\bar{2}$) θ_m/ (110) α with transformation time. (a)-(d) represents the phase map superimposed with (21$\bar{2}$) θ_m/ (110) α phase boundaries for different angular deviations. (e) Represents the statistical data of the angular deviation with the change in transformation time.

tite is formed as a result of orthorhombic distortion of austenite. The formation of MIS by interface reconstruction helps in minimizing the interfacial energy of the austenite/cementite interface. Zhang *et al.*have also shown that the MIS interface itself is semi-coherent, and complete coherence is achieved when carbon enriched MIS (when the carbon concentration in MIS is less than 18 at. % ferrite is stable, whereas when the carbon concentration in MIS is greater than 18 at. % cementite is stable) in ferrite transforms into cementite. Comparing the *ab-initio* results presented by Zhang *et al.*to the interface structure of cementite midrib and ferrite in Figure 7.6a, Figure 7.6b, and Figure 7.6c, it can be suggested that the lattice distortion observed at the interface is a MIS. Guziewski *et al.* [117, 118] have used atomistic modelling of the cementite/ferrite interface by including the MIS, and have shown existence of high dislocation density in the close vicinity of the MIS. Thus with the presence of high amounts of dislocations, MIS can act as a site for carbon accumulation during transformation, which is the likely reason for the carbon accumulation within inverse bainitic ferrite.

The next question to be answered is the presence of an incubation time for the nucleation of secondary cementite within inverse bainitic ferrite. Comparing the lattice images in Figure 7.6, it can be seen that the width of the MIS increases with the increase in transformation time (0.90 nm for Figure 7.6a, 1.5 nm for Figure 7.6b, and approx. 3 nm for Figure 7.6c). Correlating the MIS width obtained from HR-TEM images in Figure 7.6 to the quantitative carbon measurements in Figure 7.5, the atom probe interface can be sub-divided into θ_m/MIS interface, and the MIS/α interface as shown in Figure 7.8.

It can be seen from Figure 7.8 that the carbon concentration in MIS is well below the critical carbon concentration for MIS to θ transition for the 1 minute and the 3 minute isothermal hold samples (Figure 7.8a and Figure 7.8b). When the transformation time is increased, not only does the width of the MIS increase, but also the carbon concentration in the MIS is above the critical carbon concentration required for MIS to θ transition. This explains why V1 secondary cementite within inverse bainitic ferrite will only happen after 3 minute hold, and only happen in the MIS. The lattice distortion explains the angular nature of the orientation of V1 type secondary cementite.

(a)

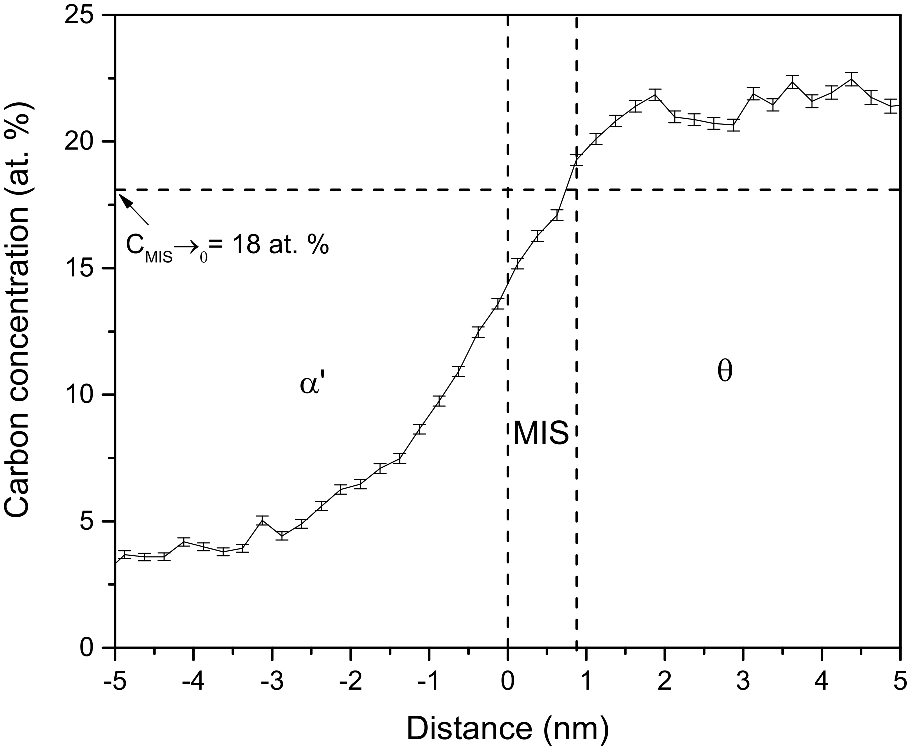
Carbon concentration (at. %)
Distance (nm)
25
20
15
10
5
0
-5
-4
-3
-2
-1
0
1
2
3
4
5
$C_{MIS}\rightarrow_{\theta}$= 18 at. %
α'
MIS
θ

(b)

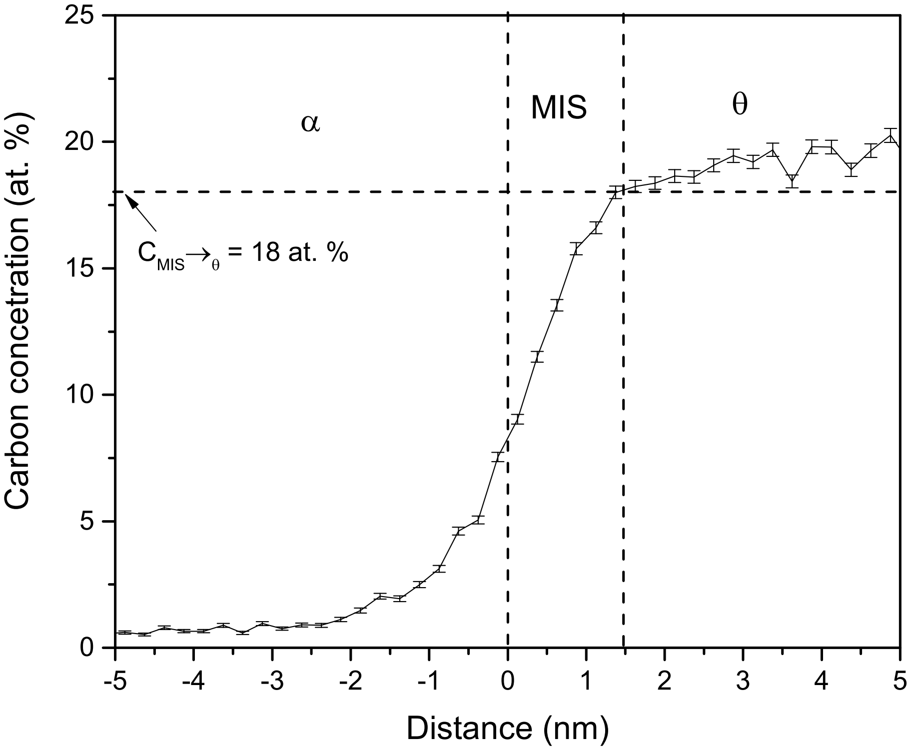
Carbon concetration (at. %)
Distance (nm)
25
20
15
10
5
0
-5
-4
-3
-2
-1
0
1
2
3
4
5
$C_{MIS}\rightarrow_{\theta}$ = 18 at. %
α
MIS
θ

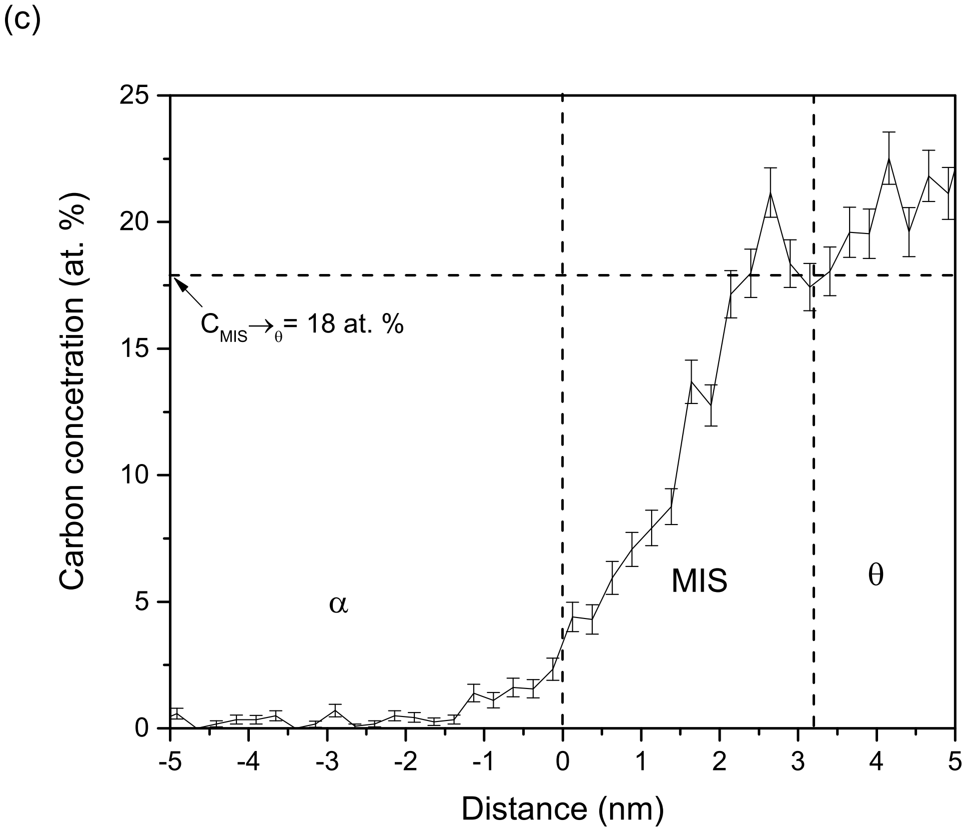

Figure 7.8: Delineation of θ_m/MIS interface and the MIS/α by correlating the MIS width measurements from Figure 7.6 to atom prob carbon concentration measurements from Figure 7.5. The critical carbon concentration above which MIS to θ transition is possible is marked by the horizontal dashed line.

7.3.2 Secondary cementite at $\alpha/\alpha'(\gamma)$ interface - V2 type

The AES results in Figure 7.4 show that the carbon concentration at the $\alpha/\alpha'(\gamma)$ interface is roughly the same for the different stages in bainite evolution. Considering the carbon content to be the measured carbon concentration of the ferrite during the 10 minutes isothermal hold (Figure 7.5d), no supersaturation of carbon of ferrite is observed at the $\alpha/\alpha'(\gamma)$ interface. The next question to be answered is the nucleation mechanism of the secondary cementite at the $\alpha/\alpha'(\gamma)$ interface which are oriented parallel to the inverse bainitic ferrite growth direction.

Once the inverse bainitic ferrite transformation starts, carbon atoms are rejected to parent austenite resulting in the growth of inverse bainitic ferrite. The local carbon concentration of austenite at the $\alpha/\alpha'(\gamma)$ interface can be predicted using the isothermal dilation curves using Equation (7.1) and Equation (7.2)

$$C_{i+1} = C_i - \frac{5.83}{(1-f_i)^2}(f_{i+1} - f_i) \tag{7.1}$$

and

$$C_{i+1} = \frac{\left[1 - \frac{1}{\left[\frac{(L_{i+1}-L_i)-B_i(f\gamma_{i+1}-f\gamma_i)}{A(f\gamma_i-f_i)} + \frac{1}{1-0.0146C_i}\right]}\right]}{0.0146} \tag{7.2}$$

The detailed derivation of Equation (7.1) and Equation (7.2) can be found in the appendix. The carbon concentration predicted from the dilation curves are compared with the kinetic model (proposed in our earlier work in Ref. [90]), and verified using experimental XRD and APT measurements. The local carbon concentration of austenite for the isothermal holding times considered in this study are tabulated in Table 7.1. It can be seen that the carbon concentration at the $\alpha/\alpha'(\gamma)$ interface increases continuously as the transformation progresses owing to the growth of inverse bainitic ferrite. The evolution of carbon concentration at the $\alpha/\alpha'(\gamma)$ interface along with the T_o curve is shown in Figure 7.9. In accordance with the classical Incomplete Transformation phenomenon of "conventional" bainite [34, 119], the transformation of ferrite must undergo a temporary halt (stasis) when the austenite carbon concentration reaches the carbon concentration predicted by T_o and the resumption of the ferrite transformation occurs by the precipitation of carbides at the $\alpha/\alpha'(\gamma)$ interface which will reduce the carbon concentration of austenite enabling the growth of ferrite. As reported by Bhadeshia and Edmonds [120], the partitioning of carbon into austenite, thereby inhibiting the growth of ferrite and the precipitation of carbides at the $\alpha/\alpha'(\gamma)$ interface are competing processes and the relative rates of

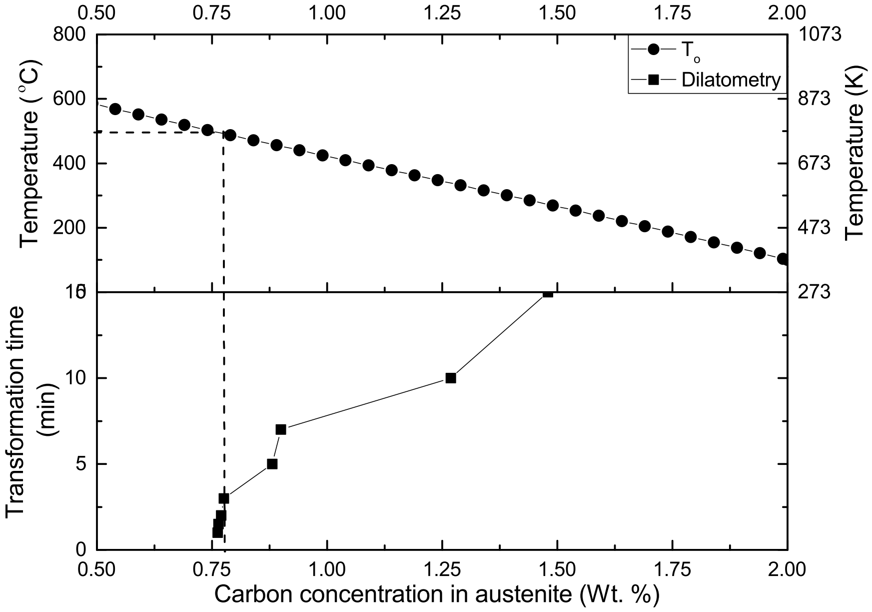

Figure 7.9: Variation in local carbon concentration in austenite predicted using Equation (7.1) and Equation (7.2) with transformation time and the T_o temperature with carbon concentration in austenite.

Table 7.1: Local carbon concentration of austenite at the austenite/ferrite interface

Transformation time (min.)	$C_{Dilatometry}$ (Wt. %)	$C_{Kinetic}$ (Wt. %)	C_{XRD} (Wt. %)	C_{APT} (Wt. %)
3	0.79	0.79	-	-
5	0.88	0.88	0.84	0.90±0.02
7	0.90	0.90	0.89	-
10	1.26	1.32	1.12	1.04±0.05

In the case of 3 minutes isothermal holding samples, the fraction of inverse bainite is too low to make accurate predictions of the local carbon concentration at the inverse bainite/austenite interface (denoted by - in Table) using XRD.
During the APT experiments, inverse bainitic ferrite/austenite interface was detected only in the 10 minutes isothermal holding sample. For the 3 minutes, 3 minutes, and 7 minutes isothermal holding samples, inverse bainitic ferrite/martensite was detected. Since the carbon concentration in martensite is inhomogeneous, no values are reported for the 3 minutes, 5 minutes, and 7 minutes isothermal holding samples.

each of the processes is dependent on the steel chemistry. Comparing the classical incomplete transformation phenomenon condition to the current set of experiments in Figure 7.9, incomplete transformation phenomenon should be observed after around 3 minutes into the transformation. Since the steel in the current study is high carbon without significant Si addition to inhibit carbide precipitation, carbide precipitation at the $\alpha/\alpha'(\gamma)$ interface will be the rate governing step. Therefore, we propose that the nucleation of secondary cementite in inverse bainite at the $\alpha/\alpha'(\gamma)$ interface is a consequence of the relative competition between the incomplete transformation phenomenon of ferrite and the resumption of ferrite transformation by the precipitation of cementite at the $\alpha/\alpha'(\gamma)$ interface; the higher carbon content and the absence of cementite inhibitors promote the precipitation of cementite at $\alpha/\alpha'(\gamma)$ interface without the observation of any stasis in the inverse bainitic ferrite transformation (Ref. Figure 7.2). Since the growth of bainitic ferrite occurs by ledge migration of ferrite [12], the precipitation of cementite occurs at the low energy planar faces of the bainitic ferrite [121–123] growing by the ledge mechanism resulting in cementite oriented parallel to the growth of the α ledge in parent austenite once the ferrite transformation has been resumed after the stasis [34, 119]. This explains the orientation of V2 type secondary cementite being parallel to the thickening direction of inverse bainitic ferrite.

7.4 Conclusions

Through APT, AES, and dilatometry, a mechanism for the nucleation of secondary cementite during inverse bainitic transformation has been proposed and the following conclusions were made:

1. Two different orientations of secondary cementite were observed during inverse bainitic transformation. Secondary cementite near the cementite midrib/ferrite interface oriented at an angle to the growth direction of ferrite (V1 type) and the second type of cementite at the ferrite/martensite(prior austenite) interface oriented parallel to the growth direction of ferrite (V2 type).

2. Through quantitative carbon concentration measurements within inverse bainitic ferrite, it was found that the inverse bainitic ferrite at the θ_m/α interface is supersaturated with carbon content much higher than the para-equilibrium carbon content. The segregation of carbon at the interface is likely due to the distortion at the θ_m/α interface and the semi-coherent θ_m/α interface formed as a result of the Metastable Intermediate Structure (MIS) formation. MIS acts as a sink for carbon atoms at the θ_m/α interface, and acts as nucleation sites for the V1 type secondary cementite.

3. The nucleation of secondary cementite in inverse bainite at the $\alpha/\alpha'(\gamma)$ interface is a consequence of the relative competition between the incomplete transformation phenomenon of ferrite and the resumption of ferrite transformation by the precipitation of cementite at the $\alpha/\alpha'(\gamma)$ interface; the higher carbon content and the absence of cementite inhibitors promote the precipitation of cementite at the $\alpha/\alpha'(\gamma)$ interface without the observation of any stasis in the inverse bainitic ferrite transformation.

Chapter 8

Dissolution of Cementite Midrib During Inverse Bainitic Transformation

8.1 Introduction

One of the findings of the microstructure evolution during inverse bainite transformation in Chapter 4 which adds to the transformation schematic proposed by Kinsman and Aaronson [46] is the dissolution of cementite midrib of inverse bainite (Stage IV of the transformation) when the transformation time is increased (refer Chapter 4) or when the temperature is close to the inverse bainite finish temperature (refer Chapter 5). This behavior is further supported by the micrograph reported in Ref. [39] for a Fe-0.82 wt. % C steel, where the transformation was conducted near the inverse bainite finish temperature. Apart from the transformation temperature being close to the inverse bainite finish temperature, the other characteristic signature which identifies the microstructure to be inverse bainite is the presence of carbides which are oriented parallel to the ferrite/martensite(prior austenite) interface Figure 8.1.

This chapter focuses on presenting 3D microstructural evidence for cementite midrib dissolution during inverse bainite transformation (refer Chapter 4) using Atom Probe Tomography (APT). It is found that the dissolution of the cementite midrib starts when then secondary carbides nucleate in a Para-Equilibrium kinetics within inverse bainitic ferrite. When the transformation time is increased further, the secondary carbides grow at the expense of cementite midrib resulting in solute transport from cementite midrib to the secondary carbides. The location of the prior cementite

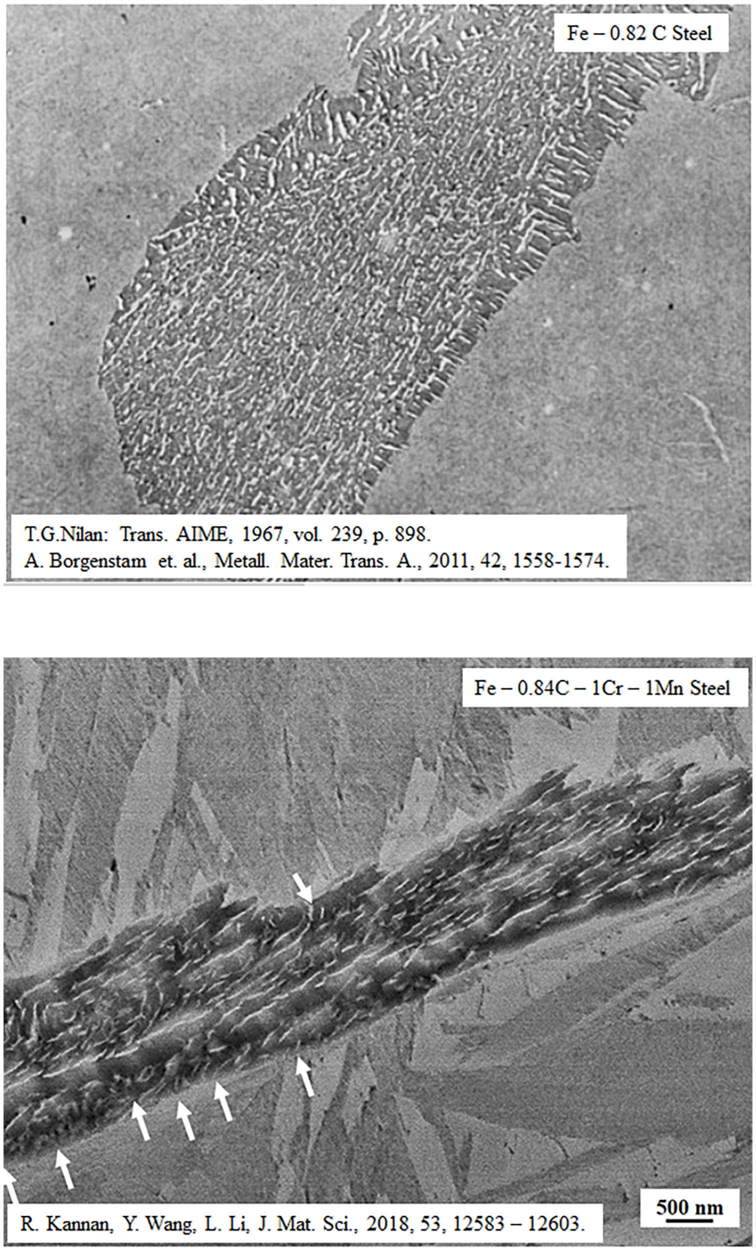

T.G.Nilan: Trans. AIME, 1967, vol. 239, p. 898.
A. Borgenstam et. al., Metall. Mater. Trans. A., 2011, 42, 1558-1574.

R. Kannan, Y. Wang, L. Li, J. Mat. Sci., 2018, 53, 12583 – 12603.

Figure 8.1: Formation of degenerated microstructure of inverse bainite obtained by isothermal transformation near inverse bainite finish temperature. Microstructure on the top taken from Borgenstam

midrib in the degenerated microstructure can be identified as solute enriched region within inverse bainitic ferrite.

8.2 Results

Figure 8.2 shows the representative degenerate microstructure of inverse bainite obtained after 10 minutes isothermal hold, the change in cementite size within inverse bainite, and the cementite fraction with the progress of transformation. It can be seen from Figure 8.2a that the microstructure is that of a typical upper bainite with ferrite and inter-lath cementite. It should be noted that the characteristic cementite midrib of inverse bainite is not discernible. Atom probe needles were extracted from similar location as shown in Figure 8.2a. From Figure 8.2b and Figure 8.2c, it can be seen that the cementite midrib size increases initially and then the size of the cementite midrib starts to decrease when the transformation time in increased beyond 3 minutes. The size of the secondary carbides increases continuously. The fraction of carbides within inverse bainite increases initially and then remains a constant when the transformation time is increased. Beyond 5-7 minutes, the characteristic cementite midrib of inverse bainite starts to dissolve and the inverse bainite microstructure gets converted to conventional upper bainite.

Figure 8.3 shows the carbon concentration proximity histograms across the inverse bainitic ferrite/cementite interface for various transformation times. It can be seen that the cementite midrib has a carbon level close to the stoichiometric concentration of carbon (25 at. %). When the transformation time is increased, the concentration of carbon in cementite decreases. It should also be noted that the carbon concentration of cementite at the ferrite/cementite interface also decreases with the increase in transformation time.

Figure 8.4a1 represents the 10 at.% iso-concentration surface along with C, Si, Cr, Mn and ions. Secondary cementite/ferrite interfaces are observed, apart from the cementite/ferrite interface, Mn-Cr-C enriched region is observed (marked by red arrow in Figure 8.4a1). Proximity histogram across one of the cementite/ferrite interface is shown in Figure 8.4b. It can be seen that the secondary cementite particle has a carbon concentration of around 18 at.%. Cr/Mn/Si partition occurs at the ferrite/secondary cementite interface. Apart from the C concentration spike from cementite, a small concentration spike around 3 nm wide is observed at 10 nm away from the secondary cementite peak. Figure 8.4c represents the magnified portion of the concentration spike away from the secondary cementite in Figure 8.4b. It can

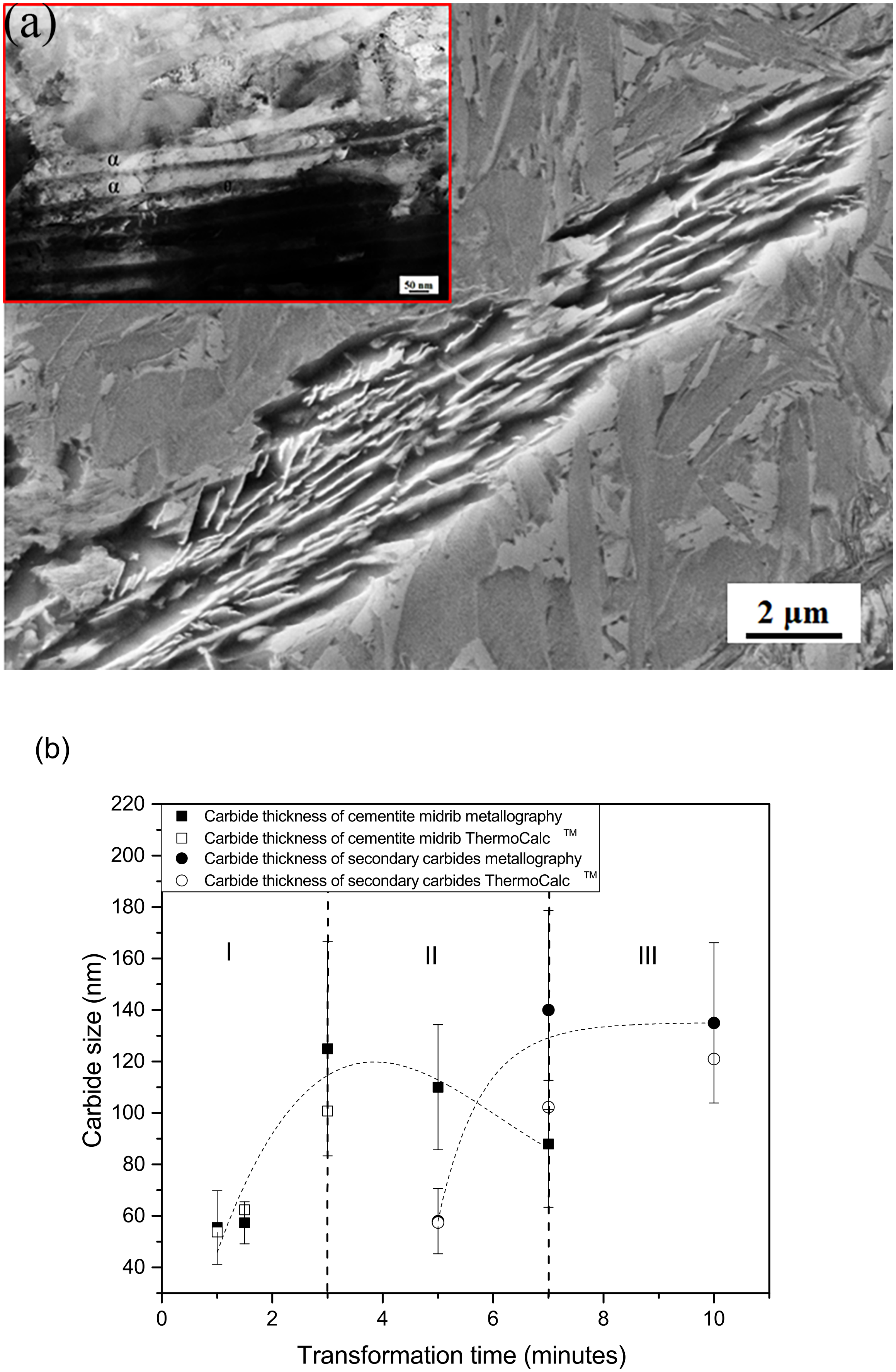
(a)
α
α
θ
50 nm
2 µm
(b)
■ Carbide thickness of cementite midrib metallography
□ Carbide thickness of cementite midrib ThermoCalc TM
● Carbide thickness of secondary carbides metallography
○ Carbide thickness of secondary carbides ThermoCalc TM
I
II
III
Carbide size (nm)
220
200
180
160
140
120
100
80
60
40
0
2
4
6
8
10
Transformation time (minutes)

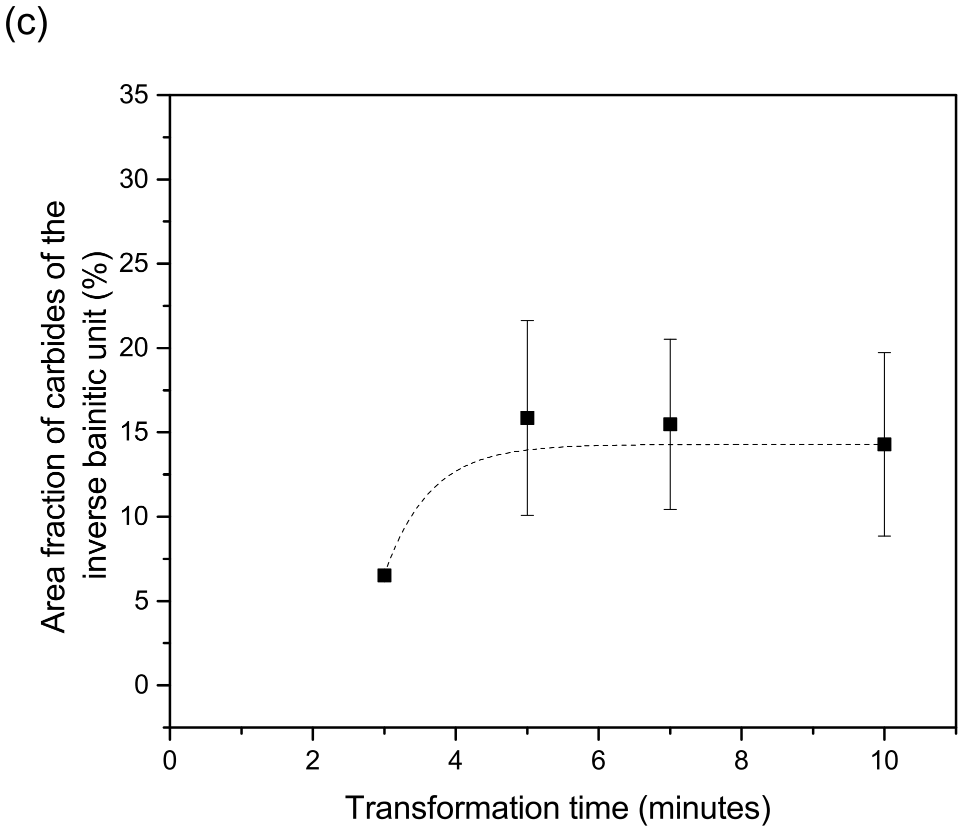

Figure 8.2: Representative degenerate microstructure of inverse bainite formed after 10 minutes isothermal hold (a). The inset in (a) shows the bright field transmission image showing ferrite and inter-lath carbides. Change in cementite size (b) and fraction (c) with the transformation time. (b) and (c) were published in our earlier article Ref. [86]

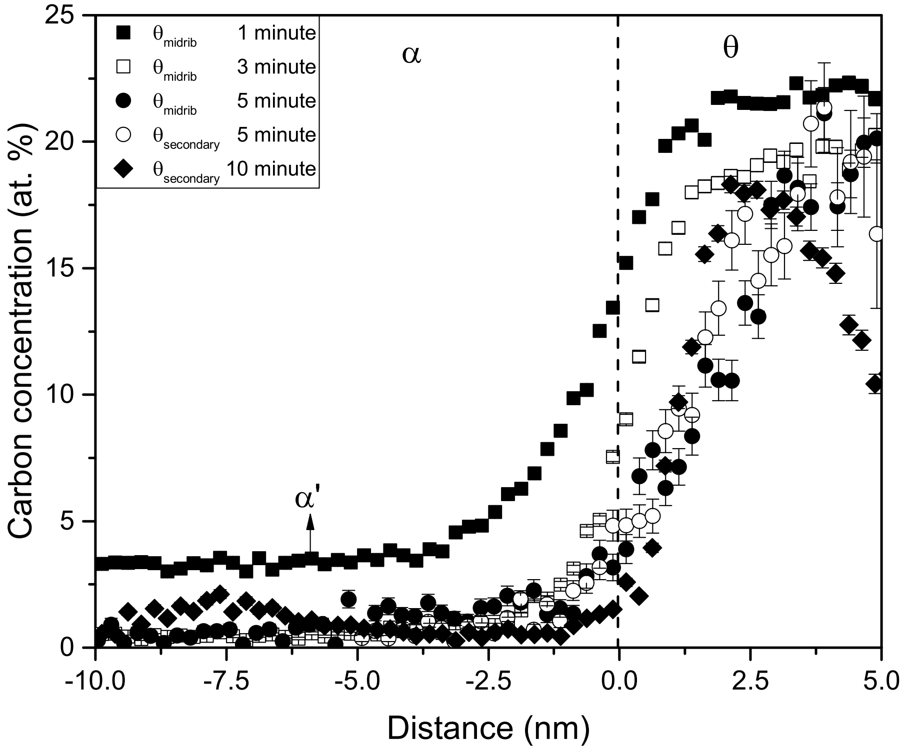

Figure 8.3: Carbon concentration profiles across the ferrite/cementite interface for various transformation times.

be seen that the concentration spike is enriched in Mn, Cr, and C as represented by the red arrow in Figure 8.4a1. The three dimensional images of the interfaces in Figure 8.4a indicate that the Mn-Cr-C enriched region appears to be an interface that has undergone dissolution. From Figure 8.4c it can also been seen that the C concentration at the interface between the concentration spike and ferrite is equal to the carbon concentration of the ferrite far away from the interface.

8.3 Discussion

Based on the quantitative carbon concentration estimation in cementite, the APT results of the degenerated microstructure in Figure 8.4, the carbide size and carbide fraction measurements in Figure 8.2, we propose the following mechanism for the dissolution of cementite midrib when the inverse bainitic transformation time is increased. We have shown that the secondary carbides within inverse bainitic ferrite follows a PE growth kinetics, and the cementite midrib growth occurs by Negligible Partitioning Local Equilibrium (NPLE) with a Si concentration spike at the interface, the concentration of Si at the ferrite/cementite midrib interface is higher in comparison with the concentration of Si at the ferrite/secondary cementite interface (Refer Chapter 6). Si has been reported as an element which increases the activity of C at the interface [124], and combined with the lower carbon concentration of secondary cementite particles, a chemical potential gradient is created between the cementite midrib and the secondary cementite particle. This chemical potential gradient drives in the migration of C from high carbon cementite/ferrite interface to the low carbon secondary cementite/ferrite interface. Thus the PE nucleation of secondary cementite in inverse bainitic ferrite starts the dissolution of cementite midrib. This is evident in the carbide size measurements in Figure 8.2, where the cementite midrib size drops when the transformation time is increased beyond 3 minutes.

To determine if the time required for nullifying the carbon flux between the cementite midrib and the secondary cementite is the same as the time required for the degenerate microstructure formation, the diffusion equation in combination with Zener's linear approximation for the interface concentration [111], and the linear relationship between cementite thickness and the carbon concentration in cementite (Ref. Li *et al.* [125]) was used. The carbon flux between the cementite midrib and secondary carbides get nullified after about 3 minutes (6 minutes total transformation time), the carbon content in cementite midrib decreases from about 25 at. % to 18 at. %, and the carbide size drops from 120 nm to around 80 nm (refer Figure 8.5).

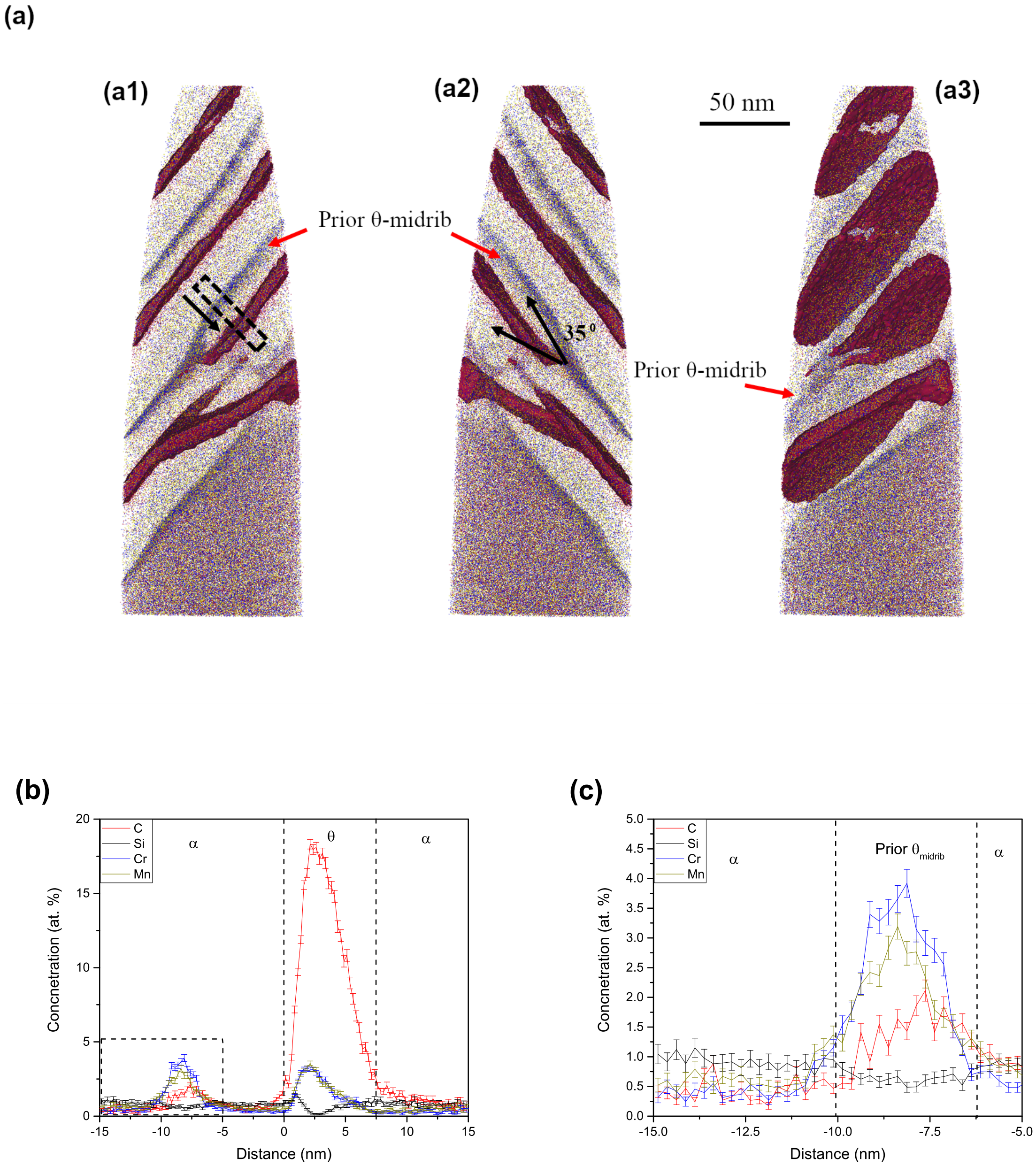

Figure 8.4: 3DAP reconstructions of the 10 minute isothermal hold sample containing the degenerated microstructure of inverse bainite. (a) 10 at.% iso-concentration surfaces with all ions superimposed indicating the cementite-ferrite interfaces. (b) Proximity histogram across one of the ferrite/cementite interface shown by box in (a). (c) Magnified portion of the proximity histogram corresponding to the rectangular region in (b).

The results of the carbide size and the carbon flux from diffusion calculation using the atom probe data as inputs agree well with our earlier carbide size measurements in Figure 8.2, providing confidence in our measurements. Thus once the carbon flux between the cementite midrib and secondary cementite is nullified in 6 minutes in to the transformation.

The next question which needs to be addressed is the driving force for the dissolution of cementite midrib when the transformation time is further increased. It can be seen from Figure 8.2 that when the transformation time is increased beyond 6 minutes, the secondary carbides are coarser than the cementite midrib. By Gibbs-Thomson effect [126], the coarser secondary cementite will start to grow at the expense of cementite midrib by the transport of solute atoms from the smaller cementite midrib to the coarser secondary cementite particles. This results in the Cr/Mn enrichment in the secondary cementite (Ref. Figure 8.4b). The dissolution of cementite midrib can progress only until the solute concentration at the interface is greater than the matrix. When the concentration of the cementite midrib/ferrite interface becomes equal to the matrix concentration, no more dissolution or coarsening will occur [127]. Since C has a higher diffusivity than the substitutional solutes, the C concentration at the cementite midrib/ferrite interface will be the rate determining step. Thus, once all the C in the cementite midrib has diffused away and the C concentration at the ferrite/cementite midrib interface has reached the matrix concentration, no more dissolution or coarsening will occur. At this moment, the substitutional solutes which have a slower diffusivity than carbon must be retained in the prior cementite location (now ferrite). Thus, a carbon/substitutional solute enriched region in ferrite must be observed, which can provide an indication of the location of prior cementite midrib in the degenerated microstructure. This explains the Mn-Cr-C enriched region in Figure 8.4a. The Mn-Cr-C rich region being the prior cementite midrib is further supported by the sympathetic nucleation of secondary cementite at an angle of 35° to the interface Mn-Cr-C enriched region (55° to the growth direction of ferrite [86]). The mechanisms involved in the dissolution of cementite midrib of inverse bainite are schematically represented in Figure 8.5 along with the experimental measurements to support the proposed mechanism.

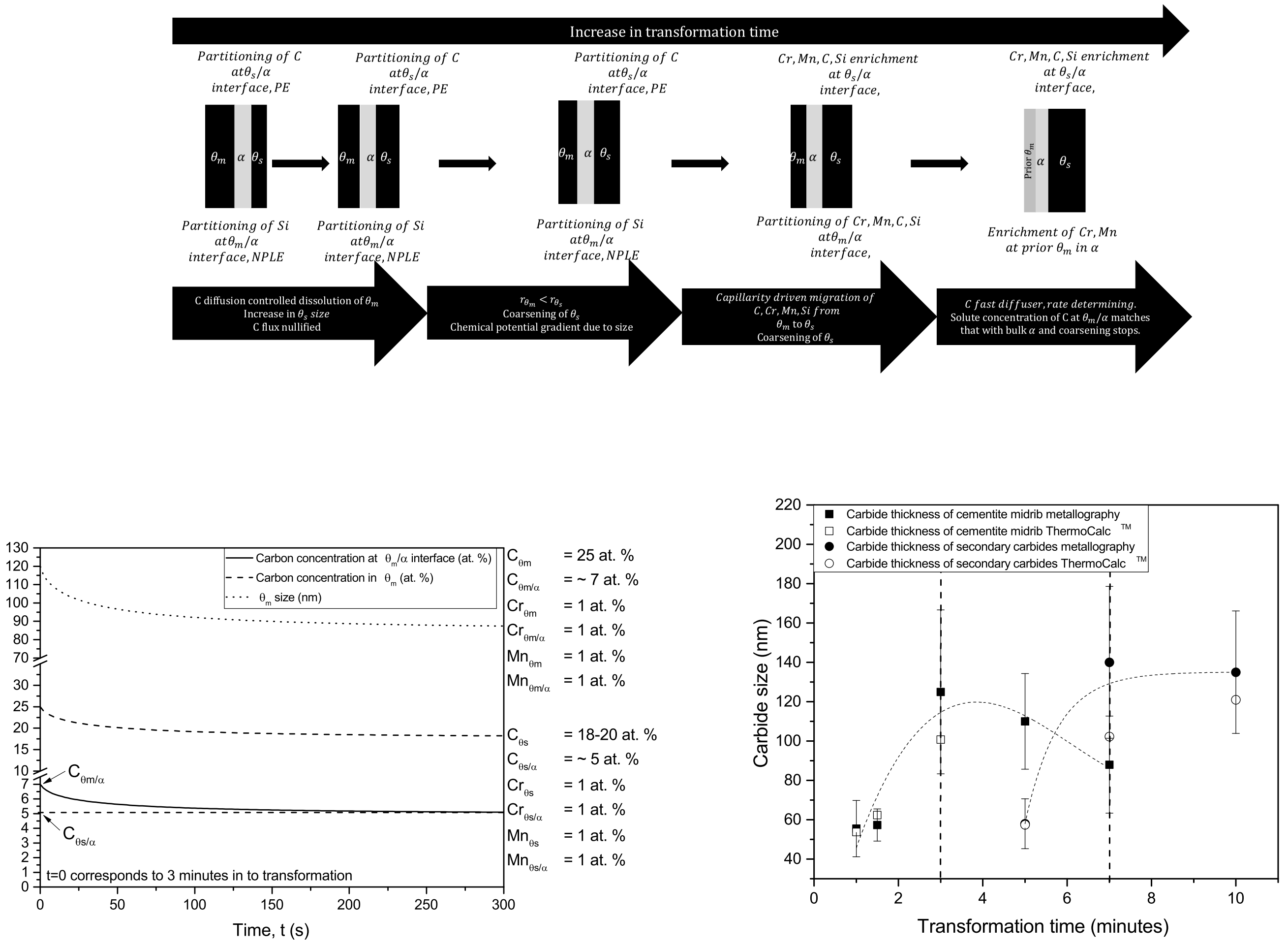

Figure 8.5: Schematic of mechanisms involved in the dissolution of cementite midrib of inverse bainite. The graphs in the bottom represent experimental diffusion calculations and the cementite size measurements.

8.4 Conclusions

In summary, a 3D microstructural evidence for cementite midrib dissolution during inverse bainite transformation is presented using Atom Probe Tomography (APT), and a mechanism for cementite midrib dissolution is proposed. The results indicate that the cementite midrib dissolution starts because of the C diffusion flux between the cementite midrib and secondary cementite. The carbon diffusion flux is caused by the NPLE growth kinetics of cementite midrib, whereas secondary cementite growth in ferrite follows a PE kinetics. By the time the C diffusion flux is nullified, the secondary carbides are coarser than the cementite midrib, and by Gibbs-Thomson effect secondary carbides grow at the expense of cementite midrib. This results in transport of solutes from the cementite midrib to the secondary cementite. This process continues until the carbon concentration at the cementite midrib/ferrite interface reaches the matrix ferrite carbon concentration. The location of the cementite midrib in the degenerated microstructure can be identified as a solute enriched region in ferrite. Further detailed investigation is needed to reveal the true nature as to why an unstable secondary cementite (forming by a PE mechanism) grows at the expense of stable cementite midrib (forming by a NPLE mechanism).

Chapter 9

Summary and Future work

9.1 Mechanism of inverse bainitic transformation in high carbon steels

Fundamental understanding of bainitic microstructures is a key element in the understanding of the bainite transformation. Little work has been made over the years to verify the existence of inverse bainite although its existence is of great importance for understanding of the eutectoid decomposition of austenite. Much of the information available in the literature are based on etched 2D sections. The aim of this thesis is to increase the understanding of the physical background of the inverse bainite transformation using both advanced characterization techniques and incorporating computational thermodynamic models. The key transformation behavior of inverse bainite presented in the current work has been compared with the other work available in the literature, which provides validity of the current work to be applicable to other high carbon steel systems. Based on the work carried out in the current thesis, a new phase transformation mechanism is proposed for inverse bainitic transformation in high carbon steels, and the following major conclusions can be drawn:

1. Through electron and atomic level characterization techniques, it was found that Inverse bainite transformation proceeds by formation of cementite midrib from parent austenite through NPLE kinetics as the first stage of transformation. During the second stage, inverse bainitic ferrite nucleation occurs in a PE mode, and when the transformation time is increased, there is a transition in kinetics from PE to NPLE. Interface velocity calculations showed that a deviation from PE occurs when the carbon concentration of the austenite at the interface reaches the bulk carbon concentration, by when the velocity of the interface

drops below the critical velocity required for substitutional solute diffusion.

2. Two different orientations of secondary carbides were observed to nucleate through PE kinetics within inverse bainitic ferrite during the third stage of the transformation. Firstly the carbides near the cementite midrib/ferrite interface oriented at 55° to the growth direction of ferrite (V1 type) and the second type of carbides at the ferrite/martensite(prior austenite) interface oriented parallel to the growth direction of ferrite (V2 type). Through carbon concentration measurements within inverse bainitic ferrite, it was found that the inverse bainitic ferrite at the θ_m/α interface is supersaturated with carbon content much higher than the para-equilibrium carbon content. The segregation of carbon at the interface is likely due to the distortion at the θ_m/α interface and the incoherent θ_m/α interface. Carbon segregated θ_m/α interface acts as nucleation sites for the V1 type secondary carbides. The nucleation of secondary carbides in inverse bainite at the $\alpha/\alpha'(\gamma)$ interface is a consequence of the relative competition between the incomplete transformation phenomenon of ferrite and the resumption of ferrite transformation by the precipitation of carbides at the $\alpha/\alpha'(\gamma)$ interface, the higher carbon content and the absence of carbide inhibitors promote the precipitation of carbides at $\alpha/\alpha'(\gamma)$ interface without the observation of any stasis in the inverse bainitic ferrite transformation.

3. When the transformation time is sufficiently long, inverse bainite microstructure becomes degenerated to be conventional upper bainite, which is the fourth stage of the transformation. It was found that the cementite midrib dissolution starts because of the C diffusion flux between the cementite midrib and secondary cementite. The carbon diffusion flux is caused by the NPLE growth kinetics of cementite midrib, whereas secondary cementite growth in ferrite follows a PE kinetics. By the time the C diffusion flux is nullified, the secondary carbides are coarser than the cementite midrib, and by Gibb's Thomson effect secondary carbides grow at the expense of cementite midrib. This results in transport of solutes from the cementite midrib to the secondary cementite. This process continues until the carbon concentration at the cementite midrib/ferrite interface reaches the matrix ferrite carbon concentration. The location of the cementite midrib in the degenerated microstructure can be identified as a solute enriched region in ferrite.

4. Using the principles of driving force for the onset of nucleation of cementite and ferrite from parent austenite, Hultgren extrapolation of A_{e3} and A_{cm} phase

boundaries, and the molar Gibbs energy change for austenite to ferrite a thermodynamic nucleation model is developed for inverse bainitic transformation, which fairly predicts the borderline between 'conventional' bainite' and 'inverse bainite' in the Fe-C system, and provide a physical explanation for the thermodynamics of nucleation during the transformation.

The results of the work are summarized as transformation characteristics exhibited by inverse bainite, in comparison with conventional bainite/Widmanstӓten ferrite, along with the tools used to characterize the transformation characteristic in Table 9.1.

9.2 Future work

The work presented in this thesis is just an initial step towards understanding the eutectoid decomposition of austenite to inverse bainite. Future challenges related to this thesis that lie ahead are of course many and most important, and further research in the following aspects is needed to better understand the transformation:

1. Though low amounts of Si does not alter the thermodynamics of nucleation during inverse bainitic transformation, the effect of Si on the transformation needs to be studied in detail to better understand the transformation. Especially the nucleation of cementite midrib a the γ/γ grain boundaries. The results presented here shows a strong non-equilibrium segregation of trace elements at the prior austenite grain boundaries, characterizing the grain boundary segregation during austenitization will prove useful in better understanding the nucleation of cementite midrib at prior austenite grain boundaries.

2. The absence of partitioning of Cr and Mn during the initial stages of cementite midrib formation and the presence of Si concentration spike was the reason for proposing an NPLE type of growth mechanism for cementite midrib. However, it is possible that the cementite midrib might have formed by a pure PE type mechanism during nucleation. Further analysis using in-situ techniques for understanding the cementite midrib nucleation will prove useful in proving the hypothesis that the cementite midrib might have formed by a pure PE type of reaction.

3. The dissolution mechanism of the cementite midrib presented in this work is a proposal, further detailed investigation is needed to better answer the question

as to why the near stoichiometric (stable) cementite midrib dissolves at the expense of non-stoichiometric (relatively unstable) secondary cementite particles.

4. The effect of prior austenite grain size, and the cooling rate to the isothermal holding temperature needs to be studied to better understand the kinetics of nucleation and growth during eutectoid decomposition of austenite to inverse bainite.

5. Computational modeling of the degenerate microstructure formation using DICTRA will prove useful in better understanding the mechanism of conversion of inverse bainite to upper bainite.

Table 9.1: Key transformation characteristics of conventional bainite and Widmanstätten ferrite compared with inverse bainite (blue font) from the current work along with the characterization tools used to provide the supporting evidences. ✓ represents consistency of the comment, × represents inconsistency, and ● represents the case where the comment is sometimes consistent.

Characteristics	Upper bainite	Lower bainite	W$_s$ ferrite	**Inverse Bainite**	**Supporting evidence**
Nucleation and growth reaction	✓	✓	✓	✓	**Dilatometry/Microscopy**
Plate shape	✓	✓	✓	✓	**TEM**
IPS Shape change with large shear	✓	✓	✓	✓	**TEM**
Lattice correspondence during growth	✓	✓	✓	✓	**TEM**
Co-operative growth of ferrite and cementite	×	×	×	×	**Microscopy**
High dislocation density	✓	✓	●	✓	**TEM/EBSD**
Has a glissile interface	✓	✓	✓	✓	**TEM**
Always has an orientation within bain region	✓	✓	✓	✓	**TEM/EBSD**
Grows across austenite grain boundaries	×	×	×	×	**Microscopy**
High Interface mobility at low temperatures	✓	✓	✓		
Reconstructive diffusion during growth	×	×	×	×	**APT**
Bulk redistribution of X atoms during growth	×	×	×	×	**APT**
Displacive transformation mechanism	✓	✓	✓	✓	**TEM**
Reconstructive transformation mechanism	×	×	×	×	**APT/TEM**
Diffusionless nucleation	×	×	×	×	**APT**
Carbon diffusion during nucleation	✓	✓	✓	✓	**APT**
Reconstructive diffusion during nucelation	×	×	×	×	**APT**
Often nucleates intragranularly on defects	×	×	×		
Diffusionless growth	✓	✓	×	×	**APT**
Local equilibrium at interface during growth	×	×	×	×	**APT**
Para-equilibrium at interface during growth (NPLE)	×	×	✓	✓	**APT**
Diffusion of carbon during transformation	×	×	✓	✓	**APT**
Carbon diffusion controlled growth	×	×	✓	✓	**APT**
Incomplete reaction phenomenon	✓	✓	×	✓	**Dilatometry/Microscopy**

Bibliography

[1] H.I. Aaronson. On the Problem of the Definitions and the Mechanisms of the Bainite Reaction. *The mechanism of Phase transformations in crystalline solids, London, Institute of Metals*, pages 270–281, 1969.

[2] E.S. Davenport and E.C. Bain. Transformation of austenite at constant subcritical temperatures. *Metallurgical Transactions*, 1(12):3503–3530.

[3] J.M. Robertson. *Journal of Iron and Steel Institute*, 119:391, 1929.

[4] T. Lyman and T.R. Troiano. *Transactions of American Institute of Mining and Met. Engineering*, page 196, 1945.

[5] T. Lyman and T.R. Troiano. *Transactions of American Society of Metals*, page 402, 1946.

[6] T. Ko and S.A. Cottrell. The formation of bainite. *Journal of the Iron and Steel Institute*, 172(3):307, 1952.

[7] L.C.D. Fielding. The bainite controversy. *Materials Science and Technology*, 29(4):383–399, 2013.

[8] A. Hultgren. *JISI*, 114:421–422, 1926.

[9] J.R. Vilella, G.E. Guellich, and E.C. Bain. On naming the aggregate constituents in steel. *Trans. ASM*, 24:225–261, 1936.

[10] M. Hillert. Mechanism and rate of decomposition from austenite. *Hardenability of alloy steels - ASM*, pages 1–65, 1939.

[11] C. Zener and J. Meder. Kinetics of the Decomposition of Austenite. *AIME*, 167:550–595, 1946.

[12] H.K.D.H. Bhadeshia. Bainite in steels, transformations, microstructure and properties accessed from https://www.phase-trans.msm.cam.ac.uk/. *IOM Communications Ltd*, pages 747–771, 2001.

[13] S.J. Matas and R.F. Hehemann. The structure of bainite in hypoeutectoid steels. *Transactions of the Metallurgical Society of AIME*, 221(1):179–185, 1961.

[14] J. Deliry. Nouveau carbure de fer. transformation bainitique dans les aciers au carbone silicium. *Memoires Scientifiques de la Revue de Metallurgie*, 62(7-8):527, 1965.

[15] J.W. Christian. The origin of surface relief effects in phase transformations. *Decomposition of austenite by diffusional processes*, pages 371–386, 1962.

[16] D.N. Shackleton and P.M. Kelly. Iron & steel inst. *Special Report*, 93:126, 1965.

[17] D.N. Shackleton and P.M. Kelly. The crystallography of cementite precipitation in the bainite transformation. *Acta Metallurgica*, 15(6):979 – 992, 1967.

[18] M. Nemoto. Growth of bainite in an iron-nickel-carbon alloy. *High Voltage Electron Microscopy*, pages 230–234, 1974.

[19] H.K.D.H. Bhadeshia. Bcc-bcc orientation relationships, surface relief and displacive phase transformations in steels. *Scripta Metallurgica*, 14(7):821 – 824, 1980.

[20] H.K.D.H. Bhadeshia and D.V. Edmonds. The bainite transformation in a silicon steel. *Metallurgical Transactions A*, 10(7):895–907, Jul 1979.

[21] H.K.D.H. Bhadeshia and D.V. Edmonds. The mechanism of bainite formation in steels. *Acta Metallurgica*, 28(9):1265–1273, Sep 1980.

[22] H.K.D.H Bhadeshia and A.R. Waugh. Bainite: An atom-probe study of the incomplete reaction phenomenon. *Acta Metallurgica*, 30(4):775 – 784, 1982.

[23] H.K.D.H. Bhadeshia. Phase transformations in ferrous alloys. *TMS-AIME, Warrendale, PA*, page 335, 1984.

[24] F. G. Caballero, M. K. Miller, S. S. Babu, and C. Garcia-Mateo. Atomic scale observations of bainite transformation in a high carbon high silicon steel. *Acta Materialia*, 55(1):381–390, 2007.

[25] F.G. Caballero, M.K. Miller, C. Garcia-Mateo, C. Capdevila, and S.S. Babu. Redistribution of alloying elements during tempering of a nanocrystalline steel. *Acta Materialia*, 56(2):188–199, Jan 2008.

[26] F. G. Caballero, M. K. Miller, and C. Garcia-Mateo. Carbon supersaturation of ferrite in a nanocrystalline bainitic steel. *Acta Materialia*, 58(7):2338–2343, 2010.

[27] F. G. Caballero, M. K. Miller, and C. Garcia-Mateo. Atom Probe Tomography Analysis of Precipitation during Tempering of a Nanostructured Bainitic Steel. *Metallurgical and Materials Transactions A*, 42(12):3660–3668, Dec 2011.

[28] A. Hultgren. Isothermal Transformation of Austenite. *Transactions of the A.S.M*, 39:915–1005, 1947.

[29] M. Hillert. Paraequilibrium. *Swedish Institute for Metals Research*, 1953.

[30] E.S. Davenport. Isothermal transformation in steels. *Trans. ASM*, 27:837–886, 1939.

[31] H.I. Aaronson. The proeutectoid ferrite and proeutectoid cementite reaction. *Decomposition of Austenite by Diffusional processes*, page 387, 1962.

[32] D. E. Coates. Diffusional growth limitation and hardenability. *Metallurgical Transactions*, 4(10):2313–2325, 1973.

[33] M. Hillert. Diffusion in growth of bainite. *Metallurgical and Materials Transactions A*, 25(9):1957–1966, 1994.

[34] W. T. Reynolds, F. Z. Li, C. K. Shui, and H. I. Aaronson. The Incomplete transformation phenomenon in Fe-C-Mo alloys. *Metallurgical Transactions A*, 21(6):1433–1463, 1990.

[35] G. Spanos. The fine structure and formation mechanism of lower bainite. *Metallurgical and Materials Transactions A*, 25(9):1967–1980, 1994.

[36] M. Hillert. Paradigm shift for bainite. *Scripta Materialia*, 47(3):175–180, Aug 2002.

[37] T.Y. Hsu. On bainite formation. *Metallurgical Transactions A*, 21(3):811–816, Mar 1990.

[38] A. Borgenstam, M. Hillert, and J. Agren. Metallographic evidence of carbon diffusion in the growth of bainite. *Acta Materialia*, 57(11):3242 – 3252, 2009.

[39] A. Borgenstam, P. Hedström, M. Hillert, P. Kolmskog, A. Stormvinter, and J. Ågren. On the Symmetry Among the Diffusional Transformation Products of Austenite. *Metallurgical and Materials Transactions A*, 42(6):1558–1574, Jun 2011.

[40] P. Kolmskog and A. Borgenstam. Eutectoid Transformations in 4.12 Mass Pct Cr 0.88 Mass Pct C Steel. *Metallurgical and Materials Transactions A*, 42(13):3941–3951, Aug 2011.

[41] P. Kolmskog. *Does Bainite form with or without diffusion? The experimental and theoretical evidence.* PhD thesis, KTH, Sweden, 2013.

[42] L. C. Chang and H. K. D. H. Bhadeshia. Microstructure of lower bainite formed at large undercoolings below bainite start temperature. *Materials Science and Technology*, 12(3):233–236, 1996.

[43] B. Josefsson and Andrenm H.O. Microstructure of granular bainite. *Journal de Physique Colloques*, 49(C6):293–298, 1988.

[44] L.C. Nilan. Morphology and kinetics of austenite decomposition at high pressure. *The American Institute of Mining, Metallurgical, and Petroleum Engineers*, pages 898–909, 1968.

[45] M. Hillert. The role of interfacial energy during solid state phase transformations. *Jernkontorets Annaler*, 141(11):757–789, 1957.

[46] K.R. Kinsman and H.I. Aaronson. The inverse bainite reaction in hypereutectoid Fe-C alloys. *Metallurgical and Materials Transactions*, 1(5):1485–1488, 1970.

[47] H.J. Lee, G. Spanos, G.J. Shiflet, and H.I. Aaronson. Mechanisms of the bainite (non-lamellar eutectoid) reaction and a fundamental distinction between the bainite and pearlite (lamellar eutectoid) reactions. *Acta Metallurgica*, 36(4):1129–1140, Apr 1988.

[48] H. Goldenstein, J. Alexander, B. Cifuentes, and A. Sinatora. Non Classical Eutectoid Decomposition Products Morphologies in Fe-Cr-C and Fe-Cr-Mo-C

Steels. *Solid - Solid Phase Transformations in Inorganic Materials , TMS*, (January), 2005.

[49] H. Goldenstein and J. A. Cifuentes. Overall kinetics and morphology of the products of austenite decomposition in a Fe-0.46 Pct C-5.2 Pct Cr alloy transformed isothermally above the bay. *Metallurgical and Materials Transactions A*, 37(6):1747–1755, Jun 2006.

[50] C. Goulas, M. G. Mecozzi, and J. Sietsma. Bainite Formation in Medium-Carbon Low-Silicon Spring Steels Accounting for Chemical Segregation. *Metallurgical and Materials Transactions A*, 47(6):3077–3087, Jun 2016.

[51] R. Kannan, Y. Wang, R. Bannister, M. Rashid, and L. Li. Homogenization of Austenite During Non-Equilibrium Heating in Hypereutectoid Steels. *Materials Science & Technology*, 2018.

[52] Y. Yang and J.T. Busby. Thermodynamic modeling and kinetics simulation of precipitate phases in AISI 316 stainless steels. *Journal of Nuclear Materials*, 448(1):282–293, 2014.

[53] A.I. Martinez-Ubeda, I. Griffiths, M.S.A. Karunaratne, P.E.J. Flewitt, C. Younes, and T. Scott. Influence of nominal composition variation on phase evolution and creep life of Type 316H austenitic stainless steel components. *Procedia Structural Integrity*, 2:958–965, 2016.

[54] W.C. Oliver and G.M. Pharr. Measurement of hardness and elastic modulus by instrumented indentation: Advances in understanding and refinements to methodology. *Journal of Materials Research*, 19(01):3–20, 2004.

[55] P.P Suikkanen, C. Cayron, A.J. DeArdo, and L.P. Karjalainen. Crystallographic Analysis of Isothermally Transformed Bainite in 0.2C–2.0Mn–1.5Si–0.6Cr Steel Using EBSD. *Journal of Materials Science & Technology*, 29(4):359–366, 2013.

[56] N. Doebelin and R. Kleeberg. Profex : a graphical user interface for the Rietveld refinement program BGMN. *Journal of Applied Crystallography*, 48(5):1573–1580, Oct 2015.

[57] K. Thompson, D. Lawrence, D. J. Larson, J.D. Olson, T.F. Kelly, and B. Gorman. In situ site-specific specimen preparation for atom probe tomography. *Ultramicroscopy*, 107(2-3):131–139, 2007.

[58] J. Takahashi, K. Kawakami, and Y. Kobayashi. Quantitative analysis of carbon content in cementite in steel by atom probe tomography. *Ultramicroscopy*, 111(8):1233–1238, 2011.

[59] H.S. Kitaguchi, S. Lozano-Perez, and M.P. Moody. Quantitative analysis of carbon in cementite using pulsed laser atom probe. *Ultramicroscopy*, 147:51–60, 2014.

[60] J.O. Andersson, T. Helander, L. Höglund, P. Shi, and B. Sundman. Thermo-Calc & DICTRA, computational tools for materials science. *Calphad*, 26(2):273–312, Jun 2002.

[61] Matcalc - Solid State and Kinetics Precipitation.

[62] R. Hossain, F. Pahlevani, and V. Sahajwalla. Effect of small addition of Cr on stability of retained austenite in high carbon steel. *Materials Characterization*, 125:114–122, Mar 2017.

[63] Q. Luo, J. Xie, and Y. Song. Effects of microstructures on the abrasive wear behaviour of spheroidal cast iron. *Wear*, 184(1):1–10, 1995.

[64] T. Chandrasekaran. Effect of microstructure and hardness on the grinding abrasive wear resistance of a ball bearing steel. *Wear*, 161(1-2):105–109, 1993.

[65] T. W. Chenje, D. J. Simbi, and E. Navara. Relationship between microstructure, hardness, impact toughness and wear performance of selected grinding media for mineral ore milling operations. *Materials and Design*, 25(03):11–18, 2004.

[66] V. Leskovek, B. Sustarsic, and G. Jutrisa. The influence of austenitizing and tempering temperature on the hardness and fracture toughness of hot-worked H11 tool steel. *Journal of Materials Processing Technology*, 178(1-3):328–334, Sep 2006.

[67] K. Abbaszadeh, H. Saghafian, and S. Kheirandish. Effect of Bainite Morphology on Mechanical Properties of the Mixed Bainite-martensite Microstructure in D6AC Steel. *Journal of Materials Science and Technology*, 28(4):336–342, 2012.

[68] Y. Tomita. Effect of microstructure on plane-strain fracture toughness of aisi 4340 steel. *Metallurgical Transactions A*, 19(10):2513–2521, Oct 1988.

[69] C.H. Young and H.K.D.H. Bhadeshia. Strength of mixtures of bainite and martensite. *Materials Science and Technology*, 10(3):209–214, Mar 1994.

[70] L.B. McCusker, R.B. Von Dreele, D.E. Cox, D. Louër, and P. Scardi. Rietveld refinement guidelines. *Journal of Applied Crystallography*, 32(1):36–50, Feb 1999.

[71] S.S. Babu, J.M. Vitek, S.A. David, T. Palmer, and J.W. Elmer. Characterization and Prediction of Austenite Formation and Decomposition in Steel Welds. *Materials Science and Technology*, pages 343–352, 2003.

[72] B.D. Cullity and S.R. Sotck. *Elements of X-ray Diffraction.* Wesley Publishing Company, 1 edition, 1956.

[73] R.N. Penha, J. Vatavuk, A.A. Couto, S. Pereira, S.A. de Sousa, and L.C.F. Canale. Effect of chemical banding on the local hardenability in AISI 4340 steel bar. *Engineering Failure Analysis*, 53:59–68, Jul 2015.

[74] W. Song, P. Choi, G. Inden, U. Prahl, D. Raabe, and W. Bleck. On the Spheroidized Carbide Dissolution and Elemental Partitioning in High Carbon Bearing Steel 100Cr6. *Metallurgical and Materials Transactions A*, 45(2):595–606, Feb 2014.

[75] S.J. Hearne and J.A. Floro. Mechanisms inducing compressive stress during electrodeposition of Ni. *Journal of Applied Physics*, 97(1):014901, Jan 2005.

[76] G. C. A. M. Janssen and J.D. Kamminga. Stress in hard metal films. *Applied Physics Letters*, 85(15):3086–3088, Oct 2004.

[77] H.R. Hertz, D.E Jones, and G.A Schott. Miscellaneous papers. *Macmillan and Co. Ltd*, 92:156–171, 1896.

[78] Q. Furnmont, M. Kempf, P.J. Jacques, M. G?ken, and F. Delannay. On the measurement of the nanohardness of the constitutive phases of TRIP-assisted multiphase steels. *Materials Science and Engineering: A*, 328(1-2):26–32, May 2002.

[79] J. Li, T. Ohmura, and K. Tsuzaki. Microstructure effect on nanohardness distribution for medium-carbon martensitic steel. *Science in China Series E*, 49(1):10–19, Jan 2006.

[80] R. Kannan, Y. Wang, and L. Li. Identification of Inverse Bainite in Fe-0.84C-1Cr-1Mn Hypereutectoid Low Alloy Steel. *Metallurgical and Materials Transactions A*, 48(3):948–952, Mar 2017.

[81] N. Zhong, X. Wang, Z. Guo, and Y. Rong. Orientation Relationships between Ferrite and Cementite by Edge-to-edge Matching Principle. *Journal of Materials Science & Technology*, 27(5):475–480, 2011.

[82] M. Hillert. Phase Equilibria, Phase Diagrams and Phase Transformations - Their Thermodynamic Basics, 2008.

[83] I. Miroshnichenko. *Crytallization Processes.* 1966.

[84] D.V. Malakhov, D. Panahi, and M. Gallerneault. On the formation of intermetallics in rapidly solidifying Al–Fe–Si alloys. *Calphad*, 34(2):159–166, 2010.

[85] R.G. Purdy, D.V. Malakhov, and H. Zurob. Driving Forces for the Onset of Precipitation in the Course of Multicomponent Alloy Solidification. In *Proceeding of the 6th international school-conference, "Phase Diagrams In materials Science",*, pages 20–41, 2004.

[86] R. Kannan, Y. Wang, and L. Li. Microstructural Evolution of Inverse Bainite in a Hypereutectoid Low-Alloy Steel. *Metallurgical and Materials Transactions A*, 48(12):6038–6054, Dec 2017.

[87] N.F. Kennon and N.A. Kaye. Isothermal transformation of austenite to pearlite and upper bainite in eutectoid steel. *Metallurgical Transactions A*, 13(6):975–978, Jun 1982.

[88] H.I. Aaronson, W.T. Reynolds, and G.R. Purdy. Coupled-solute drag effects on ferrite formation in Fe-C-X systems. *Metallurgical and Materials Transactions A*, 35(4):1187–1210, Apr 2004.

[89] M. M. Aranda, R. Rementeria, C. Capdevila, and R. E. Hackenberg. Can Pearlite form Outside of the Hultgren Extrapolation of the Ae3 and Acm Phase Boundaries? *Metallurgical and Materials Transactions A*, 47(2):649–660, Feb 2016.

[90] R. Kannan, Y. Wang, and L. Li. A dilatometric analysis of inverse bainite transformation. *Journal of Materials Science*, 53(5):3692–3708, Mar 2018.

[91] H.K.D.H. Bhadeshia, S. A. David, J. M. Vitek, and R. W. Reed. Stress Induced Transformation to Bainite in Fe-Cr-Mo-C Pressure Vessel Steel. *Materials Science and Technology*, 7:686–698, 1991.

[92] A. Grajcar, W. Zalecki, P. Skrzypczyk, A. Kilarski, A. Kowalski, and S. Kołodziej. Dilatometric study of phase transformations in advanced high-strength bainitic steel. *Journal of Thermal Analysis and Calorimetry*, 118(2):739–748, Sep 2014.

[93] G. Xu, F. Liu, L. Wang, and H. Hu. A new approach to quantitative analysis of bainitic transformation in a superbainite steel. *Scripta Materialia*, 68(11):833–836, Jun 2013.

[94] J. Pak, D. Woo, and H.K.D.H. Bhadeshia. Bainite : Fragmentation of crystallographically homogeneous domains. *International Journal of Materials Research*, 103(4):476–482, 2012.

[95] J.M. Prado, J.J. Catalan, and M. Marsal. Dilatometric study of isothermal phase tranformation in a C-Mn steel. *Journal of Materials Science*, 25(4):1939–1946, Apr 1990.

[96] H. Modin and S. Modin. Pearlite and bainite structure in a eutectoid carbon steel-an electron microscopy investigation. *Jernkont.Ann.*, 139(8):481–515, 1955.

[97] M. Militzer, R. Pandi, and E. B. Hawbolt. Ferrite nucleation and growth during continuous cooling. *Metallurgical and Materials Transactions A*, 27(6):1547–1556, Jun 1996.

[98] H.K.D.H. Bhadeshia and R. Honeycombe. *Heat Treatment of Steels: Hardenability.* Elsevier Ltd, 4 edition, 2017.

[99] H.K.D.H. Bhadeshia and R. Honeycombe. *Solutes that Substitute for Iron.* Elsevier Ltd, 4 edition, 2017.

[100] T. Skaland, Ø. Grong, and T. Grong. A model for the graphite formation in ductile. *Metallurgical Transactions A*, 24(10):2347–2353, Oct 1993.

[101] C. Labrecque and M. Gagné. Ductile Iron: Fifty Years of Continuous Development. *Canadian Metallurgical Quarterly*, 37(5):343–378, Dec 1998.

[102] J.Y. Park, K. Taek Choi, J.A. Szpunar, K. Hwan Oh, and H. Yong Ra. Effect of Mn negative segregation through the thickness direction on graphitization characteristics of strip-cast white cast iron. *Scripta Materialia*, 46(3):199–203, Feb 2002.

[103] Y. Zhang and D.M. Schleich. Preparation and Characterization of Iron Manganese Carbide by Reaction of the Oxides and Carbon in Nitrogen. *Journal of Solid State Chemistry*, 110(2):270–273, Jun 1994.

[104] M. Calcagnotto, D. Ponge, and D. Raabe. On the Effect of Manganese on Grain Size Stability and Hardenability in Ultrafine-Grained Ferrite/Martensite Dual-Phase Steels. *Metallurgical and Materials Transactions A*, 43(1):37–46, Jan 2012.

[105] M. J. Peet, S.S. Babu, M.K. Miller, and H. K. D. H. Bhadeshia. Tempering of low-temperature bainite. *Metallurgical and Materials Transactions A*, 48(7):3410–3418, Jul 2017.

[106] P. Lejček. Principles of Non-equilibrium Segregation. In *Grain Boundary Segregation in Metals*, pages 153–171. Springer, Berlin, Heidelberg, 2010.

[107] X.L. He, Y.Y. Chu, and J.J. Jonas. The grain boundary segregation of boron during isothermal holding. *Acta Metallurgica*, 37(11):2905–2916, Nov 1989.

[108] R.G. Faulkner. Non-equilibrium grain-boundary segregation in austenitic alloys. *Journal of Materials Science*, 16(2):373–383, Feb 1981.

[109] J. Wu and S. Song. A unified model of grain-boundary segregation kinetics. *Journal of Applied Physics*, 110(6):063531, Sep 2011.

[110] M.K. Miller and R.G. Forbes. Data Analysis. In *Atom-Probe Tomography: The Local Electrode Atom Probe*, pages 303–345. Springer US, Boston, MA, 2014.

[111] C. Zener. Theory of Growth of Spherical Precipitates from Solid Solution. *Journal of Applied Physics*, 20(10):950–953, Oct 1949.

[112] G. Inden. Kinetics of Phase Transformation in Multi-Component Systems. pages 113–140. Springer, Dordrecht, 2008.

[113] C. R. Hutchinson, A. Fuchsmann, and Y. Brechet. The diffusional formation of ferrite from austenite in Fe-C-Ni alloys. *Metallurgical and Materials Transactions A*, 35(4):1211–1221, Apr 2004.

[114] R.A. Mesquita, C.A. Barbosa, E.V. Morales, and H.J. Kestenbach. Effect of Silicon on Carbide Precipitation after Tempering of H11 Hot Work Steels. *Metallurgical and Materials Transactions A*, 42(2):461–472, Feb 2011.

[115] M.M. Aranda, R. Rementeria, J. Poplawsky, E. Urones-Garrote, and C. Capdevila. The role of C and Mn at the austenite/pearlite reaction front during non-steady-state pearlite growth in a Fe-C-Mn steel. *Scripta Materialia*, 104:67–70, 2015.

[116] X. Zhang, T. Hickel, J. Rogal, S. Fähler, R. Drautz, and J. Neugebauer. Structural transformations among austenite, ferrite and cementite in Fe-C alloys: A unified theory based on ab initio simulations. *Acta Materialia*, 99:281–289, 2015.

[117] M. Guziewski, S.P. Coleman, and C.R. Weinberger. Atomistic investigation into the atomic structure and energetics of the ferrite-cementite interface : The Bagaryatskii orientation. *Acta Materialia*, 119:184–192, 2016.

[118] M. Guziewski, S.P. Coleman, and C.R. Weinberger. Atomistic investigation into the mechanical properties of the ferrite-cementite interface: The Bagaryatskii orientation. *Acta Materialia*, 144:656–665, 2018.

[119] H. I. Aaronson, W. T. Reynolds, and Gary R. Purdy. The incomplete transformation phenomenon in steel. *Metallurgical and Materials Transactions A*, 37(6):1731–1745, 2006.

[120] H.K.D.H. Bhadeshia and D.V. Edmonds. The mechanism of bainite formation in steels. *Acta Metallurgica*, 28(9):1265–1273, Sep 1980.

[121] V.K. Heikkinen. The formation of planar band colonies in vanadium-bearing mild steels. *Acta Metallurgica*, 21(5):709–714, 1973.

[122] K. Campbell and R.W.K. Honeycombe. The isothermal decomposition of austenite in simple chromium steels. *Metal Science*, 8(1):197–203, 1974.

[123] R.W.K. Honeycombe and R.F. Mehl. Transformation from austenite in alloy steels. *Metallurgical Transactions A*, 7(7):915–936, Jul 1976.

[124] K.H. Kim, J.S. Lee, and D.L. Lee. Effect of silicon on the spheroidization of cementite in hypereutectoid high carbon chromium bearing steels. *Metals and Materials International*, 16(6):871–876, Dec 2010.

[125] Y.J. Lia, P. Choi, C. Borchers, Y.Z. Chen, S. Goto, D. Raabe, and R. Kirchheim. Atom probe tomography characterization of heavily cold drawn pearlitic steel wire. *Ultramicroscopy*, 111(6):628–632, 2011.

[126] D.A. Porter, K. E. Easterling, and M.Y. Sherif. *Phase transformations in metals and alloys.*

[127] J. Moon, C. Lee, S. Uhm, and J. Lee. Coarsening kinetics of TiN particle in a low alloyed steel in weld HAZ: Considering critical particle size. *Acta Materialia*, 54(4):1053–1061, Feb 2006.

[128] M. Onink, C.M. Brakman, F.D. Tichelaar, E.J. Mittemeijer, S. van der Zwaag, J.H. Root, and N.B. Konyer. The lattice parameter of austenitte and ferrite in Fe-C alloys as function of carbon concentration and temperature. *Scripta Metallurgica et Materialia*, 29(c):1011–1016, 1993.

[129] J.Y. Chae, J.H. Jang, G. Zhang, K.H. Kim, J.S. Lee, H.K.D.H. Bhadeshia, and D.W. Suh. Dilatometric analysis of cementite dissolution in hypereutectoid steels containing Cr. *Scripta Materialia*, 65(3):245–248, 2011.

[130] A. Jablonka, K. Harste, and K. Schwerdtfeger. Thermomechanical properties of iron and iron-carbon alloys: density and thermal contraction. *Steel Research*, 62(1):24–33, 1991.

[131] C. Garcia de Andres, F.G. Caballero, and C. Capdevila. Dilatometric characterization of pearlite dissolution in 0.1C-0.5Mn low carbon low manganese steel. *Scripta Materialia*, 38(12):1835–1842, 1998.

[132] H. K. D. H. Bhadeshia. Thermodynamic analysis of isothermal transformation diagrams. *Metal Science*, 16(3):159–166, Mar 1982.

[133] F.G. Caballero, C. Capdevila, and C. García De Andrés. Modelling of kinetics and dilatometric behaviour of austenite formation in a low-carbon steel with a ferrite plus pearlite initial microstructure. *Journal of Materials Science*, 37(16):3533–3540, 2002.

[134] J.W. Christian. Formal Theory of Transformation Kinetics. In *The Theory of Transformations in Metals and Alloys*, pages 529–552. 2002.

[135] Y. Liu, D. Wang, F. Sommer, and E.J. Mittemeijer. Isothermal austenite-ferrite transformation of Fe-0.04 at.% C alloy: Dilatometric measurement and kinetic analysis. *Acta Materialia*, 56(15):3833–3842, 2008.

[136] F. Liu, F. Sommer, C. Bos, and E. J. Mittemeijer. Analysis of solid state phase transformation kinetics: models and recipes. *International Materials Reviews*, 52(4):193–212, Jul 2007.

[137] A. Van der Ven and L. Delaey. Models for precipitate growth during the γ to α + γ transformation in Fe-C and Fe-C-M alloys. *Progress in Materials Science*, 40(3):181–264, Jan 1996.

[138] M. Takahashi. *Reaustenitisation from bainite in steels*. PhD thesis, University of Cambridge, 1992.

[139] H. Stuart and N. Rindley. Thermal expansion of cementite and other phases. *Journal of the Iron and Steel Institute*, 204:711–717, 1966.

[140] C. Garcia-Mateo, F.G. Caballero, C. Capdevila, and C. Garcia de Andres. Estimation of dislocation density in bainitic microstructures using high-resolution dilatometry. *Scripta Materialia*, 61(9):855–858, Nov 2009.

[141] J. Wang, P. J. Van Der Wolk, and S. Van Der Zwaag. On the influence of alloying elements on the bainite reaction in low alloy steels during continuous cooling. *Journal of Materials Science*, 35(17):4393–4404, 2000.

[142] H. Chen, A. Borgenstam, J. Odqvist, I. Zuazo, M. Goune, J. Ågren, and S. van der Zwaag. Application of interrupted cooling experiments to study the mechanism of bainitic ferrite formation in steels. *Acta Materialia*, 61(12):4512–4523, Jul 2013.

[143] H. Chen and S. van der Zwaag. Predicting the Effect of Mo, Ni, and Si on the Bainitic Stasis. *Metallurgical and Materials Transactions A*, 45(8):3429–3437, Jul 2014.

[144] S. Ranganathan and M. Von Heimendahl. The three activation energies with isothermal transformations: applications to metallic glasses. *Journal of Materials Science*, 16(9):2401–2404, Sep 1981.

Appendix 1: Mathematical Treatment of Inverse Bainite Transformation

A1.1 Introduction

The unique two-stage dilatation curve observed during the inverse bainite transformation (Refer Chapter 3) provides a kinetic signature for the existence of inverse bainite. This two stage behavior is also observed in 51CrV4 steel studied by Goulas *et al.* [50] (Ref. Figure A1.1) where they have shown the existence of inverse bainite during isothermal treatment at 510 ° C. This provides confidence in the dilatometry measurements in the current work, and indicates that the dilation data should be treated with care so that the initial volumetric contraction should not be neglected as an instrumental artifact. In this section, the two stage dilation is analyzed to understand the transformation kinetics. A data conversion algorithm is proposed to extract the bainitic phase fractions from the raw dilatometry data. The proposed data extraction algorithm is generic that relies only on the density of phases involved in the transformation. To verify the extracted phase fraction, a thermo-kinetic model is developed using the principles of diffusion and Johnson–Mehl–Avrami–Kolmogorov kinetics. The predicted phase fractions by the kinetics model agree fairly well with the experimental phase fraction results from dilatometry, metallography, and XRD. The two-stage transformation can be explained by the kinetics of inverse bainite as a diffusion-controlled transformation product. Though the transformation kinetics change from PE to NPLE at prolonged transformation times, a complete PE assumption predicts phase fraction close enough to the actual experimental phase fraction.

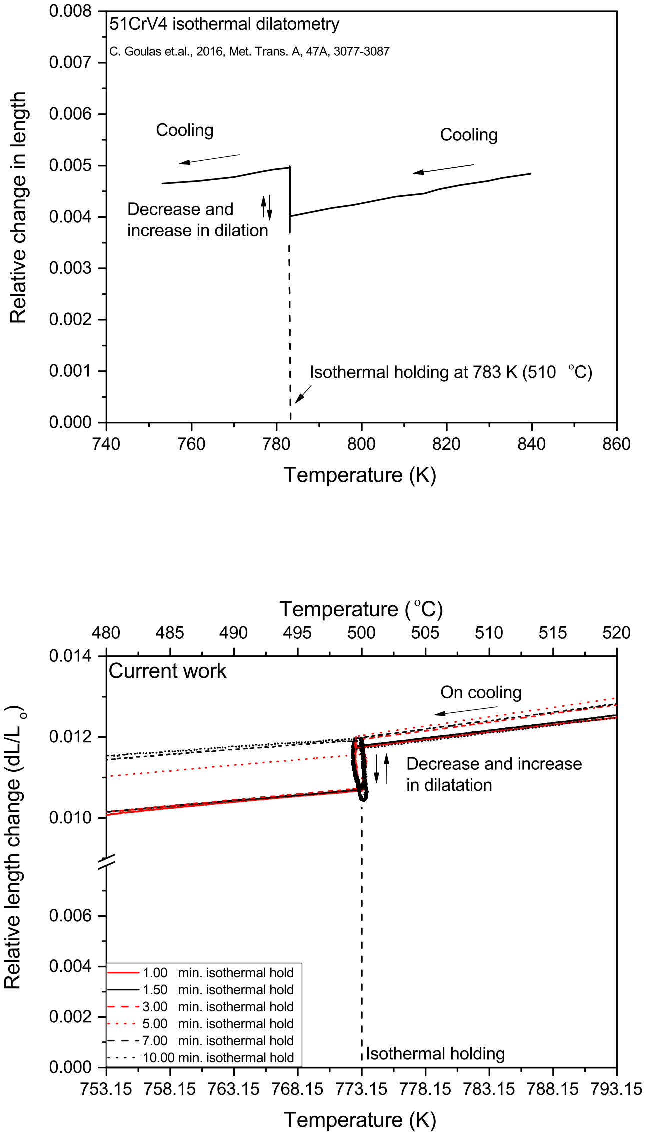

Figure A1.1: Comparison of the isothermal dilation data reported by Goulas *et al.*in a 51CrV4 steel to the current work. Note the two stage dilation behavior characteristic of inverse bainite transformation.

A1.2 Results

A1.2.1 Dilatometry

A representative complete dilatation profile in Figure A1.2 shows the absence of any phase transformation upon cooling from 1323.15 K (1050 ° C) to the 773.15 K (500 ° C). During the 773.15 K (500 ° C) isothermal hold, the bainitic transformations are recorded. On-cooling from the isothermal hold to the room temperature the martensitic transformation is recorded. The recorded dilatation data before the start of the isothermal hold is due to the thermal shrinkage of austenite and not from any phase transformations. All untransformed austenite at the end of the isothermal hold will be fully transformed into martensite/retained austenite constituents, thus enabling a definitive measurement of phases that have transformed during the isothermal hold. It is to be brought to the readers attention that the expansion (0.143 % strain) at austenitization in Figure 1 is the instrumental drift due to sudden change in mode of operation of the dilatometer setup from continuous heating to isothermal holding. It is clear from the inset in Figure A1.2 that the instrumental drift lasts for about 30 seconds after which there is no change in the dilatometric strain. The austenitization temperature of 1323.15 K (1050 ° C) employed in the current study is much higher

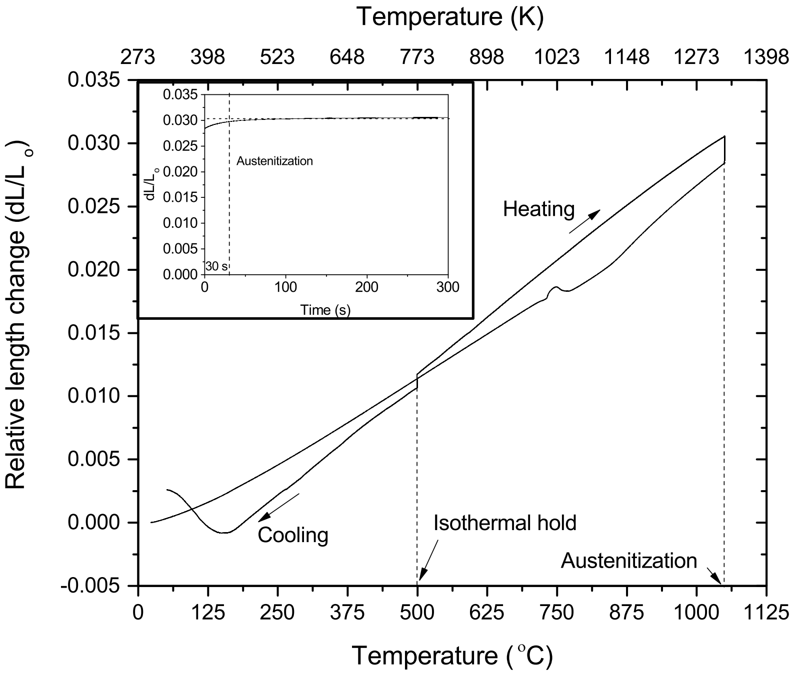

Figure A1.2: Representative complete dilatation profile of the sample for the heating schedule mentioned in the experimental section.

than the equilibrium A_{cm} temperature (860 ° C) measured using ThermoCalc. This further goes to show that the expansion (0.143 % strain) at austenitization is indeed an instrumental drift. Such an instrumental drift was also observed in our experiments reported in Ref. [26].

In the case of 1 minute and 1.5 minutes isothermal hold, only volumetric contraction was observed. When the isothermal holding time is increased to 3 minutes and beyond, a transition in dilatation from volumetric contraction to volumetric expansion was observed after approximately 75 seconds in to the transformation. In order to accurately determine the transition from volumetric contraction to volumetric expansion, the derivative of the relative length change $\left(\frac{d\left(\frac{dL}{L_o}\right)}{dt}\right)$ is plotted as a function of time for the 3 minutes, 5 minutes, 7 minutes, and 10 minutes isothermal holds in Figure A1.3.

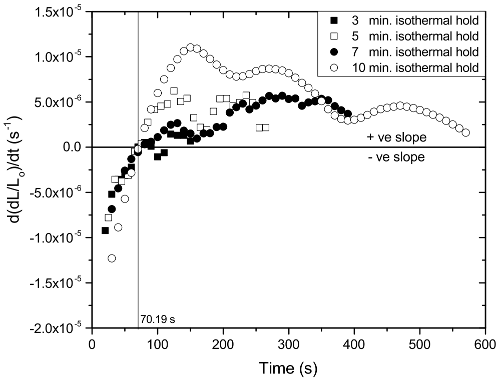

Figure A1.3: Derivative of relative length change plotted as a function of transformation time for the 3 minutes, 5 minutes, 7 minutes, and 10 minutes isothermal hold samples.

The change in sign of the derivative from negative to positive occurs at about 70 seconds. It is notable that this change from volumetric contraction to volumetric expansion occurs at the same point for all the heat treatments, providing confidence in the repeatability of the dilatometry measurements. Thus, using the derivative of dilatation, a continuous two-stage dilatation has been deconvoluted into two subsequential transformations. The first being the bainitic cementite transformation and the second being the bainitic ferrite transformation, as shown in [80].

A1.2.2 a posteriori microscopy and assumptions for the algorithm to extract phase fraction and the kinetic model

To understand the elemental partitioning behavior during the transformation, EDX line scans were performed at the inverse bainite/martensite (retained austenite) interface. Figure A1.4a and Figure A1.4c shows the partitioning behavior at the inverse bainitic cementite/martensite (retained austenite) interface. It is seen that only carbon redistributes at the interface, the heavy elements (Cr, Mn) are not detected to have partitioned during the transformation. A local carbon depletion on account of cementite transformation is observed. Figure A1.4b and Figure A1.4d shows the partitioning behavior at the inverse bainitic ferrite/martensite (retained austenite) interface. Again, it is seen that only carbon partitions at the interface, the heavy elements (Cr, Mn) are not partitioned during the transformation. A local carbon enrichment is observed at the ferrite/martensite interface.

From the above presented evidences, the following assumptions and inputs were made for the extraction of phase fraction from the dilatometry data and for the development of a kinetics model:

1. No phase transformations occur during the continuous cooling prior to the isothermal hold; the microstructure consists entirely of austenite. The recorded dilatation prior to the isothermal hold are entirely due to the thermal contraction of austenite.

2. The two-stage dilatation curve recorded for inverse bainitic transformation can be deconvoluted into two individual dilatometry curves, one for the inverse bainitic cementite transformation from austenite, and the other for the inverse bainitic ferrite transformation from austenite.

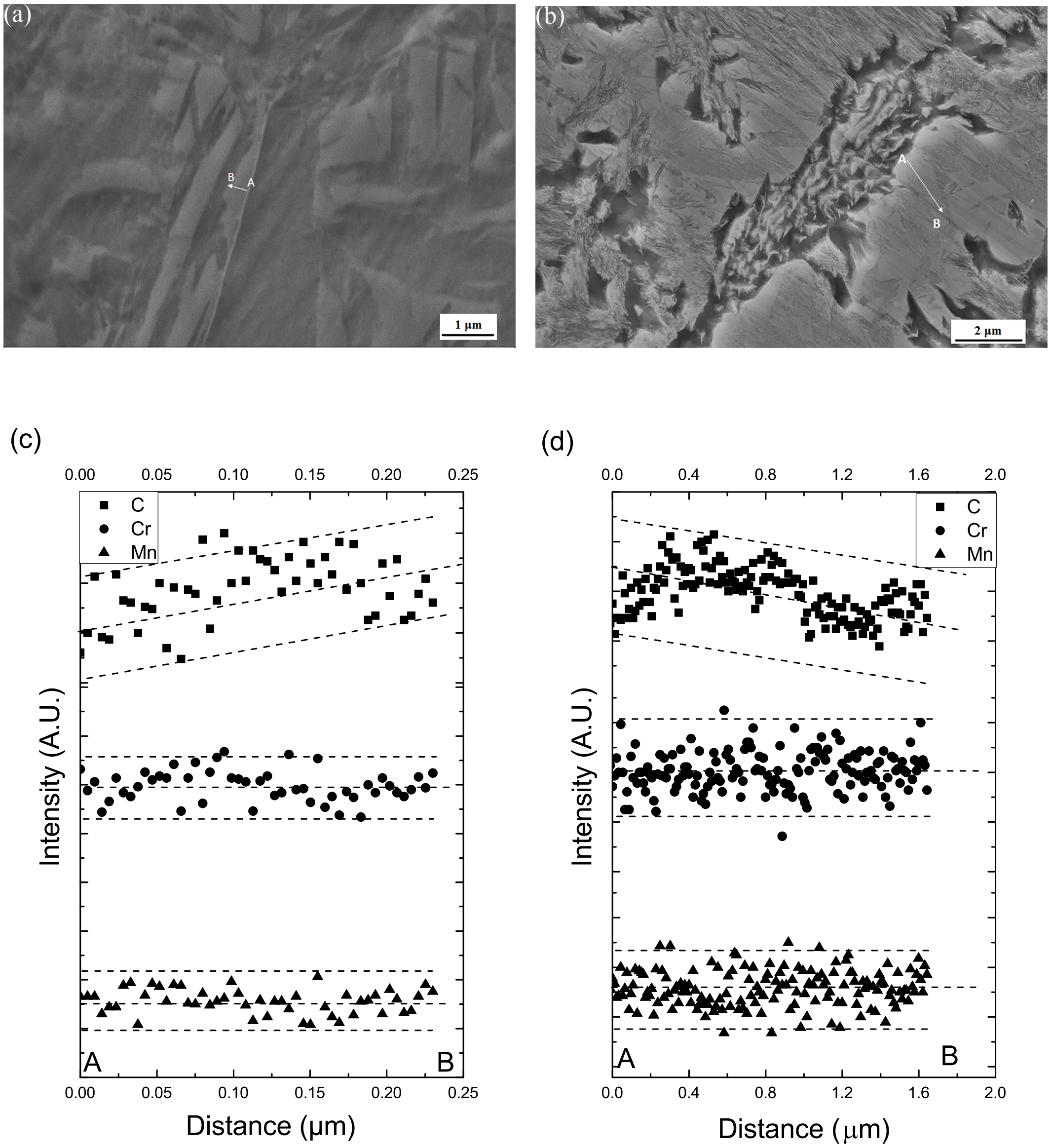

Figure A1.4: (a) Secondary electron SEM image of the 1 minute isothermal hold sample. Line AB represents the EDX line scan direction. (b) EDX line scan profiles corresponding to line ab in (a)

3. The inverse bainitic transformation proceeds by a para equilibrium (PE) mode, i.e. only diffusion of carbon is considered during the growth and the transformation is controlled by the diffusion of carbon. Diffusion of heavy elements including Cr and Mn are considered negligible so that the ratio between Fe and Cr/Mn remain a constant as the transformation progresses.

A1.3 Algorithm to extract phase fraction from raw dilatometry data

An algorithm is developed by considering the changes in lattice parameter of parent austenite, while it undergoes the phase transformations during the isothermal hold. The decrease in dilatation during the inverse bainitic cementite transformation is attributed to the decrease in lattice parameter of parent austenite, likewise the increase in dilatation during the inverse bainitic ferrite transformation is attributed to the increase in lattice parameter of austenite. The lattice parameter of austenite as a function of temperature and carbon content is given by [128]

$$a_\gamma(\chi_{C_\gamma,T}) = (0.36308 + 0.00075\chi_{C_\gamma}) + \{1 + (24.92 - 0.61\chi_{C_\gamma})10^{-6}[T - 1000]\}$$

where χ_{C_γ} is the atomic fraction of carbon in austenite and T is the temperature in Kelvin. Since, the temperature of transformation is fixed in the current experiments, the decrease in dilatation is attributed to decrease in carbon content of austenite during its transformation into cementite. Similarly, the increase in dilatation can be explained due to the transformation of austenite into ferrite which causes an increase in carbon content of the untransformed austenite. Thus, one can expect the carbon concentration of austenite to follow a similar trend as the dilatation curves in Figure A1.2. The lattice parameter of cementite is assumed to be the stoichiometric value, and even with a considerable enrichment of Cr/Mn in the cementite, the influence on the atomic volume is assumed to be negligible [129]. The list of symbols and their meaning used in the development of the algorithm to extract phase fraction data are shown in Table A1.2. The approximations used in the derivation of the algorithm are discussed during the course of the development.

Table A1.2: Nomenclature of the symbols used

Symbol	Name	Units
V	Total volume of the sample	μm^3
m_T	Total mass of the sample	gm
V_o	Initial volume of the sample	μm^3
ρ_o	Initial density of the sample	$gm(\mu m^{-3})$
ρ_i	Density of constituent i	$gm(\mu m^{-3})$
λ_i	Ratio of density of sample to density of the phase$\left(\frac{\rho_o}{\rho_i}\right)$	
$\rho_{\gamma(T,C)}$	Density of austenite at temperature T and carbon content C	$gm\mu m^{-3}$
$\rho_{\gamma(T,C^{\gamma'})}$	Density of austenite at Temperature T and carbon content after primary cementite transformation	$gm\mu m^{-3}$
C_γ	Carbon content of austenite	$Wt.\%$
C_θ	Equilibrium carbon content of cementite	$Wt.\%$
f_γ	Fraction of austenite	
f_θ	Fraction of cementite	
f_p	Fraction of ferrite + cementite	

First stage of Inverse bainitic reaction: Formation of the primary cementite unit

Our previous articles [80] on the microstructure characterization during the transformation of inverse bainite revealed that the first stage of dilatation involves the formation of cementite midrib of inverse bainite microstructure. Elemental partitioning characteristics presented in Figure A1.4 shows that the partitioning of heavy elements (Cr and Mn) is negligible. The total volume of the sample after the transformation can be given by the volume of all the constituents present after the transformation.

$$V = \sum_{i=1}^{i=n} V_i \tag{A1.1}$$

where V is the total volume of the sample, and V_i is the volume of constituent i. V_i can be calculated using the mass fraction of constituent i (f_i) and its density as (ρ_i)

$$V_i = m_S \frac{f_i}{\rho_i}$$

The mass fraction of constituent i is given by

$$f_i = \frac{m_i}{m_S} * \rho_i$$

Thus, Equation (A1.1) can be simplified as

$$V = m_S \sum_{i=1}^{i=n} \frac{f_i}{\rho_i}$$

The mass of the sample (m_S) can be written in terms of the initial volume of the sample (V_o) and the initial the density of sample (ρ_o), giving

$$V = V_o \sum_{i=1}^{i=n} \frac{\rho_o f_i}{\rho_i}$$

$$\frac{V}{V_o} = \sum_{i=1}^{i=n} \lambda_i f_i \tag{A1.2}$$

For the current study, Equation (A1.2) has two terms, one for the cementite midrib, and the other for the carbon depleted austenite after cementite transformation.

$$\frac{V}{V_o} = \lambda_\gamma f_\gamma + \lambda_\theta f_\theta$$

and from mass conservation condition,

$$f_\gamma + f_\theta = 1$$

$$\frac{V}{V_o} = \lambda_\gamma - \lambda_\gamma f_\theta + \lambda_\theta f_\theta = \lambda_\gamma + f_\theta(\lambda_\theta - \lambda_\gamma)$$

Since the experiments are performed in isothermal holding condition, differentiating with respect to time gives,

$$\frac{1}{V_o}\frac{dV}{dt} = \frac{\partial \lambda_\gamma}{\partial t} - f_\theta \frac{\partial \lambda_\gamma}{\lambda t} + \frac{\partial f_\theta}{\partial t}(\lambda_\theta - \lambda_\gamma) \tag{A1.3}$$

Equation (A1.3) is with the assumption that density of cementite and hence λ_θ does not vary with carbon concentration. In Equation (A1.3), the ratio of sample density to the density of austenite is taken as λ_γ ($\lambda_\gamma = \frac{\rho_o}{\rho_{\gamma(T,C)}}$).

$$\frac{\partial \lambda_\gamma}{\partial t} = -\frac{\rho_o}{\rho_{\gamma(T,C)}}\frac{1}{\rho_{\gamma(T,C)}}\frac{\partial \rho_\gamma}{\partial t} = -\frac{\rho_o}{\rho_{\gamma(T,C)}}\frac{1}{\rho_{\gamma(T,C)}}\frac{\partial \rho_\gamma}{\partial C_\gamma}\frac{\partial C_\gamma}{\partial t} \tag{A1.4}$$

Jablonka *et al.* [130] fitted the variation in density of austenite with carbon content at constant temperature and found that the density of austenite varies linearly with carbon content. The density function of austenite at constant temperature is given by

$$\rho_{\gamma(T,C)} = \rho_{\gamma(T,C=0)}(1 - 0.0146\%C) \tag{A1.5}$$

$$\frac{\partial \rho_{\gamma(T,C)}}{\partial C_\gamma} = -\rho_{\gamma(T,C=0)}0.0146 \tag{A1.6}$$

Substituting Equation (A1.5) and Equation (A1.6) in Equation (A1.4),

$$\frac{\partial \lambda_\gamma}{\partial t} = \frac{\rho_o}{\rho_{\gamma(T,C=0)}}\frac{0.0146}{(1 - 0.0146\%C)^2}\frac{\partial C_\gamma}{\partial t} \tag{A1.7}$$

Substituting Equation (A1.7) in Equation (A1.3), the volume change rate can now be described by the following differential equation,

$$\frac{1}{V_o}\frac{dV}{dt} = \frac{\rho_o}{\rho_{\gamma(T,C=0)}}\frac{0.0146}{(1 - 0.0146\%C)^2}\frac{\partial C_\gamma}{\partial t}(1 - f_\theta) + \frac{\partial f_\theta}{\partial t}\rho_o\left[\frac{\rho_{\gamma(T,C)} - \rho_\theta}{\rho_{\gamma(T,C)}\rho_\theta}\right] \tag{A1.8}$$

The second term on the right hand side in the above equation is negligible and is assumed zero because the fraction of cementite that nucleate and grow at the start of transformation is small, and the rate of change in fraction of cementite formed is also small. Therefore, Equation (A1.8) can be simplified as

$$\frac{1}{V_o}\frac{dV}{dt} = \frac{\rho_o}{\rho_{\gamma(T,C=0)}}\frac{0.0146}{(1-0.0146\%C)^2}\frac{\partial C_\gamma}{\partial t}(1-f_\theta) \tag{A1.9}$$

Writing mass balance with respect to carbon,

$$C_\gamma f_\gamma + C_\theta f_\theta = 0.84$$

$$C_\gamma = \frac{0.84-6.67f_\theta}{1-f_\theta}$$

$$\frac{\partial C_\gamma}{\partial t} = -\frac{5.83}{(1-f_\theta)^2}\frac{\partial f_\theta}{\partial t} \tag{A1.10}$$

Substituting Equation (A1.10) in Equation (A1.9),

$$\frac{1}{V_o}\frac{dV}{dt} = -\frac{\rho_o}{\rho_{\gamma(T,C=0)}}\frac{0.0146}{\left[1-0.0146\left(\frac{0.84-6.67f_\theta}{1-f_\theta}\right)\right]^2}\frac{5.83}{(1-f_\theta)}\frac{\partial f_\theta}{\partial t} \tag{A1.11}$$

The term $\left[1-0.0146\left(\frac{0.84-6.67f_\theta}{1-f_\theta}\right)\right]^2$ is approximately equal to 1. Therefore, Equation (A1.11) can be simplified as

$$\frac{3}{L_o}\frac{dL}{dt} = -\frac{\rho_o}{\rho_{\gamma(T,C=0)}}0.0146\frac{5.83}{(1-f_\theta)}\frac{\partial f_\theta}{\partial t}$$

$$\frac{dL}{dt} = \frac{\rho_o L_o 0.08511}{3\rho_{\gamma(T,C=0)}}\frac{\partial(ln(1-f_\theta))}{\partial t}$$

Which leaves an Euler type integration scheme as below,

$$\frac{L_2-L_1}{K} = ln\left[\frac{1-f_2}{1-f_1}\right]$$

that calculates the fraction of cementite as a function of dilatation obtained from raw dilatometry data.

$$f_{1+i} = 1-\left[(1-f_i)exp\left(\frac{L_{i+1}-L_i}{K}\right)\right] \tag{A1.12}$$

where

$$K = \frac{\rho_o L_o 0.08511}{3\rho_{\gamma(T,C=0)}}$$

Equation (A1.12) calculates the fraction of cementite as a function of dilatation obtained from raw dilatometry data.

During the derivation of phase fraction of cementite, in Equation (A1.8), it is assumed that the contribution by term $\frac{\partial f_\theta}{\partial t}\rho_o\left[\frac{\rho_{\gamma(T,C)}-\rho_\theta}{\rho_{\gamma(T,C)}\rho_\theta}\right]$ to the phase fraction calculation is negligible. Once, the phase fraction were calculated, the value of the term $\frac{\partial f_\theta}{\partial t}\rho_o\left[\frac{\rho_{\gamma(T,C)}-\rho_\theta}{\rho_{\gamma(T,C)}\rho_\theta}\right]$ was determined to be 2x10^{-6}. Error is calculated in the 7 min. isothermal hold sample by accounting this term into phase fraction calculation and it was found that the average error caused by not accounting this term is 7.6x10^{-4} i.e. 0.076%. The error caused is negligible, therefore the approximation is valid. During the derivation of phase fraction of cementite, in Equation (A1.11), it is assumed that the term $\left[1-0.0146\left(\frac{0.84-6.67f_\theta}{1-f_\theta}\right)\right]^2$ is close to unity. Once, the phase fraction were calculated, the value of the term $\left[1-0.0146\left(\frac{0.84-6.67f_\theta}{1-f_\theta}\right)\right]^2$ was calculated and the average value was found to be 0.97653. Error in the phase fraction is calculated by accounting this term, and the absolute average error caused by the approximation is 6.13x10^{-4} i.e. 0.061%, which is negligible. Therefore the approximation is justified.

Second stage of Inverse bainitic reaction: Formation of ferrite and secondary carbides

The dilatation involving the formation of ferrite and secondary carbides is treated as a pearlitic type reaction without carbon redistribution, i.e. whatever carbon is rejected due to the formation of ferrite is used up locally in the formation of secondary carbides. Performing a similar analysis as for the first stage of the transformation,

$$\frac{1}{V_o}V = \lambda_\gamma f_\gamma + \lambda_{\alpha+carbides} f_{\alpha+carbides}$$

For isothermal transformation, differentiating with respect to time,

$$\frac{1}{V_o}\frac{dV}{dt} = \lambda_\gamma\frac{\partial f_\gamma}{\partial t} + \lambda_{\alpha+carbides}\frac{\partial f_{\alpha+carbides}}{\partial t}$$

Since,

$$\frac{\partial f_{\alpha+carbides}}{\partial t} = -\frac{\partial f_\gamma}{\partial t}$$

$$\frac{1}{V_o}\frac{dV}{dt} = \frac{\partial f_{\alpha+carbides}}{\partial t}(\lambda_{\alpha+carbides} - \lambda_\gamma)$$

$$\frac{3}{L_o}\frac{dL}{dt} = \frac{\partial f_{\alpha+carbides}}{\partial t}\rho_o\left[\frac{\rho_\gamma - \rho_{\alpha+carbides}}{\rho_{\alpha+carbides}\rho_\gamma}\right]$$

Which on simplification gives a formula to calculate the fraction of ferrite and secondary carbides from the dilatation data for each time step.

$$f_{i+1} = f_i + \frac{L_{i+1} - l_i}{K_1} \tag{A1.13}$$

where

$$K_1 = \frac{\rho_o L_o}{3}\left[\frac{\rho_{\gamma(T,C\gamma')} - \rho_{\alpha+carbides}}{\rho_{\alpha+carbides}\rho_{\gamma(T,C\gamma')}}\right]$$

ρ_P is the density of ferrite and secondary carbides mixture which is obtained from rule of mixtures as [130]

$$\rho_P = \frac{\rho_\theta \rho_\alpha}{a\rho_\theta + (1-a)\rho_\alpha}$$

Here a is the mass fraction of ferrite obtained from the equilibrium phase diagram.

A1.4 Estimation of local carbon concentration in austenite using dilation curves

Carbon content estimation during first stage of transformation

The volume of specimen during the transformation is given by

$$\gamma \rightarrow \gamma_{carbondepleted} + \theta_{primary}$$

$$V = \sum V_i$$

$$V = \sum \frac{m_T f_i}{\rho_i}$$

$$V = V_o \sum \frac{\rho_o f_i}{\rho_i}$$

$$\frac{V}{V_o} = \sum \lambda_i f_i$$

For the decrease portion of dilatation, i.e. cementite formation from austenite, there is carbon redistribution. The carbon content of the parent austenite decreases due to the formation of austenite, because of which there is a decreased dilatation during the initial formation of cementite. Writing the above equation for the formation of cementite from austenite,

$$\frac{V}{V_o} = \lambda_\gamma f_\gamma + \lambda_\theta f_\theta$$

$$\frac{V}{V_o} = \lambda_\gamma - \lambda_\gamma f_\theta + \lambda_\theta f_\theta = \lambda_\gamma + f_\theta(\lambda_\theta - \lambda_\gamma)$$

Since the experiments are performed in isothermal holding condition, differentiating with respect to time gives,

$$\frac{1}{V_o}\frac{dV}{dt} = \frac{\partial \lambda_\gamma}{\partial t} - f_\theta \frac{\partial \lambda_\gamma}{\lambda t} + \frac{\partial f_\theta}{\partial t}(\lambda_\theta - \lambda_\gamma) \tag{A1.14}$$

The above equation is with the assumption that density of cementite does not vary with carbon concentration. In the above equation $\lambda_\gamma = \frac{\rho_o}{\rho_{\gamma(T,C)}}$.

$$\frac{\partial \lambda_\gamma}{\partial t} = -\frac{\rho_o}{\rho_{\gamma(T,C)}}\frac{1}{\rho_{\gamma(T,C)}}\frac{\partial \rho_\gamma}{\partial t} = -\frac{\rho_o}{\rho_{\gamma(T,C)}}\frac{1}{\rho_{\gamma(T,C)}}\frac{\partial \rho_\gamma}{\partial C_\gamma}\frac{\partial C_\gamma}{\partial t} \tag{A1.15}$$

$$\rho_{\gamma(T,C)} = \rho_{\gamma(T,C=0)}(1 - 0.0146\%C) \tag{A1.16}$$

$$\frac{\partial \rho_{\gamma(T,C)}}{\partial C_\gamma} = -\rho_{\gamma(T,C=0)}0.0146 \tag{A1.17}$$

Substituting Equation (A1.16) and Equation (A1.17) in Equation (A1.15),

$$\frac{\partial \lambda_\gamma}{\partial t} = \frac{\rho_o}{\rho_{\gamma(T,C=0)}}\frac{0.0146}{(1 - 0.0146\%C)^2}\frac{\partial C_\gamma}{\partial t} \tag{A1.18}$$

Substituting Equation (A1.18) in Equation (A1.14),

$$\frac{1}{V_o}\frac{dV}{dt} = \frac{\rho_o}{\rho_{\gamma(T,C=0)}}\frac{0.0146}{(1 - 0.0146\%C)^2}\frac{\partial C_\gamma}{\partial t}(1 - f_\theta) + \frac{\partial f_\theta}{\partial t}\rho_o\left[\frac{\rho_{\gamma(T,C)} - \rho_\theta}{\rho_{\gamma(T,C)}\rho_\theta}\right]$$

Approximation 1: The second term in the above equation is negligible and is assumed zero.

$$\frac{1}{V_o}\frac{dV}{dt} = \frac{\rho_o}{\rho_{\gamma(T,C=0)}}\frac{0.0146}{(1 - 0.0146\%C)^2}\frac{\partial C_\gamma}{\partial t}(1 - f_\theta) \tag{A1.19}$$

Writing mass balance with respect to carbon,

$$C_\gamma f_\gamma + C_\theta f_\theta = 0.84$$

$$\begin{aligned} C_\gamma &= \frac{0.84 - 6.67 f_\theta}{1 - f_\theta} \\ \frac{\partial C_\gamma}{\partial t} &= -\frac{5.83}{(1-f_\theta)^2}\frac{\partial f_\theta}{\partial t} \end{aligned} \tag{A1.20}$$

Substituting Equation (A1.20) in Equation (A1.19),

$$\frac{1}{V_o}\frac{dV}{dt} = -\frac{\rho_o}{\rho_{\gamma(T,C=0)}}\frac{0.0146}{\left[1 - 0.0146\left(\frac{0.84-6.67f_\theta}{1-f_\theta}\right)\right]^2}\frac{5.83}{(1-f_\theta)}\frac{\partial f_\theta}{\partial t}$$

$$\begin{aligned} \frac{3}{L_o}\frac{dL}{dt} &= -\frac{\rho_o}{\rho_{\gamma(T,C=0)}}0.0146\frac{5.83}{(1-f_\theta)}\frac{\partial f_\theta}{\partial t} \\ \frac{dL}{dt} &= \frac{\rho_o L_o 0.08511}{3\rho_{\gamma(T,C=0)}}\frac{\partial(ln(1-f_\theta))}{\partial t} \end{aligned}$$

Which leaves an Euler typer integration scheme as below,

$$\frac{L_2 - L_1}{K} = ln\left[\frac{1-f_2}{1-f_1}\right]$$

Which on further simplification leaves,

$$f_{1+i} = 1 - \left[(1-f_i)exp\left(\frac{L_{i+1}-L_i}{K}\right)\right] \tag{A1.21}$$

Where

$$K = \frac{\rho_o L_o 0.08511}{3\rho_{\gamma(T,C=0)}}$$

Thus, once the phase fraction of initial cementite nuclei is obtained from raw dilatometry data, the fraction can be substituted in Equation (A1.19) to leave an Euler integration scheme for carbon content in austenite as below:

$$C_{i+1} = C_i - \frac{5.83}{(1-f_i)^2}(f_{i+1} - f_i) \tag{A1.22}$$

Carbon content estimation during second stage of transformation

Once the phase fraction of the second stage of reaction is determined following the steps mentioned in the previous article, we can back calculate the carbon content of austenite during the second stage of transformation.

$$\frac{V}{V_o} = k\lambda_\gamma + f_p(\lambda_p - \lambda_\gamma)$$

Here k is the fraction of austenite left untransformed after stage one of the transformation.

$$\frac{1}{V_o}\frac{dV}{dt} = k\frac{\partial\lambda_\gamma}{\partial t} - f_p\frac{\partial\lambda_\gamma}{\partial t} + (\lambda_p - \lambda_\gamma)\frac{\partial f_p}{\partial t}$$

$$\frac{1}{V_o}\frac{dV}{dt} = \frac{\partial\lambda_\gamma}{\partial t}(k - f_p) + (\lambda_p - \lambda_\gamma)\frac{\partial f_p}{\partial t} \tag{A1.23}$$

From the previous model [],

$$\frac{\partial\lambda_\gamma}{\partial t} = \frac{\rho_o}{\rho_{\gamma(T,C=0)}}\frac{0.0146}{(1-0.0146\%C)^2}\frac{\partial C_\gamma}{\partial t} \tag{A1.24}$$

Substituting Equation (A1.24) in the Equation (A1.23),

$$\frac{1}{V_o}\frac{dV}{dt} = \frac{\rho_o}{\rho_{\gamma(T,C=0)}}\frac{0.0146}{(1-0.0146\%C)^2}\frac{\partial C_\gamma}{\partial t}(k - f_p) + (\lambda_p - \lambda_\gamma)\frac{\partial f_p}{\partial t}$$

$$\frac{3}{L_o}\frac{dL}{dt} = \frac{\rho_o}{\rho_{\gamma(T,C=0)}}\frac{0.0146}{(1-0.0146\%C)^2}\frac{\partial C_\gamma}{\partial t}(k - f_p) + (\lambda_p - \lambda_\gamma)\frac{\partial f_p}{\partial t}$$

$$\frac{3}{L_o}\frac{dL}{dt} = \frac{\rho_o}{\rho_{\gamma(T,C=0)}}(k - f_p)\frac{\partial\left[\frac{1}{(1-0.0146\%C_\gamma)}\right]}{\partial t} + \rho_o\left[\frac{\rho_\gamma - \rho_p}{\rho_\gamma\rho_p}\right]\frac{\partial f_p}{\partial t}$$

$$\frac{dL}{dt} = \frac{\rho_o L_o}{3\rho_{\gamma(T,C=0)}}(k - f_p)\frac{\partial\left[\frac{1}{(1-0.0146\%C_\gamma)}\right]}{\partial t} + \frac{\rho_o L_o}{3}\left[\frac{\rho_\gamma - \rho_p}{\rho_\gamma\rho_p}\right]\frac{\partial f_p}{\partial t}$$

$$\frac{dL}{dt} = A(k - f_p)\frac{\partial\left[\frac{1}{(1-0.0146\%C_\gamma)}\right]}{\partial t} + B\frac{\partial f_p}{\partial t}$$

A and B are material constants given by

$$A = \frac{\rho_o L_o}{3\rho_{\gamma(T,C=0)}}$$

$$B_i = \frac{\rho_o L_o}{3}\left[\frac{\rho_{\gamma i} - \rho_p}{\rho_{\gamma i}\rho_p}\right]$$

Once the carbon content at each time step is determined, we can calculate $\rho_{\gamma i}$ for the carbon content and substitute in B. The above equation leaves an Euler type integration scheme which can be used to calculate the carbon content of austenite during the second stage of the transformation, with carbon content of austenite calculated from the first stage as the initial input.

$$C_{i+1} = \frac{\left[1 - \frac{1}{\left[\frac{(L_{i+1}-L_i)-B_i(f\gamma_{i+1}-f\gamma_i)}{A(f\gamma_i-f_i)} + \frac{1}{1-0.0146C_i}\right]}\right]}{0.0146} \tag{A1.25}$$

A1.5 Kinetic model for inverse bainitic transformation

Here an attempt is made to model the transformation of inverse bainite using the principles of carbon diffusion and Johnson Mehl Avrami Kolmogorov (JAMK) kinetic equation. The assumption made in the kinetic model is that the transformation is controlled by the diffusion of carbon, which is a valid assumption referring to the experimental results presented in Figure A1.4.

Relative length change

The relative length change during a dilatometry experiment consists of contributions from the phase transformation and thermal deformation of individual phases [131].

$$\left(\frac{\delta L}{L_o}\right)_{total} = \left(\frac{\delta L}{L_o}\right)_{transformation} + \left(\frac{\delta L}{L_o}\right)_{thermal}$$

Since the experiments are performed under an isothermal condition, the contribution of thermal component of the relative length change is a constant and only the isothermal bainitic phase transformation needs to be take into account to model the relative length change. The overall relative length change due to phase transformation can be divided into two stages, the first stage of $\gamma \to \gamma + \theta$ transformation and the second stage of $\gamma + \theta \to \gamma + \alpha + \theta$.

$$\left(\frac{\delta L}{L_o}\right)_{transformation} = \left(\frac{\delta L}{L_o}\right)_{\gamma\to\gamma+\theta} + \left(\frac{\delta L}{L_o}\right)_{\gamma\to\gamma+\theta}$$

and the total relative length change is given by

$$\left(\frac{\delta L}{L_o}\right)_{total} = \left(\frac{\delta L}{L_o}\right)_{\gamma\to\gamma+\theta} + \left(\frac{\delta L}{L_o}\right)_{\gamma\to\gamma+\theta} + \left(\frac{\delta L}{L_o}\right)_{thermal}$$

With the assumption of isotropic volume change, the relative change in length can be expressed as a function of volume fraction of the phase and volume of the unit cell of individual phases as [132, 133]

$$\left(\frac{\delta L}{L_o}\right)_{\gamma\to\gamma+\theta} = \frac{1}{3}\frac{\left[V^o_\gamma(a^o_\gamma)^3 - V_\gamma a^3_\gamma - \frac{V_\theta}{3}a_\theta b_\theta c_\theta\right]}{V^o_\gamma(a^o_\gamma)^3} \tag{A1.26}$$

and

$$\left(\frac{\delta L}{L_o}\right)_{\gamma+theta\to\gamma+\theta} = \frac{1}{3}\frac{\left[V^o_\gamma(a^o_\gamma)^3 + \frac{V^o_\theta}{3}a^o_\theta b^o_\theta c^o_\theta - 2a^3_\alpha V_\alpha - V_\gamma a^3_\gamma\right]}{V^o_\gamma(a^o_\gamma)^3 + \frac{V^o_\theta}{3}a^o_\theta b^o_\theta c^o_\theta} \tag{A1.27}$$

Therefore, the total relative length change during the first stage of transformation is given by

$$\left(\frac{\delta L}{L_o}\right)_{total} = \frac{1}{3}\frac{\left[V^o_\gamma(a^o_\gamma)^3 - V_\gamma a^3_\gamma - \frac{V_\theta}{3}a_\theta b_\theta c_\theta\right]}{V^o_\gamma(a^o_\gamma)^3} + \left(\frac{\delta L}{L_o}\right)_{thermal} \tag{A1.28}$$

and

$$\left(\frac{\delta L}{L_o}\right)_{total} = \frac{1}{3}\frac{\left[V^o_\gamma(a^o_\gamma)^3 + \frac{V^o_\theta}{3}a^o_\theta b^o_\theta c^o_\theta - 2a^3_\alpha V_\alpha - V_\gamma a^3_\gamma\right]}{V^o_\gamma(a^o_\gamma)^3 + \frac{V^o_\theta}{3}a^o_\theta b^o_\theta c^o_\theta} + \left(\frac{\delta L}{L_o}\right)_{thermal} \tag{A1.29}$$

for the second stage of inverse bainitic transformations. The above equation has two unknowns, namely phase fraction and the lattice parameters of individual phases. The extraction of phase fraction and lattice parameter data are explained next.

Phase fraction

Using the JMAK kinetic principle, the phase fraction is obtained by calculating the volume of all growing particles. Using the concept of extended transformed volume during which the hard impingement is ignored, the actual fraction can be calculated. The actual transformed volume fraction can be obtained as [134]:

$$df = 1 - exp\left(-\frac{V^e}{V}\right) \tag{A1.30}$$

Where V^e is the extended volume and V is the total volume of the system. The extended volume is given by [135]

$$V^e = \int_0^t V\dot{N}(\tau)Y(\tau)d\tau \tag{A1.31}$$

where $\dot{N}(\tau)$ is the nucleation rate per unit volume, $Y(\tau)$ is the volume of each nuclei at time τ. The particle volume $Y(\tau)$ is given by [136]

$$Y(\tau) = g\left(\int vdt\right)^{\frac{d}{m}} \tag{A1.32}$$

Where g is the particle geometry factor (g=1 for cubic growth and g=$\frac{4\pi}{3}$ for spherical growth), d is the dimensionality of growth and m is the growth parameter (m=1 for interface controlled growth and m=2 for diffusion controlled growth) and v is the interface velocity.

From Section A1.2.2, the transformation proceeds by diffusion of carbon. Therefore the interface velocity v is the diffusion coefficient of carbon. In the case of cementite nucleation (first stage of dilatation) the growth is determined by the diffusion of carbon toward cementite (D_θ) and during the second stage of transformation, the growth of ferrite is governed by the diffusion of carbon into the surrounding austenite (D_γ). Considering a three dimensional growth of the bainitic unit, Equation (A1.32) becomes

$$Y(\tau) = \left[\int D_o^\theta exp\left(\frac{-Q_D^\theta}{RT}\right)dt\right]^{\frac{3}{2}} \tag{A1.33}$$

for the first stage of the transformation and

$$Y(\tau) = \left[\int D_o^\gamma exp\left(\frac{-Q_D^\gamma}{RT}\right)dt\right]^{\frac{3}{2}} \tag{A1.34}$$

for the second stage of the transformation.

For the initial stage of cementite nucleation, the critical nucleation rate per unit volume ($\dot{N}_\theta$) was measured using the average primary cementite size measured from ThermoCalc. The nucleation density ($\dot{N}_\theta$) was take as $\dot{N}_\theta = d_\theta^{-3}$. For the growth of ferrite, once the cementite has nucleated along the austenite grain boundaries, ferrite nucleation can occur in the carbon depleted region of the parent austenite. The width of the carbon depleted region can be predicted by *a posteriori* Auger analysis using a similar line scan as shown in Figure A1.4 at the inverse bainitic carbide/martensite (parent austenite at the isothermal hold) interface. Since the inverse bainitic carbide forms by depletion in carbon content of the parent austenite, a similar carbon concentration profile to the one illustrated in Figure A1.5 is expected. Thus enabling the width of the carbon depleted region . Therefore the nucleation

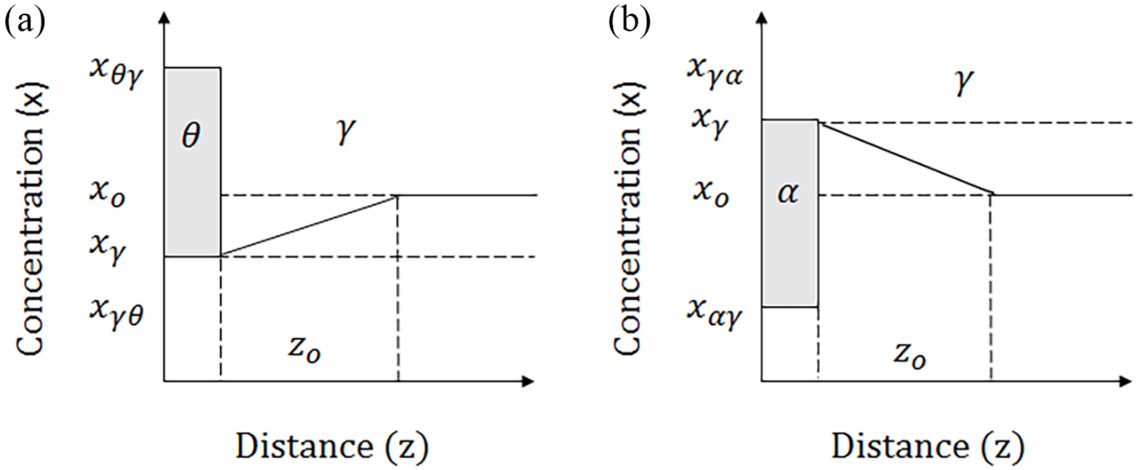

Figure A1.5: Local concentration profile vs. distance in austenite at (a) θ/γ interface and (b) θ/α interface

density ($\dot{N}_\alpha$) can be given by ($\frac{1}{d_{dep}^3}$) where d_{dep} is the width of the carbon depleted region in parent austenite. Thus, substituting Equation (A1.33) and Equation (A1.34) in Equation (A1.31) an expression for extended volume can be obtained as

$$V_e^\theta = V\left[D_o^\theta exp\left(\frac{-Q_D^\theta}{RT}\right)dt\right]^{\frac{3}{2}} \tag{A1.35}$$

for cementite, and

$$V_e^\alpha = V\left[D_o^\gamma exp\left(\frac{-Q_D^\gamma}{RT}\right)dt\right]^{\frac{3}{2}} \tag{A1.36}$$

for ferrite. Substituting Equation (A1.35) and Equation (A1.36) in Equation (A1.30), expressions for phase fraction can be obtained as

$$f_\theta^{i+1} - f_\theta^i = 1 - exp\left[\dot{N}_\theta\left(D_o^\theta exp\left(\frac{-Q_D^\theta}{RT}\right)(t_{i+1} - t_i)\right)^{\frac{3}{2}}\right] \tag{A1.37}$$

and

$$f_\alpha^{i+1} - f_\alpha^i = 1 - exp\left[\dot{N}_\alpha\left(D_o^\gamma exp\left(\frac{-Q_D^\gamma}{RT}\right)(t_{i+1} - t_i)\right)^{\frac{3}{2}}\right] \tag{A1.38}$$

The phase fractions obtained using Equation (A1.37) and Equation (A1.38) can be compared with the phase fraction obtained from dilatometry using Equation (A1.12) and Equation (A1.13). With the phase fraction of individual phases determined, they can be used to measure the relative length change as discussed in Section A1.5 and Equation (A1.28) and Equation (A1.29). To determine the time instant from when Equation 18 needs to be applied to calculate the inverse bainitic ferrite fraction, one has to know the carbon content of the austenite. With the carbon content of austenite, the thermodynamic driving force for the formation of ferrite from austenite can be calculated using ThermoCalc. The local carbon content determination of austenite is discussed next.

Local carbon concentration and transition in kinetics

The concentration profile of austenite at the θ/γ and θ/α interface are shown in Figure A1.5. Here $x_{\theta\gamma}$ is the carbon concentration of cementite (6.67 Wt.%), $x_{\alpha\gamma}$ is the carbon concentration of cementite (0.02 Wt.%), $x_{\gamma\theta}$ is the carbon concentration of austenite in equilibrium with cementite, and $x_{\gamma\alpha}$ is the carbon concentration of austenite in equilibrium with ferrite. Concentrations $x_{\gamma\theta}$ and $x_{\gamma\alpha}$ can be obtained by constructing tie line at the experimental temperature (773.15 K) and determining the carbon concentration at the extended γ/θ and γ/α phase boundaries as shown in Figure A1.6.

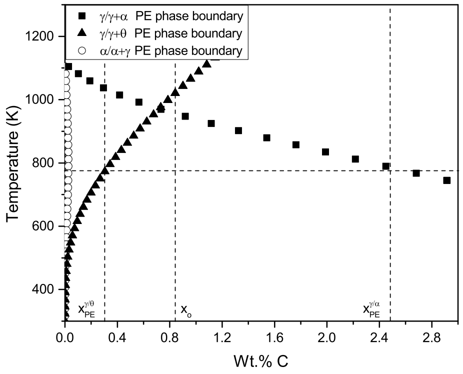

Figure A1.6: Paraequilibrium phase boundaries predicted using TCFE6 database of ThermoCalc

The width of the carbon concentration profile in austenite is z_o, which at the final instant of a transformation is available using the EDX/Auger line scan profiles. The concentration profile ahead of the interface can be given by an exponential function for diffusion-controlled phase transformations as [137]

$$x = x_o + (x_{\gamma\theta} - x_o)exp\left(\frac{-z}{z_o}\right) \tag{A1.39}$$

for cementite in austenite, and

$$x = x_o + (x_{\gamma\alpha} - x_o)exp\left(\frac{-z}{z_o}\right) \tag{A1.40}$$

for ferrite in austenite. Differentiating with time

$$\frac{dx}{dt} = -\left(\frac{x_{\gamma\theta} - x_o}{z_o}\right)exp\left(\frac{-z}{z_o}\right)\frac{dz}{dt}$$

$$x_{i+1} - x_i = -\left(\frac{x_{\gamma\theta} - x_o}{z_o}\right)exp\left(\frac{-z_i}{z_o}\right)(z_{i+1} - z_i) \tag{A1.41}$$

Where z_i is the thickness of the cementite at instant i. Similarly for the ferrite transformation

$$x_{i+1} - x_i = -\left(\frac{x_{\gamma\alpha} - x_o}{z_o}\right)exp\left(\frac{-z_i}{z_o}\right)(z_{i+1} - z_i) \tag{A1.42}$$

Calculation procedure for carbon concentration from cementite thickness and carbon concentration profile measurements

1. Through *a posteriori* SEM analysis, we have the final thickness (z_f) of θ and α.
2. Using the carbon diffusion equation, the cementite thickness at different time instants are back calculated.
3. The z_o input for Equation (A1.41) and Equation (A1.42) is obtained from EDX line scan profiles at different isothermal holding times.

The prediction of local carbon concentration of austenite, helps in determining the point where the inverse bainitic ferrite starts to form. Based on our previous investigation on microstructural evolution during inverse bainitic transformation, the inverse bainitic ferrite starts to form when the molar Gibb's free energy for austenite to ferrite transformation is negative (or a positive driving force for the reaction). The carbon content at which the molar Gibb's free energy become negative can be predicted using ThermoCalc [60]. With the carbon concentration predicted from ThermoCalc, transition point for the change in kinetics can be measured. The prediction of the local carbon concentration of austenite, helps in determining the lattice parameter of austenite using [91]

$$a_{o\gamma} = 0.3573 + 0.33w_c^{\gamma} + 0.0095w_Mn^{\gamma} + 0.006w_Cr^{\gamma} \tag{A1.43}$$

With the room temperature lattice parameter of austenite determined using the above equation, the lattice parameter of austenite at the isothermal holding temperature of 773.15 K was calculated using [133]

$$a_{\gamma} = a_{o\gamma}[1 + \beta_{\gamma}(T - 300)] \tag{A1.44}$$

where β_{γ} is the thermal expansion coefficients of austenite and with a value of $\beta_{\gamma} =$ 2.065 x 0^{-5} K^{-1} [138]. The lattice parameters of ferrite and cementite were assumed to be independent of carbon concentration, and were calculated for the isothermal holding temperature of 773.15 K. The lattice parameters of ferrite and cementite are give by [133]

$$a_{\alpha} = a_{o\alpha}[1 + \beta_{\alpha}(T - 300)] \tag{A1.45}$$

$$a_{\theta} = a_{o\theta}[1 + \beta_{\theta}(T - 300)] \tag{A1.46}$$

$$b_{\theta} = b_{o\theta}[1 + \beta_{\theta}(T - 300)] \tag{A1.47}$$

$$c_{\theta} = c_{o\theta}[1 + \beta_{\theta}(T - 300)] \tag{A1.48}$$

Where β_{α} and β_{θ} are the thermal expansion coefficients of ferrite and cementite. The value of the linear thermal expansion coefficient of ferrite considered in the calculations is $\beta_{\alpha} =$ 1.244 x 10^{-5} K^{-1} [138]. $a_{o\theta}$, $b_{o\theta}$, $c_{o\theta}$ were taken as 0.4524, 0.5088, and 0.6742 nm respectively [139]. β_{θ} is given by [133, 139]

$$\beta_{\theta} = 6.0\ X\ 10^{-6} + 3\ X\ 10^{-9}(T - 273) + 1.0\ X\ 10^{-11}(T - 273)^2 \tag{A1.49}$$

With the lattice parameters of individual phases determined, they can be used to measure the relative length change as discussed in Section A1.5 and Equation (A1.28) and Equation (A1.29).

A1.6 Results from the proposed algorithm and the kinetic models

The relative length change recorded from the dilatometry experiments, and the predictions from the developed kinetic model (Section A1.5) for all the isothermal holding experiments are presented in Figure A1.7. It can be seen that the two stage transformation can be well explained by considering the inverse bainitic transformation to be a diffusion controlled transformation. The phase fraction of inverse bainite obtained from dilatometry (Section A1.3), and the kinetic model (Section A1.5) for all the isothermal holding experiments are presented in Figure A1.8. It can be seen that the phase fraction calculated using the proposed algorithm is in agreement with the predicted phase fraction using the kinetic diffusion controlled model and the phase fraction evolution follows JMAK type of kinetics.

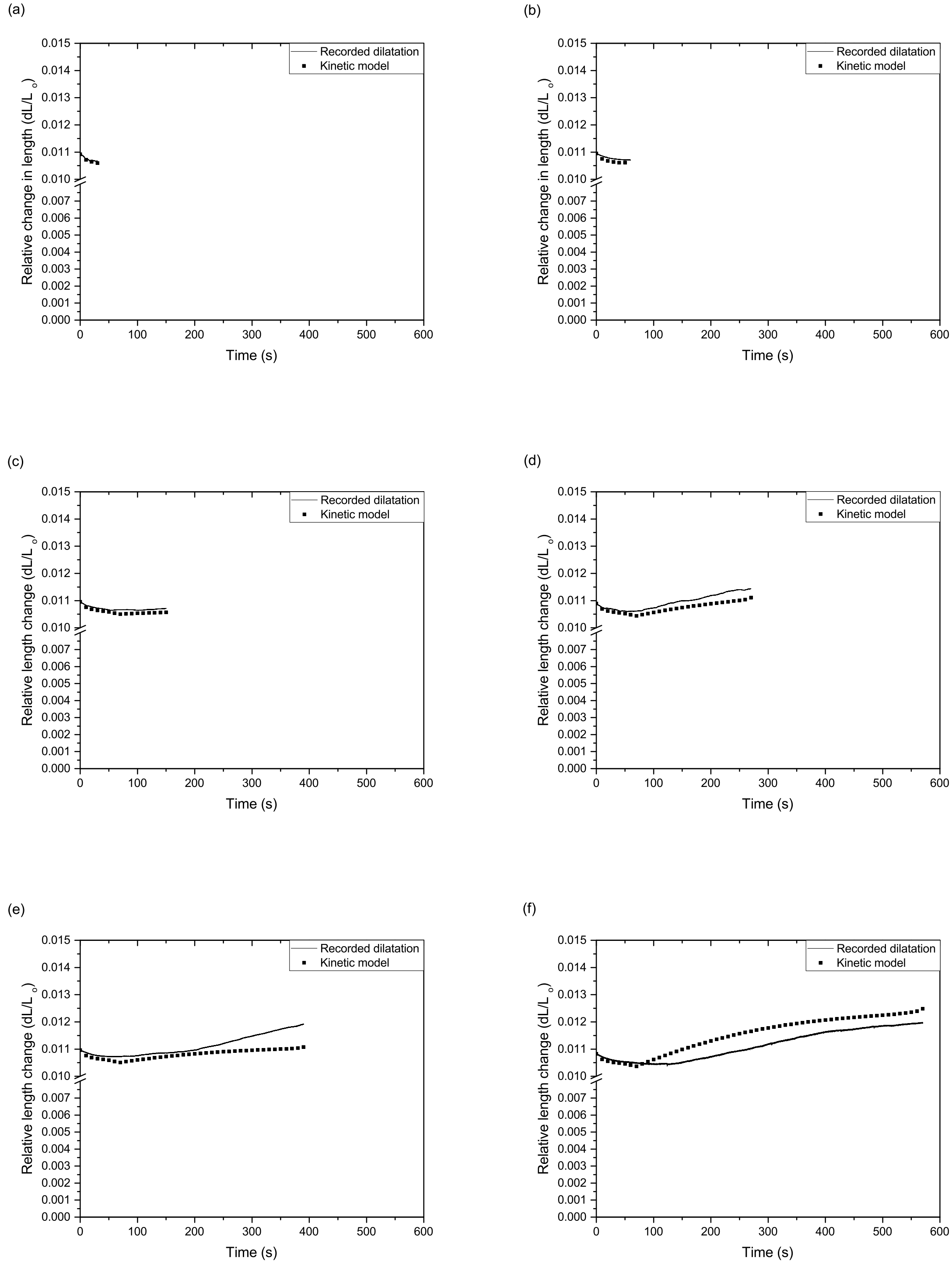

Figure A1.7: Comparison between the recorded relative length change data and the relative length change calculated using the kinetic model.

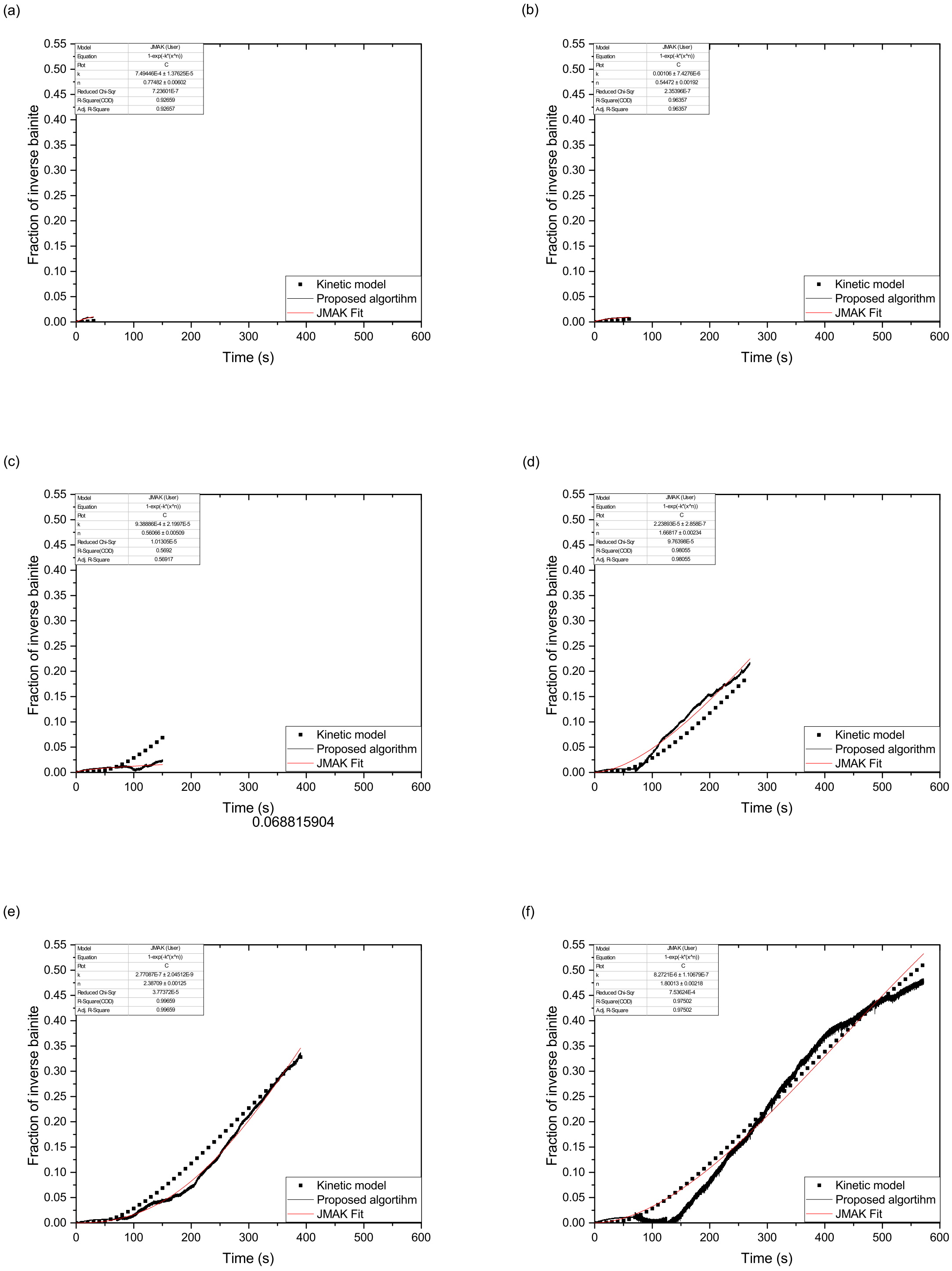

(a)

Model	JMAK (User)
Equation	1-exp(-k*(x^n))
Plot	C
k	7.49446E-4 ± 1.37625E-5
n	0.77482 ± 0.00602
Reduced Chi-Sqr	7.23601E-7
R-Square(COD)	0.92659
Adj. R-Square	0.92657

(b)

Model	JMAK (User)
Equation	1-exp(-k*(x^n))
Plot	C
k	0.00106 ± 7.4276E-6
n	0.54472 ± 0.00192
Reduced Chi-Sqr	2.35396E-7
R-Square(COD)	0.96357
Adj. R-Square	0.96357

(c)

Model	JMAK (User)
Equation	1-exp(-k*(x^n))
Plot	C
k	9.38886E-4 ± 2.1997E-5
n	0.56066 ± 0.00509
Reduced Chi-Sqr	1.01305E-5
R-Square(COD)	0.5692
Adj. R-Square	0.56917

(d)

Model	JMAK (User)
Equation	1-exp(-k*(x^n))
Plot	C
k	2.23893E-5 ± 2.858E-7
n	1.66817 ± 0.00234
Reduced Chi-Sqr	9.76398E-5
R-Square(COD)	0.98055
Adj. R-Square	0.98055

(e)

Model	JMAK (User)
Equation	1-exp(-k*(x^n))
Plot	C
k	2.77087E-7 ± 2.04512E-9
n	2.38709 ± 0.00125
Reduced Chi-Sqr	3.77372E-5
R-Square(COD)	0.99659
Adj. R-Square	0.99659

(f)

Model	JMAK (User)
Equation	1-exp(-k*(x^n))
Plot	C
k	8.2721E-6 ± 1.10679E-7
n	1.80013 ± 0.00218
Reduced Chi-Sqr	7.53624E-4
R-Square(COD)	0.97502
Adj. R-Square	0.97502

Figure A1.8: Comparison between the phase fraction of inverse bainite obtained from the proposed algorithm and the kinetic model. The red curve represents the JMAK fit.

To confirm theoretical calculations of phase fraction, the fraction of bainite in each sample were calculated using area analysis by thresholding in ImageJ^{TM}software and using Rietveld refinement of the XRD data on all the samples (Ref. [86] for the complete XRD profiles of the samples). Five optical micrographs at different magnifications were analyzed using ImageJ^{TM}to obtain the bainite fractions for each sample. It is assumed that all the white-etching constituent was martensite/retained austenite and the dark etching constituent was assumed to be bainite. The comparison between theoretical calculations, experimental bainite fractions using ImageJ, and quantitative XRD are shown in Figure A1.9. As can be seen, the calculated phase fraction from the model is well in agreement with the phase fraction obtained from the experiment.

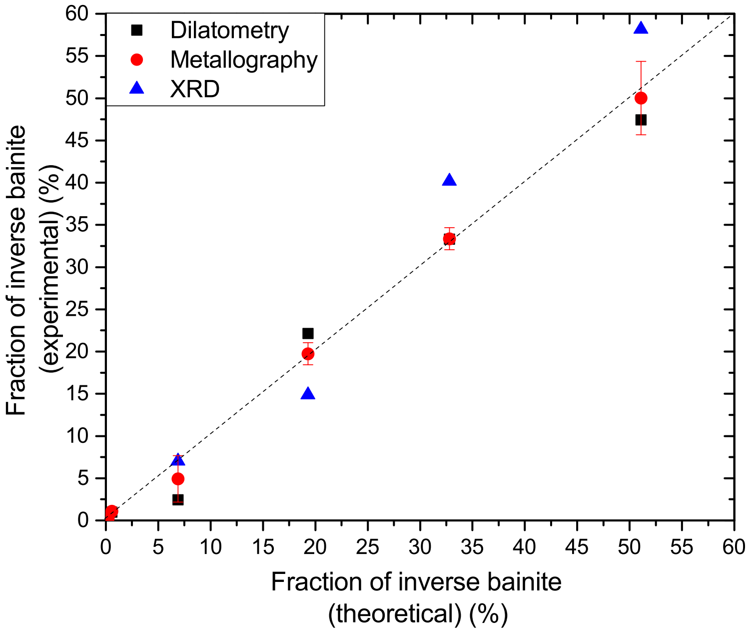

Figure A1.9: Comparison between theoretically calculated phase fraction to the actual phase fraction calculated by image processing from metallography and Rietveld refinement of XRD data.

A1.7 Discussion

In this paper, an attempt is made to quantify the observed two stage dilatation data for inverse bainitic transformation. The two stage dilatation is deconvoluted using the derivative of the length change, which enables the treatment of the raw dilatometry curve into two separate dilatation curves, one for the inverse bainitic cementite and the other for the inverse bainitic ferrite. The governing equation for the mathematical approach is the conservation of mass. With the information on the individual constituent densities, conversion to volume fraction is straight forward. The kinetics model is significant in the sense that, the predicted dilatation and the phase fraction are derived from the experimental electron microscopic analysis and the principles of thermodynamics, and independent of the recorded dilatation data. The governing equation for the kinetic model is the JMAK kinetic equation, using the concept of extended volume. The two stage transformation of inverse bainite is included in the kinetic model using the principles of driving force.

The proposed approach is generic in the sense, it can be applied to any alloy system undergoing multiple transformations simultaneously, and at any isothermal transformation temperature. With the knowledge of constituent densities and using Thermo-Calc software package, the governing equations in both the above proposed methodologies can be rewritten to suit the particular alloy system or the transformation temperature under study.

The predicted dilatation and the phase fractions do not match one to one with the recorded dilatation. Several factors can be responsible for this error in the predicted dilatation. Firstly, for the sake of mathematical simplicity, the kinetics model is derived with an assumption of an exponential function for carbon concentration at the inverse bainite/austenite interface. In reality, the concentration profile at the interface as shown in Figure A1.4 may not be exactly an exponential decay or an exponential growth. Secondly, the degenerate microstructure formation is not taken into account in the kinetic model, which can be a likely reason for the deviation between the recorded dilatation and the predicted dilatation. Finally, we have reported that the inverse bainitic microstructure has an inherently higher dislocation density than that of "conventional" bainite [86]. Garcia-Mateo *et al.* [140] have shown that the presence of dislocation in bainitic microstructure can alter the experimentally determined dilatation curve. Therefore, the current kinetic analysis, which does not take into account the presence of any dislocations, can be a likely reason for the observed deviation between the theoretically calculated dilatation and the experimentally recorded dilatation. The variation in the predicted dilatation eventually causes a deviation between the measured and the predicted phase fractions. The predicted phase fraction from the dilatometry data conversion algorithm and the kinetic model seems to match with the experimentally measured phase fractions using metallography and XRD during the initial stage of the transformation. When the transformation time is increased, a deviation in the phase fractions is observed. The likely reasoning for the deviation is that as the transformation progresses, the transformation interface can turn form a true paraequilibrium (PE) interface to a Negligible Partitioning Local Equilibrium (NPLE) interface as reported by Wang et al. [141] for bainitic transformations. In such a transition from PE to NPLE, the heavy elements (Cr and Mn) may partition locally at the interface but not through bulk redistribution. This local partitioning at the interface give rise to a concentration spike at the interface, whose width is of atomic dimensions [141]. It has been reported by Chen at al. Ref. [142,143] that such a local partitioning of Cr and Mn at the interface can retard the kinetics of the bainitic ferrite transformation. Since, the EDX results in the current analysis does not have an atomic level spatial resolution, Atom Probe Tomography (APT) is necessary to verify the Cr and Mn partitioning locally at the interface and hence the transition from a PE interface to NPLE interface. This likely explains the deviation between the predicted and the experimental phase fractions in Figure 8. Further APT analyses are being planned to verify NPLE interface of inverse bainite and the results will be published separately.

For the experiments in the present study, the Avrami exponents from fitting the phase fraction data to JMAK equation are summarized in Table A1.3. It can be seen that there is a sudden increase JMAK exponents after the transformation time of 3 minutes, such a behavior needs further discussion. The JMAK exponents can be combined as nucleation and growth parameters [144] using the relation

Table A1.3: JMAK exponents derived from fitting the phase fraction data

Isothermal duration (minutes)	JMAK exponent (n)
1.00	0.72063 ± 0.00552
1.50	0.53310 ± 0.00190
3.00	0.39454 ± 0.00227
5.00	1.44950 ± 0.00175
7.00	2.06841 ± 0.00123
10.00	1.75000 ± 0.00252

$$n = a + bc \tag{A1.50}$$

where a is the nucleation dependent term (0 for zero nucleation rate, 1 for constant nucleation rate, 0<a<1 for decreasing nucleation rate, and a>1 for increasing nucleation rate), b and c are growth dependent terms (b is the dimensionality of growth and c = 1 for interface controlled growth, c=0.5 for diffusion controlled growth). The growth of initial cementite nuclei is one dimensional growth (increase in length of midrib cementite) by diffusion of carbon. Thus, the term bc of Equation (A1.50) will be 0.5 during the initial stages of transformation (1 min., 1.5 min. and 3 min. of isothermal hold). Once the ferrite nucleation is complete, the growth occurs in two dimensions (increase in length and thickening of inverse bainitic ferrite) through diffusion of carbon, in which case bc of Equation (A1.50) will be 1. During the second stage of inverse bainite transformation (5 min., 7 min., and 10 min.), the nuclei for inverse bainite are already present (from 1 min., 1.5 min., and 3 min.), but the thermodynamic driving force for formation of cementite midrib from supersaturated austenite is always positive (as reported in our previous article) to form more nuclei of inverse bainitic unit. Thus the nucleation rate for inverse bainitic cementite is a constant. Therefore, the nucleation term a in Equation (A1.50) for the growth stage of inverse bainite (5 min., 7 min., and 10 min.) is 1. During the initial stages of the transformation (1 min., 1.5 min., and 3 min.) the cementite nuclei are site saturated at the parent austenite and the nucleation rate is close to 0. Thus, the nucleation term a in Equation (A1.50) is 0. This explains the fitted values of the JMAK exponents in Table A1.3, the sudden increase in the magnitude of JMAK exponents and the nucleation and growth behavior of inverse bainite.

A1.8 Conclusions

In this paper, an attempt is made to quantify the observed two stage dilatation data for inverse bainitic transformation. A numerical approach based on the conservation of mass is developed for the quantification of phase fraction of inverse bainite during the isothermal transformation. In order to understand the nature of inverse bainitic transformation, a kinetic model is developed using the concept of PE kinetics and JMAK kinetic equation. The predicted results from the kinetic model are in fair agreement with the results from dilatometry. Thus, the two stage transformation can be well explained by considering the inverse bainitic transformation to be a diffusion controlled transformation.

Appendix 2: FIB/TEM lift out locations

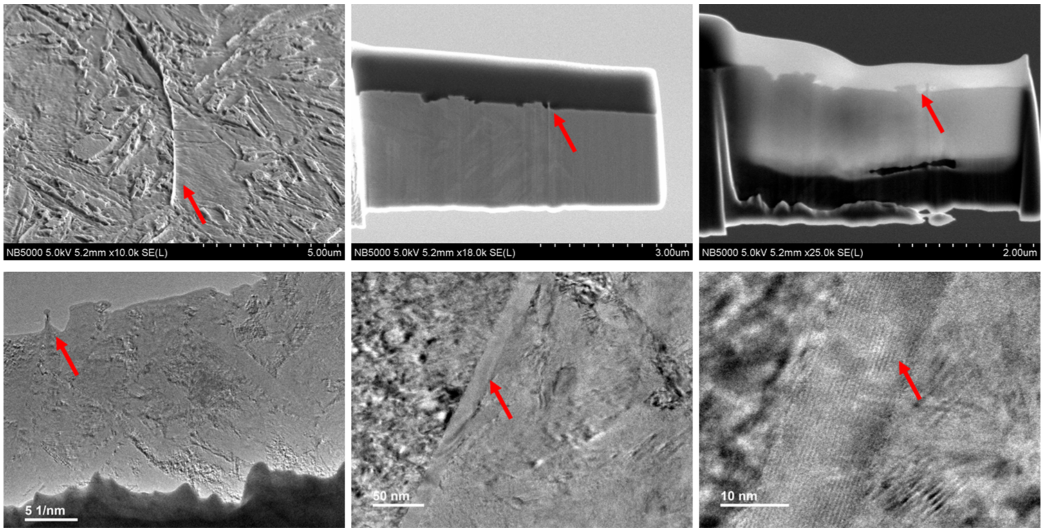

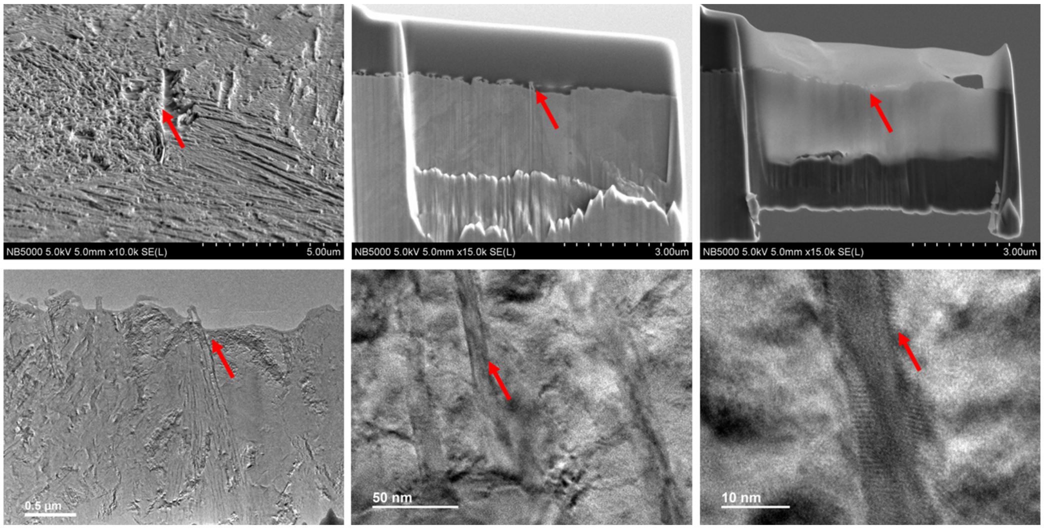

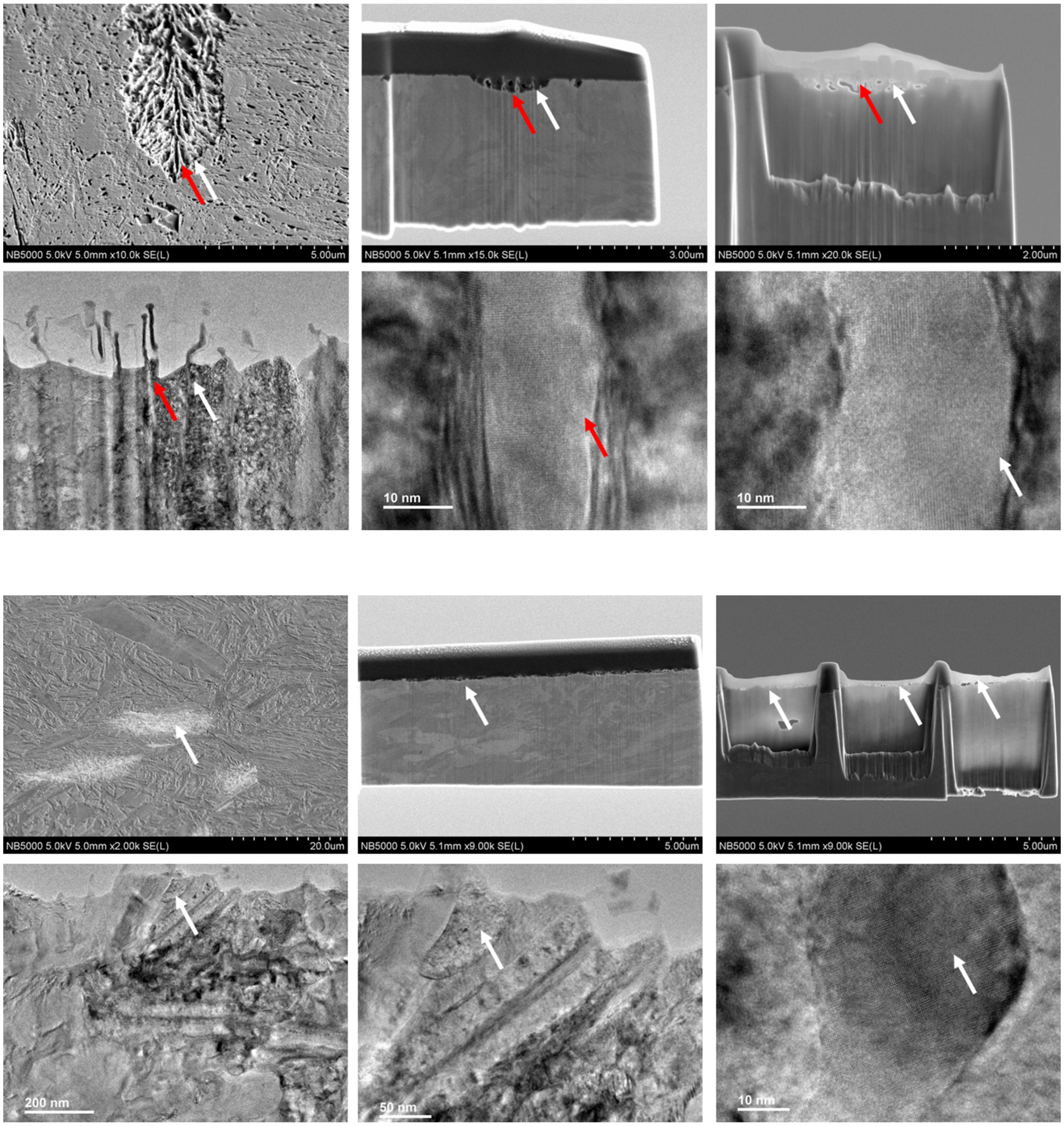

Figure A2.1: FIB liftout sequence and locations for HRTEM analysis. The location of cementite midrib and secondary cementite particles are marked by red and white arrow respectively.